Young, Massive Star Clusters in the Antennae

Thesis by

Micol Huw Christopher

In Partial Fulfillment of the Requirements

for the Degree of

Doctor of Philosophy

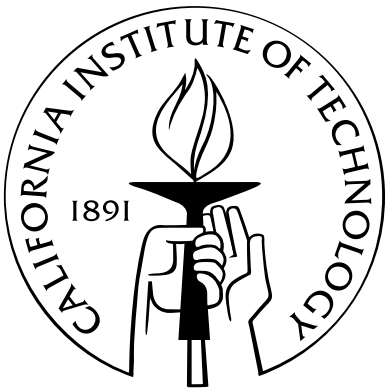

California Institute of Technology

Pasadena, California

2008

(Defended March 21, 2008)

To Chin,

Thank you!

Acknowledgements

There's a certain amount of pressure, I have realized, in writing acknowledgements. If my grad school career is any indication, this is the only part of my thesis that many future students will ever read!

All that said, there are so many people who have helped make the completion of this Ph.D. program a reality. I'd like to begin by thanking my advisor, Nick Scoville. Nick, thank you for being the perfect advisor for me - I don't know many advisors who would have not only put up with but continued to support and encourage someone who took such a different path to completing his thesis. Thank you for your guidance and insight in framing this project, your advice at the numerous times when it seemed like we had reached an insurmountable barrier, and your encouragement to pursue my love of teaching even before my thesis was completed. I would not have been writing these acknowledgements were it not for all that you have done for me!

I would like to also thank Lee Armus for all of his thoughts and ideas on this project. Our times observing together certainly made me a better research astronomer and this project would not have turned out the way it did without all of your input! You'll be happy to know that I've moved on from meat and actually added vegetables to my sandwiches now!

This work has been enhanced greatly by all the discussions I've had with Francois Schweizer. Francois, your expertise in this field is amazing — our conversations really helped to focus this thesis and your infectious enthusiasm helped me keep going!

A big thank you goes to colleagues who have shared with me their own research and data on the Antennae. Bradley Whitmore, Francois Schweizer, and Rupali Chandar gave me access to their exquisite HST imaging of the Antennae and worked tirelessly to match our cluster sample to their studies! Bernhard Brandl let us use the Palomar WIRC imaging of the Antennae before publication - this image was critical to us as we used it in our cluster selection. David Clark, Bernhard Brandl, and Steve Eikenberry gave us photometry for their entire sample of clusters in the Antennae, which allowed us to compute photometric masses for our clusters. Christine Wilson allowed and encouraged us to use her existing OVRO observations of the Antennae as a basis for our high resolution imaging and very kindly sent us electronic, reduced versions of her observations!

I would like to thank a few colleagues at Caltech in particular for their help with this project.

David Frayer and Eva Schinnerer introduced me to starburst galaxies and the art of NIRPSEC observations! John Carpenter and others in the OVRO group were incredibly helpful in learning how to observe, reduce, and analyze OVRO data. Naveen Reddy gave me a great crash course in LRIS observing and even helped out on a few observing runs! Thank you as well to my committee, Roger Blandford, Judy Cohen, Richard Ellis, Lynne Hillenbrand, Nick Scoville, and Francois Schweizer for all of your suggestions and guidance in undertaking this project!

OVRO deserves a particularly important mention as they provided a large part of my funding and support through the years! Thank you as well to the W.M. Keck Observatory for the wonderful facility that allowed this work to become a reality! Both of these facilities are funded heavily through NSF, and I thank them for their generous contributions!

Socially, I cannot thank enough all of the wonderful fellow grad students and postdocs that I've had the privilege of working with and around these past 8 1/2 years. To my classmates Edo and David, thank you for making first year classes an enjoyable experience! To my many office-mates during the years, thank you for putting up with the large number of Diet Mountain Dew cans! To the late lunch-crowd, thank you for the fun conversations and very welcome break from work! To the Astronomy department sports teams - Supernovae and Dwarf Stars, Ether Binge and Frank and Brooks Posse, the Cataclysmic Variables - I had such a great time through our athletic highs (I think we won a few championships, right?) and lows (at least we scored in the second half of that basketball game)! One advantage of being in grad school for so long is that I've had a chance to get to know so many grad students in the department - I can honestly say that I have enjoyed the time spent with everyone! The Astro Department is very special, and I'm really lucky to have been a part of it! I would also like to thank my roommates and friends outside the department over the years: Matt, Meg, James, Charlene, Dave, Neal, Tim, Carlos, Ted! You made coming home from work a fun experience and definitely helped to keep me sane!

To my new colleagues at Mt. SAC - thank you for your patience with me as I finished this thesis up! Your friendly encouragement and nudging were great! Sorry that it took so long - but at least I beat the planetarium!

To the church community at Pasadena Presbyterian Church - you adopted me from the moment that I arrived here at Caltech. Thank you for your warm friendships and support through this whole process and for giving me a chance to come into my own as a member of the church. I admire greatly what you stand for.

To the Griffith Park hiking crowd - we started off as fellow hikers and quickly became friends! Thank you for your support and gentle reminders that this thesis needs to get done! I am forever in debt to you all too since through you I met Chin!

To my mom and dad, I cannot thank you enough for all of the love and support you have given me. You created a rich environment of learning and education and encouraged me to pursue my

dreams, even when they took me far away from home! Thank you for never forcing any boundaries on me as to what I should study; thank you for teaching me so early on the importance of inquiry and of learning, of having an appetite for knowledge. I would not be where I am today if it were not for all that you have done for me! To my grandparents, Mamaw and Papaw, you always encouraged me to do the best I could - to never stop learning - I hope I've made you proud!

Finally, to Chin, my beautiful fiancee - I'm not sure I can fully put into words how much you mean to me! This thesis would not have been finished without all of your amazing love, your hugs of motivation when I was down, your patience, and your continual encouragement that I can do this! Thank you for believing in me even when I didn't believe in myself! I owe so much to you, my love! Your whole family has been so encouraging of me - I'm very excited that they are now my family too! And of course, hi to the munchkins! Thanks guys!

Chin, I can't wait to begin our married life together just 8 days after graduation! What a momentous summer! Now we can finally take time to travel! I love you!

Abstract

While massive star clusters have been detected in almost every galaxy with appreciable star formation, they are most prevalent in interacting and merging galaxies. As many as 95% of these clusters will ultimately be disrupted, often in the first 10 Myr, but those clusters that do survive may be the progenitors of globular clusters. Many questions exist regarding these massive clusters and the processes that lead to their formation and disruption, including the uniformity of these processes within a galaxy and between galaxies with different degrees of cluster formation (e.g., quiescent spirals, starbursts, and merging systems). To address these questions, we present a detailed spectroscopic survey of young, massive star clusters in the Antennae, one of the best examples of cluster formation in a merging galaxy.

Using near-infrared imaging, we selected a sample of 117 clusters to observe with a combination of near-infrared and optical spectroscopy at the W.M. Keck Observatory. These clusters were chosen to sample the major star-forming regions within the Antennae. This is the largest spectroscopic survey of young massive star clusters in any merging galaxy.

Comparing the equivalent widths of hydrogen recombination lines and CO absorption bandheads to the population synthesis models of Starburst99, we measure the age of each cluster. More than half of the clusters show the simultaneous presence of hydrogen recombination lines and CO bandheads, which is not predicted by an instantaneous burst model of cluster formation. We determine that cluster formation is better modeled by a 5 Myr duration constant rate burst of star formation, which we apply to our cluster measurements. We find the vast majority of clusters have ages between 7 and 12 Myr, with a few younger clusters. Comparing cluster ages with predictions of the temporal evolution of cluster luminosity, we find the lack of older ($>$ 12 Myr) clusters (and to a lesser extent younger ($<$ 7 Myr) clusters) is not a selection effect but a true deficit. Variation in cluster ages exists with location in the Antennae, with the youngest clusters found in the overlap region where the disks of the two galaxies coincide. We interpret these age variations as an indication that cluster disruption rates differ by location within the Antennae.

Cluster masses are measured by comparing the extinction-corrected K-band luminosity with model luminosity predictions. We find most cluster masses are between 10^5 and 10^6 $M_\odot$with a median cluster mass around 3.5×10^5 $M_\odot$. Substantial variation exists in masses between different

regions, with the overlap region having the most massive clusters on average. These mass differences can be interpreted as size-of-sample effects and our results are consistent with a uniform cluster initial mass function throughout the Antennae.

Improved spatial resolution CO (1-0) observations of the Antennae show that younger clusters coincide with areas of enhanced molecular gas concentration and, not surprisingly, also have on average higher extinctions. From two metallicity tracers, we find cluster metallicities consistent with solar values. Based on CO bandhead and SiI equivalent widths in the near-infrared spectra, we uncover strong evidence of a substantial population of M2–M4 supergiants in many of the older clusters.

Contents

List of Figures

List of Tables

Chapter 1

Introduction: Massive Star Clusters in the Antennae

1.1 Massive Star Clusters

Studies of many types of galaxies (from the Milky Way and quiescent spiral galaxies to starburst and merging galaxies) reveal that a large fraction of star formation occurs in clusters, groups, and associations. These range in size from only a handful of stars to over 10^7 stars in some of the most massive clusters (McCrady, 2005). Indeed, Lada & Lada (2003) suggest that almost all of the local star formation in the Milky Way may occur in clusters. Star formation in clusters is particularly intense within starburst and merging systems, where thousands of clusters—many with masses of 10^5 $M_\odot$ and higher—are often detected. These massive clusters, dubbed super star clusters or massive star clusters, have garnered much excitement over the past 20 years because of their possible role as progenitors to globular clusters (e.g., Gilbert & Graham, 2007), and the similarities they exhibit to less massive associations and clusters seen locally (e.g., Whitmore et al., 2007; Whitmore, 2003). While much debate exists on this issue, for the sake of this thesis we will consider a cluster to be simply a group of stars, without requiring the group to be gravitationally bound.

Prior to the launch of the Hubble Space Telescope (HST), only a handful of observations had been made of massive star cluster systems in other galaxies. For example, Schweizer (1982) and Lutz (1991) observed 6 and 14 bluish knots within merger remnants NGC 7252 and NGC 3597 respectively. Both studies suggest these knots are young star clusters formed as part of the merger process in each system. However, the knots were not resolved in either observation. Arp & Sandage (1985) obtained spectra of 2 blue knots within NGC 1569 and determined they were most likely clusters and not very bright individual stars.

The true revolution in the study of massive star clusters came with the increased resolution and sensitivity of HST. One of the earliest HST studies of massive star clusters was the work

of Holtzman et al. (1992), which detected more than 60 clusters in NGC 1275. These clusters are less than 300 million years old and most are found to be smaller than 15 pcs in diameter. Whitmore et al. (1993) and Miller et al. (1997) detected nearly 500 clusters in NGC 7252 that could be broken up into three distinct age ranges ($<$ 10 Myr, 650 Myr, and a cluster population from the progenitor galaxies). The massive star cluster population of the Antennae was also studied in great detail with HST, both before (Whitmore & Schweizer, 1995) and after (Whitmore et al., 1999) refurbishment. At least 800 and perhaps as many as 8000 star clusters have been found in the Antennae and, as with NGC 7252, Whitmore et al. (1999) find multiple age populations in the Antennae ($<$ 20 Myr, 100 Myr, 500 Myr, and a progenitor population). Massive star cluster systems have been studied in detail with HST for over 15 nearby merger systems as well as numerous starburst and spiral galaxies (see Ho (1997); Whitmore (2003); Larsen & Richtler (2000)).

Massive star clusters are found in essentially all types of galaxies undergoing active star formation (Kissler-Patig, 2000). They are particularly plentiful in merging systems and starbursts, with the largest concentrations found in merging galaxies (Whitmore, 2003). Indeed, more than 1000 clusters have been found in at least three merging systems: NGC 1275 (Carlson et al., 1998), NGC 3256 (Zepf et al., 1999), and the Antennae (Whitmore et al., 1999). In these systems, the youngest clusters tend to be found in the region where the merging galaxies overlap (Mengel, 2001; Scoville et al., 2000; Jog & Solomon, 1992). Starburst galaxies still frequently possess rich cluster populations, but only contain $\sim 10\%$ as many clusters as merging systems (Ho, 1997). Less than half of the light from young stars in starburst galaxies is produced in clusters, with the remainder coming from isolated stars (Meurer et al., 1995). In both starbursts and merging galaxies, a correlation exists between the number of young clusters and the overall star formation rate of the system (Mengel, 2001). Star clusters have even been found within isolated, non-starburst spiral galaxies (e.g. Carollo et al., 1997; Larsen & Richtler, 2000). Even in these systems, the number of young clusters is directly correlated with the star formation rate (Larsen & Richtler, 1999).

Massive star cluster masses lie in a range from 10^3–10^8 $M_\odot$ (Whitmore, 2003) with typical sizes of 3–6 parsecs (Whitmore, 2003; Schweizer et al., 1996; Miller et al., 1997; Whitmore et al., 1997; Carlson et al., 1998; Whitmore et al., 1999). While most massive star clusters observed are young (since these are the brightest clusters), a large number of massive star clusters have been dated at over 500 Myrs (Zepf et al., 1995; Schweizer et al., 1996; Schweizer & Seitzer, 1998). The older clusters are more than several hundred crossing times old and therefore likely bound.

1.1.1 Formation Mechanisms for Massive Star Clusters

Based on a Salpeter IMF, O stars are expected in clusters with $M > 10^4$ $M_\odot$. However, strong winds from these young O stars should disrupt and ultimately expel any remaining gas in a parent molecular cloud within a crossing time, thereby halting star formation and establishing a maximum

cluster mass of $\sim 10^4$ $M_\odot$ (Hills, 1980; Elmegreen & Efremov, 1997; Scoville et al., 2001). Even if more massive clusters formed, they would be bound only if the star formation efficiency of the cluster exceeded $\sim$ 0.2–0.5 (Hills, 1980; Verschueren & David, 1989), an efficiency difficult to achieve in the presence of O stars (Elmegreen, 1983). Indeed, for lower-mass embedded clusters (likely without O stars) in the solar neighborhood, Lada & Lada (2003) find star formation efficiencies $\sim$ 0.1 with a maximum efficiency of 0.33. This theoretical 10^4 $M_\odot$ limit for bound clusters matches the upper mass limit of Milky Way open clusters (Bruch & Sanders, 1983; Battinelli et al., 1994) and the truncation in the Hα luminosity function in M51 (Scoville et al., 2001).

Despite this theoretical cluster mass limit, young massive star clusters in merging galaxies, starbursts, and spiral galaxies exist with masses $> 10^4$ $M_\odot$. Furthermore, many globular clusters in the Milky Way and other galaxies exceed this $> 10^4 M_\odot$ limit; the peak of the log-normal mass distribution for Milky Way globular clusters is 2×10^5 $M_\odot$, well above the 10^4 $M_\odot$ limit (Harris, 2001). High-mass clusters thus are not only created but also survive for billions of years, forcing theories of cluster formation to adjust accordingly.

There are a number of explanations for the formation of high-mass clusters. A non-Salpeter IMF would reduce the number of high-mass stars formed in the cluster, thus reducing the disruptive effect of stellar winds. Lower metallicities within the clusters would reduce the effectiveness of radiation in disrupting the gas in a cloud (Elmegreen, 1983). Lower-mass clusters may merge to form more massive clusters (e.g., Tan & McKee, 2001). Finally, higher pressure conditions (likely from shocks) would increase the difficulty in dispersing gas from the cluster, thus resulting in a higher star formation efficiency. There is still debate, however, as to whether these higher pressure conditions require the large velocity dispersions between clusters seen in the collision of two galaxies (Kumai et al., 1993; Bekki et al., 2004) or could occur naturally in the disks of spiral galaxies (Irwin, 1994; Jog & Solomon, 1992; Schweizer et al., 1996; Elmegreen & Efremov, 1997).

An additional key question is whether the same processes describe the formation of clusters in starburst/merging galaxies and in quiescent spiral galaxies, such as the Milky Way. Open clusters and OB associations in the Milky Way are significantly less massive (by $> 1000\times$ in many instances) than young massive star clusters in merging systems such as the Antennae. Gallagher & Smith (2004) argue that star formation processes differ from starburst and merging systems to quiescent spiral galaxies. They suggest that high pressures in the interstellar medium as well as molecular cloud interactions are responsible for star clusters in mergers and starbursts. In contrast, within quiescent systems, they argue cluster formation is simply an extension of normal star formation processes. On the other hand, Elmegreen & Efremov (1997), Whitmore (2003), and Larsen (2002) argue that there is a universal cluster initial mass function (CIMF) that applies for starburst and merging systems as well as quiescent galaxies. The luminosity function of clusters (which can be taken as an approximate mass function under the assumption that clusters are all the same age) is a power

law with an index ≈ -2 for all observed cluster systems, including quiescent spirals and mergers and starbursts. There is a strong correlation between the luminosity of the brightest cluster in a galaxy and the number of clusters in the system (Whitmore, 2003; Larsen, 2002). This correlation holds not only for merging and starburst systems but also for normal spiral galaxies. Whitmore (2008) argue that more luminous (and therefore more massive) clusters are seen in merging and starburst systems simply because there are more clusters in the systems, and not because of different physical processes. They suggest that the CIMF is universal across mergers, starburst, and quiescent galaxies, and that the presence of more massive clusters in mergers is simply the statistical effect of greater sampling of the CIMF. We note that for very well-studied cluster samples, such as the Antennae (Whitmore et al., 1999; Mengel et al., 2005) and M51 (Gieles et al., 2006b) there is evidence that the luminosity function is actually a broken power law with a steeper slope at higher luminosities. This broken power law has been interpreted either as the beginning of the evolution of a young cluster population into a globular cluster population (see discussion in §1.1.2) or as a truncation to the CIMF at high masses (Gieles et al., 2006a,b).

1.1.2 The Massive Star Cluster to Globular Cluster Connection

Substantial evidence suggests that the massive star clusters seen in merging systems may be the progenitors of globular clusters. As discussed above, at least some massive star clusters are bound, and massive star clusters and globular clusters have similar radii and masses (eg. Schweizer et al., 1996; Miller et al., 1997; Whitmore, 2003).

Globular cluster populations in many elliptical galaxies are typically bimodal in color (see Zepf & Ashman (1993); Ostrov et al. (1993); Gebhardt & Kissler-Patig (1999); Larsen et al. (2001); Kundu & Whitmore (2001); and the review in Brodie & Strader (2006)). This bimodality is indicative of two globular cluster populations of differing metallicity, a metal-poor blue population and a metal-rich red population (Brodie & Strader, 2006). Additionally, elliptical galaxies have a higher specific frequency of globular clusters compared with spiral galaxies (Ashman & Zepf, 1992; Zepf & Ashman, 1993). One explanation for these observations is that the violent merger process that formed the elliptical galaxies produced a large number of new star clusters that, with time, evolved into the metal-rich globular cluster population. The progenitor globular cluster populations of the merging galaxies account for the metal-poor population (Ashman & Zepf, 1992). While the merger model is very popular in explaining the bimodal color distribution of globular clusters, there are challenges to the model and alternatives have been proposed (see Forbes et al. (1997); Cote et al. (1998); and review in Brodie & Strader (2006)).

The mass and luminosity functions of massive star clusters and globular clusters are not consistent. For globular clusters in the Milky Way and other systems, the luminosity and mass functions are both fit by a Gaussian distribution with a peak around 2×10^5 $M_\odot$ plus a low-mass/luminosity

tail (Harris, 2001; Richtler, 2003; Brodie & Strader, 2006). In contrast, in the ~ 20 systems where it has been measured, the massive star cluster luminosity function is a power law with index of ≈ -2 (see references in Whitmore (2003), Table 1; and Larsen (2006a,b)). Because of the difficulty in measuring the masses of individual massive star clusters within a system, only four systems outside of the Milky Way and Magellanic Clouds have measured cluster mass functions: M51 (Bik et al., 2003; Scoville et al., 2001), NGC 3310 and NGC 6745 (de Grijs et al., 2003b,a) and the Antennae (Zhang & Fall, 1999; Fall, 2004). For all these systems, the cluster mass function is consistent with a power law with index of ≈ -2 (Larsen, 2006a; Whitmore et al., 2007). Interestingly, the mass functions for giant molecular clouds, presumably the precursors of massive star clusters, are also typically power laws with slope of ≈ -1.6 (Scoville & Sanders, 1987).

If massive star clusters are the progenitors of globular clusters, their mass function must evolve with time to resemble the globular cluster mass function through mass loss within a cluster or the total disruption of some clusters. One of the most complete treatments of the evolution of the cluster mass function is by Fall & Zhang (2001), who consider the effect of three main processes: disruption from stellar evolution (supernovae, stellar winds, etc.), internal relaxation by two-body scattering, and gravitational shocks from clusters passing near the disk or bulge of the galaxy. When a cluster becomes gravitationally unbound, it is disrupted. This disruption happens in the early stages of a cluster's life primarily because winds from massive stars within the cluster remove the remaining interstellar medium, dramatically reducing the mass of the cluster (Fall, 2006). Recent studies of the Antennae have suggested that as many as 9 out of every 10 clusters formed may be disrupted in the first 10 Myr (Mengel et al., 2005; Fall et al., 2005; Gilbert & Graham, 2007). Similar rates of disruption are also found for Milky Way clusters (Lada & Lada, 2003). This disruption is independent of cluster mass (Fall et al., 2005). At early times stellar evolution most affects clusters at the high end of the cluster mass function, but at later times gravitational shocking dominates. Low-mass clusters primarily evolve via two-body relaxation. Fall & Zhang (2001) find that after approximately 12 Gyr both a power law and truncated power law initial cluster mass function will evolve to resemble the Milky Way globular cluster mass function, including a peak around 2×10^5 $M_\odot$ and the low-mass tail. Thus, increased interest exists in studying young massive star clusters as they likely provide an opportunity to study globular clusters as they form.

1.2 The Antennae (NGC 4038/NGC 4039)

Lying at a distance of only 19.2 Mpc (Whitmore et al., 1999), the Antennae, composed of two spiral galaxies (NGC 4038 / NGC 4039), is the closest example of an on-going major galaxy merger (Whitmore & Schweizer, 1995). It is also the first of the eleven systems included in the Toomre sequence (Toomre, 1977), suggesting that it is early in the merger process. Owing to its relative

proximity and rich population of star clusters, the Antennae is also perhaps the most widely studied merger system.

1.2.1 Dynamics of the Merger

According to dynamical models, the two disk galaxies in the Antennae first interacted around 200 Myr before its present configuration (Barnes, 1988; Mihos et al., 1993); in this first interaction the tidal tails were created (Whitmore et al., 1999). The two galaxies are currently separating (Mengel, 2001), but models suggest that within 100 Myr the merger will be complete (Barnes, 1988). The velocity fields of gas within NGC 4038 and NGC 4039 show clear deviations from pure disk rotation, while still maintaining some traces of the original disks, confirming kinematically that the merger is in an intermediate stage (Burbidge & Burbidge, 1966; Rubin et al., 1970; Amram et al., 1992). Star formation has increased steadily since the first interaction of the two galaxies and will reach its peak in 100 Myr when the merger is complete (Mihos et al., 1993). Star formation currently in the Antennae has been estimated at 20 $M_\odot$ yr^{-1} (Gilbert & Graham, 2007; Zhang et al., 2001). One advantage of the Antennae is that the two spiral galaxies are seen at large inclination, making the study of activity within the system easier (Kassin et al., 2003).

1.2.2 Massive Star Clusters in the Antennae

Some of the earliest work on star clusters in the Antennae was completed by Rubin et al. (1970), who took spectrograms of eighteen knots of enhanced emission. Whitmore & Schweizer (1995) and Whitmore et al. (1999) imaged the Antennae with HST in four broad bands (U, B, V, and I) plus Hα and found the system to be rich with young, massive star clusters. Indeed, they found between 800 and 8000 clusters in the system. The large uncertainty in the number of clusters derives from the difficulty in separating faint clusters from bright individual stars. Since the work of Whitmore et al. (1999), the Antennae cluster populations have been examined through near-infrared broad-band and narrow-band imaging studies (Mengel et al., 2005; Brandl et al., 2005), which identify over 1000 and just under 200 clusters respectively. Some spectroscopy has been conducted on selected clusters in the Antennae (see Gilbert et al. (2000); Mengel et al. (2001, 2002); Gilbert & Graham (2007)), but the total number of clusters studied spectroscopically in the Antennae is only ~ 25.

The massive star clusters in the Antennae mostly fall within the eighteen star-forming regions studied by Rubin et al. (1970), but there are still a substantial number of clusters lying outside of those regions. Figure 5a of Whitmore et al. (1999) shows these 18 knots (identified by letters), which they break into five main star-forming regions. In our study, we will focus on three of these five regions: the overlap region, which lies between the two galaxies in the region where the galaxy disks appear to coincide; the western loop, a loop of star formation to the west of the nucleus of

NGC 4038; and the northeast region, found to the north of the overlap region and to the east of the NGC 4038 nucleus. Additionally, we will consider a region of star formation not discussed as its own region in Whitmore et al. (1999): the NGC 4039 arms area, located in knots A and AA in Figure 5a of Whitmore et al. (1999).

1.2.3 Age Distribution of Clusters

The massive star clusters in the Antennae can be divided into four distinct populations based on their age (Whitmore et al., 1999). The youngest group of clusters, which is identified through Hα imaging, is less than 20 Myr old. Additional populations are found with ages of 100 and 500 Myr, along with a population of older clusters created in the individual galaxies prior to the beginning of the merger event. Whitmore et al. (1999) suggest that the 500 Myr population is a result of the first encounter of the two galaxies, acknowledging that the discrepancy between this 500 Myr age and the 200 Myr age for the first encounter, predicted by Mihos et al. (1993), is within their margin of error for cluster ages.

The population that has been studied most thoroughly is the young ($<$ 20 Myr) population (see Mengel (2001); Gilbert & Graham (2007)). Clusters in this age range are found throughout all star-forming regions in the Antennae. However, the youngest clusters ($<$ 10 Myr) are found in the overlap region and the western loop. Many of these youngest clusters are heavily obscured by dust (see the R cluster sample of Zhang et al. (2001) and the red clusters in Figure 3 of Whitmore et al. (1999)). Examining this young population, Mengel et al. (2005) find a peak cluster age of 10 Myr. However, they caution that this is a selection effect because clusters are brighter in the near-infrared between the ages of 6–20 Myr (Leitherer et al., 1999). Considering a mass-limited cluster sample gives a less-biased view of the age distribution. With such a mass-limited sample, the number of clusters is found to drop off logarithmically as a function of age (Figure 11 of Mengel et al. (2005) and Figure 2 of Fall et al. (2005)). This dropoff has been interpreted as the rapid disruption of clusters in their first 10 Myr (Whitmore, 2004; Mengel et al., 2005; Fall et al., 2005; Gilbert & Graham, 2007). Indeed Mengel et al. (2005) calculate that approximately 70% of all clusters will be destroyed in the first 10 Myr. Similar infant mortality of these clusters has also been seen in the Milky Way (Lada & Lada, 2003) and other systems (Chandar et al., 2005).

1.2.4 Mass Distribution of Clusters

Determining the mass of star clusters outside of the Milky Way neighborhood is extremely difficult. Dynamical mass estimates require both high-resolution (R $>$ 7500) spectroscopy to calculate velocity dispersions and accurate measurements of cluster radii, which is not a trivial task at the distance of the Antennae where $1'' = 93$ pc. In the Antennae only 5 clusters, all in the western loop or northeast

region, have dynamical mass estimates (Mengel et al., 2002).

However, mass measurements have been made of a larger number of Antennae clusters by comparing the observed luminosity of a cluster with the predicted luminosity from population synthesis models. These photometric estimates are less accurate than dynamical measurements because they rely on accurate values for age and extinction and the quality of the synthesis models. The only mass survey of a large sample of Antennae clusters is in Mengel et al. (2005). They find a mass distribution best fit by a broken power law with a turnover mass around 3×10^5 $M_\odot$, but caution that selection biases and uncertainties in mass measurements have strong effects on the measured mass distribution. A handful of other studies (Gilbert et al., 2000; Mengel et al., 2001; Gilbert & Graham, 2007) have measured the masses for small samples (< 10) of Antennae clusters, and their mass estimates are consistent with the mass distribution found by Mengel et al. (2005).

The cluster luminosity function is more easily measured within the Antennae. A number of studies have measured the luminosity function and find it to be a power law with slope near -2 (Whitmore et al., 1999; Mengel et al., 2005). This power law slope is consistent with measurements of more than 20 other galaxies with massive star clusters (Whitmore, 2003; Larsen, 2006a,b).

1.2.5 Observing Clusters At Different Wavelengths

Because the Antennae is one of the closest and most easily observed ongoing galaxy-galaxy mergers, it has been well studied at many wavelengths. Studies of the cluster population have focused primarily on optical and near-infrared wavelengths (e.g., Whitmore & Schweizer, 1995; Whitmore et al., 1999; Mengel et al., 2005; Brandl et al., 2005), but many observations at other wavelengths have been compared with the results from cluster population studies.

Zhang et al. (2001) provide an excellent analysis of the correlation between Antennae clusters and observations at wavelengths ranging from radio to soft X-rays. They find that embedded clusters, which are all very young ($<$ 10 Myr), are well correlated with long wavelength observations of the Antennae, including mid-infrared and far-infrared (Vigroux et al., 1996; Mirabel et al., 1998; Evans et al., 1997), millimeter (Wilson et al., 2000), and radio (Hibbard et al., 2001; Neff & Ulvestad, 2000). In comparison, the older and non-embedded clusters are correlated better with shorter wavelength observations, including far-ultraviolet (Neff et al., 1997) and X-rays (Fabbiano et al., 2003). One of the biggest problems in examining these correlations is the great disparity in spatial resolution of different wavelength surveys. For instance, the best 60μm study of the Antennae (Evans et al., 1997) has a spatial resolution of 17$''$, corresponding to 1.5 kpc at the distance of the Antennae, more than 30 times larger than the resolution of optical HST studies.

A number of studies have examined the overlap region at various wavelengths and compared their findings to the cluster distribution. This region contains the youngest and some of the most massive clusters in the Antennae (Whitmore et al., 1999). Half of the CO emission lies in the overlap region

in molecular cloud complexes ranging in mass from 2×10^6 to 9×10^8 $M_\odot$ (Wilson et al., 2000, 2003a; Stanford et al., 1990). The spatial agreement between young star clusters and the CO gas in the overlap region is not excellent, with some young star clusters as far removed as 2 kpc from the nearest appreciable CO emission. The brightest peak in mid-IR observations of the Antennae (Mirabel et al., 1998) coincides with a single cluster in the overlap region. Indeed, Mirabel et al. (1998) claim 15% of the mid-IR flux of the Antennae comes from this cluster, although recent studies have suggested that it may only contribute 4% of the total mid-IR flux (Mengel et al., 2005). This cluster, originally identified in Whitmore & Schweizer (1995) as [WS95]-80, is also the brightest optical cluster (after correcting for extinction) and the brightest radio source in the Antennae (Whitmore & Zhang, 2002). [WS95]-80 has been found to have an age of less than 4 Myr and a mass exceeding 10^7 $M_\odot$ (Gilbert et al., 2000).

Outside of the overlap region, studies have attempted to link radio and X-ray sources to Antennae clusters. Whitmore & Zhang (2002) find that 34% of 6-cm continuum radio sources (taken from Neff & Ulvestad (2000)) match up with optical clusters, and 85% of the brightest thermal radio sources have optical counterparts. This result is interesting because if the thermal radio sources are still embedded in large molecular gas and dust clouds they may be so heavily obscured as to not be visible in the optical survey. From this finding, the authors estimate that around 6 Myr is required for a cluster to clear out enough molecular gas and dust in order to reduce extinction levels to around $A_V = 1$. In Clark et al. (2007), the authors search for near-IR cluster counterparts to the 48 X-ray point sources identified in the Chandra survey of Fabbiano et al. (2001). They find 13 clusters with X-ray counterparts. These clusters are spread throughout the Antennae, especially in the overlap region and the disk of NGC 4038 (including both the western loop and the northeast region). Not included in these 13 counterparts is one X-ray source (X-37), which is also coincident with a near-infrared source. We obtained spectra of this near-infrared source, which revealed that the near-infrared and X-ray source was in fact a background quasar at a redshift of 0.26 (Clark et al., 2005).

1.3 A Spectroscopic Survey of Antennae Clusters

Despite a number of studies of the cluster populations in the Antennae, a detailed spectroscopic survey has not been undertaken. The largest spectroscopic survey for the Antennae is 17 young clusters, most located in the overlap region (Gilbert & Graham, 2007). This survey obtained high-resolution spectra ($R\sim$ 24,600) of the Brγ line. Spectroscopic surveys, while observationally time intensive, are extremely powerful because cluster spectra reveal much more about the contents and properties of a cluster than simply an image or set of images. The evolution of emission and absorption in hydrogen recombination lines, the appearance and subsequent weakening of the CO

bandheads produced by giant and supergiant populations, and the thermal contribution from dust and gas can all be seen in optical and near-infrared spectroscopy and used to estimate ages and masses of clusters. Additionally, emission lines can give direct measurements of cluster extinctions and metallicities without relying upon age measurements or synthesis models.

In this work, we present a spectroscopic survey of 117 clusters and the two nuclear regions of the Antennae. These spectra were selected in order to sample almost all regions within the Antennae containing active star formation. With these spectra and the population synthesis models of Starburst99 (Leitherer et al., 1999), we are able to measure a number of properties for each cluster, including age, mass, extinction, and metallicity. We will evaluate these cluster properties as they relate to location within the Antennae and present the first statistical analysis of the differences in cluster age and mass between different regions in the Antennae. We will additionally evaluate proposed cluster formation mechanisms and test some assumptions made in previous studies of the Antennae, including solar metallicity and an instantaneous burst of star formation. In Chapter 2 we discuss the selection procedures for the 117 clusters in our sample. We additionally detail the near-infrared and optical spectroscopic observations taken at the W.M. Keck Observatory, describe the reduction process, and present representative spectra from our sample. The following chapter (Chapter 3) describes six key diagnostic lines in our spectra that can be compared with population synthesis models to measure cluster properties. We describe each of these lines and summarize the measured equivalent widths for our cluster sample.

In Chapter 4 we derive consistent age estimates for each cluster and find that an instantaneous burst of star formation is unable to adequately describe the measured equivalent widths. Instead, we argue that a 5 Myr duration constant rate burst of star formation more appropriately fits the observed cluster equivalent widths. We analyze the cluster age distribution and discuss statistical differences between the ages of clusters in different regions of the Antennae. We also describe new CO (1-0) observations of the Antennae that we have combined with the observations of Wilson et al. (2000) to produce the highest resolution CO (1-0) maps of the Antennae. We compare these high-resolution maps with our observed cluster locations and ages.

In Chapter 5 we derive extinctions for the sample of clusters with Hα and Hβ emission line equivalent widths and analyze the variation in extinction with cluster location and age. Using the measured extinctions and photometric observations from Brandl et al. (2005) we measure photometric masses for clusters and test statistically the variation in cluster mass with location and age. We follow this analysis with a detailed examination of selection effects in our observations and particularly in our age and mass distributions and compare our distributions with previous studies.

In Chapter 6 we measure metallicities within the Antennae using two different tracers and confirm previous assumptions of solar metallicity. We also use near-infrared spectra to examine the giant and supergiant populations within the Antennae. Finally, in Chapter 7 we summarize our observations

and discuss the implications of our results for cluster formation theories.

Chapter 2

Optical and Near-Infrared Spectroscopy of 117 Antennae Clusters

2.1 Summary of Antennae Cluster Sample

Using the W.M. Keck Observatory, we obtained a combination of near-infrared and optical spectra of 117 clusters in the Antennae as well as the two nuclear regions. §2.2 details the process of selecting these 117 clusters. The near-infrared spectrograph NIRSPEC (McLean et al., 1998) was used for the near-infrared spectra, while LRIS, the Low-Resolution Imaging Spectrometer (Oke et al., 1995), was used for the optical spectra. Near-infrared spectra were taken using 14 different long slits (Table 2.1). With the exception of slit 11, each slit was observed in both H and K band. Slit 11 only has K band data because weather conditions forced an early end to observations for the night. Spectra were obtained for 42 clusters as well as across the nuclei of both NGC 4038 and NGC 4039. Four clusters (12, 49, 54, and 63) were observed in two different slits.

Six different LRIS slitmasks of Antennae clusters were observed over the course of three days (Table 2.2). The LRIS-B detector was not available on January 15, 2004, so masks 4 and 5 have only red side spectra and mask 6, which was observed both on January 15 and January 18, 2004, has ten minutes of blue side data compared with forty minutes for the red side. In total, 110 different clusters were observed with LRIS as well as the nuclei of both NGC 4038 and NGC 4039. 65 of these clusters have both red and blue spectra, while 44 have only red spectra, and one has only a blue spectrum. 29 clusters were observed in more than one mask.

Thirty-five clusters were observed with at least one LRIS detector and in at least one NIRSPEC band. Twenty of these clusters were observed with both LRIS detectors and in both NIRSPEC bands. Seventy-four clusters have only LRIS spectra, while 7 have only NIRSPEC observations. In Table 2.3 we provide more details about the distribution of cluster observations across the LRIS red

Table 2.1. Summary of NIRSPEC Observations

Date	Seeing (K Band)	Slit #	Band	Int. Time (s)	PA	Airmass
02/23/03	0.76″	1	H	1800 (6 x 300)	6°	1.31
			K	1800 (6 x 300)	6°	1.28
		2	H	900 (3 x 300)	-68°	1.31
			K	900 (3 x 300)	-68°	1.35
		3	H	900 (3 x 300)	78°	1.42
			K	900 (3 x 300)	78°	1.50
		4	H	240 (2 x 120)	-66°	1.63
			K	240 (2 x 120)	-66°	1.59
02/24/03	0.57″	5	H	900 (3 x 300)	51°	1.28
			K	900 (3 x 300)	51°	1.35
		6	H	600 (2 x 300)	10°	1.41
			K	360 (2 x 180)	10°	1.47
		7	H	360 (2 x 180)	60°	1.59
			K	360 (2 x 180)	60°	1.53
04/09/03	1.20″	8	H	1500 (5 x 300)	7°	1.36
			K	1500 (5 x 300)	7°	1.30
		9	H	1200 (4 x 300)	74°	1.32
			K	1200 (4 x 300)	74°	1.38
		10	H	900 (3 x 300)	13°	1.49
			K	600 (2 x 300)	13°	1.57
01/14/04	0.80″	11	K	600 (2 x 300)	40°	1.70
01/15/04	1.20″	12	H	1200 (2 x 600)	-48°	1.31
			K	900 (3 x 300)	-48°	1.35
		13	H	1200 (2 x 600)	63°	1.29
			K	1200 (2 x 600)	63°	1.28
		14	H	1200 (2 x 600)	-27°	1.31
			K	1200 (2 x 600)	-27°	1.36

Table 2.2. Summary of LRIS Observations

Date	Seeing	Mask #	Int. Time (min)	PA	Airmass	# of Slits on Antennae
03/08/03	0.80″	1	45 (4 × 10; 1 × 5)	0°	1.30	20
		2	55 (5 × 10; 1 × 5)	0°	1.29	18
		3	55 (5 × 10; 1 × 5)	20°	1.50	15
01/15/04	1.75″	4	60 (6 × 10)	-20°	1.34	14[a]
		5	40 (4 × 10)	0°	1.28	12[a]
		6[b]	30 (3 × 10)	20°	1.38	14[a]
01/18/04	1.04″	6[b]	10 (1 × 10)	20°	1.40	14

[a]Only LRIS-R data available

[b]Mask 6 observed both on 01/15/04 and 01/18/04. LRIS-B data only available on 01/18/04.

Table 2.3. Distribution of Cluster Observations Across LRIS Detectors and NIRSPEC Bands

LRIS		NIRSPEC		# of
Blue	Red	H	K	Clusters
Y	Y	N	N	40
N	Y	N	N	34
Y	Y	Y	Y	20
N	Y	Y	Y	9
Y	Y	N	Y	5
N	N	N	Y	4
N	N	Y	Y	3
N	Y	N	Y	1
Y	N	N	N	1
Total with LRIS B = 66				
Total with LRIS R = 109				
Total with NIRSPEC H = 32				
Total with NIRSPEC K = 42				

and blue detectors and the NIRSPEC H and K bands.

Table 2.4 lists the location of the 117 clusters in our sample. In keeping with the existing literature, we identify cluster locations as offsets from [WS-95]-442, a bright cluster near the nucleus of NGC 4038 (Whitmore & Schweizer, 1995). The specific LRIS slitmasks and NIRSPEC slits in which each cluster was observed, as well as cross-references to the cluster samples of Whitmore & Schweizer (1995), Whitmore et al. (1999), Mengel et al. (2005), and Brandl et al. (2005), are also included in Table 2.4. In total, 95 clusters have matches with the Whitmore & Schweizer (1995) survey, 90 clusters with the Mengel et al. (2005) survey, and 82 clusters with the Brandl et al. (2005) survey. For the Whitmore et al. (1999) survey we only matched our clusters with the 50 brightest clusters in their survey and found 28 matches. As the spatial resolution of our observations is less than the resolution of the HST images of Whitmore & Schweizer (1995) and Whitmore et al. (1999), some of our clusters match with more than one cluster from those studies. Table 2.5 gives the same information for our 8 observations of the nuclear regions of the Antennae. In Figure 2.1, each of the 117 clusters in our sample is identified on top of a Ks band image of the Antennae (Brandl et al., 2005). The clusters are color-coded based on the instruments (LRIS and NIRSPEC) with which they were observed. Blue clusters have both LRIS and NIRSPEC spectra, while black and red clusters were only observed with LRIS and NIRSPEC respectively. Figures 2.2, 2.3, and 2.4 give higher detail maps of the Antennae and identify each cluster by its number in Table 2.4.

As seen in Figure 2.1, the clusters in our sample are well distributed throughout the Antennae. Forty clusters are located in the western loop, 38 in the northeast region, 23 in the overlap region, and 16 are associated with the nucleus of NGC 4039 and star formation arm coming off the nucleus. The boundaries of these regions are indicated in the figure. Including a large number of clusters

Table 2.4. Antennae Cluster Sample

#	Offset[a]		Blue	Red	H	K	WS95[b]	W99[c]	M05[d]	B05[e]
	RA	Dec	Masks	Masks	Slits	Slits	Matches	Matches	Matches	Matches
1	-7.12	-85.94	2, 6	2, 6	-	-	6	-	1066	-
2	-6.41	-83.49	2, 6	2, 6	-	-	11	-	1063	83
3	-9.89	-82.56	1, 3	1, 3	-	-	12	-	1062	75
4	-9.51	-77.44	1, 3	1, 3	-	-	17, 18, 19	-	-	80
5	-8.56	-74.61	1, 3	1, 3	-	-	20	-	1052	-
6	-8.41	-70.14	1, 2, 3, 6	1, 2, 3, 6	-	-	27	-	1042	81
7	-6.22	-65.87	-	2	-	-	-	-	-	-
8	-2.68	-64.50	2, 6	2, 6	-	-	42	-	1031	-
9	-1.46	-62.42	2, 6	2, 6	-	-	45, 47	-	1020	92
10	3.98	-60.24	-	-	4	4	-	-	1013	-
11	5.87	-59.43	-	5	-	-	62	45	1001	-
12	1.65	-59.15	3	3	4, 7	4, 7	61	36	998, 1005	99
13	6.54	-58.26	-	4	-	-	67	-	990	-
14	3.92	-57.95	2	2	7	7	70	-	983, 991	105
15	28.05	-57.59	-	1, 4	2	2	80	-	-	157
16	21.40	-57.24	2, 6	2, 6	-	-	75, 77	-	972, 982, 985	132
17	5.55	-57.01	-	4, 5	7	7	84	-	974, 978	105
18	4.63	-57.00	2	2	-	-	79, 82	-	977	105
19	22.74	-54.78	2, 6	2, 6	2	2	89, 90	9, 11, 14, 20, 30, 33, 39	959	136
20	22.97	-48.78	6	5, 6	-	-	99	-	-	-
21	20.66	-48.32	2	2	-	-	-	-	-	131
22	25.42	-47.44	3	3	-	-	-	-	935, 937, 938	-
23	23.83	-47.35	-	5, 6	-	-	101	-	937, 941	145
24	24.96	-44.38	3	2, 3	-	-	-	-	-	-
25	26.91	-42.93	-	-	-	3	-	-	910	-
26	25.24	-42.84	-	2	3	3	115	-	912	148
27	22.56	-42.79	-	5	-	-	-	-	-	-
28	32.92	-40.86	-	4	-	-	117	-	899	-
29	33.75	-40.84	1	1	3	3	117, 119	17, 19	-	176
30	25.95	-40.66	-	2	-	-	-	-	896	-
31	26.36	-39.11	-	2	-	-	-	-	884	-
32	31.53	-38.98	-	4	-	-	124	-	891	168
33	22.46	-38.83	-	5	-	-	125	-	-	139
34	30.81	-37.21	-	4	-	-	127	-	870	166
35	22.62	-34.93	-	5	-	-	-	-	-	-
36	38.94	-34.07	3	3	-	-	142	5	847	198
37	30.09	-32.51	1	1, 4	-	-	148	-	832	163
38	34.01	-31.13	-	5	-	-	-	-	-	177
39	33.95	-28.70	-	5	-	-	161	-	798, 800, 804	181
40	-23.30	-27.22	3	3	-	-	166	-	777	-
41	-23.98	-25.58	3	3	-	11	170, 172	-	769	55
42	25.93	-24.69	-	1	13	13	180	-	770	153
43	27.76	-23.75	-	-	-	13	188	-	747, 755, 762	160
44	-28.38	-23.40	6	6	-	-	193	-	739, 745	51
45	25.18	-22.99	-	1	-	-	195	-	-	151
46	-24.06	-22.46	-	3	-	-	-	-	-	-
47	-28.94	-21.49	-	-	-	9	-	-	-	-
48	32.49	-21.46	2	2, 4	13	13	203, 205	-	-	173
49	-26.78	-20.93	6	6	9, 12	9, 12	208, 213	8	711	53
50	35.79	-20.61	-	6	-	-	210	-	723, 728	-
51	33.87	-20.53	2	2, 5	13	13	214	-	719, 727	180
52	-16.35	-19.39	6	6	-	11	219, 226, 230	-	681, 696	-
53	35.88	-19.33	-	6	13	13	224, 227, 228	-	684	191
54	-16.38	-18.11	6	6	9	9, 11	242	-	676	65
55	-14.72	-17.94	-	-	-	9	236, 243	25	677, 682	68
56	34.77	-15.79	2	2	-	-	266, 268	-	651	185
57	34.77	-15.79	2	2	-	-	266, 268	-	651	185
58	37.07	-15.66	-	6	-	-	264	-	638	-
59	36.64	-14.21	-	4, 5	-	-	275, 276, 278, 282	35	615	192
60	-37.38	-13.41	-	2	-	-	289	-	604	-

from all of the major star-forming regions of the Antennae in our sample will allow us to assess the variation in cluster properties within each of the regions, as well as between the regions themselves.

Table 2.4 (cont'd)

#	Offset[a] RA	Offset[a] Dec	Blue Masks	Red Masks	H Slits	K Slits	WS95[b] Matches	W99[c] Matches	M05[d] Matches	B05[e] Matches
61	-35.67	-12.85	-	4	12	12	292, 297	22	591, 600, 602, 604	39
62	-11.93	-12.38	6	6	-	11	301	28	593	-
63	-37.37	-11.37	-	2	1, 12	1, 12	317	31	572	35
64	35.28	-10.79	-	4	-	-	322	-	564	188
65	-9.93	-10.54	-	4	-	11	320, 321, 324, 327	-	561	79
66	-36.65	-10.45	-	4	-	-	323, 329	-	563, 572	38
67	31.31	-10.13	-	5	-	-	331	-	574	171
68	-38.04	-9.98	-	-	12	12	338, 339, 340	40, 46	551	34
69	38.45	-9.82	1	1	-	-	336	37	549	-
70	33.72	-9.55	2	2	5	5	342	15	544	182
71	-36.18	-9.23	-	2	-	-	345, 347	-	560	38
72	34.46	-8.64	2	2, 4	-	5	349, 354	-	543	-
73	31.62	-7.31	-	5	-	-	-	-	528	170
74	37.49	-7.29	1	1	-	5	362, 370, 374	-	519	195
75	27.51	-6.52	6	6	-	-	382	-	502	-
76	38.60	-5.60	1	1	5	5	386, 388	-	499, 501, 505	199
77	26.20	-5.28	-	4	-	-	384, 389, 392	18	469, 488, 491	154
78	28.36	-4.84	2, 6	2, 6	14	14	396	-	474	162
79	-36.66	-4.07	3	3	1	1	405	2, 29	450, 479	37
80	29.74	-3.65	2	2	-	-	409, 415	-	465	165
81	28.19	-3.18	-	-	14	14	-	-	429, 435	209
82	41.72	-3.09	2	2	5	5	417	16	446	209
83	25.11	-2.50	-	4	-	-	423	-	426, 438	149
84	29.58	-2.38	6	6	-	-	415, 420	-	401, 412, 435	164
85	42.34	-2.31	2	2	5	5	428	10	408, 430	209
86	20.71	-0.44	-	5	-	-	443	41	-	135
87	-0.23	-0.33	1	1	6	6	442, 450	3, 4	380	96
88	-36.08	3.23	-	4	1	1	479, 481, 485	12, 47, 50	294, 309	40
89	20.61	3.52	-	5	-	-	-	-	-	133
90	-35.33	3.88	3	3	1	1	483, 487	-	294	43
91	16.23	5.26	6	-	-	-	498	-	-	125
92	22.79	8.24	-	5	-	-	-	-	237, 244	-
93	18.80	9.60	1, 3, 6	1, 3	-	-	514	-	-	128, 129
94	22.70	11.87	-	5	-	-	522, 527	-	212	144
95	17.97	11.94	2	2, 4	-	-	524	-	-	127
96	17.94	13.03	2	2, 4	-	-	537	24	214	127
97	2.74	13.54	1, 3	1, 3	6	6	535, 538, 539, 541	42	198, 201, 204	107
98	19.03	15.42	2	2	-	-	-	-	194	-
99	16.98	15.81	-	4	-	-	553	-	-	126
100	-23.83	18.73	3	3, 4, 5	8	8	560, 561	44	169	58
101	-23.83	18.73	3	3, 5	-	-	560, 561	44	169	58
102	-23.86	20.14	3	3, 5	-	-	571, 581	-	151, 156, 159, 162	-
103	3.69	21.09	6	6	-	-	592	-	-	110
104	-23.54	22.32	1	1, 3, 5	8	8	605	1	142	60
105	-25.21	22.72	3	3	-	-	-	-	-	-
106	4.47	23.28	6	6	-	-	-	-	-	112
107	-24.34	23.89	3	3	-	-	620	-	128	59
108	-23.34	24.62	-	5	8	8	623, 630, 635	-	111, 112	59
109	-25.28	25.59	3	3	8	8	640	43	92	56
110	-19.94	26.37	-	1, 4	-	-	648	-	93	63
111	-21.12	27.74	-	4	-	-	-	-	76	-
112	-14.54	30.21	3	3	-	-	677, 680	-	57	71
113	-14.83	31.35	3	3	-	-	691	-	-	-
114	-4.87	31.35	1	1	-	-	690	32	45	91
115	-0.72	33.75	6	6	-	-	701, 702	-	21	103
116	-14.89	33.77	3	3	-	-	-	-	-	-
117	-4.17	34.05	1	1	-	-	704	-	-	-

[a]Offsets are in arcseconds from Cluster 442 in Whitmore & Schweizer (1995), which is Cluster 87 in our sample. Cluster 87 is at α=12^{h}01^{m}52.891^s, δ=-18°52′09.49″.

[b]Whitmore & Schweizer (1995)

[c]Whitmore et al. (1999) - Note that only the 50 brightest clusters, contained in Table 1 of Whitmore et al. (1999) are included.

[d]Mengel et al. (2005)

[e]Brandl et al. (2005)

Table 2.5. Nuclear Region Observations

#	Offset[a] RA	Offset[a] Dec	Blue Masks	Red Masks	H Slits	K Slits	WS95[b] Matches	W99[c] Matches	M05[d] Matches	B05[e] Matches
4039 Nucl S	7.68	-62.70	1	1	-	-	-	-	-	-
4039 Nucl	7.66	-61.81	1	1	4	4	49	-	1017	-
4039 Nucl N	7.64	-60.98	1	1	-	-	51	-	-	-
4039 Nucl SE	8.50	-62.17	-	-	4	4	-	-	1017	-
4039 Nucl NW	6.82	-61.45	-	-	4	4	49	-	-	-
4038 Nucl S	0.50	3.39	1	1	6	6	-	-	306	-
4038 Nucl	0.66	4.67	1	1	6	6	492	-	280, 289	-
4038 Nucl N	0.82	5.95	1	1	6	6	500, 501, 503	34, 38	260	-

[a]Offsets are in arcseconds from Cluster 442 in Whitmore & Schweizer (1995), which is Cluster 87 in our sample. Cluster 87 is at α=12^{h}01^{m}52.891^s, δ=-18°52′09.49″.

[b]Whitmore & Schweizer (1995)

[c]Whitmore et al. (1999) - Note that only the 50 brightest clusters, contained in Table 1 of Whitmore et al. (1999) are included.

[d]Mengel et al. (2005)

[e]Brandl et al. (2005)

2.2 Cluster Selection

Our cluster sample was selected from near-infrared observations of the Antennae (Brandl et al., 2005) with the Wide-Field Infrared Camera (WIRC) (Wilson et al., 2003b) at Palomar Observatory. Using a Ks band image reduces the effects of extinction, which tend to obscure the youngest clusters, particularly in the overlap region, in optical images. Using SExtractor (Bertin & Arnouts, 1996), we identified a sample of 108 objects, as well as the nuclei of NGC 4038 and 4039, in the Ks band image.

Selecting clusters throughout the major star-forming regions in the Antennae is critical for constraining the formation mechanisms of these young, massive star clusters. Previous spectroscopic work on the Antennae has focused either on samples of 4–5 clusters scattered throughout the Antennae (Mengel et al., 2001, 2002) or upon a larger sample (~ 20) located only within the overlap region (Gilbert, 2002; Gilbert & Graham, 2007). By observing a large number (> 15) of clusters in each of these four regions of active star formation in the Antennae we can search for variations in cluster properties—particularly age, mass, extinction, and metallicity—with location. Different regions have pronounced differences in molecular gas content (Wilson et al., 2000, 2003a) and are subject to differing tidal forces as part of the merger event. With our sample we can directly compare variations in cluster properties with variations in the formation environment, thus constraining formation mechanisms.

We chose a subset of these 108 clusters for our near-infrared spectroscopy, selecting clusters that would sample the four main regions of active star formation within the Antennae. Within a given region we further narrowed our sample by selecting the brightest Ks band clusters and clusters aligned so that three or more could be observed within a single slit.

We selected clusters for optical spectroscopy slitmasks with first priority given to those in our near-infrared sample. Additional clusters were chosen for the optical spectroscopy masks to maximize the number of clusters on each mask and to select brighter clusters from the Ks band image. We used **slitassign**, written by Kurt Adelberger, to determine the best arrangement of clusters on each mask. Since the clusters for the optical study were selected from the near-infrared image, the high extinctions in some parts of the Antennae, especially the overlap region, meant that approximately 5% of the clusters were not detected optically.

2.2.1 Identification of Additional Clusters

During our spectroscopy, a number of additional clusters were detected serendipitously along the NIRSPEC and LRIS slits. In most cases these additional clusters appeared in the WIRC Ks band image but were either too faint or in too close proximity to other clusters to be flagged using SExtractor. Of the 117 clusters that are included in our sample, 60 were originally identified using

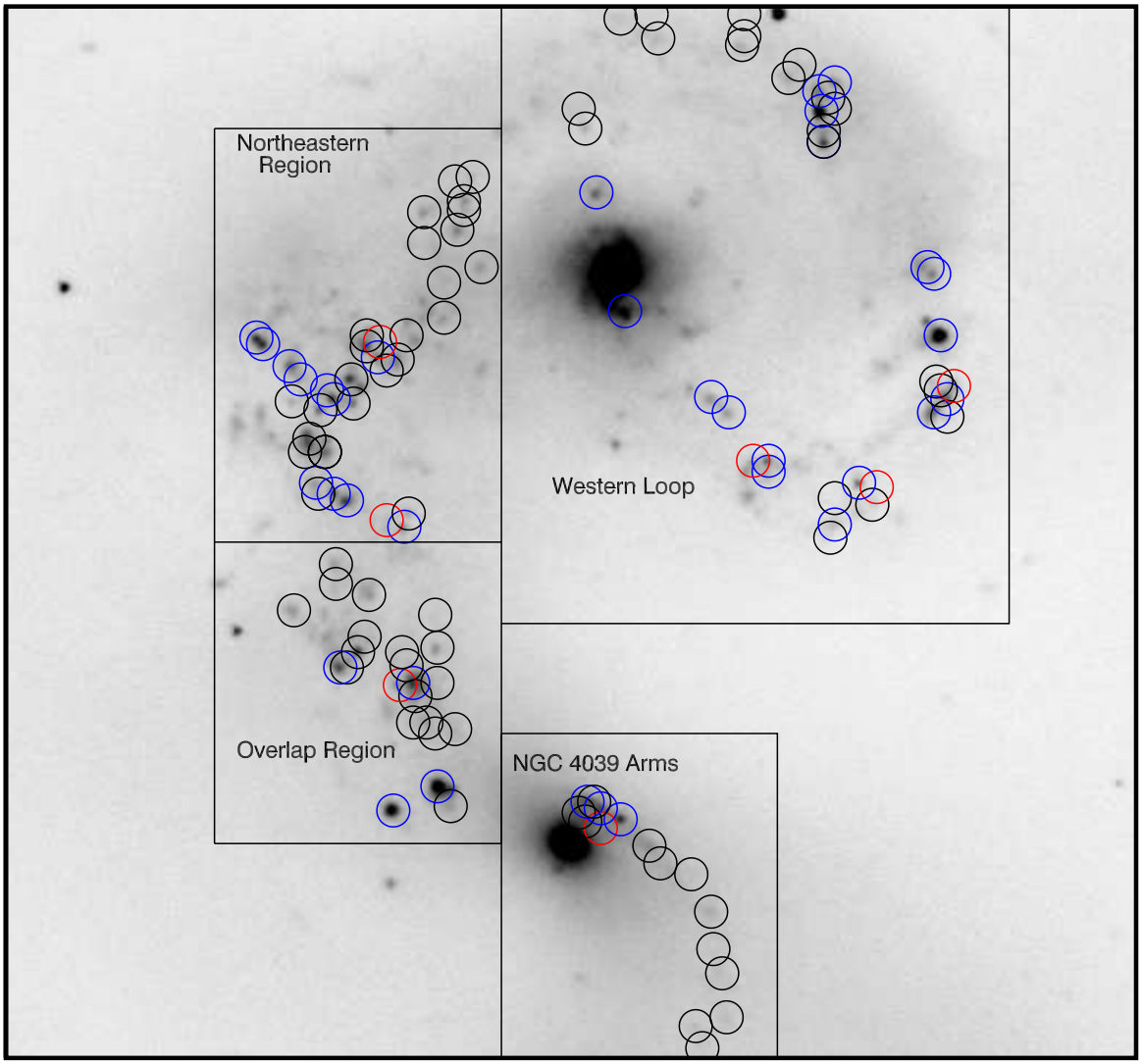

Figure 2.1 Antennae clusters observed in our spectroscopic sample overlaid upon a Ks band image from Brandl et al. (2005). Clusters marked in blue were observed with both NIRSPEC and LRIS, clusters in black only with LRIS, and clusters in red only with NIRSPEC. The boundaries of the four major star-forming regions we studied are marked. Higher-detail maps with individual clusters identified by number are found at Figures 2.2, 2.3, and 2.4.

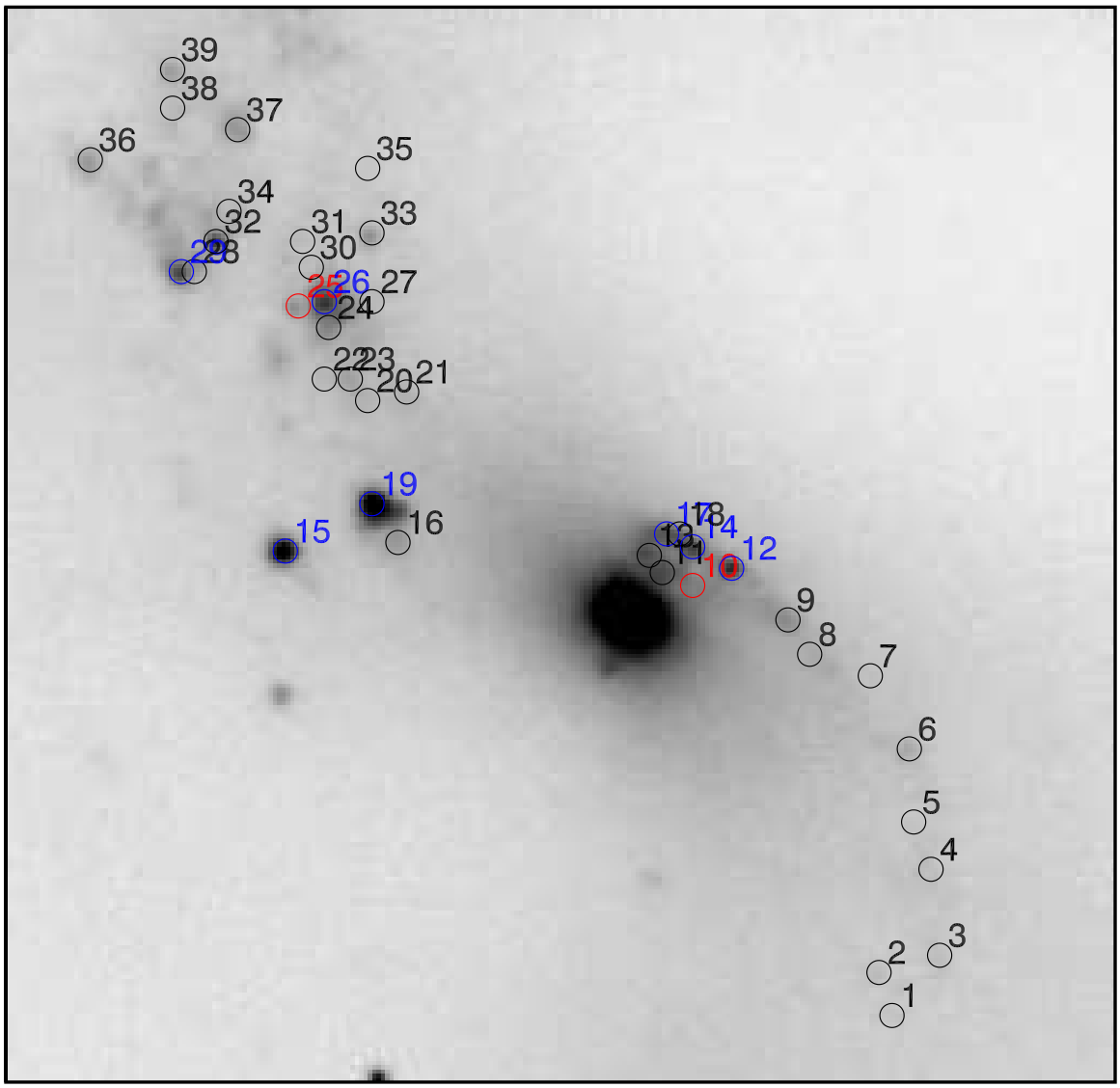

Figure 2.2 Antennae clusters observed in the NGC 4039 arms and overlap regions overlaid upon a Ks band image from Brandl et al. (2005). Clusters marked in blue were observed with both NIRSPEC and LRIS, clusters in black only with LRIS, and clusters in red only with NIRSPEC. The labels correspond to the cluster numbers found in Table 2.4.

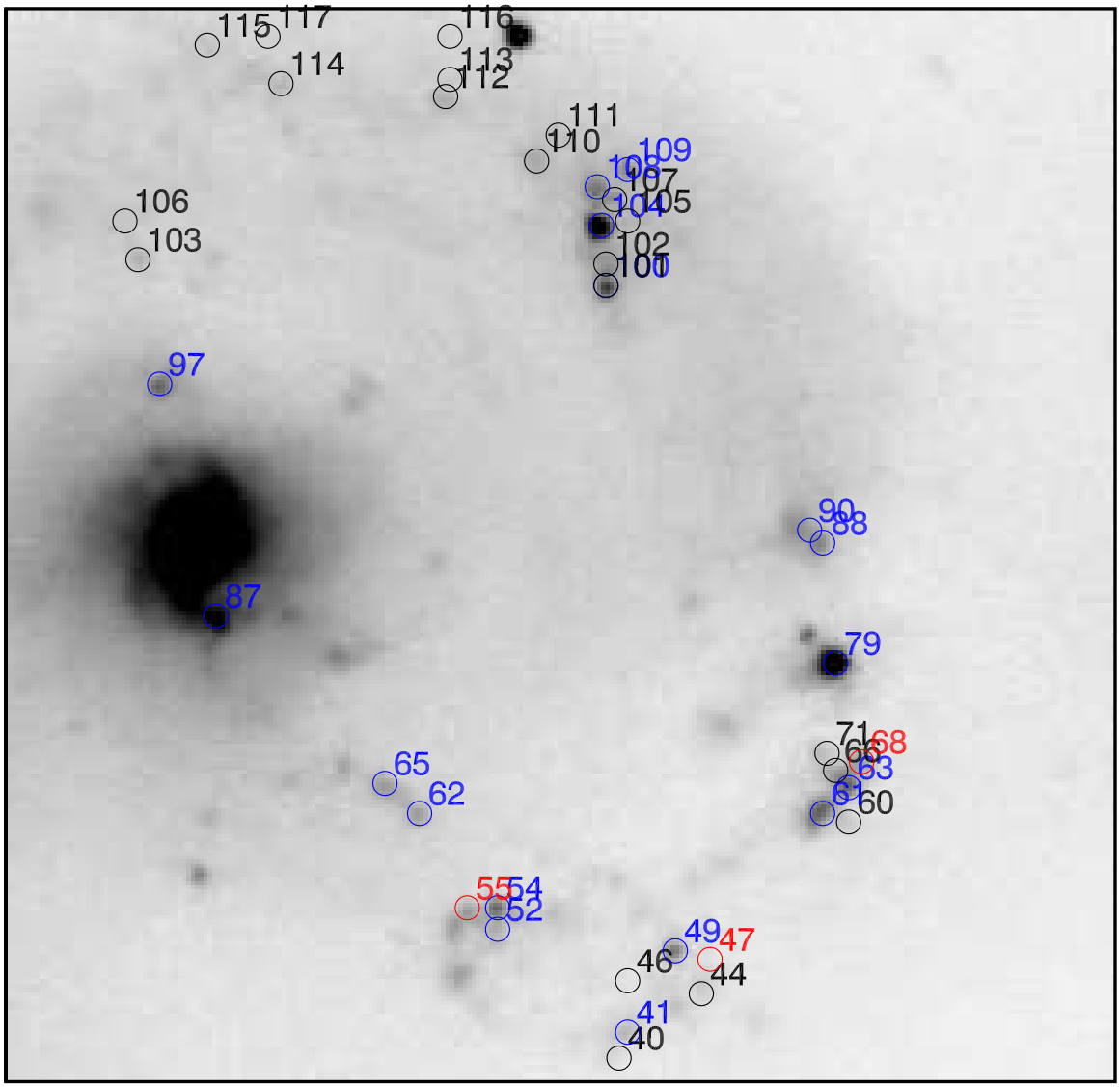

Figure 2.3 Antennae clusters observed in the Western Loop overlaid upon a Ks band image from Brandl et al. (2005). Clusters marked in blue were observed with both NIRSPEC and LRIS, clusters in black only with LRIS, and clusters in red only with NIRSPEC. The labels correspond to the cluster numbers found in Table 2.4.

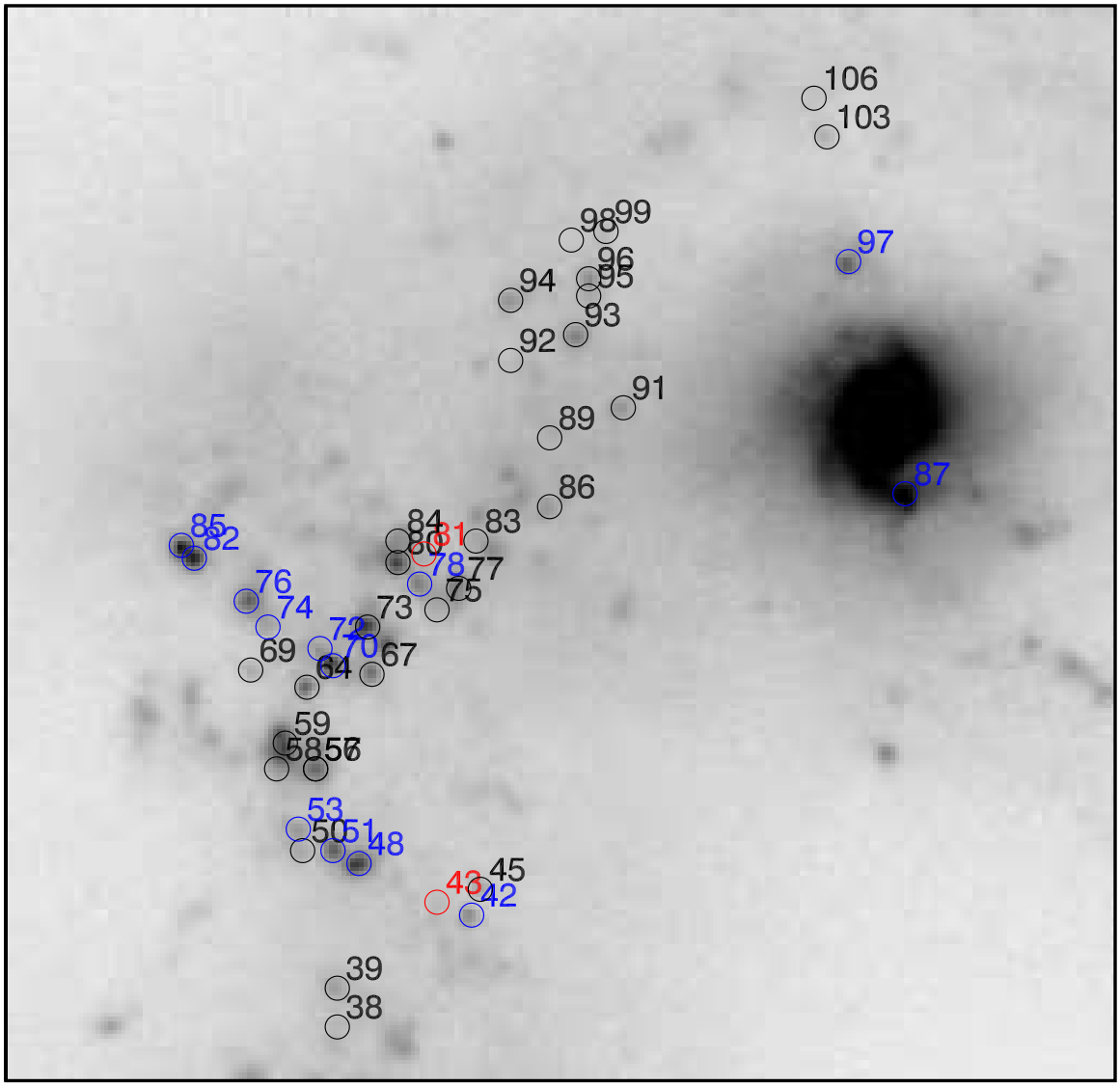

Figure 2.4 Antennae clusters observed in the northeast region overlaid upon a Ks band image from Brandl et al. (2005). Clusters marked in blue were observed with both NIRSPEC and LRIS, clusters in black only with LRIS, and clusters in red only with NIRSPEC. The labels correspond to the cluster numbers found in Table 2.4.

SExtractor in the WIRC Ks band image and the remainder were identified during the course of the spectroscopy. All 117 clusters, including those uncovered during our observations, were identified in optical HST images (Whitmore et al., 1999).

2.2.2 Magnitude Distribution of Clusters

The 32 brightest clusters in the flux-limited sample produced by SExtractor were all included in our observations. The remaining 85 clusters in our study were either selected from amongst the fainter clusters in the SExtractor sample or uncovered from our spectroscopy. Of the 117 clusters in our sample, 82 are also part of the 219 clusters uncovered by Brandl et al. (2005) in their own analysis of J and Ks WIRC images of the Antennae. Even though Brandl et al. (2005) and our survey used the same Ks band WIRC image for cluster selection and detection, our SExtractor analysis did not account for the effects of background subtraction in cluster identification and flux measurements. Therefore, when we need to rely on accurate photometry to discuss selection biases or measure cluster masses, we will use the Ks magnitudes calculated in Brandl et al. (2005).

In Figure 2.5 we plot the Ks band magnitude distribution for the 219 clusters in Brandl et al. (2005) and the 82 clusters in our sample with matches in the Brandl et al. (2005) sample. The Brandl sample peaks near an M_{Ks} = -14 and falls off at fainter luminosities, consistent with their limiting photometric magnitudes and completeness levels (Brandl et al., 2005; Clark et al., 2007). In comparison, our sample peaks almost 1 magnitude brighter at M_{Ks} = -15 and falls off at fainter magnitudes. When we separate the cluster magnitude distribution of our survey between the 60 clusters that were identified with SExtractor and the 57 that were discovered as part of the observations we see few differences in the distribution except that the original clusters are on average 0.3–0.5 mags brighter than the discovered clusters. This is not surprising as the original sample was selected to include the most easily detected clusters in the Ks band image of the Antennae.

Establishing a completeness limit for our sample is impossible due to the way our survey is constructed, but we do observe 69% of the clusters from Brandl et al. (2005) with $M_{Ks} < -15.5$. Our survey also covers 60% of clusters with M_{Ks} between -15.5 and -15. Only at magnitudes fainter than M_{Ks} = -15 do we miss a significant fraction of clusters.

2.3 Observations

2.3.1 NIRSPEC Near-Infrared Spectroscopy

Near-infrared H and K band spectra of the Antennae cluster sample were obtained separately with the Near-Infrared Echelle Spectrograph (NIRSPEC, McLean et al., 1998) at the W.M. Keck Observatory. The observations were taken over five nights during three observing runs from February

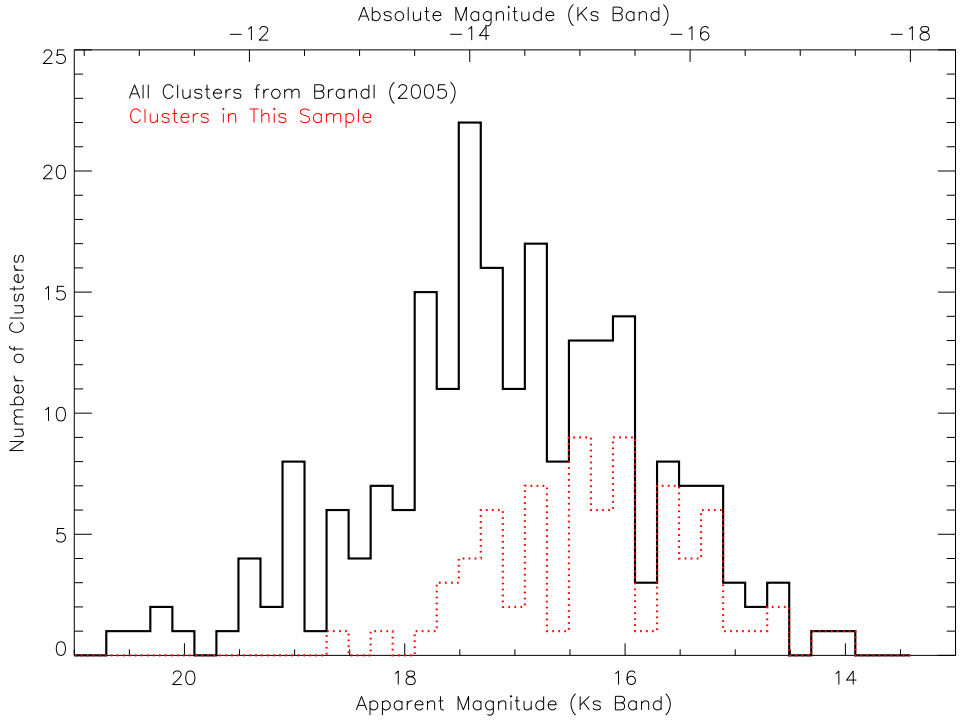

Figure 2.5 Distribution of Cluster Magnitudes for the 219 clusters (black) observed by Brandl et al. (2005). In red, we plot the magnitude distribution for the 82 clusters in our sample that are also part of the Brandl et al. (2005) survey. We assume a distance modulus of 31.41.

2003 to January 2004 (Table 2.1). We used a 42″ long-slit with a scale of 0.144″/pixel. For the H band observations, we used the Nirspec 5 (N5) filter with cross-disperser setting of 37.0, giving a spectral coverage of 1.54–1.83μm and a wavelength scale of 2.77Å/pixel. For the K band spectra, we used the Nirspec 7 (N7) filter with cross-disperser setting of 35.71, resulting in a spectral coverage of 2.05–2.47μm and a scale of 4.13Å/pixel. These settings allow for spectral coverage of the entire H band transmission window. However, the entire K band transmission window from 1.95 to 2.5μm could not be covered in a single cross-disperser setting. We chose the 2.05 - 2.47μm range in order to include all of the key K band age diagnostic lines (e.g., HeI redshifted to 2.059μm, Brγ at 2.166μm, the CO 2-0 absorption bandhead at 2.294μm, and up to 6 additional CO bandheads).

The seeing during the near-infrared observations varied significantly between nights (see Table 2.1). The best seeing was 0.57″ (in K band) on February 24, 2003, and the worst seeing (1.2″) occurred both on April 9, 2003 and January 15, 2004. Each night slit widths were adjusted for the seeing conditions. For February 24, 2003, we used the 0.57″ wide slit, while for the four other nights we used the 0.76″ wide slit, the widest slit available for NIRSPEC. For the two nights with the worst seeing conditions, the slit width was only about 2/3 of the seeing, so there were significant slit losses.

Initial centering and alignment of each slit was done using offsets and position angles calculated

from the WIRC Ks band image. Short on-source–off-source differenced images of the clusters in each slit were taken using the Slit-Viewing Camera (SCAM) of NIRSPEC and any necessary corrections to the offsets and position angles were made. Between two and six individual spectral exposures were taken in H and K band for each of the 14 slits. The integration times per exposure were typically five minutes, but as short as two minutes for the galaxy nuclei and as long as ten minutes for fainter clusters. Table 2.1 lists the total integration time for each slit in each band, as well as details about the individual exposures. Between each individual spectral exposure, the pointing center was offset along the slit between 5 and 15″ to allow for on-source sky subtraction. The offset was calculated for each slit to ensure that all the clusters remained on the slit and that clusters were not differenced onto another cluster. To confirm that the clusters remained centered in the slit, a continuous loop of short, five to ten second images was taken using SCAM during each spectral exposure. In approximately half of our exposures the clusters would slowly drift out of the slit in as little as one minute. We applied slight offsets during the course of the spectral integration to bring the clusters back within the slit. After all the spectral exposures were completed for a slit in either the H or K band and before the telescope was moved or the position angle adjusted, calibration lamp spectra were taken. The calibration spectra included a 10.5 second flatfield using the internal quartz-halogen white-light source, a 10.5 second dark frame, and 2.5 second neon and argon arc lamps for use in wavelength calibration.

A series of standard stars were observed as atmospheric calibrators. These calibrators were selected to have airmasses within 0.1 of the Antennae observations. Most calibrators were actually within 0.05 of the on-source observations. We used late F/early G and A0 dwarfs as calibrators for H and K band respectively. A0V dwarfs, while fewer in number, are excellent calibrators for the K band because their only significant variation from a blackbody spectrum in our observing window is Brγ absorption. For one H band observation (slit 7) we had to use an A0V star for atmospheric calibration because of the higher airmass of the cluster spectra. Table 2.6 gives the atmospheric calibrators observed during each of our five nights, their airmasses, and the Antennae slits to which they were applied.

2.3.2 LRIS Optical Spectroscopy

Optical spectra of the Antennae cluster sample was obtained using the Low-Resolution Imaging Spectrometer (Oke et al., 1995) at the W.M. Keck Observatory. The observations were taken during two runs: a one-night run in March 2003, and a two-night run in January 2004 (Table 2.2). Combining the LRIS-Red and LRIS-Blue detectors, we obtained continuous spectral coverage from $\sim$ 3200 to 9200Å, allowing us to cover most of the key optical diagnostic lines from [OII] at 3727Å on the blue end to the Calcium Triplet at 8498, 8552, and 8662Å on the red end. We used the D560 dichroic with the 400/3400 grism for the blue side and the 400/8500 grating for the red side to obtain

Table 2.6. Atmospheric Calibrators for NIRSPEC Observations

Date	Standard Star	Stellar Name	Band	Airmass	Slits
02/23/03	HD135299	G2V	H	1.24	1,2
	BD+442224	G2V	H	1.41	3,4
	HD132072	AOV	K	1.18	1
	HD119398	A0V	K	1.41	2
	HD116405	A0V	K	1.45	3,4
02/24/03	HD121867	G2V	H	1.32	5,6
	HD93185	A0V	H	1.50	7
	HD121884	AOV	K	1.39	5
	HD93185	A0V	K	1.50	6,7
04/09/03	HD130958	G2V	H	1.27	8,9
	HD94467	F9V	H	1.46	10
	HD138062	AOV	K	1.25	8
	HD93427	AOV	K	1.42	9,10
01/14/04	HD85589	AOV	K	1.58	11
01/15/04	HD10044	G2V	H	1.33	12,13,14
	HD93036	AOV	K	1.33	12,13,14

a spectral coverage of 3200–5700Å in the blue and 5400–9200Å in the red. This configuration yields a wavelength scale of 1.74Å/pixel on the blue side and 1.28Å/pixel on the red. The exact wavelength range covered depends on the location of the individual slit on the slitmask. The spatial pixel scale is a good complement to the NIRSPEC observations: 0.215″/pixel for LRIS-R and 0.135″/pixel for LRIS-B. Due to instrument problems, LRIS-B was not available on the night of January 15, 2004.

Six different slitmasks were used in the LRIS Antennae observations. The production files for each mask were made using **AUTOSLIT3**, written by Judy Cohen. In §2.2 we have discussed the selection of clusters for each mask. The field of view for LRIS is $6' \times 8'$ (Oke et al., 1995); however the Antennae only occupies a region of $1.5' \times 2.5'$. We could only include 12–20 Antennae clusters on each mask. We prepared the masks so that the position angle of the mask matched the Antennae hour angle at the time of observation to within approximately 10°.

Due to the uncertainty in predicting seeing conditions and the faintness of some of the clusters in our sample, we used a slitwidth of 1.5″ for each slit in our masks. Even though the spectral resolution is reduced with this wider slit, it is still sufficient for the key science: measuring fluxes and equivalent widths for the optical diagnostic lines. While the seeing was good for two of the three nights (see Table 2.2), we had 1.75″ seeing on January 15, 2004, resulting in non-negligible slit loss even with the 1.5″ slits. For the March 8, 2003 masks (#1–3) we used 4″ long slits. As we will discuss below (§2.4.2.3), identifying background regions was occasionally difficult for the short slits. Therefore, for the observations in January 2004 (masks #4–6), we increased the slitlength to 5″, trading off a reduced number of slits in each mask in return for better background subtraction.

AUTOSLIT3 maximizes the slitlengths in each individual mask, so some slits were greater than the 4″ or 5″ minimum for each mask.

Each mask was aligned on the field by using four to six square alignment slits that were centered on bright field stars surrounding the Antennae. Images were taken of the field and of the mask and a pixel offset between the alignment star locations and the alignment star slits was calculated and applied to bring the alignment stars into the alignment slits. Once the mask was aligned on the field, individual spectral exposures were taken simultaneously on the red and blue sides with an integration time of ten minutes. For the first three masks, which contained some of the brightest clusters in our sample, an initial five minute spectral exposure was taken to test for saturation levels. Small offsets (less than 1″) were applied between exposures. The net offset from the cluster center was never more than 1″ in order to insure that the clusters did not move off the ends of the 4–5″ slits.

A series of calibrator spectra were obtained twice for each mask: in the afternoon and after the spectral observations on each mask. The calibration spectra were an arc spectra with argon, cadmium, mercury, neon, and zinc lamps and a flatfield using the built-in halogen lamp. For the red-side observations, we used the night-time calibration spectra. For the blue side, however, the night-time flatfields were used along with the afternoon arc spectra. The afternoon arc spectra were chosen because two of the lamps for the blue side (zinc and cadmium) require over two minutes to warm up sufficiently to produce strong lines.

Two standard flux calibrator stars, Feige67 and G191B2B, were observed each night using the 1.5″ wide longslit mask included in LRIS. We took three spectra on each calibrator and dithered 10 to 20″ along the 175″ slit between individual exposures. Flatfields and arc lamps for the longslit were taken in the afternoon and immediately following each flux calibrator star.

2.4 Reduction

For both the NIRSPEC and LRIS reduction we created a suite of new IDL scripts to complement existing IRAF and IDL routines. Except as otherwise noted, all of the routines discussed below were written by us specifically for this project. While the basic structure of the LRIS and NIRSPEC reduction was similar, there were substantial variations in the actual reduction process.

2.4.1 NIRSPEC Reduction

2.4.1.1 Preliminary Reduction and Straightening

A composite flat field was created for each day of observations by combining the individual flat field calibration lamps taken after each slit. The flat field was normalized using the median value of the central dispersion row. A bad pixel mask was formed by combining a dead pixel list taken from the

composite flat field and a hot pixel list taken from a composite dark exposure (median-combined from ten dark exposures).

Bright cosmic rays were removed by replacing individual pixels more than 5σ above the median value of the surrounding pixels with that median value. The individual exposures were then divided by the composite flat field and bad pixels identified in the bad pixel mask were replaced with the median value of surrounding pixels.

To remove the night sky lines and sky background, we subtracted individual exposures offset by 5–15″ along the slit. We chose this on-source background subtraction over the subtraction of off-source exposures because there was ample space between individual clusters within a given slit and it yielded more observing time on the clusters themselves.

NIRSPEC spectra have spatial and spectral distortions that must be removed during the reduction process. The spatial distortion corrections were calculated once for each night by measuring the position of five to seven sources at each pixel along the dispersion axis. These sources were selected from the brightest atmospheric calibrator spectra and chosen to span the entire spatial extent of the NIRSPEC slit. The traces of these five to seven sources were fit with polynomials to determine the spatial distortion correction. This routine was modified from the **REDSPEC** package written by Lisa Prato.

We used a similar technique to remove the spectral distortion for the image and calculate a wavelength solution. A solution was determined for each band and slit. For our H band observations, we used the argon arc lamp calibrator image, while the neon arc lamp was used for K band calibration. Fifteen to twenty lines were identified in each arc lamp image and traced along the spatial extent of the slit. These traces were fit by polynomials to calculate the spectral distortion correction. Each of the background-subtracted on-source exposures was straightened using the spatial and spectral distortion corrections.

In some cases, the night sky line subtraction is not perfect and residual night sky line emission (or negative values if over-subtraction occurred) remains in the differenced exposure. For each of the straightened and differenced exposures, we calculated a median residual sky spectrum by taking the median value of the non-cluster regions of each differenced exposure at each wavelength pixel. This residual sky spectrum was subtracted from each spatial column and was very effective in removing the over or under-subtraction of the night background.

The Gaussian pixel center for the brightest cluster in the slit was measured for each individual exposure, and the derived offsets between exposures were applied to align the individual exposures. When necessary, pixel rebinning was done using cubic interpolation. The individual, aligned exposures were summed to produce a composite exposure for each slit in each band.

2.4.1.2 Atmospheric/Systematics Calibration

The reduction of the atmospheric calibrators (listed in Table 2.6) was identical to that of the cluster observations. After the composite exposure was produced for each calibrator, we extracted a spectrum for the calibrator using a wide (5× the seeing) aperture to provide a high signal-to-noise spectrum. The calibrator stars (late F and early G dwarfs for H band, and A0 dwarfs for K band) are largely featureless, except for substantial Brγ absorption in the K band and a few features at $< 5\%$ absorption in both H and K bands. To remove these features we used template spectra from Meyer et al. (1998) in the H band and Wallace & Hinkle (1997) in the K band. These template spectra are at a spectral resolution of 3000, compared with R $\sim$ 1100–1500 for our observations of the atmospheric calibrators, so each template spectrum was first smoothed to the resolution of the matching atmospheric calibrator. Stellar absorption centers were measured in both the template spectrum and the calibrator spectrum to remove any spectral offset. The H band template spectra covered the entire wavelength range of the H band atmospheric calibrator observations; however, for the K band observations, the template spectra ended at 2.4μm while our observations extended redward to 2.47μm. We assumed a featureless blackbody for the template spectra from 2.4–2.47μm. The atmospheric correction was calculated by dividing the calibrator spectrum by the shifted template spectrum and normalizing the result at the center of the band.

The best atmospheric calibration was selected and applied to each slit by dividing the combined source exposure by the atmospheric correction calculated from the calibrator observed closest in airmass to the source observations. The calibrators chosen for each slit are listed in Table 2.6. Any spectral offset between the atmospheric correction and the source spectra were measured by comparing the location of atmospheric absorption features and applying an offset to the atmospheric correction if necessary. Typical offsets were less than 0.1 pixels. The atmospheric calibration removes both the effects of the atmosphere and variations in NIRSPEC system throughput as a function of wavelength.

The final spectrum for each cluster was extracted from the atmospherically calibrated composite exposure. For isolated clusters an aperture with width 5× the seeing was used. If part of another cluster fell within this aperture region, as often happened for more crowded slits, the largest aperture possible was selected, extending out to the minimum between the clusters.

2.4.2 LRIS Reduction

2.4.2.1 Preliminary Reduction and Straightening

Each raw LRIS image was prepared for analysis by trimming the overscan region and correcting the bias using IRAF routines, **preplrisb** and **twoampproc**, for the blue and red sides, respectively. These routines were written by Alice Shapley and Kurt Adelberger.

The LRIS exposures are comprised of a series of strips, one for each slit in the slitmask. We identified the pixel ranges corresponding to each individual slit in the mask. The individual spectral exposures, arc lamps, and flat fields for each strip were extracted from the output LRIS exposure and all subsequent reduction dealt only with the individual strips and not the composite mask exposures. A constant pixel offset in the spatial direction existed between the afternoon and nighttime LRIS-B arc lamp spectra. This offset was measured manually and applied to the afternoon arcs to make sure that the correct arc was extracted for each strip.

The response of the flatfield for each strip was calculated using the IRAF routine, **response**, and applied to each arc lamp and on-source exposure. Unlike a traditional flatfield, the **response** function calculated a Legendre polynomial fit to the average flatfield along the dispersion axis and then returned the deviation from this fit at each pixel. The response for the flux calibrator was calculated in the same manner, so applying the flux calibration will remove the overall spectral shape of the flatfield. Preliminary cosmic ray removal was done using the IRAF routine, **xzap**. **Xzap** is very good at removing one-pixel, isolated cosmic rays, but less successful at identifying cosmic ray events spread over multiple pixels. These multiple-pixel events were identified and removed later in the reduction process.

The pixel offsets between individual exposures of the same slit were calculated by comparing the centers of cluster spectra. We found the offsets to be similar for each slit in a mask, so for fainter clusters we took as the pixel offset the average offset for that mask. We found very good agreement between our measured pixel offsets and the size of the dithering between exposures.

There is a curvature of up to 20 pixels in the spectra for each individual slit, especially on the blue side, which needs to be corrected for by tracing the spectra along the dispersion axis. To prepare for this tracing, each exposure on a slit was background-subtracted by a preliminary manual identification of the background region, shifted by the spatial offsets calculated above, and then summed to produce a composite background-subtracted exposure for each slit. The spectrum was traced by calculating the Gaussian centers of the spectrum along the dispersion axis and fitting these centers with a third-degree polynomial. Wavelength regions around emission lines were excluded from the fitting. If a good fit could not be made using the Gaussian centers, the spectrum was traced by calculating emission centroids along the dispersion axis. In less than 5% of the slits, where neither the Gaussian centering or the centroid calculations yielded good polynomial fits, the centers were manually identified at 20–30 spots along the dispersion axis and then fit by a cubic polynomial. The cosmic-ray cleaned, flatfielded individual exposures for a given slit were then straightened using the spectrum center tracing.

To calculate the wavelength solution, we extracted a 1-d spectrum from the arc lamp exposure for each slit using that slit's tracing. Individual arc lines within the spectrum were marked using the IRAF routine, **identify**, and the wavelength solution was determined by fitting a fifth-order

Legendre polynomial to these line identifications. For the red side of the detector, the neon and argon lines were typically dominant, while for the blue side neon, zinc, and cadmium lines dominate. The wavelength solution was applied to each individual exposure using the combined IRAF routines, **refspec** and **dispcor**.

These wavelength-corrected exposures were then each individually shifted by the spatial offsets calculated above to produce a series of wavelength-corrected, straightened, aligned exposures for each slit. Cosmic rays not previously removed by **xzap** were identified manually by searching for large variations between the individual exposures at each pixel and removed by linear interpolation along the dispersion axis.

2.4.2.2 Alignment with HST Imaging

The Antennae has a significant diffuse ionized background varying across the entire system. There are a number of regions that are strong in Hα but which are not bright enough to be detected in broadband optical or near infrared images. Therefore, careful selection of the regions within each slit to use for background subtraction was critical in order to avoid these regions of nebular Hα emission.

In order to identify regions of Hα emission we made use of the HST imaging of the Antennae from Whitmore et al. (1999). Using the position of each observed cluster in the Ks band images and the position angle of each slit mask, we calculated the V, B, and Hα emission profiles along the slit in the HST images, assuming a slit width of 1.5″. Similar emission profiles along the slit were constructed of our own cluster spectroscopy using a $\sim$ 150Å region free of emission and absorption features near the middle of the blue and red observations to measure the B and V band profiles, respectively. An Hα profile was also constructed from our spectral observations by summing over a 30Å region centered on the Hα line. By simultaneously plotting the LRIS B, V, and Hα profiles, along with the HST B, V, and Hα profiles, we aligned the red and blue observations with each other and with the HST imaging (see Figure 2.6).

2.4.2.3 Background Subtraction and Aperture Selection

Since we used shorter 4 to 5″ slits in order to maximize the number of clusters that could be observed on each mask, background subtraction was often very difficult and required identifying the background regions within a complex field and often near to the Antennae clusters themselves. However, with the HST imaging we could accurately identify regions of enhanced Hα emission displaced from the Antennae clusters as well as additional faint clusters undetected in our spectroscopy and avoid these regions in determining the background. Figure 2.7 illustrates four slits representative of some of the challenges in background identification, including strong Hα emission on one but not both clusters in a slit (top left), multiple clusters with spatially overlapping emission (top right), rising

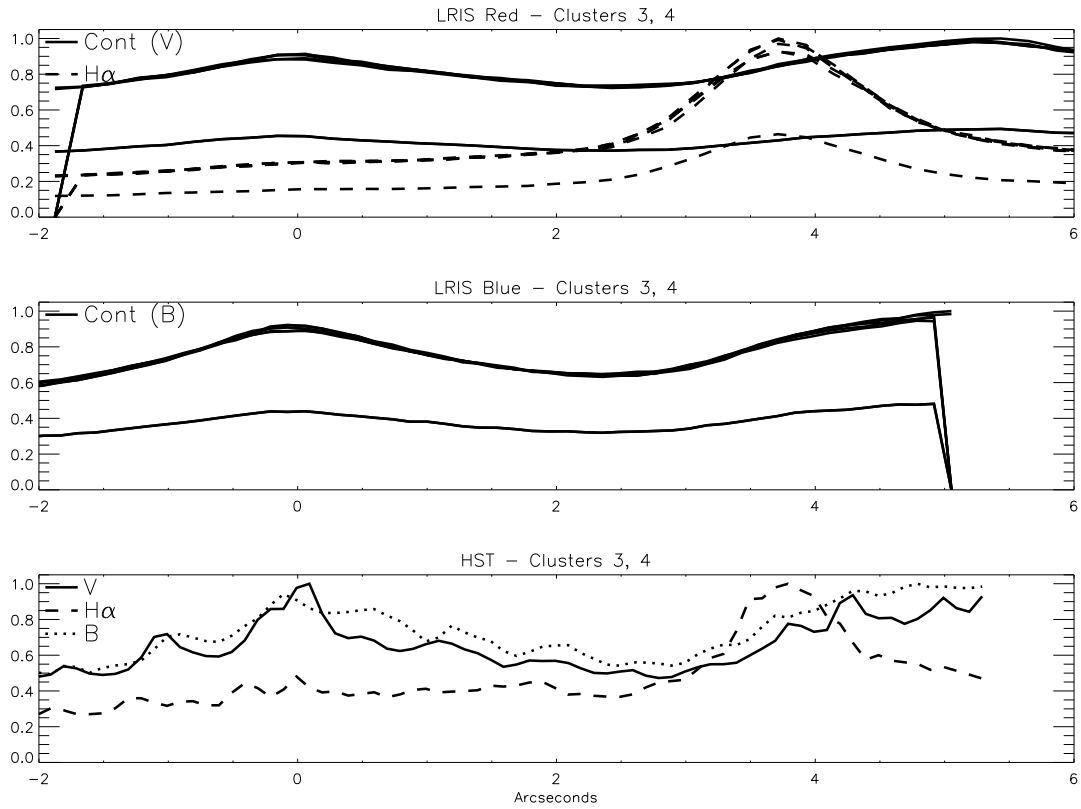

Figure 2.6 Alignment of LRIS Observations with HST Images for Clusters 3 and 4. The top plot shows the red continuum which mimics the V band (solid line) and Hα (dashed line) profiles calculated from our LRIS spectroscopy for each individual exposure on the slit. The middle plot shows the LRIS blue continuum, a surrogate for the B band, while the bottom plot contains the V band (solid line), B band (dotted line), and Hα (dashed line) constructed from the HST imaging of Whitmore et al. (1999). The LRIS and HST profiles were aligned and normalized prior to plotting.

diffuse Hα emission away from the cluster (bottom left), and a two cluster slit with one cluster strong in the blue and the other in the red (bottom right).

For most slits we identified background regions on either side of the Antennae cluster(s) approximately 2″ from the cluster centers and used both regions to calculate the background. However, in some regions where the cluster lay near the edge of the slit or when there was enhanced emission away from the clusters, only one background region was selected. The background was calculated separately for each exposure.

The apertures for each cluster were identified after background subtraction and selected to trace each cluster down to 10% of the peak value in the LRIS continuum profiles. Some slits contained multiple clusters that overlapped at greater than 10% of the peak, and in these cases, as with the NIRSPEC observations, the apertures for each cluster extended to the minimum in the profile between the clusters.

We selected the same spatial regions for background subtraction and aperture extraction in both

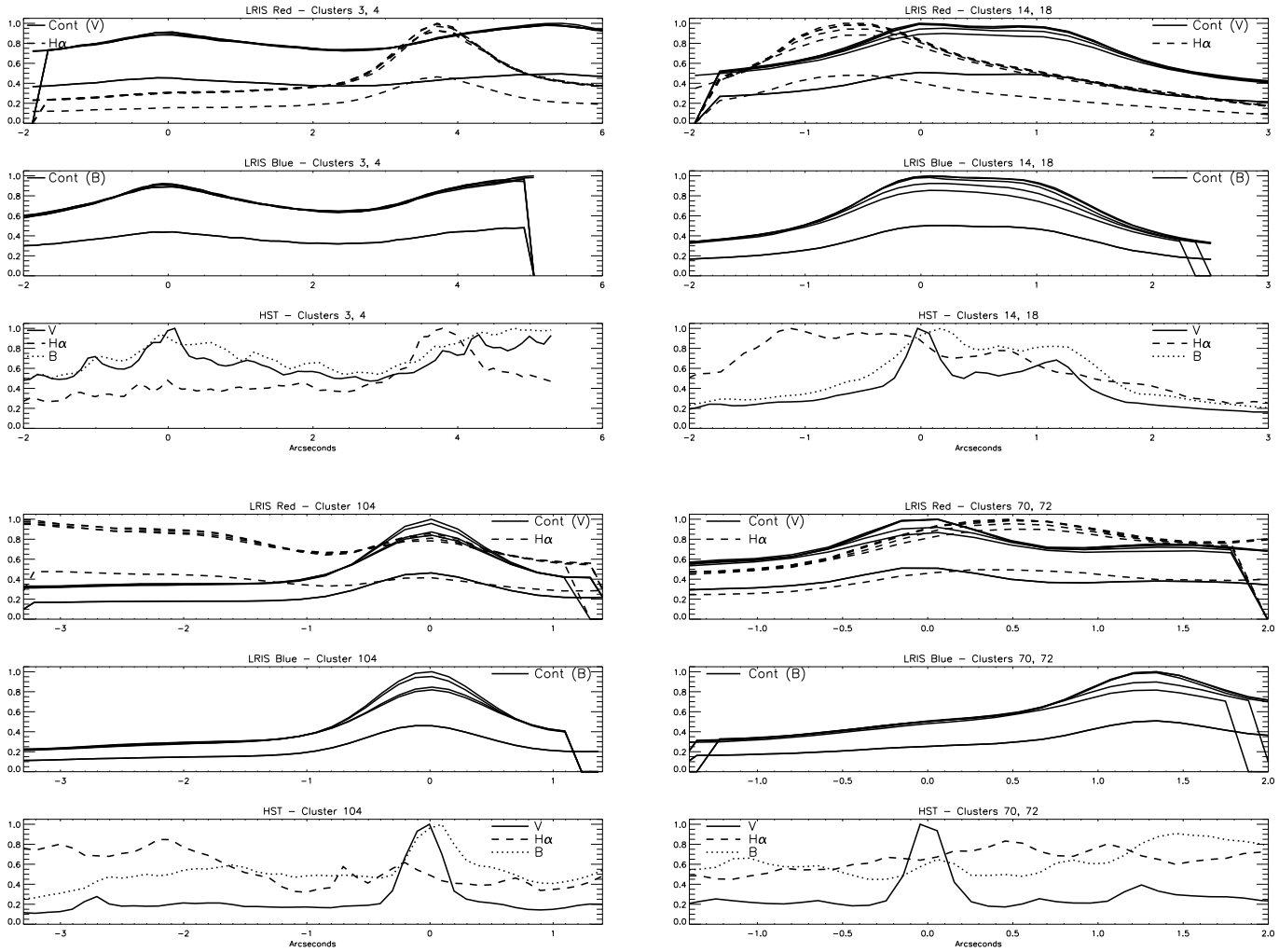

Figure 2.7 Four sets of emission profiles illustrating challenges in identifying background regions in LRIS spectra. Each set of three plots has the same format as that in Figure 2.6. Particular challenges include: strong Hα emission on one but not both clusters in a slit (top left), multiple clusters with spatially overlapping emission (top right), rising diffuse Hα emission away from the cluster (bottom left), and a two-cluster slit with one cluster strong in the blue and the other in the red (bottom right).

the LRIS-Blue and LRIS-Red observations. Because of the large amount of diffuse ionized emission within the Antennae, selecting the same background regions and apertures is critical in order to compare line widths and fluxes of emission lines measured in the red and blue sides. The red and blue slits do not always have the same spatial extent, which created difficulties for clusters near the edges of slits. In these cases we always selected the red and blue apertures to be identical, even if that required ignoring part of the cluster observed in only the blue or red detector. An identical blue and red background region could not be determined for approximately 15% of the clusters with both red and blue observations. For these clusters we determined the backgrounds individually for both sides and flagged them for careful scrutiny when examining emission line fluxes and equivalent widths.

2.4.2.4 Flux Calibration

The reduction strategy used for the LRIS cluster spectra was modified for longslit observations and employed to reduce the two flux calibrators, Feige67 and G191B2B. Using template spectra for these two standards from the NOAO **onedstds.spec50cal** IRAF library, a Mauna Kea extinction curve from the **onedstds** library, and the airmass of the calibrator observations, a predicted template spectrum was generated for each flux calibrator. This predicted template spectrum was divided by the observed flux calibrator spectrum normalized by the exposure time to derive a sensitivity function. Each exposure of a cluster spectrum was divided by the sensitivity function to calculate a flux-calibrated exposure. All of the March 2003 LRIS observations were flux calibrated using Feige67 while all of the January 2004 observations used G191B2B. A final flux-calibrated spectrum was produced for each cluster by averaging over the flux-calibrated spectra extracted from each individual exposure.

The red and blue spectra of each cluster overlap spectrally between 5400 and 5700Å. The exact overlap regions depend on the location of slits within each mask. In Figure 2.8 we plot the median red flux versus the median blue flux in the spectral overlap region for each cluster and see for the most part good agreement. The clusters are color-coded based on the slit mask. Slitmasks 4 and 5 are not included since only red-side observations were taken for these masks. Clusters in slitmasks 2 and 6 both tend to slightly higher red fluxes in the spectral overlap region, particularly mask 6 where the median red/blue flux ratio is 1.3 (see Table 2.7 for details on each individual mask). Mask 6 was observed in the red side over two days (see Table 2.2) while the blue side was only observed on the second of those days. Differences in flux calibration of the red side between the two nights may account for the higher red side fluxes in mask 6. Based on the variation in the red and blue fluxes we place an uncertainty in the optical flux calibration at around 30%. We corrected the LRIS-B spectrum of each cluster to match the LRIS-red spectrum in the spectral overlap region. The choice to match the blue to the red is arbitrary, so while absolute flux levels are uncertain, the relative flux

Table 2.7. Comparing LRIS-Red and LRIS-Blue Fluxes in Spectral Overlap Region

Mask[a]	# of Clusters	Median Red / Blue Flux
1	13	0.94
2	11	1.12
3	20	0.90
6	11	1.30

[a]Masks 4 and 5 excluded because of no LRIS-blue observations

calibration between the red and blue sides, important when comparing emission line fluxes from the two sides, should be fairly accurate.

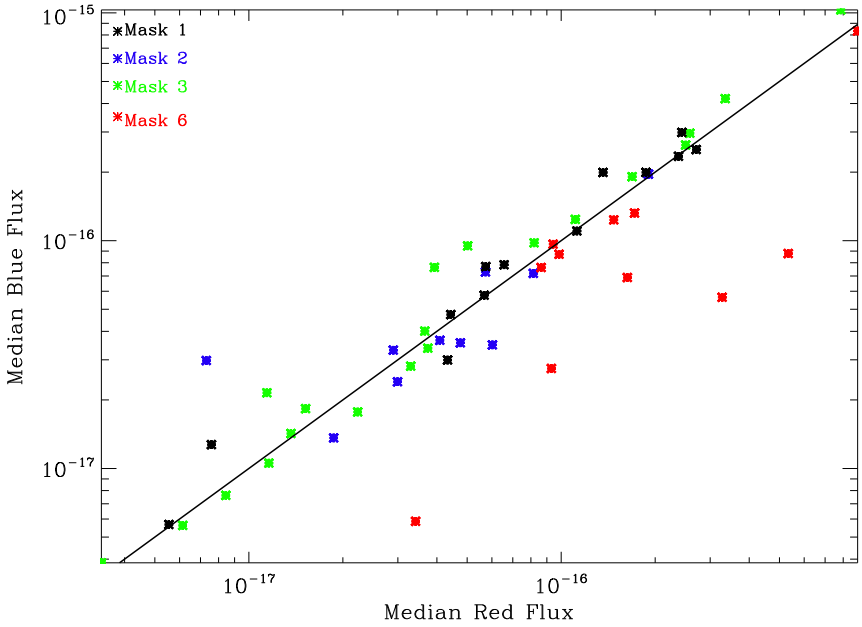

Figure 2.8 Comparing LRIS-Red and LRIS-Blue Fluxes in the Spectral Overlap Region. For each cluster the median blue and red fluxes in the spectral overlap region are plotted against one another. The spectral overlap region, covered by both the LRIS-blue and LRIS-red observations is roughly from 5400Å to 5700Å. The points are color-coded based on the slitmask.

2.5 Optical and Near-Infrared Spectra

In Figures 2.9–2.13 we plot LRIS blue and red and NIRSPEC H and K band spectra for four Antennae clusters and the two nuclear regions. These spectra are representative of different cluster spectra found in our sample. The major emission and absorption lines are indicated in each figure, redshifted

to z=0.0054, the systemic redshift of the Antennae. Each spectrum is plotted logarithmically in intensity and offset vertically for clarity. The LRIS red spectra have a large dynamic range in the strength of the emission lines, particularly Hα. Therefore, the LRIS red spectra are broken into two wavelength ranges: 5500–7500Å, where strong emission lines dominate, and 7500–9200Å, where the emission lines are weaker and important absorption diagnostic features, such as Calcium Triplet, appear.

The four clusters shown in Figures 2.9–2.13 sample three star formation regions within the Antennae: the western loop (Clusters 79 and 104), the northeast (Cluster 82), and the overlap region (Cluster 19). There are significant variations in the strength of the emission lines and absorption features, indicating clusters of differing age and extinction. In Cluster 19 the ionized hydrogen emission lines (indicated in red) are extremely strong, a sign of a younger aged ($<$ 5–7 Myr) cluster. Even higher-level Paschen, Brackett, and Pfund series lines are visible in the Cluster 19 spectra. In Cluster 79, in comparison, Hα, Hβ, and Brγ are seen in emission but higher Balmer lines are detected in absorption, indicative of a slightly older population. Cluster 104 shows no ionized hydrogen emission in the near-infrared or optical but strong absorption in the higher Balmer lines. CO absorption bandheads, which arise in the atmospheres of giants and supergiants and are thus indicative of a slightly older ($>$ 8 Myr) cluster, are also clearly evident in the H and K band spectra of Clusters 79, 82, and 104 (as well as the nuclear spectra). These features are not seen in Cluster 19, the youngest of the four clusters. We note that these spectra begin to reveal the difficulties in matching the observed strengths of emission and absorption lines to synthesis models: Hydrogen emission lines should be seen in emission only for clusters younger than 5–7 Myr, while CO bandheads should only appear in clusters older than 8 Myr. Yet, Clusters 79 and 82 have both CO bandheads and hydrogen emission lines. In Chapter 4 we will address this discrepancy in much more detail.

In Chapter 3 we measure the equivalent widths of six key emission and absorption lines in the Antennae spectra, and in subsequent chapters use these equivalent widths to constrain properties of the clusters, including age, mass, extinction, and metallicity.

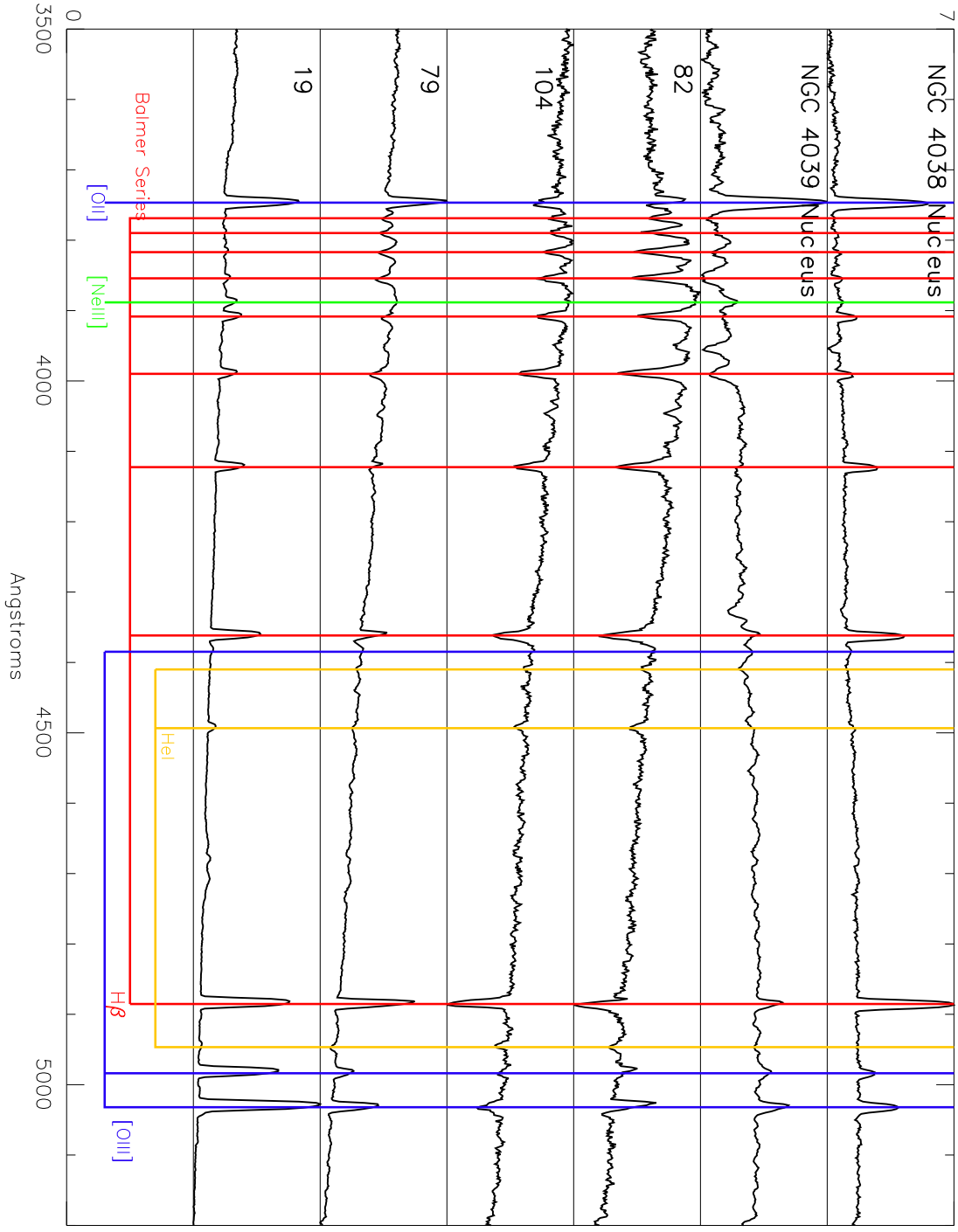

Figure 2.9 LRIS-Blue Spectra of Four Clusters and the Two Nuclear Regions. The four clusters sample three different star-forming regions: the overlap region (Cluster 19), the western loop (Clusters 79 and 104), and the northeast region (Cluster 82). Each individual spectrum is scaled logarithmically and offset vertically for clarity. Key emission and absorption features are indicated at z=0.005, the bulk redshift of the Antennae.

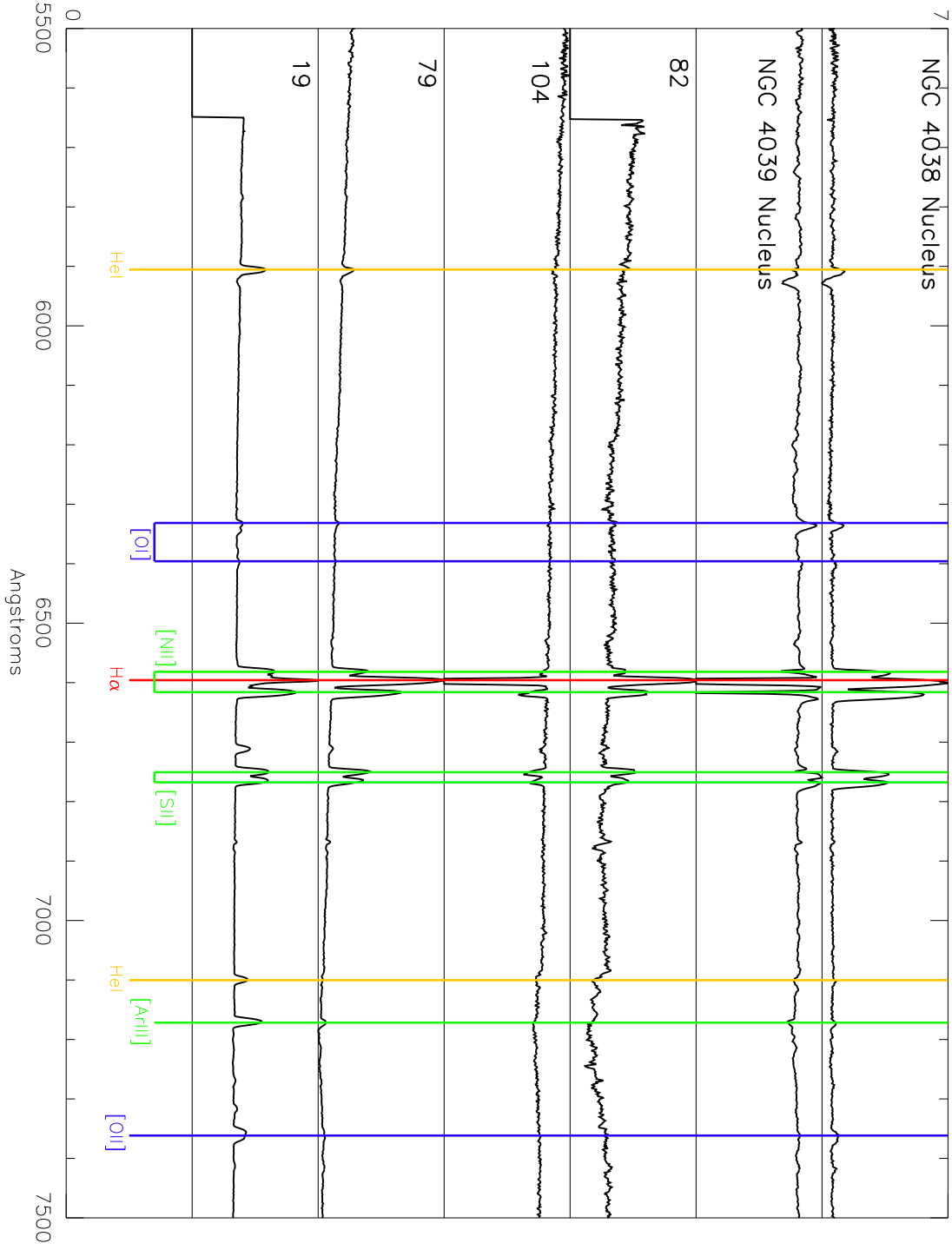

Figure 2.10 LRIS-Red Spectra from 5500–7500Å of Four Clusters and the Two Nuclear Regions. Each spectrum is scaled logarithmically and offset vertically for clarity. Key emission lines are indicated at z=0.005, the bulk redshift of the Antennae.

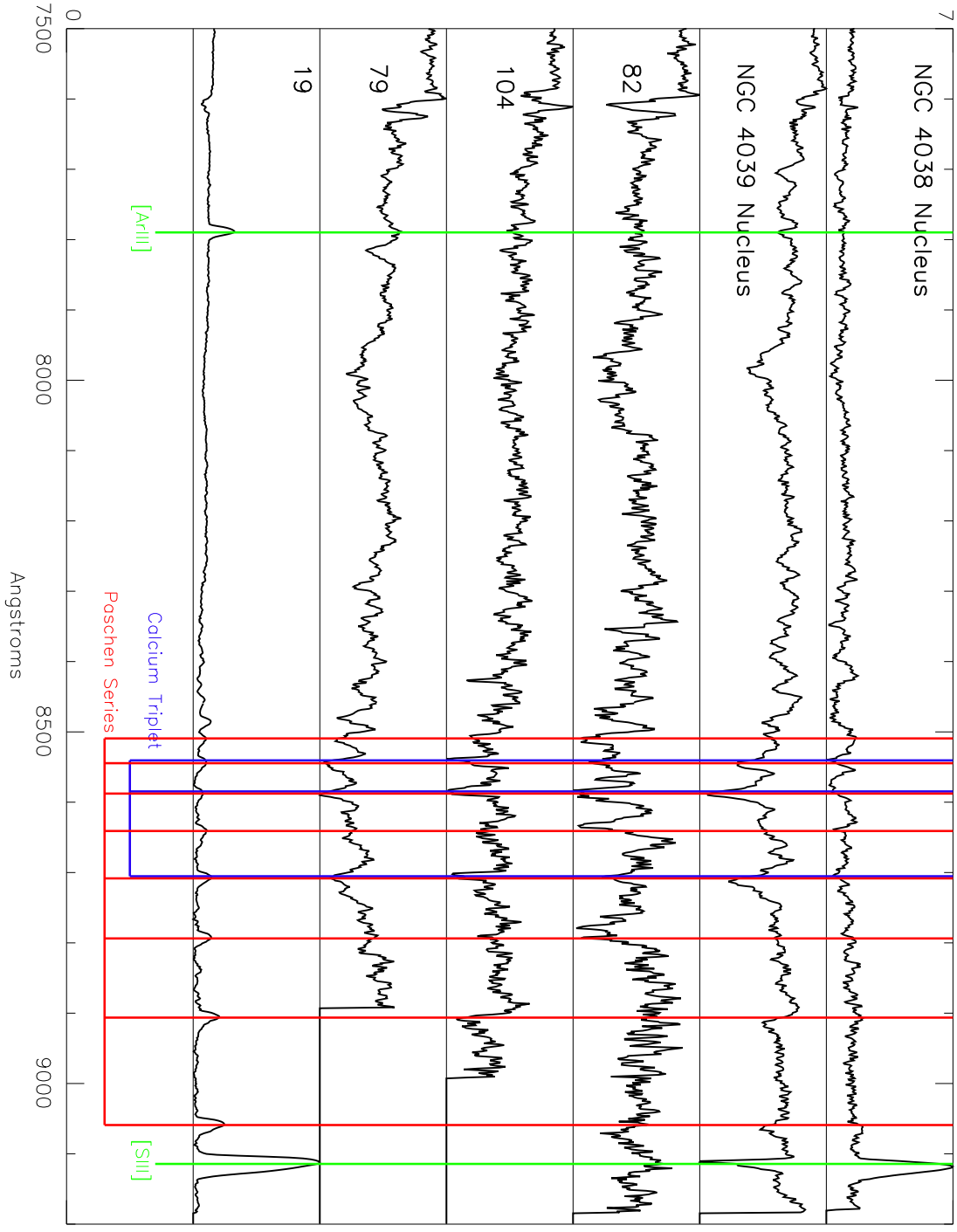

Figure 2.11 LRIS-Red Spectra from 7500–9200Å of Four Clusters and the Two Nuclear Regions. Each spectrum is scaled logarithmically and offset vertically for clarity. Key emission and absorption lines are indicated at z=0.005, the bulk redshift of the Antennae.

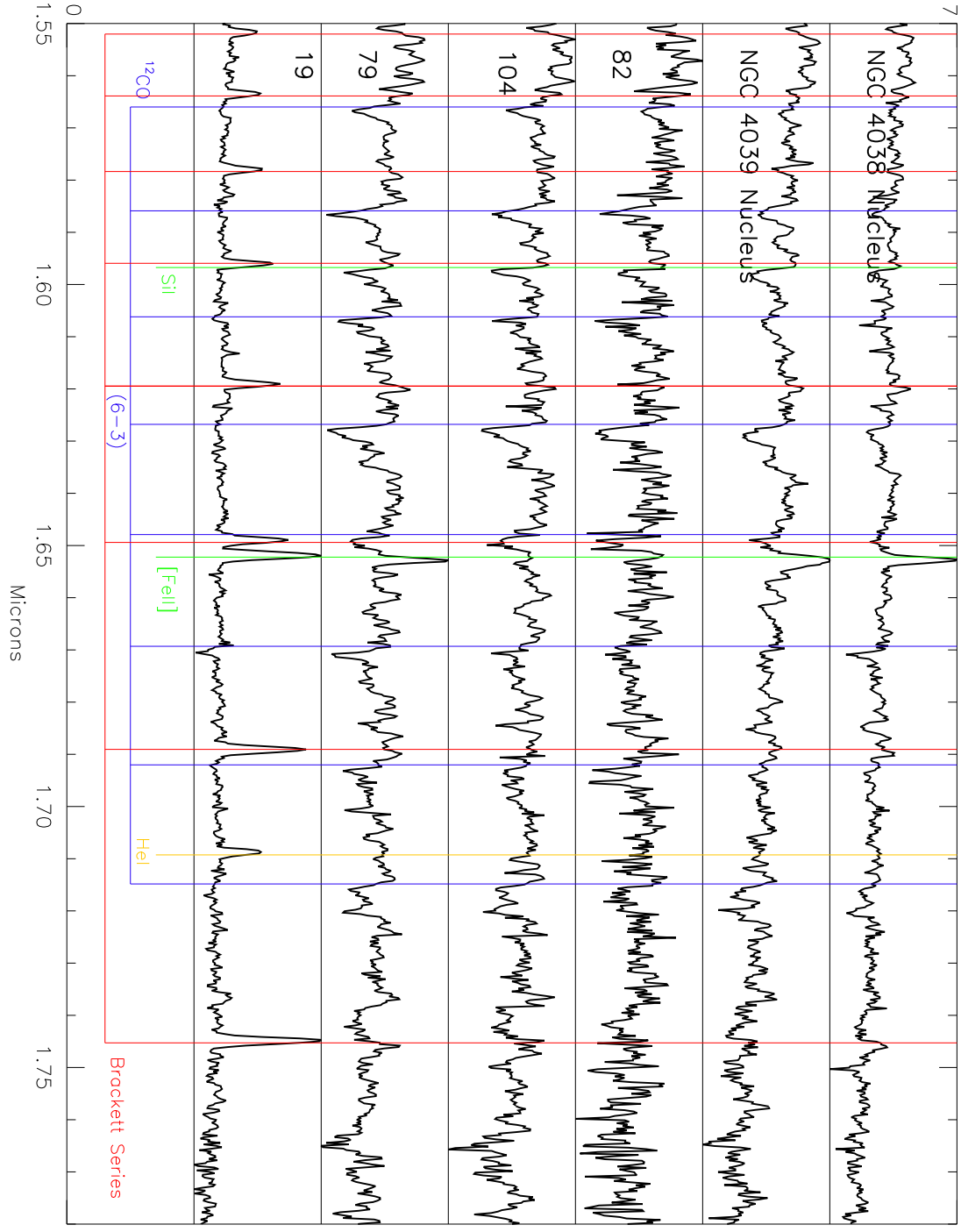

Figure 2.12 NIRSPEC H band Spectra of Four Clusters and the Two Nuclear Regions. Each spectrum is scaled logarithmically and offset vertically for clarity. Key emission and absorption lines are indicated at z=0.005, the bulk redshift of the Antennae.

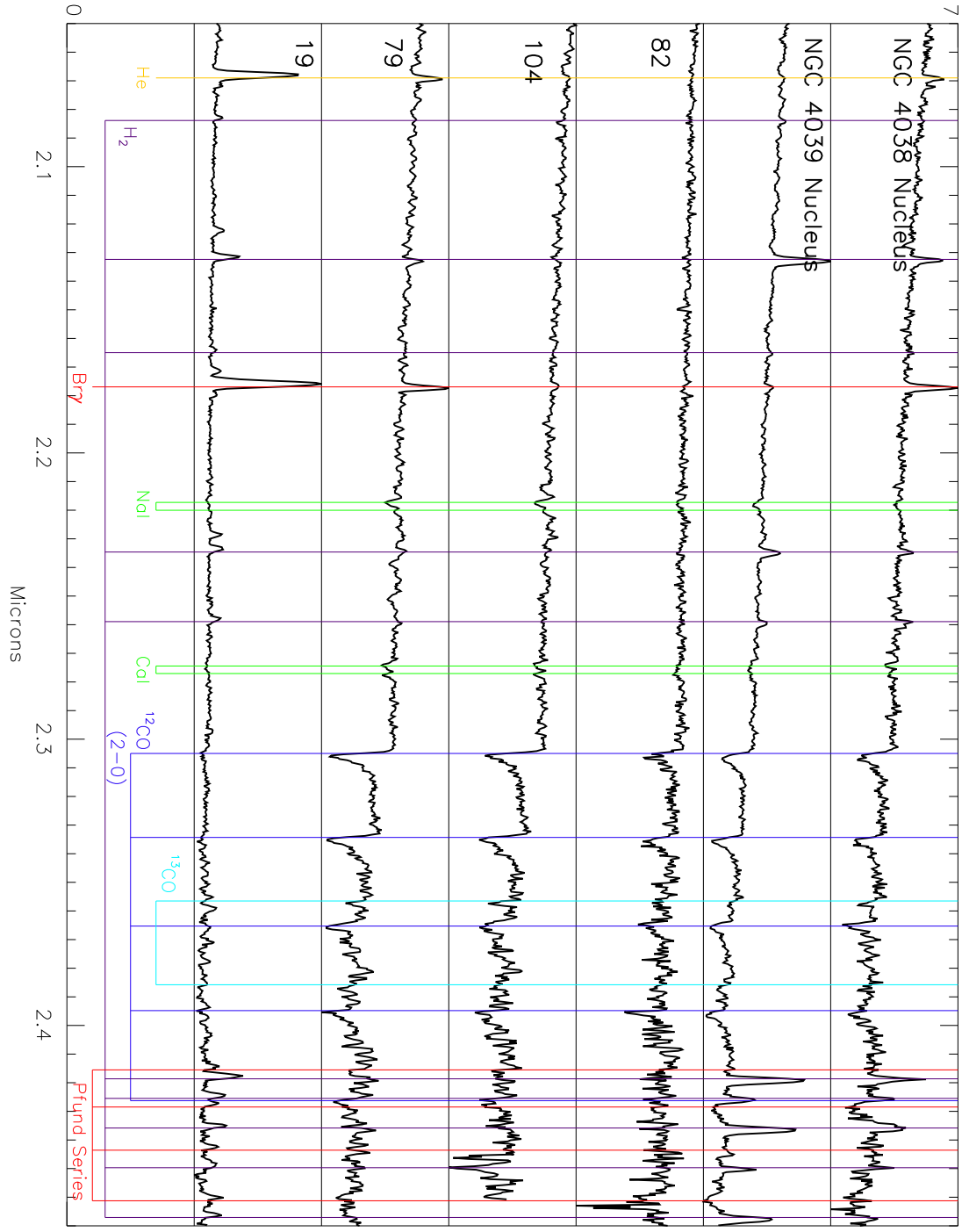

Figure 2.13 NIRSPEC K Band Spectra of Four Clusters and the Two Nuclear Regions. Each spectrum is scaled logarithmically and offset vertically for clarity. Key emission and absorption lines are indicated at z=0.005, the bulk redshift of the Antennae.

Chapter 3

Population Synthesis Models and Antennae Cluster Equivalent Widths

Population synthesis models simulate the temporal evolution of star cluster spectra and from these spectra predict the evolution of many cluster properties, including the equivalent widths of emission and absorption lines, and cluster absolute magnitudes and colors. Comparing observed equivalent widths and luminosities for clusters with the predictions from population synthesis models allows for an estimation of many key properties of a cluster, most notably age and mass.

In this chapter we will discuss in detail Starburst99, the population synthesis model used in this study, and the measurement of six key equivalent widths in our spectra that will be used to estimate the age of the Antennae clusters.

3.1 Starburst99

Population synthesis models produce time-dependent spectra for star-forming regions/clusters by combining observed stellar spectra and model atmosphere spectra with stellar evolution models. Important cluster age diagnostics, such as the equivalent widths of hydrogen recombination emission lines and the strength of the CO absorption bandheads, are measured from these model cluster spectra. In this study we will focus upon six particular diagnostic lines: three hydrogen recombination lines (Hα, Hβ, and Brγ), two CO bandheads (CO (2-0) at 2.29μm and CO (6-3) at 1.62μm), and the Calcium Triplet.

A number of evolutionary synthesis models exist (i.e., Bruzual & Charlot, 1993; Leitherer et al., 1999; Bruzual & Charlot, 2003). For this project we chose Starburst99[1] (Leitherer et al., 1999) because of its widespread use in cluster studies and the ability to easily modify the models to more completely match physical conditions in the Antennae. In particular, the models can be modified

[1] see http://www.stsci.edu/science/starburst99

to allow for a non-instantaneous, yet non-continuous burst of star formation. Starburst99 uses stellar evolutionary models from the Geneva group (Schaller et al., 1992; Schaerer et al., 1993a,b; Charbonnel et al., 1993; Meynet et al., 1994) with model atmospheres of Lejeune et al. (1997). A major update was made to Starburst99 in December 2004 (Vázquez & Leitherer, 2005) to include the stellar evolution models of the Padova group (Fagotto et al., 1994), which are generally taken to be most accurate in modeling clusters older than 10^8 yr.

Starburst99 models exist for a range in metallicity, initial mass functions, and star formation profiles. Five metallicities, ranging from 5% solar to twice solar, are available. The behavior of the hydrogen recombination line equivalent widths does not change significantly with metallicity (see the left plot of Figure 3.1). The drop in hydrogen recombination line equivalent widths is later and more gradual for lower-metallicity clusters. In contrast, substantial differences exist in the CO bandhead equivalent width evolution between different metallicity clusters (see the right plot of Figure 3.1). The CO bandheads appear earlier and are stronger at their peaks for higher metallicity clusters. For our studies we have adopted the solar metallicity model, which has been suggested in previous studies of the Antennae (e.g., Mengel, 2001). Additionally, our own measurements of metallicity (§6.1) indicate solar or near-solar metallicities for all clusters in our Antennae sample.

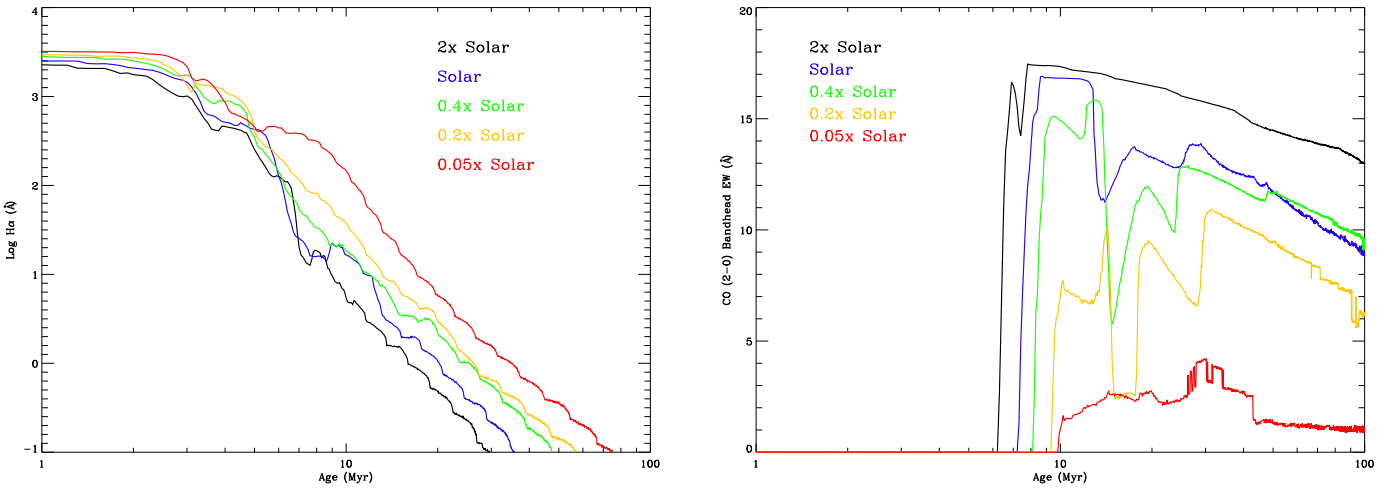

Figure 3.1 The Effect of Metallicity in the Evolution of the Hα emission-line (left) and CO (2-0) Bandhead (right) Equivalent Widths in Starburst99. The five metallicity models in Starburst99 are plotted for 1–100 Myr. These models all assume an instantaneous burst and a Salpeter IMF with 100 $M_\odot$ upper mass limit. The behavior of the CO (6-3) bandhead equivalent width (not shown here) is similar to the CO (2-0) bandhead equivalent width behavior, although with reduced equivalent widths. The Hβ and Brγ equivalent widths (not shown here) have similar behavior to the Hα equivalent width.

Three initial mass functions (IMFs) are included: a Salpeter IMF ($\alpha = 2.35$) with lower mass cutoff at $1M_\odot$ and upper mass cutoff at $100M_\odot$, a truncated Salpeter IMF with upper mass cutoff at $30M_\odot$, and a steeper IMF ($\alpha = 3.3$) with mass range 1–$100M_\odot$. This steeper IMF resembles

the Miller-Scalo IMF for high mass ($> 10M_{\odot}$) stars. There has been significant discussion in the literature about the IMF of massive star clusters. Measuring the IMF of a cluster is difficult, especially for more distant systems, because it requires a dynamical mass measurement, which in turn requires sufficient spectral resolution to measure velocity dispersions within the cluster, and sufficient spatial resolution to measure the cluster radius. Smith & Gallagher (2001) analyze one cluster in starburst galaxy M82 and find it to likely be a Salpeter IMF with a low-mass stellar cutoff around 2–3 $M_{\odot}$. McCrady et al. (2003) find a similar, but not as drastic, deficit in low-mass stars for one M82 cluster, but in general find reasonable agreement with either a Salpeter IMF with a 2 $M_{\odot}$ lower mass cutoff or a Kroupa IMF with a lower mass limit of 0.1 $M_{\odot}$. Looking at the Antennae, Mengel et al. (2002) analyze the IMF for four Antennae clusters and find slight indications that the IMF may vary with location in the Antennae. However, they find best agreement with a traditional Salpeter IMF. Based on these findings, we have adopted this traditional Salpeter IMF with stellar masses ranging from 1–100 $M_{\odot}$ for our study.

Two star formation profiles are also available: an instantaneous burst and continuous star formation at a fixed rate. We have created a third star formation profile: a 5 Myr duration constant rate burst of star formation. This profile is intermediate between the instantaneous and continuous profiles, and we will argue below more accurately models the conditions within the Antennae. To construct this 5 Myr duration constant rate burst model, we combined instantaneous burst models from Starburst99:

$$\mathrm{EW(t)} = \begin{cases} \frac{\sum_{i=0}^{t} \mathrm{EW_i C_i}}{\sum_{i=0}^{t} \mathrm{C_i}} & \mathrm{t} < 5\mathrm{Myr} \\ \frac{\sum_{i=t-5Myr}^{t} \mathrm{EW_i C_i}}{\sum_{i=t-5Myr}^{t} \mathrm{C_i}} & \mathrm{t} > 5\mathrm{Myr} \end{cases}$$

where $\mathrm{EW_i}$ and $\mathrm{C_i}$ are the equivalent width and appropriate continuum level measured in Starburst99 for an instantaneous burst of a cluster with age i Myr.

In Figure 3.2 we plot the temporal evolution of six key diagnostic lines for these three star formation profiles. For the hydrogen recombination lines, the major difference between the three star formation profiles is the age where the recombination line equivalent widths begin to decrease significantly (due to the lack of hot, young, main sequence stars). In an instantaneous burst this dropoff begins around 4–5 Myr, while for the 5 Myr duration burst it occurs around 3 Myr later at 7–8 Myr. In the continuous star formation profile, the equivalent widths of the hydrogen recombination lines are always high because of the continuous addition of new young hot stars. The CO bandheads as well as the Calcium Triplet absorption features also vary between the star formation profiles. While the bandheads and Calcium Triplet features appear at about the same age for all profiles (7–8 Myr for CO bandheads, 3–4 Myr for Calcium Triplet), the time required to reach their peak values differs between the three star formation profiles. For the instantaneous case, the CO bandheads reach their peak in less than 1 Myr after the first appearance of the bandheads, while it takes 5 Myr

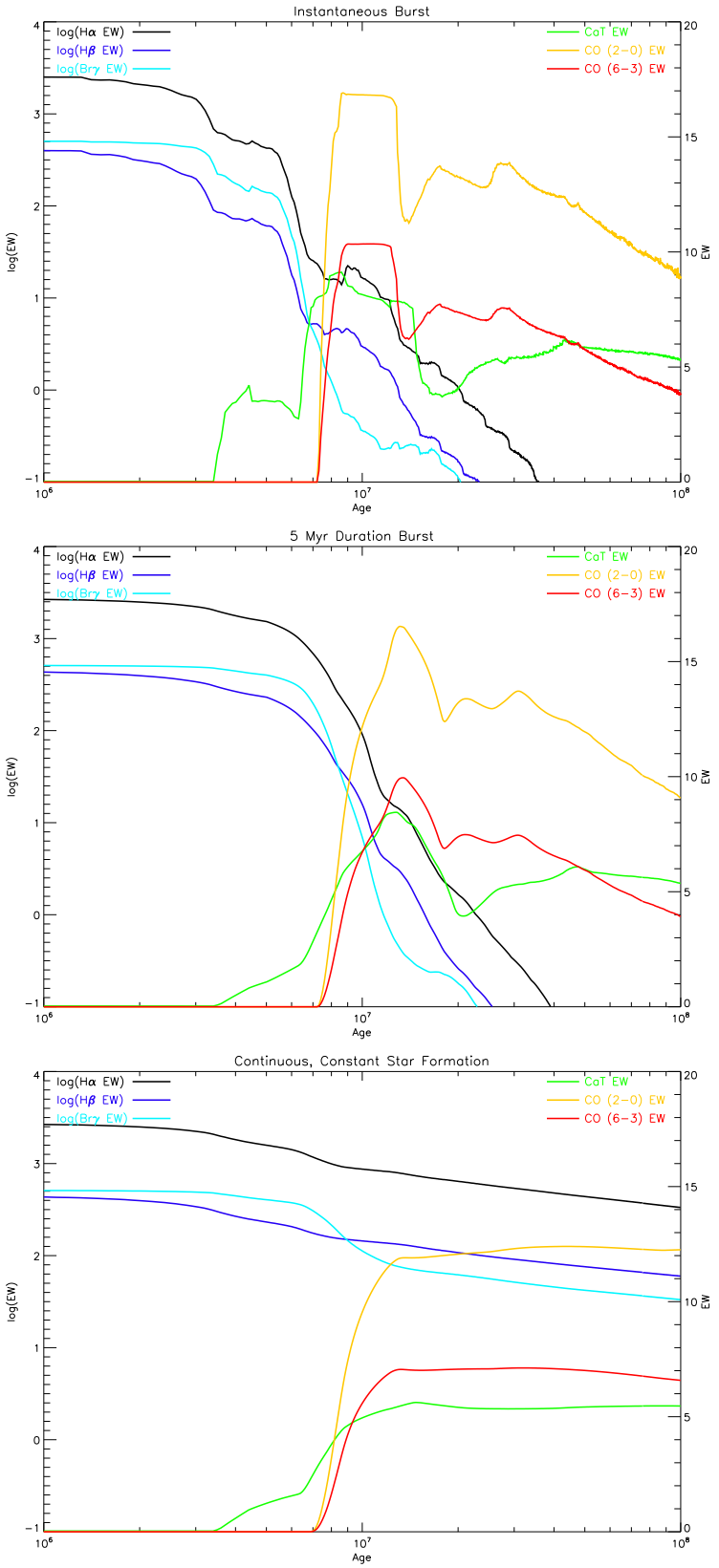

Figure 3.2 Evolution of Six Key Age Diagnostic Lines as calculated by Starburst99 for an instantaneous burst (top), a 5 Myr duration constant rate burst of star formation (middle), and continuous, constant star formation (bottom). The logarithm of the emission equivalent width is plotted for the hydrogen lines, while the absorption equivalent width in angstroms is plotted for the CO bandheads and calcium triplet feature.

for the 5 Myr duration burst and continuous star formation models. The CO bandhead equivalent widths fall off past 30 Myr for both the instantaneous burst and the 5 Myr duration burst, but for the continuous star formation model, the CO bandhead equivalent widths remain at their peak values out past 100 Myr. For our analysis, we will initially consider the instantaneous burst, as star formation within a cluster is normally assumed to be instantaneous. However, we will find that a 5 Myr duration constant rate burst of star formation better fits the Antennae clusters.

3.2 Equivalent Widths

In §3.1 we briefly discussed six emission and absorption lines whose observed equivalent widths can be compared with predictions from Starburst99 to determine cluster properties, particularly age. In this section we will describe each of those diagnostic lines in greater detail and discuss the equivalent width values measured in our clusters.

3.2.1 Hydrogen Emission Lines

Hydrogen recombination lines are often indicative of hot O stars and as such are a hallmark of young (< 10 Myr) clusters (Leitherer & Heckman, 1995). The spectra for Cluster 19, one of our youngest clusters, show a number of prominent hydrogen recombination lines, including Balmer and Paschen series lines in the LRIS spectra and Brackett lines in the NIRSPEC spectra (see Figures 2.9, 2.10, and 2.13). These recombination lines are all indicated by red in the figures and in many cases are much stronger than the continuum, making measurements of their equivalent widths straightforward. Starburst99 calculates hydrogen recombination line fluxes from the number of HI ionizing photons, determined from integration of the cluster spectra blueward of 912Å (Leitherer & Heckman, 1995; Leitherer et al., 1999). This emission line flux is then converted in Starburst99 to a hydrogen recombination line equivalent width using continuum levels set from the model cluster spectra.

For the Antennae clusters, we measured the hydrogen emission line fluxes and equivalent widths for three of the strongest hydrogen recombination lines (Hα, Hβ, and Brγ). We extracted the fluxes and equivalent widths over a wavelength range of ~ 20Å for Hα and Hβ and 40Å for Brγ and determined the continuum for each line by fitting a 50–80Å region on each side of the line (Table 3.1). The continuum regions were selected to be as close as possible to the emission lines but yet free of contamination from other emission lines. In particular, we set the Hα continuum region outside of the [NII] doublet that surrounds Hα. The equivalent width is calculated by: $\mathrm{EW} = \int_{\lambda_\mathrm{i}}^{\lambda_\mathrm{f}} \frac{\mathrm{S_{spec}} - \mathrm{S_{cont}}}{\mathrm{S_{cont}}} \mathrm{d}\lambda$ where $\mathrm{S_{spec}}$ and $\mathrm{S_{cont}}$ are the values of the measured spectrum and fitted continuum respectively, λ_i and λ_f are the boundaries of the line integration range.

The main uncertainty in the equivalent width measurements is the continuum levels. For each cluster we used the 3σ limits on the continuum on either side of the emission line to produce lower-

Table 3.1. Parameters for Equivalent Width Measurements

Line	Line Integration Limits (Rest λ in Å)	Continuum Integration Limits (Rest λ in Å)	
		Blue	Red
Hα	6553–6573	6467–6517	6607–6657
Hβ	4851–4871	4775–4825	4885–4935
Brγ	21642–21680	21550–21630	21700–21780
CaII	8483–8513	8453–8483	8513–8527
CaII	8527–8557	8513–8527	8557–8587
CaII	8647–8677	8617–8647	8677–8707
CO (6-3) bandhead	16175–16220	16145–16175	16255–16285
CO (2-0) bandhead	22924–22977	22885–22915	—

and upper-limit continuum fits. The uncertainty in the equivalent width values was calculated using these lower and upper limits to the continuum fit.

Table 3.2 contains the measured equivalent widths for the three hydrogen recombination lines. For easier comparison with the Starburst99 models, the logarithm of the equivalent widths are listed. In total, 93 clusters along with 3 nuclear observations have Hα detections, 44 clusters plus 6 nuclear observations have Hβ detections, and 41 clusters along with 6 nuclear observations have Brγ detections. For clusters observed multiple times, the equivalent width measurements are typically in good agreement, although there are a few situations where equivalent widths do not agree within the 3σ errors. In these cases, we have selected the recombination line equivalent width measurement from the highest signal-to-noise observation. For 10 clusters, Hα appears as an absorption trough instead of an emission line (e.g., Cluster 104 in Figure 2.10). This is not intrinsic absorption, however, but rather oversubtraction of the cluster background due to spatially varying hydrogen emission levels across the slit (see §2.4.2.3). For Hβ and higher-order Balmer lines (see 3700–4400Å in Figure 2.9), any apparent trough in continuum emission is likely real absorption of the recombination line because the diffuse background emission in Hβ and higher-order Balmer lines is much weaker than for Hα.

Table 3.2. Equivalent Width Measurements

#	Hα	Hβ	Brγ	CaT	CO 2-0	CO 6-3
	Log (EW in Å)				EW in Å	
	3σ limits on EW listed.					
1	-0.51–0.49					
2	-0.03–0.45					
3	1.43–1.50					
4	2.30–2.35	1.47–1.52				
5	1.85–2.08	0.69–1.13				
6	1.24–1.33					
7	2.00–2.22					
8	1.85–1.95	1.28–1.40				
9	1.82–1.87	1.10–1.16				
10			1.60–1.72		7.42–14.32	6.28–11.08
11	2.63–2.64					
12	1.96–2.01	0.55–0.84	0.83–1.08		14.40–17.37	4.08–7.80
13	2.64–2.65					
14	2.50–2.51	1.64–1.66	0.90–1.12		12.42–16.26	2.19–8.53
15	3.15–3.25		2.61–2.67			
16	2.44–2.46	1.43–1.45				
17	2.30–2.31		0.99–1.15		15.95–19.90	2.17–6.51
18	2.14–2.16	1.37–1.40		1.31–2.34		
19	2.39–2.40	1.90–1.92	2.30–2.32		3.58–5.31	1.57–3.53
20	1.58–1.69	0.44–1.14				
21	1.04–1.35					
22	2.88–3.00	2.08–2.14				
23	2.68–2.80	2.30–3.10				
24	3.09–3.23	2.11–2.20				
25			1.69–1.85		9.51–13.63	
26	2.33–2.54		1.93–1.97		7.01–9.73	4.75–8.79
27	2.37–2.51					
28	3.11–3.22					
29	2.63–2.64	2.11–2.12	2.27–2.31		6.26–8.47	0.79–6.51
30	3.09–3.32					
31	2.62–2.75					
35	2.71–2.87					
36	2.77–2.78	2.16–2.17				
37	2.40–2.43	0.97–1.07				
38	2.49–2.56					
39	2.27–2.31					
40	2.41–2.45	1.61–1.66				
41	2.13–2.16	1.29–1.32	1.32–1.71		21.40–30.86	
42	2.21–2.24		1.78–1.90			
43			2.21–2.43		3.68–30.51	
44	2.78–2.89	1.76–1.83				
45	3.20–3.24					
46	2.22–2.25					
47			2.25–3.50			
48	2.36–2.38		1.04–1.20		10.02–13.65	3.83–6.25
49	2.15–2.17	1.08–1.16	0.98–1.19		13.50–18.39	5.14–8.93
51			-0.18–0.46		12.38–16.38	3.35–7.82
52	2.19–2.25	1.11–1.24	1.02–1.27		6.36–14.41	
53	1.97–2.02		0.66–0.97		10.79–18.13	6.35–12.21
54	2.29–2.33	1.06–1.20	1.06–1.22		13.07–20.17	4.44–8.22
55			1.91–2.02		1.26–13.08	
56	2.53–2.55	1.65–1.66		0.00–1.09		
57	2.53–2.55	1.65–1.66		0.00–1.13		
58	2.03–2.05					
59	1.79–1.81			0.46–1.21		
60	2.75–2.80					
61	2.46–2.47		1.73–1.77		8.30–12.51	2.45–5.53
62	2.88–2.92	2.08–2.17	2.19–2.32		18.11–26.58	
63	2.32–2.33		1.29–1.35		15.27–16.94	7.43–9.45

Table 3.2 (cont'd)

#	Hα	Hβ	Brγ	CaT	CO 2-0	CO 6-3
	Log (EW in Å)				EW in Å	
	3σ limits on EW listed.					
64	1.56–2.04					
65	2.34–2.37		1.64–1.80		13.07–23.87	
66	2.33–2.34					
68			1.80–1.90		1.93–10.56	4.20–10.23
69	1.20–1.40	0.04–0.57				
70	1.79–1.82		0.67–0.85		17.26–18.77	3.94–7.06
71	2.56–2.58					
72	1.97–2.03		1.10–1.50		0.00–13.40	
73	1.29–1.57					
74	1.70–1.73	0.72–0.82	0.00–1.10	0.00–3.93	0.00–10.66	
75	2.86–2.91	1.90–1.96				
76	2.32–2.33	1.41–1.43	1.06–1.17	0.00–2.19	14.58–17.09	1.55–4.21
77	2.64–2.66					
78	2.37–2.40	1.66–1.75	1.53–1.69			6.73–12.48
79	2.00–2.01	0.99–1.02	0.95–1.03	1.07–1.79	16.74–17.62	6.48–8.06
80	2.29–2.34			1.36–4.29		
81			2.18–2.55			
82	1.37–1.40		0.00–0.40	0.86–2.01	16.77–20.15	4.55–7.05
83	2.54–2.56					
84	1.97–2.00	1.11–1.20				
85	1.17–1.20			1.20–2.22	15.60–18.24	4.08–7.72
86	2.52–2.54					
87	2.31–2.31	1.42–1.43	1.44–1.57		2.44–7.55	2.53–5.79
88	2.28–2.29		1.48–1.54		11.69–15.67	5.85–8.09
89				1.42–2.63		
90	2.31–2.32	1.47–1.48	1.29–1.44		12.25–17.91	5.03–8.70
91	2.21–2.28	1.60–1.70				
92	2.56–2.81					
94	3.66–3.83					
96	1.41–1.53					
97			0.00–0.97	0.00–2.27	7.11–16.73	7.90–13.28
99	1.45–1.80					
100	1.89–1.90	1.10–1.14	0.99–1.04		16.69–18.57	5.09–6.79
101	1.99–2.01	1.23–1.26				
102	1.79–1.81	1.01–1.06				
104			0.13–0.36	2.06–3.01	15.99–17.29	4.63–7.06
105				0.39–2.75		
106		0.00–0.58				
107				1.39–3.78		
108	2.18–2.20		1.22–1.29		13.15–16.57	2.08–5.83
109	1.98–2.04	1.13–1.17	0.13–0.36		15.99–17.29	4.63–7.06
110	2.36–2.47					
111	2.13–2.28					
112	3.17–3.27	2.39–2.48				
113	2.77–2.91	1.73–1.85				
114	2.88–2.91	2.01–2.03				
116	2.30–3.12	1.40–1.66				
117	1.26–1.67					
4039 Nucl S		0.47–0.54		2.22–3.07		
4039 Nucl		0.69–0.74	0.03–0.25	2.78–3.15	10.39–11.30	4.18–4.79
4039 Nucl N		1.06–1.10		2.41–3.13		
4039 Nucl SE			0.40–0.63		8.34–10.45	3.02–4.98
4039 Nucl NW			-0.05–0.46		11.19–12.76	2.77–4.22
4038 Nucl S	1.96–1.99	1.38–1.43	0.70–0.86	1.75–3.16	7.48–9.14	3.85–5.06
4038 Nucl	2.41–2.42	1.78–1.80	0.97–1.05		9.93–10.88	2.96–3.93
4038 Nucl N	2.66–2.68	2.11–2.16	1.56–1.60		6.89–8.27	2.43–3.84

3.2.2 CO Absorption Bandheads

The CO absorption bandheads in the near-infrared provide an age indicator for older stellar populations ($>$ 7–8 Myrs). CO bandheads result from the frequency-convergence of P rotational-vibrational transitions to create a continuous absorption trough. The CO absorption bandheads are most prominent in giant and supergiants and increase in strength with reduced effective temperature, not appearing in stars hotter than early K giants and increasing to a maximum in mid-late M supergiants (Kleinmann & Hall, 1986; Origlia et al., 1993).

Evolutionary synthesis modeling has focused on the ^{12}CO (6-3) bandhead at 1.62μm and the ^{12}CO (2-0) bandhead at 2.29μm. These are the strongest CO bandheads in H and K band respectively (see Figures 2.12 and 2.13). Origlia et al. (1999) and Starburst99 derived the temporal evolution of the CO (2-0) and CO (6-3) bandhead equivalent widths in clusters (Figure 3.2) using the observations of the CO bandheads in individual stars. These models reveal that for an instanta-

neous burst cluster, the CO bandheads are initially undetected, but at the appearance of the first red supergiants at 7–8 Myr quickly reach an absorption maximum which remains until 12 Myr. After 12 Myr, the CO bandhead equivalent widths slowly decline through 100 Myr, with small increases around 18 and 28 Myrs.

We measured the equivalent widths for the CO (2-0) and CO (6-3) bandheads in the Antennae clusters using the line and continuum ranges from Origlia et al. (1993) and Kleinmann & Hall (1986). These ranges (Table 3.1) are standard for the CO bandhead equivalent width measurements and are identical to those used in the Starburst99 models. The CO (6-3) bandhead continuum was calculated in a similar manner to the hydrogen recombination lines by a linear fit to a 30Å region on either side of the bandhead. However, in the K band, there is a deficit in emission redward of 2.29μm because of the CO (2-0) band and higher (3-1, 4-2, etc.) bandheads. Therefore, for the CO (2-0) bandhead the continuum was taken as a constant equal to the median value in the blue-side continuum window. The uncertainty in the CO (2-0) and CO (6-3) bandhead equivalent widths was estimated from the uncertainties in the continuum measurements as before.

The CO (2-0) bandhead was detected in 37 of the 42 clusters observed in the K band as well as all 6 K band observations of the nuclear regions. Similarly, the CO (6-3) bandhead was detected in 29 of the 32 clusters observed in H band along with all 6 H band observations of the nuclear regions. The CO bandhead equivalent widths can be reduced by non-stellar continuum emission from hot dust. Contamination from dust emission is possible in K band but should be relatively small, if existent, in H band. Therefore the measured CO bandhead equivalent widths could be viewed as lower limits to the true values.

3.2.3 Calcium Triplet

The Calcium Triplet (CaT), three absorption lines of singly-ionized calcium at rest wavelengths of 8498, 8542, and 8662Å, first appears in clusters at an age of 3–4 Myr, approximately 4 Myr prior to the appearance of CO bandheads. The CaT equivalent width corresponds to the sum of the equivalent widths of the three absorption lines. For individual stars, the CaT equivalent width is found to be positively correlated with metallicity (Diaz et al., 1989; Xu, 1991; Mallik, 1994). The CaT equivalent widths are strongest in giant and supergiant stars of solar or higher metallicity (Diaz et al., 1989). Incorporating observations of individual stars into population synthesis models, Garcia-Vargas et al. (1998) find that for an instantaneous burst the equivalent width of the CaT feature peaks at 8–10 Myr with the appearance of red supergiants, approximately 4–5 Myr after the CaT is first detectable (see Figure 3.2). This is in contrast to the CO bandheads which reach their maximum equivalent width values within 0.5 Myr of their first appearance. Starburst99 calculates the evolution of the CaT equivalent width in a similar fashion to Garcia-Vargas et al. (1998).

To measure the CaT equivalent width in our Antennae cluster spectra we used 30Å extraction

regions centered on each of the three absorption lines (Table 3.1). These intervals are the same as those used by Starburst99 and Diaz et al. (1989). As with the hydrogen recombination lines (§3.2.1), we linearly fit for the continuum using windows on either side of each absorption line. The region around the CaT lines has a greater number of emission and absorption lines than around most of the hydrogen recombination lines, so we were only able to use 30Å continuum windows. Uncertainties in the equivalent widths were calculated in an identical fashion to those for the hydrogen recombination lines and CO bandheads.

The Calcium Triplet absorption lines are marked in blue in Figure 2.11. Each CaT absorption line is nearly coincident with a Paschen series hydrogen recombination line. The Paschen lines lie at 8502, 8545, and 8665Å, compared with 8498, 8542, and 8662Å for the CaT lines. This only creates difficulty for clusters from 3–5 Myr, however, because for clusters younger than 3 Myr the CaT absorption lines have not appeared yet and for older clusters the higher level Paschen lines have already weakened.

We detect the CaT feature in 19 Antennae clusters as well as in four of the eight spectra taken on the nuclear regions (Table 3.2). For the remainder of the Antennae clusters with LRIS red observations, the signal-to-noise ratio was insufficient to measure the CaT equivalent width. Therefore, a lack of CaT equivalent width measurement in Table 3.2 should not necessarily be taken as a sign that no CaT absorption is present.

3.3 Equivalent Width Summary and Implications for Cluster Ages

Figure 3.3 shows the equivalent width distributions for each of the six age diagnostics, along with the evolutionary tracks from Starburst99 for an instantaneous burst. The number of clusters included is listed in each plot. All of the hydrogen emission lines have a roughly Gaussian distribution with pronounced peaks at log(Hα EW) = 2.35, log(Hβ EW) = 1.1, and log(Brγ EW) = 1.05. The recombination line equivalent width distributions peaks are in the range where the equivalent width has just begun to fall off from its peak values. The CaT equivalent widths measured are all below 4Å, which suggests that these clusters must have been observed soon after the CaT absorption appears as older clusters ($>$ 7–8 Myr) have CaT EWs greater than 4Å. The CO (2-0) bandhead equivalent width distribution is spread out between 8–18Å, with a slight peak at 16–17Å, near the maximum predicted value of the bandhead from Starburst99 models. In contrast, the CO (6-3) bandhead equivalent width peaks from 3–8Å, which falls 4–5Å below the peak values. From the CO (2-0) and CO (6-3) EW measurements, we can see that the dilution of the CO (2-0) absorption bandhead by hot dust emission must be small. Any significant dilution ($>$ 5Å) would require intrinsic CO (2-0) EW values too high to match the Starburst99 models.

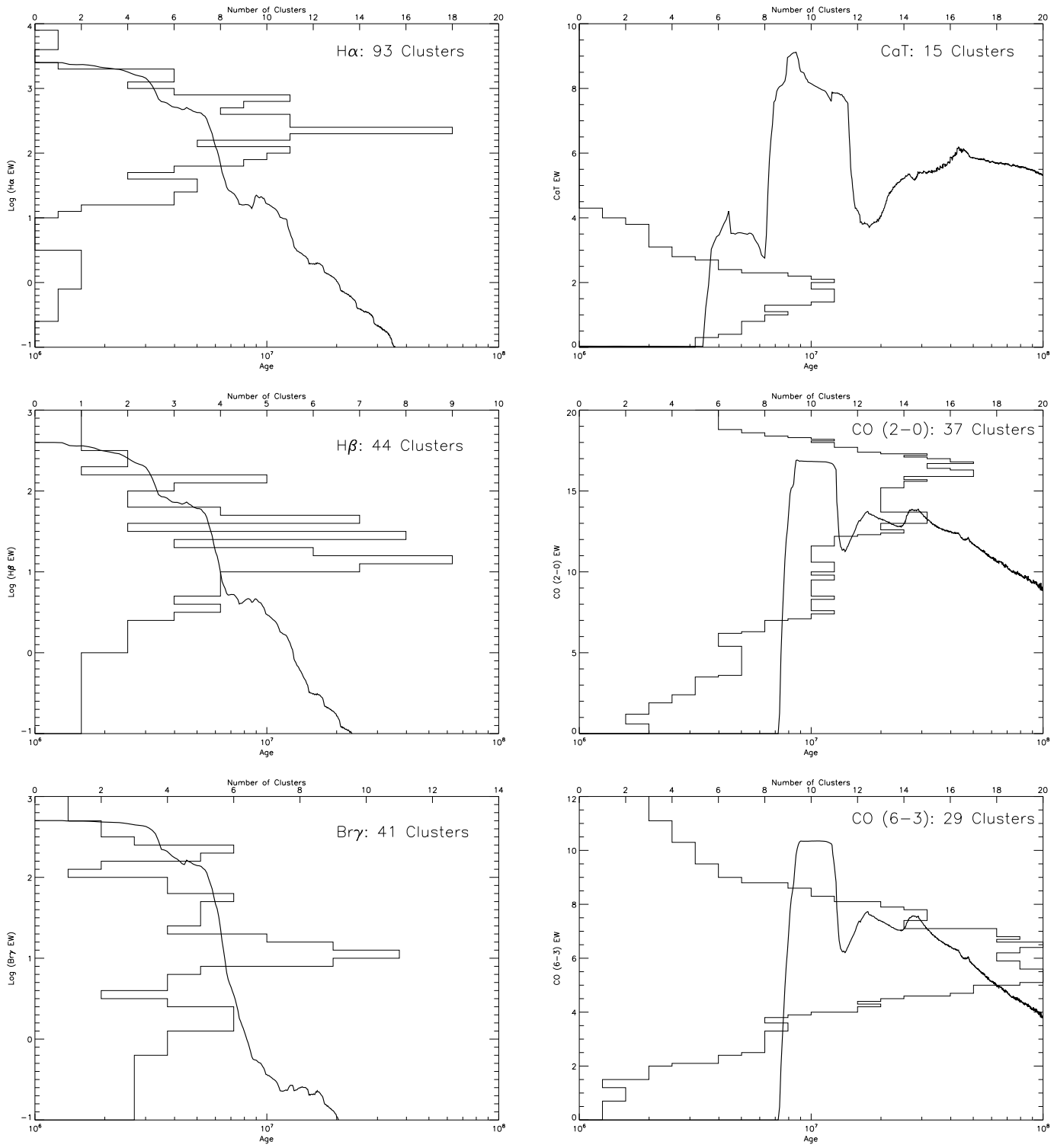

Figure 3.3 Distribution of Equivalent Widths for Six Age Diagnostics with Instantaneous Burst. The measured EWs are binned at a resolution ΔEW=0.1Å for the absorption lines and Δlog(EW)=0.1 for the hydrogen recombination lines. Bins count all clusters whose 3σ EW range falls into the bin interval. Thus a cluster will likely be found in more than one bin. The total number of clusters included for each line are indicated in each plot. For each diagnostic line the temporal evolution of the equivalent width from Starburst99 (assuming solar metallicity and an instantaneous burst) is overplotted from 1 to 100 Myr logarithmically.

Table 3.3. Number of Clusters Observed ($> 3\sigma$) in Age Diagnostic Lines

Line	Clusters	Nuclear Regions	Total	Total Observations in Band	Detection Rate
Hα	93	3	96	115	83%
Hβ	44	6	50	72	69%
Brγ	41	6	47	48	98%
CaT	15	4	19	115	17%
CO (2-0)	37	6	43	48	90%
CO (6-3)	29	6	35	38	92%

In Table 3.3 we list the number of clusters and nuclear spectra with equivalent widths detected at a $> 3\sigma$ significance in each diagnostic line. Also included are the total number of clusters and nuclear regions observed in the bands (LRIS Red and Blue, NIRSPEC H and K), allowing us to calculate a detection rate. With the exception of the CaT line, the detection rates are high, particularly in the near-infrared diagnostic lines. The CaT detection rate is low compared to the other optical lines because some spectra had lower signal-to-noise ratios.

The high detection rates in both the hydrogen recombination lines and the CO bandheads is unexpected. Based on the Starburst99 models for an instantaneous burst (see the top plot of Figure 3.2), hydrogen recombination lines suggest a younger cluster (< 8 Myr) while CO bandheads indicate an older population (> 8 Myr). Such high detection rates of both the CO bandheads and the hydrogen recombination lines are not compatible for an instantaneous burst. In the following chapter we will explore the implications of the simultaneous detection of hydrogen lines and CO bandheads in the majority of near-infrared clusters as we attempt to measure the age of each cluster. We will conclude that a 5 Myr duration constant rate burst of star formation is more consistent with the observed equivalent widths, as it allows for the presence of CO bandheads and hydrogen lines at the same time (see the middle plot of Figure 3.2).

Chapter 4

Antennae Cluster Ages

In order to understand the cluster formation processes within the Antennae, it is critical to measure cluster ages. In this chapter we will first describe the process by which we use population synthesis models to translate observed equivalent widths into age estimates. We will then present evidence that an instantaneous burst is NOT a good representation of star formation in the Antennae and instead determine that a 5 Myr duration constant rate burst of star formation is a better model. We will calculate the ages for the Antennae clusters assuming a 5 Myr duration burst model by combining the age estimates from each diagnostic line and conclude by studying the variation in cluster ages with other properties, such as location and environment.

4.1 Translating Equivalent Widths into Cluster Ages

Translating a measured diagnostic line equivalent width into a cluster age is challenging. The measured equivalent width ranges (Table 3.2) are 3σ limits. For each equivalent width measured, we constructed an equivalent width probability distribution that was Gaussian with 3σ limits given by our measurements (see top plots of Figure 4.1). We divided up the equivalent width probability distribution into intervals (0.01Å for absorption lines and log(EW in Å) = 0.004 for emission lines) and for each interval found the ages predicted by Starburst99 models. In some cases an equivalent width interval predicts more than one age and in these cases both possible ages are included but weighted with lower probability. An age probability distribution for each equivalent width measurement was determined by combining the Gaussian equivalent width distribution with the age/equivalent width relationship and normalizing the result. At younger ages ($<$ 20 Myr), the evolutionary synthesis models have a fair amount of uncertainty. We have assumed that the models are accurate to within 1 Myr, so for each age probability distribution we convolve it with a 1 Myr-wide window to take into account this uncertainty to derive our final age probability distributions (see the bottom plots of Figure 4.1).

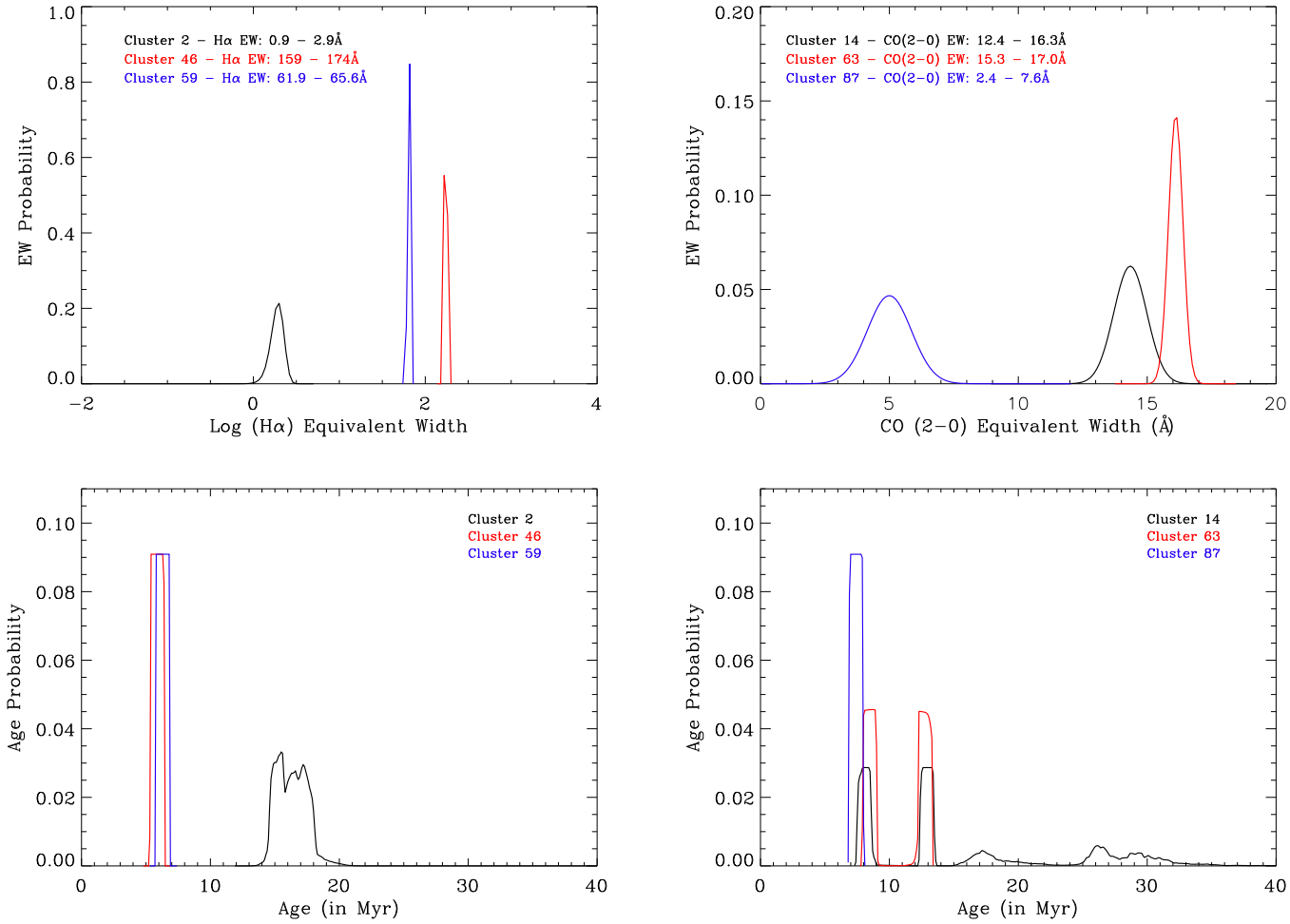

Figure 4.1 Derivation of Age Probability Distribution for Two Age Diagnostic Lines. Plots on the left show the derivation of the age probability distribution for three clusters (color-coded) based on the measured Hα equivalent width. The plots on the right show the derivation of the age probability distribution for three different clusters based on the CO (2-0) bandhead equivalent width. The top plots show the Gaussian probability distribution of the equivalent width based on the 3σ limits to the equivalent widths, given in Table 3.2. The bottom plots are the age probability distributions assuming an instantaneous burst and a 1 Myr uncertainty in the evolutionary synthesis models. We calculate age probabilities out to 100 Myr, but only plot to 40 Myr here because these clusters have zero probability of an age $>$ 40 Myr.

4.2 Evaluating an Instantaneous Burst Model

In our discussion of the measured equivalent widths for the cluster sample (§3.3) we began to highlight a difficulty with applying the instantaneous burst star formation profile to the Antennae clusters: the simultaneous detection of hydrogen emission lines and CO bandheads. Indeed, all 38 clusters and 6 nuclear region observations with CO bandhead detections were also detected in at least one hydrogen line. In Figure 3.3 we see that the Hα emission line equivalent distribution is greatest around log(Hα EW) = 1.8–3, corresponding to an age of $\sim$ 3.5–7 Myr. The peak of the observed log(Hα EW) distribution is at 2.35, corresponding to an age of 5.7 Myr. The other hydrogen lines have similar peaks corresponding to ages from 4–7 Myr. However, an examination of the instantaneous burst model in Starburst99 (Figure 3.2 (top)) shows that CO bandheads do not appear until after 7.5 Myr and, based on the observed equivalent width values for the CO bandheads (Figure 3.3), the ages predicted by the CO bandheads are mostly $>$ 8 Myr—more than 2 Myr larger than the most common ages predicted by the hydrogen lines.

This incompatibility between the CO bandheads and the hydrogen emission lines can be further seen in Figure 4.2, where we plot the age probability distribution for each diagnostic line summed over all clusters. The three hydrogen emission line diagnostics are on the left side of Figure 4.2, so we can easily compare the predicted ages from these lines. We expect the age distributions to be similar, as most clusters with Brγ or Hβ observations also have Hα measurements, and the hydrogen emission lines are tracing the same stellar population component in each cluster. We find good agreement with all three lines having a peak between 5.5 and 6.5 Myr. In fact, statistically the hydrogen emission lines predict $>$ 96% of clusters have an age less than 10 Myr (Figure 4.3). All three lines have a secondary peak between 3 and 4 Myr.

The age distributions for clusters based on the CO bandhead equivalent widths (middle right and bottom right panels of Figure 4.2) are significantly older than the distributions based on hydrogen emission lines. Both the CO (2-0) and CO (6-3) bandheads have age peaks around 8 Myr and 12 Myrs. The 12 Myr peak is more pronounced in the CO (2-0) bandhead than in the CO (6-3) bandhead. This is because many of the CO (6-3) equivalent widths fail to reach the maximum CO (6-3) equivalent width values predicted by Starburst99 and therefore do not coincide with the 12 Myr age when the CO bandhead equivalent is falling off after reaching its maximum (Figure 3.3). Figure 4.2 also shows that the bandheads are consistent with some clusters with ages in the 20–100 Myr age range. This is due to the large number of clusters with moderate CO bandhead absorption (9–13Å for the CO (2-0) bandhead and 4–8Å for the CO (6-3) bandhead), which predict either young (8 Myr) clusters or older 40–100 Myr clusters (see Figure 3.3). Statistically half of the CO (6-3) clusters and almost a third of the CO (2-0) clusters should have ages greater than 20 Myr (Figure 4.3). This stands in contrast to the other 4 tracers which predict no 20 Myr or older

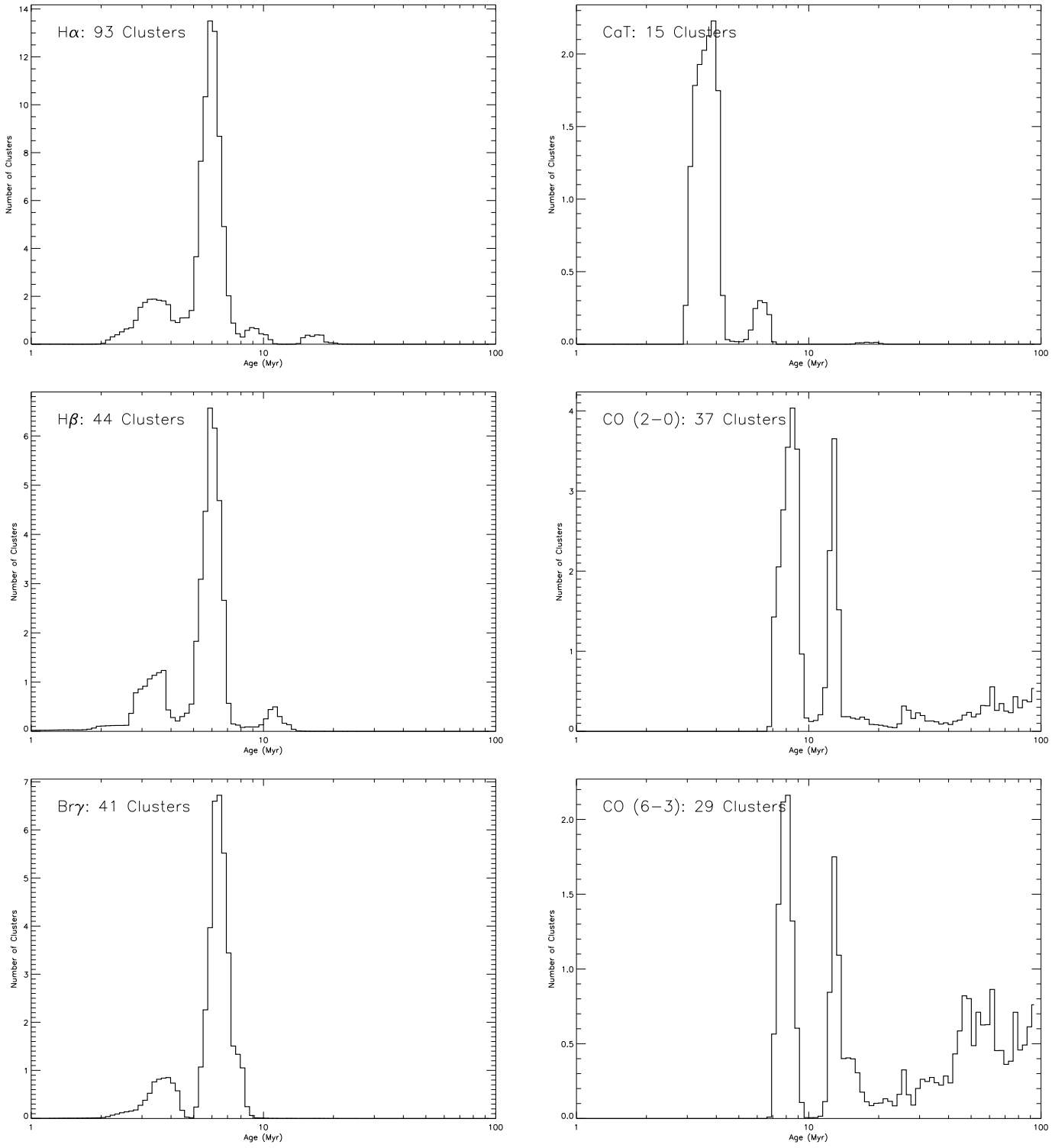

Figure 4.2 Distribution of Antennae Cluster Ages for Each Diagnostic Lines Assuming an Instantaneous Burst. The plots are made by summing the age probability distributions measured for each cluster for each line. The number of clusters included in each plot is indicated in the figures. The age probabilities are binned into logarithmic bins with $\Delta\log(\mathrm{Age}) = 0.02$.

clusters.

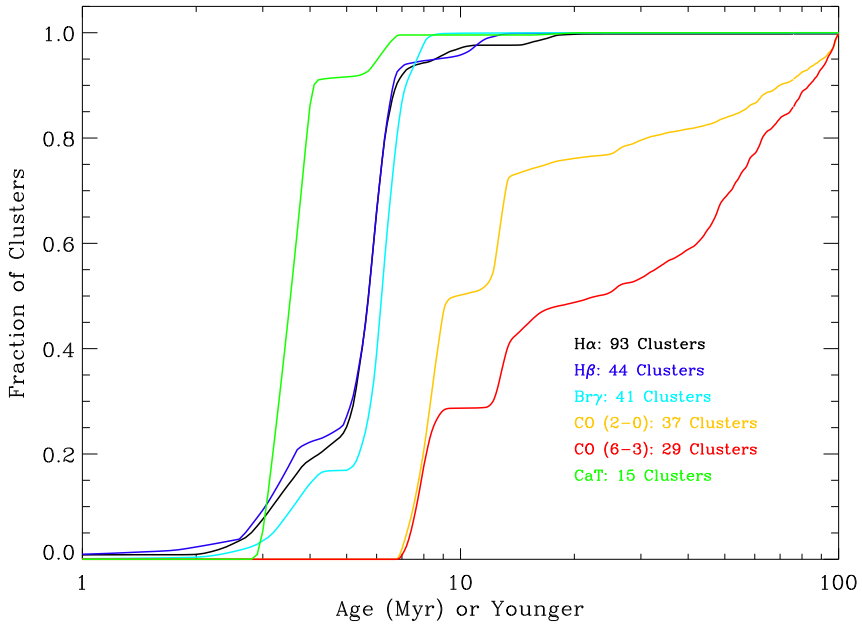

Figure 4.3 Cumulative Distribution of Cluster Ages for the Diagnostic Lines Assuming an Instantaneous Burst. The percentage of clusters predicted to be younger than a given age is plotted for each diagnostic line. Of particular note is the good agreement between the ionized hydrogen tracers (Hα, Hβ, and Brγ) which all predict young ($<$ 10 Myrs) ages. In comparison the CO bandheads both predict a broader age distribution beginning with 8 Myr clusters and extending to 100 Myr clusters.

The Calcium Triplet absorption feature is only detected in 15 clusters in our sample. For all those clusters, however, young ages are predicted, with a strong peak at 3.5 Myr and a weaker peak near 6 Myr. All but 3 of these 15 clusters also have strong hydrogen emission, supporting the young age measurements.

If the clusters with strong hydrogen emission and the clusters with CO bandheads comprised distinct subsets of our sample, then the instantaneous burst model would be ideal, easily identifying the younger clusters (with hydrogen emission) and the older clusters (with CO bandheads). However, as mentioned above, all clusters with CO bandhead detections also had at least one hydrogen line detection. Clearly, it will be impossible to determine a single age for these clusters based on their CO bandhead and hydrogen recombination line equivalent widths using the instantaneous burst model. We note that adopting a non-solar metallicity while maintaining an instantaneous burst would not solve the problems of simultaneous CO bandheads and hydrogen emission. For the three metallicity models with greater than 20% solar metallicity, the CO bandheads still appear approximately 2 Myr after the hydrogen emission lines should disappear (see Figure 3.1). The 20% and 5% solar metallicities do allow for simulataneous CO bandheads and hydrogen emission, but the measured CO bandhead equivalent widths well exceed the maximum equivalent widths predicted by these

models.

Since an instantaneous burst model does not adequately describe the star formation within the Antennae clusters, in the next two sections we will examine alternative star formation models.

4.3 Rejection of a Continuous Star Formation Model

As discussed above (§3.1), Starburst99 contains models for both an instantaneous burst of star formation and continuous star formation at a constant rate. We can immediately rule out continuous star formation, however, based on the strength of the observed equivalent widths. In Figure 4.4 we plot the equivalent width distributions for the six diagnostic lines on top of the Starburst99 models for continuous star formation at a constant rate. Two problems immediately arise. In the continuous star formation model, the hydrogen recombination line equivalent widths do not drop off as in the instantaneous burst model but rather remain at a high level past 100 Myr. Indeed the equivalent widths drop by less than one decade over 100 Myr in the continuous model compared with almost 7 decades for the instantaneous burst. A majority of the measured hydrogen equivalent widths are below the minimum values predicted for a continuous star formation model and thus inconsistent with a continuous burst. Likewise, the maximum CO (2-0) bandhead equivalent width out to 100 Myr for the continuous star formation model is 12.2Å. Figure 4.4 clearly shows that the majority of the measured CO (2-0) bandhead equivalent widths lie above this 12.2Å maximum. The continuous star formation model is in fact a much worse representation of the Antennae clusters than the instantaneous burst.

4.4 Testing Other Star Formation Models

As neither the instantaneous burst nor the continuous star formation model allow for cluster age determinations that are consistent across all six diagnostic lines, we examine additional star formation profiles not included in Starburst99. Two variations to the models were considered: a superposition of two instantaneous burst clusters and a non-instantaneous star formation burst of duration up to 20 Myr. Both of these star formation models are supported by conditions within the Antennae and are actually more appropriate than an instantaneous burst model.

4.4.1 Superposition of Two Instantaneous Bursts

At the 19.2 Mpc distance to the Antennae (Whitmore et al., 1999), $1''$ corresponds physically to 93 pc. The typical seeing of our observations was around $0.9''$ (Tables 2.1 and 2.2), which is 84 pc at the distance of the Antennae. The radii of Antennae star clusters have been measured between 4–6 pc (Mengel et al., 2002), so clusters are far from resolved in our observations. Additionally, comparing

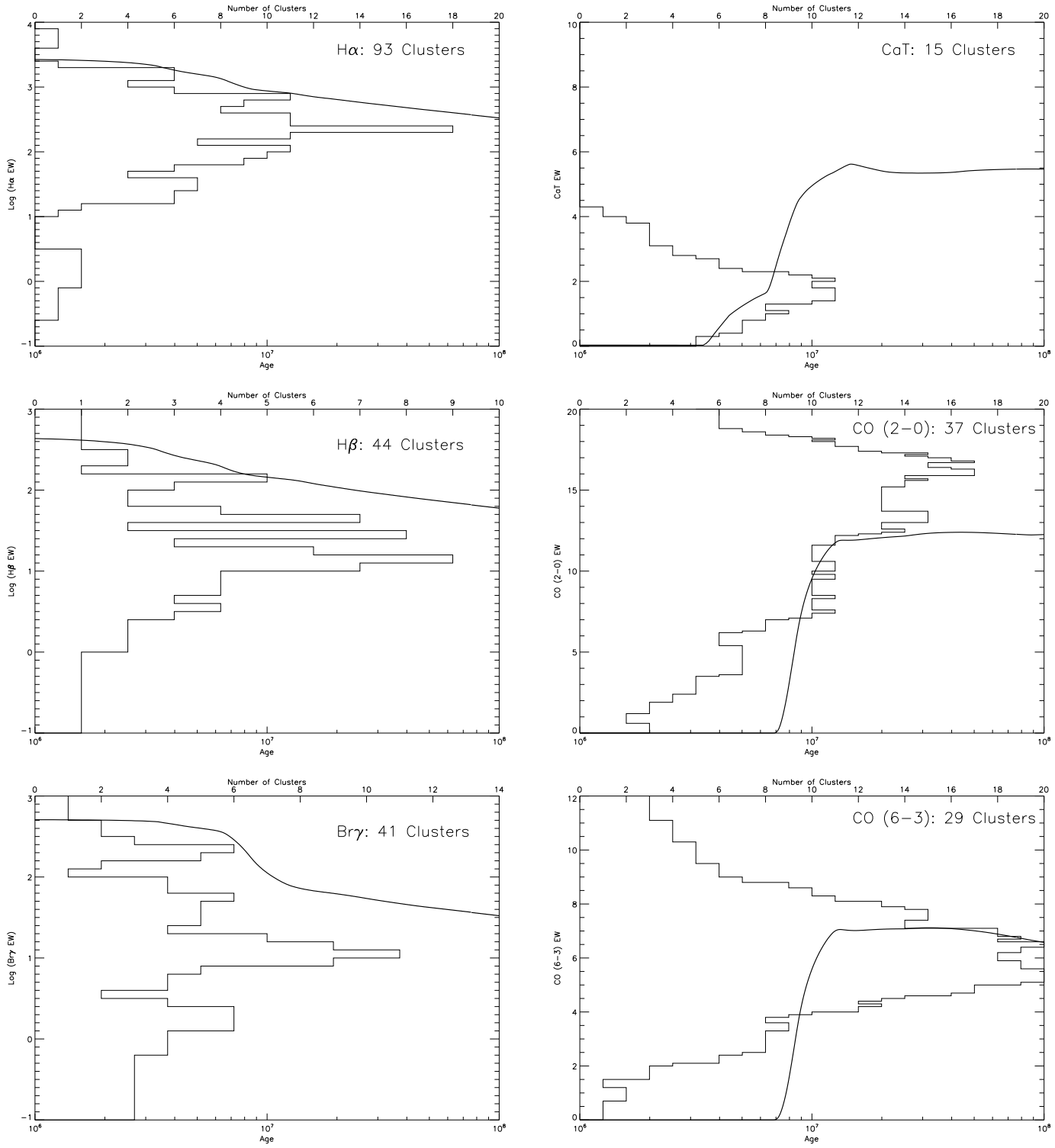

Figure 4.4 Distribution of Equivalent Widths for Six Age Diagnostics with Continuous Star Formation. The measured equivalent widths are binned at a resolution ΔEW=0.1Å for the absorption lines and Δlog(EW)=0.1 for the hydrogen recombination lines. Bins count all clusters whose 3σ equivalent width falls into the bin interval. Thus a cluster will likely be found in more than one bin. The total number of clusters included for each line are indicated in each plot. For each diagnostic line the temporal evolution of the equivalent width from Starburst99 (assuming solar metallicity and continuous star formation) is overplotted from 1 to 100 Myr logarithmically. The measured equivalent widths are clearly incompatible with a continuous star formation profile.

our observations to the HST images of Whitmore et al. (1999) we find that approximately half of our clusters in our observations are found to actually be a superposition of multiple clusters. Thus a star formation profile consisting of multiple instantaneous burst clusters of differing ages superimposed on each other is appropriate from a physical perspective.

4.4.2 Non-Instantaneous Star Formation Burst

Assuming a sound speed of a few km/s (Bastian et al., 2006; Dyson & Williams, 1997), star formation could take a few Myr to propagate over the typical size of a massive star cluster. Therefore it is reasonable to assume that we are not in fact observing an instantaneous burst of star formation but rather a short duration burst of star formation. As we will discuss more in §7.2.1, a short duration burst has been seen in a number of systems, including R136 in 30 Doradus (Massey & Hunter, 1998). In considering possible star formation profiles, we consider bursts of duration up to 20 Myr, in keeping with crossing times within Antennae clusters and observations of cluster formation in other galaxies.

4.4.3 Evaluating Between a Superposition of Instantaneous Bursts and a Non-Instantaneous Burst of Star Formation

We constructed models for the temporal evolution of the six diagnostic lines assuming these two types of star formation profiles: a superposition of two instantaneous bursts and a non-instantaneous burst of star formation. We considered a superposition of two instantaneous bursts with age separation between the bursts starting at 0.5 Myr and continuing in 0.5 Myr intervals to 20 Myr. For a separation of x Myr, we calculated the equivalent width evolution by:

$$\mathrm{EW(t,x)} = \begin{cases} \mathrm{EW_t} & \mathrm{t < x\ Myr} \\ \frac{\mathrm{EW_t C_t + EW_{t-x} C_{t-x}}}{\mathrm{C_t + C_{t-x}}} & \mathrm{t > x\ Myr} \end{cases}$$

where $\mathrm{EW_r}$ and $\mathrm{C_r}$ are the equivalent width and appropriate continuum level measured in Starburst99 for an instantaneous burst of a cluster with age r Myr.

Similarly we also considered non-instantaneous, constant bursts of star formation of durations from 0.5 Myr to 20 Myr, sampled in 0.5 Myr intervals. For a burst of duration x Myr, we determined the equivalent width evolution by:

$$\mathrm{EW(t,x)} = \begin{cases} \frac{\sum_{i=0}^{t} \mathrm{EW_i C_i}}{\sum_{i=0}^{t} \mathrm{C_i}} & \mathrm{t < x\ Myr} \\ \frac{\sum_{i=t-x\ \ Myr}^{t} \mathrm{EW_i C_i}}{\sum_{i=t-x\ \ Myr}^{t} \mathrm{C_i}} & \mathrm{t > x\ Myr} \end{cases}.$$

In Figure 4.5 we plot the evolution of the Hα and CO (2-0) bandhead equivalent widths for a

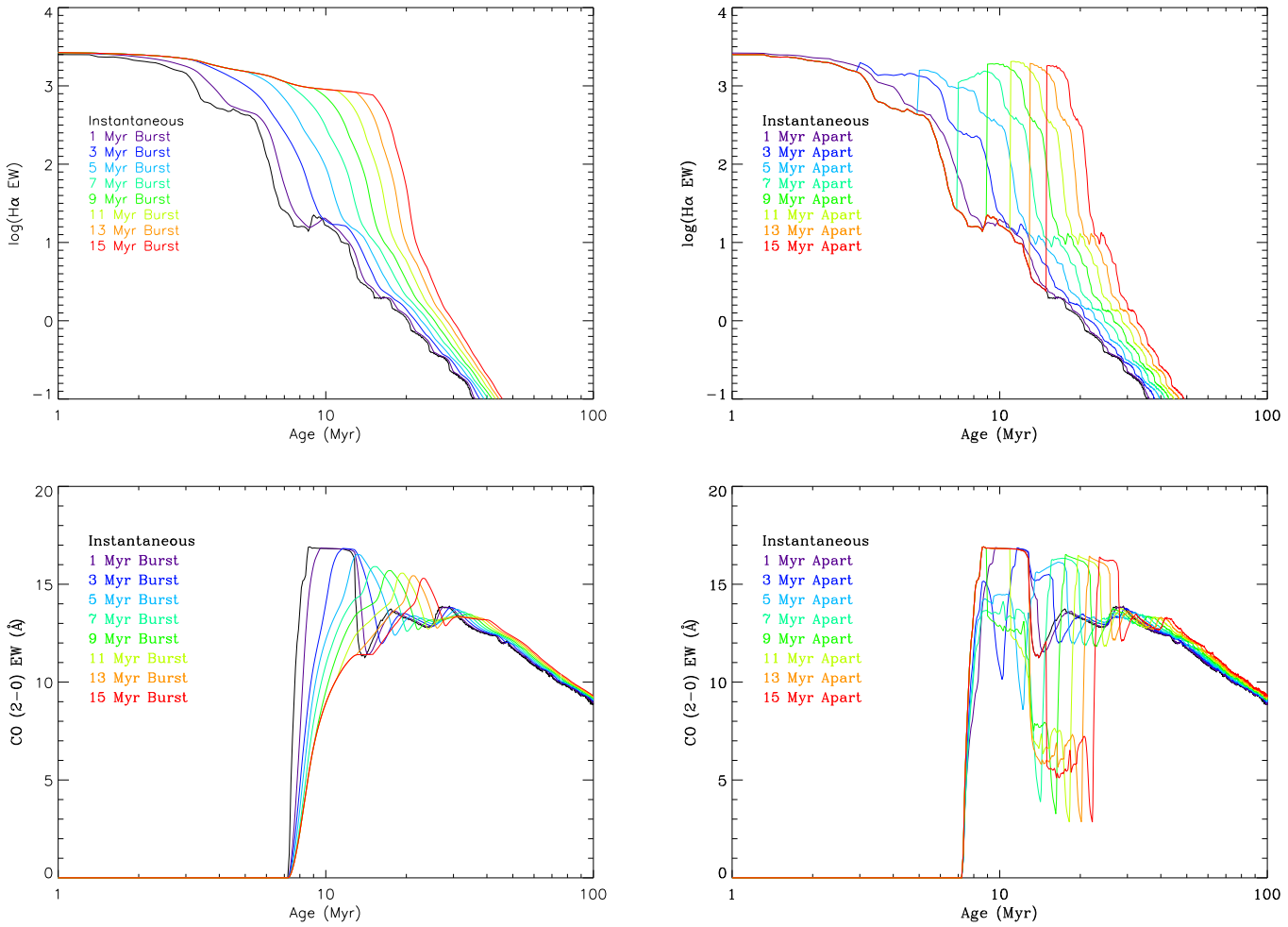

Figure 4.5 Hα (top) and CO (2-0) Bandhead (bottom) Equivalent Width Evolution for Non-Instantaneous Bursts (Left) and the Superposition of Two Clusters (Right). These Hα and CO (2-0) equivalent width models are very representative of the equivalent width models of all three hydrogen lines and the two CO bandheads respectively. In the superposition of two clusters model the clusters are assumed to be of equal mass and each formed in an instantaneous burst. The age shown is the age since the burst began (non-instantaneous) or since the first cluster formed (superposition).

non-instantaneous burst of star formation with varying duration (left) and a superposition of two equal mass clusters with varying age differences (right). The evolution of equivalent widths for the superposition of two instantaneous burst models resemble an instantaneous burst until the time that the second burst begins. Following this second burst, the models almost reset themselves and appear very similar to an instantaneous burst cluster offset by the number of years between the two bursts. This behavior appears for all of the diagnostic lines and is likely due to the fact that the younger burst is typically much more luminous than the original burst and thus dominates the output of the cluster. From these models, we can see that while a superposition of two bursts separated by > 7 Myr does not work well in explaining the simultaneous presence of the CO bandheads and hydrogen emission lines, a smaller age separation could be a possibility.

For the models of a non-instantaneous burst of star formation we find very different behavior (left plots of Figure 4.5). With increasing burst length the cluster age where the hydrogen emission line equivalent width falls off is increased. Indeed, for the instantaneous burst the falloff is most pronounced around 5–6 Myr, but increases to 9–10 Myr for a 5 Myr burst and to almost 20 Myr for a 15 Myr burst. The CO (2-0) bandhead equivalent width also varies with burst length. The bandheads appear near 8 Myr for all burst lengths, but the age where the bandhead equivalent widths reach their peak increases with the burst length. For an instantaneous burst the equivalent width peak is reached near an age of 8.5 Myr, compared with 12 Myr for a 5 Myr duration burst, and 28 Myr for a 15 Myr duration burst.

From examining the models, we discovered that the easiest way to account for the simultaneous presence of CO bandheads and hydrogen emission lines is if the CO bandheads are observed soon after their first appearance (i.e., in the time when the CO bandhead equivalent width is rising to its maximum value). Based on this, we placed a constraint on the range of burst durations by looking for models where the time of the rise of the CO bandhead equivalent width corresponds to the time when the Hα equivalent width is falling off and reaches log(Hα EW) = 2–2.5, the peak of the Hα equivalent width distribution (see Figure 3.3). We found the best agreement to occur for star formation profiles with a burst duration from 3 to 7 Myr (see Figure 3.2 (middle) for the 5 Myr burst example). A burst length shorter than 3 Myr meant that the hydrogen lines would disappear before the CO bandheads appear and a burst length longer than 7 Myr meant that the hydrogen emission line equivalent widths would only begin to fall off well after the CO bandheads had appeared.

To more specifically determine the best star formation profile model to use and to confirm our selection of a non-instantaneous burst over a superposition of clusters, we calculated the ages predicted by each diagnostic line for each cluster using all of the superposition and non-instantaneous star formation burst models, a total of 80 models. The ages were calculated in the same manner as described for the instantaneous burst case (§4.1). We examined every cluster that had more than one diagnostic line detected and determined the model or models that gave the most consistent ages

between the lines. The model that was most successful in yielding consistent ages for a cluster across all the lines was the model of a 5 Myr duration constant rate burst of star formation. We adopt this model for the remainder of our analysis of the Antennae clusters.

4.5 Examining The 5 Myr Duration Burst of Star Formation Model

The evolutionary synthesis tracks for the six age diagnostic lines assuming a 5 Myr duration constant rate burst of star formation are plotted in the middle plot of Figure 3.2. In Figure 4.6 we plot the distribution of ages predicted for all our clusters by each of the six diagnostic lines. For comparison, we have also included with dashed lines the age distributions assuming an instantaneous burst, as seen in Figure 4.2. The most notable difference between the 5 Myr duration burst ages and the instantaneous burst ages is that the hydrogen recombination lines are on average 3 Myr older in the 5 Myr duration burst model. Indeed, the Hα age distribution peaks around 9 Myr, compared with 6 Myr for the instantaneous burst. Likewise, the Hβ and Brγ distributions peak at 10 Myr and 9.5 Myr in the 5 Myr duration model compared with 6 and 6.5 Myr respectively in the instantaneous burst model. The Calcium Triplet ages are also older in the 5 Myr duration burst model by around 3 Myr, with a peak age just shy of 7 Myr. On the other hand, the CO bandhead age distributions for the 5 Myr duration burst are similar to the instantaneous burst distributions. The CO (2-0) bandhead still has two main age peaks, which are located at 8.5 and 12 Myr, the same ages as for the instantaneous burst model. Likewise, the CO (6-3) bandhead has a single prominent age peak at 9 Myr, about 0.5 Myr older than in the instantaneous case. Due to the older ages predicted by the hydrogen recombination lines in the 5 Myr duration burst model, the agreement between the CO bandheads and the hydrogen lines is very good, with all three emission lines and both CO bandheads having prominent peaks in the 8.5–10 Myr age range.

We note that the discussion so far has only looked at each of the six age diagnostics separately. In the next section (§4.6) we will derive an age for each cluster by combining the age estimates (assuming the 5 Myr duration burst model) from each of the observed diagnostic lines.

4.6 Deriving Ages Across Diagnostic Lines

We manually determine the age of each cluster based on the ages predicted by the individual diagnostic lines. The age probability distribution for an individual diagnostic line usually contains from one to a few probability peaks ($> 5\%$ probability) at different ages. These peaks are seldom wider than 1–2 Myr. We identify age ranges where the probability peaks for individual diagnostic lines overlap and take these age ranges as possible ages for the cluster. For some clusters, there are

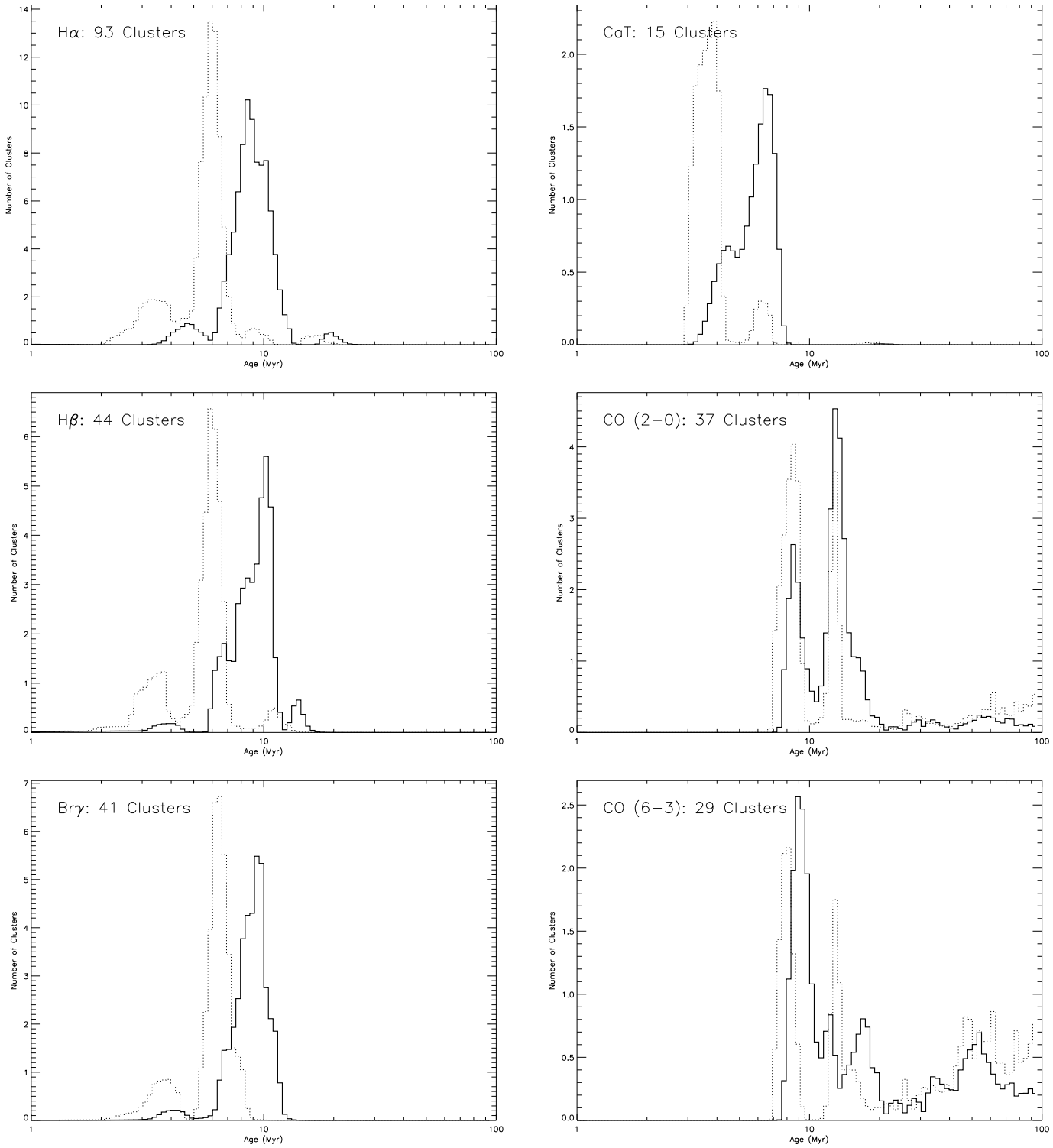

Figure 4.6 Distribution of Antennae Cluster Ages for Six Diagnostic Lines Assuming a 5 Myr Duration Burst (solid lines). The plots are made by summing the age probability distributions measured for each cluster for each line. The age probabilities are binned into logarithmic bins with $\Delta\log(\mathrm{Age}) = 0.02$. For comparison, the age distributions for an instantaneous burst are shown using dashed lines.

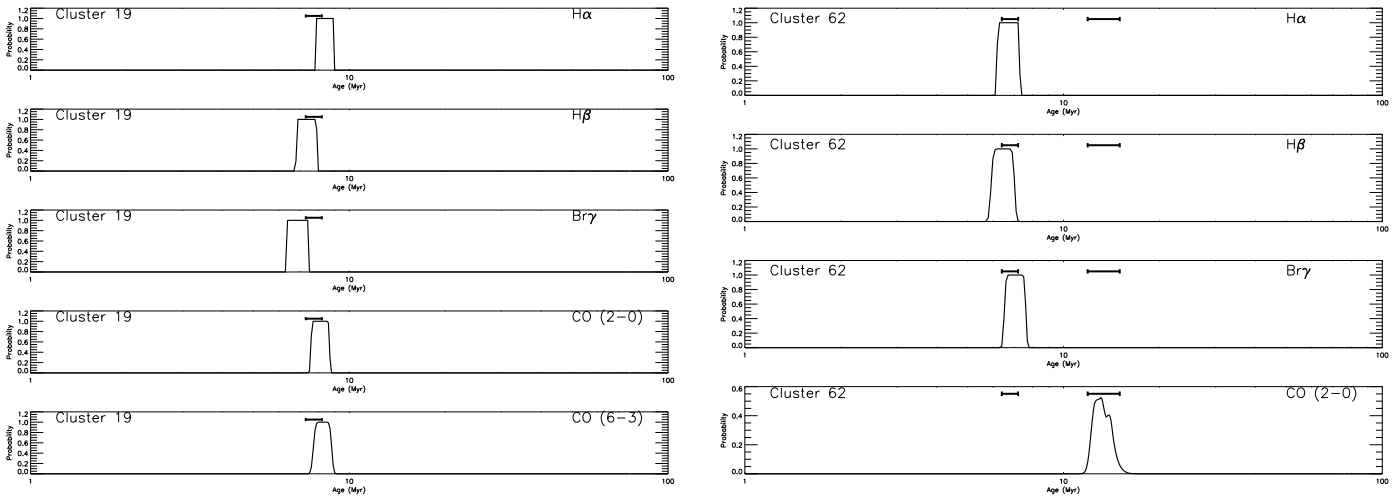

Figure 4.7 Deriving Ages Across Diagnostic Lines for Cluster 19 (left) and Cluster 62 (right). The age probabilities for each observed diagnostic line (calculated assuming a 5 Myr duration burst) are plotted individually. The regions that have been identified as possible age ranges for each cluster are marked by solid black lines.

diagnostic lines with age probability peaks that do not overlap with age probability peaks from other diagnostic lines. In these cases, we take these non-overlapping probability peaks and also include them as possible cluster ages. In Figure 4.7 we illustrate this process for determining a cluster age by showing the individual age distributions predicted for two clusters in our sample. The solid black bars at the top of each plot indicate the final age estimates for that cluster. In Cluster 19 (left) the age peaks of all five diagnostic lines overlap between 7.3 and 8.2 Myr, so only one age range is necessary for this cluster. On the other hand, in Cluster 62 the hydrogen emission lines all predict an age from 6.4 to 7.2 Myr. The CO (2-0) bandhead, however, suggests an older age (11.9–15 Myr). Cluster 62 thus has two possible age ranges.

In Table 4.1 we list the age estimates for each cluster as well as the diagnostic lines that support that age determination. Ten clusters were not detected in any diagnostic lines and are not included in the table. In Table 4.2 we summarize the number of age ranges determined for a cluster, breaking up the analysis by the number of diagnostic lines observed. In total, 181 age ranges were used to completely describe the possible ages of the 117 clusters and 8 nuclear region observations. 60% of clusters can be described by a single age estimate and the largest number of age estimates necessary for a cluster is four. As further evidence for the strength of the 5 Myr duration burst model, using an instantaneous burst model, 287 age ranges would be needed for the same 117 clusters and 8 nuclear regions, including 6 clusters that required 7 or more age regions.

Table 4.1. Solar Metallicity Age Measurements

#	# of Lines (Myr)	Age Range	Lines	#	# of Lines (Myr)	Age Range	Lines
1	1	**17.0–23.7**	**Hα**			16.2–20.4	CO(6-3)
2	1	**17.2–21.8**	**Hα**			32.2–36.2	CO(6-3)
3	1	**10.5–11.6**	**Hα**	51	3	**9.9–11.0**	**Brγ CO(2-0) CO(6-3)**
4	2	**8.3–9.2**	**Hα Hβ**			14.8–17.7	CO(2-0)
5	2	**9.8–10.7**	**Hα Hβ**	52	4	**9.4–9.8**	**Hα Hβ Brγ CO(2-0)**
6	1	**11.1–12.3**	**Hα**	53	4	**9.7–10.1**	**Hα Brγ CO(2-0) CO(6-3)**
7	1	**8.8–10.1**	**Hα**			13.5–17.5	CO(2-0) CO(6-3)
8	2	**9.5–10.2**	**Hα Hβ**	54	5	**9.2–9.7**	**Hα Hβ Brγ CO(6-3)**
9	2	**9.7–10.7**	**Hα Hβ**			11.3–16.8	CO(2-0)
10	3	**8.9–10.7**	**Brγ CO(2-0) CO(6-3)**			17.0–19.3	CO(6-3)
		13.6–17.7	CO(6-3)	55	2	**7.4–8.3**	**Brγ CO(2-0)**
11	1	**7.2–8.2**	**Hα**	56	3	3.3–4.9	CaT
12	5	**10.3–10.5**	**Hα Hβ Brγ CO(6-3)**			**7.7–8.5**	**Hα Hβ**
		11.6–16.0	CO(2-0)	57	3	3.3–4.9	CaT
13	1	**7.2–8.2**	**Hα**			**7.7–8.5**	**Hα Hβ**
14	5	**9.0–10.3**	**Hα Hβ Brγ CO(2-0) CO(6-3)**	58	1	**9.2–10.2**	**Hα**
		14.9–17.8	CO(2-0)	59	2	3.7–5.3	CaT
15	2	**3.6–4.9**	**Hα Brγ**			**9.8–10.9**	**Hα**
16	2	**8.6–8.7**	**Hα Hβ**	60	1	**6.7–7.8**	**Hα**
17	4	**8.9–9.3**	**Hα Brγ CO(6-3)**	61	4	**8.4–8.8**	**Hα Brγ CO(2-0) CO(6-3)**
		12.0–14.8	CO(2-0)	62	4	**6.4–7.2**	**Hα Hβ Brγ**
18	3	**8.9–9.9**	**Hα Hβ**			11.9–15.0	CO(2-0)
		5.4–7.1	CaT	63	4	**8.4–9.2**	**Hα Brγ**
19	5	**7.3–8.2**	**Hα Hβ Brγ CO(2-0) CO(6-3)**			11.7–12.8	CO(2-0) CO(6-3)
20	2	**10.1–11.2**	**Hα Hβ**			14.4–15.6	CO(2-0) CO(6-3)
21	1	**11.2–13.5**	**Hα**	64	1	**9.5–10.9**	**Hα**
22	2	**6.0–7.1**	**Hα Hβ**	65	3	**8.0–8.8**	**Hα Brγ**
23	2	0.0–4.6	Hβ			11.2–16.8	CO(2-0)
		6.7–7.9	**Hα**	66	1	**8.2–9.2**	**Hα**
24	2	**5.7–6.1**	**Hα Hβ**	68	3	**8.4–8.6**	**Brγ CO(2-0) CO(6-3)**
25	2	**8.5–8.9**	**Brγ CO(2-0)**			15.1–20.4	CO(6-3)
		17.4–18.5	CO(2-0)			32.4–35.8	CO(6-3)
26	4	**8.2–9.2**	**Hα Brγ CO(2-0) CO(6-3)**	69	2	**11.9–12.6**	**Hα Hβ**
		16.4–20.1	CO(6-3)	70	4	**9.5–10.4**	**Hα Brγ CO(6-3)**
		33.3–36.0	CO(6-3)			12.4–14.1	CO(2-0)
27	1	**7.7–8.8**	**Hα**	71	1	**7.4–8.4**	**Hα**
28	1	**4.2–5.8**	**Hα**	72	3	**9.3–9.8**	**Hα Brγ CO(2-0)**
29	5	**7.0–8.0**	**Hα Hβ Brγ CO(2-0) CO(6-3)**	73	1	**10.5–11.8**	**Hα**
30	1	**3.2–5.7**	**Hα**	74	5	7.2–7.8	CO(2-0) CaT
31	1	**6.9–8.1**	**Hα**			**10.4–11.0**	**Hα Hβ Brγ**
35	1	**6.5–7.8**	**Hα**	75	2	**6.7–7.4**	**Hα Hβ**
36	2	**6.7–6.8**	**Hα Hβ**	76	6	3.5–6.6	CaT
37	2	**7.8–8.9**	**Hα**			**8.8–9.1**	**Hα Hβ Brγ CO(6-3)**
		9.9–11.0	Hβ			11.6–15.8	CO(2-0)
38	1	**7.5–8.6**	**Hα**	77	1	**7.1–8.1**	**Hα**
39	1	**8.3–9.3**	**Hα**	78	4	**7.9–8.6**	**Hα Hβ Brγ**
40	2	**7.7–8.8**	**Hα Hβ**			10.9–17.1	CO(6-3)
41	4	**8.9–9.3**	**Hα Hβ Brγ**	79	6	4.9–6.4	CaT
		12.0–14.8	CO(2-0)			**9.9–10.2**	**Hα Hβ Brγ CO(6-3)**
42	2	**8.5–8.6**	**Hα Brγ**			12.5–14.0	CO(2-0)
43	2	**6.2–7.5**	**Brγ**			16.6–35.3	CO(6-3)
		8.1–20.2	CO(2-0)	80	2	6.1–7.8	CaT
44	2	**7.2–7.6**	**Hα Hβ**			**8.2–9.3**	**Hα**
45	1	**3.7–5.0**	**Hα**	81	1	**5.8–7.4**	**Brγ**
46	1	**8.5–9.6**	**Hα**	82	5	4.7–6.6	CaT
47	1	**0.8–8.4**	**Brγ**			8.6–10.2	CO(6-3)
48	4	**8.7–9.1**	**Hα Brγ CO(2-0) CO(6-3)**			**10.8–11.8**	**Hα Brγ**
		17.3–19.2	CO(2-0)			12.2–14.4	CO(2-0)
49	5	**9.6–10.0**	**Hα Hβ Brγ CO(6-3)**	83	1	**7.4–8.5**	**Hα**
		11.4–16.4	CO(2-0)	84	2	**9.5–10.4**	**Hα Hβ**

Table 4.1 (cont'd)

#	# of Lines	Age Range (Myr)	Lines	#	# of Lines	Age Range (Myr)	Lines
85	4	5.2–7.0	CaT			10.9–12.8	CO(2-0)
		8.5–10.5	CO(6-3)			14.4–17.1	CO(2-0)
		11.9–13.1	**Hα CO(2-0)**	109	5	**10.3–10.5**	**Hα Hβ Brγ CO(6-3)**
86	1	**7.5–8.5**	**Hα**			12.2–14.4	CO(2-0)
87	5	**8.6–9.0**	**Hα Hβ Brγ CO(2-0) CO(6-3)**	110	1	**7.7–8.9**	**Hα**
88	4	**8.3–9.1**	**Hα Brγ**	111	1	**8.5–9.8**	**Hα**
		9.5–11.5	CO(2-0) CO(6-3)	112	2	**3.3–4.7**	**Hα Hβ**
		16.9–35.3	CO(2-0) CO(6-3)	113	2	**7.1–7.7**	**Hα Hβ**
89	1	**5.7–7.2**	**CaT**	114	2	**6.4–7.3**	**Hα Hβ**
90	5	**8.7–9.2**	**Hα Hβ Brγ CO(6-3)**	116	2	**7.8–8.5**	**Hα Hβ**
		10.5–17.4	CO(2-0)	117	1	**10.3–11.7**	**Hα**
		16.4–20.2	CO(6-3)	4039 Nucl S	2	6.3–7.5	CaT
91	2	**8.4–8.8**	**Hα Hβ**			**12.1–13.4**	**Hβ**
92	1	**6.8–8.1**	**Hα**	4039 Nucl	5	6.5–7.6	CaT
94	1	**0.0–1.7**	**Hα**			8.8–9.4	CO(2-0) CO(6-3)
96	1	**10.5–11.6**	**Hα**			**10.6–11.7**	**Hβ Brγ**
97	4	3.5–6.7	CaT			60.3–65.1	CO(2-0)
		11.1–11.7	**Brγ CO(2-0) CO(6-3)**	4039 Nucl N	2	6.4–7.5	CaT
		14.8–16.8	CO(2-0) CO(6-3)			**9.8–10.8**	**Hβ**
99	1	**10.0–11.3**	**Hα**	4039 Nucl SE	3	**8.3–9.4**	**CO(2-0) CO(6-3)**
100	5	**9.7–10.1**	**Hα Hβ Brγ CO(6-3)**			10.0–11.1	Brγ
		12.3–14.2	CO(2-0)	4039 Nucl NW	3	9.0–9.2	CO(2-0) CO(6-3)
101	2	**9.3–10.4**	**Hα Hβ**			**10.2–10.7**	**Brγ CO(2-0)**
102	2	**9.9–10.9**	**Hα Hβ**			47.6–53.2	CO(2-0)
104	4	6.2–7.4	CaT	4038 Nucl S	6	6.1–7.5	CaT
		10.2–10.5	**Brγ CO(6-3)**			**9.3–9.6**	**Hα Hβ Brγ CO(2-0) CO(6-3)**
		12.2–14.4	CO(2-0)	4038 Nucl	5	**8.3–8.7**	**Hα Hβ Brγ CO(2-0) CO(6-3)**
105	1	**4.2–7.1**	**CaT**			69.0–73.5	CO(2-0)
106	1	**12.6–16.2**	**Hβ**	4038 Nucl N	5	6.9–7.1	Hα Hβ
107	1	**6.1–7.6**	**CaT**			**8.0–8.3**	**Hα Brγ CO(2-0) CO(6-3)**
108	4	**8.7–9.6**	**Hα Brγ CO(6-3)**				

Table 4.2. Distribution of the Number of Age Ranges

Number of Lines	Number of Age Ranges 1	2	3	4	Total
1	39	-	-	-	39
2	24	8	-	-	32
3	1	7	2	-	10
4	2	7	7	-	16
5	3	7	2	3	15
6	-	1	1	1	3
Total	69	30	12	4	115[a]

[a]Including the 8 observations of NGC 4038/NGC 4039 nuclei. 10 clusters had no detectable lines.

In determining possible age ranges (Table 4.1), we have included all age peaks with $> 5\%$ probability in an least one tracer. In many cases, even if a cluster has more than one possible age range, there is a single age range that is supported by all observed lines. In total, 78 out of 115 clusters and nuclear regions (68%) have an age estimation that used all observed diagnostic lines (Table 4.3). This compares to only 69 clusters (60%) for the instantaneous burst. These numbers are slightly misleading, however, since 39 clusters were only observed in one line (normally Hα). Additionally, many of the clusters that were observed in only two lines were observed in two hydrogen lines. These lines typically predict the same ages. If we exclude clusters only observed in one tracer and clusters observed in two tracers, where both are hydrogen lines, we are left with 50 clusters and nuclear regions. 16 of these 50 clusters (32%) have a coherent age predicted by all observed lines. In comparison, only 7 (14%) have a coherent age using the instantaneous burst model, largely because of disagreement between ages predicted by hydrogen lines and by the CO bandheads. Extending this analysis one step forward, 82% of these 50 clusters have ages supported

Table 4.3. Analysis of the Number of Lines Used For an Age Determination

	5 Myr Duration Burst	Instantaneous Burst
All Clusters and Nuclear Regions		
All Observed Diagnostic Lines Used	78 / 115 (68%)	69 / 115 (60%)
All or All-But-One Observed Diagnostic Line Used	106 / 115 (92%)	91 / 115 (79%)
Excluding Clusters with One Line and Clusters with only Hydrogen Emission		
All Observed Diagnostic Lines Used	16 / 50 (32%)	7 / 50 (14%)
All or All-But-One Observed Diagnostic Line Used	41 / 50 (82%)	26 / 50 (52%)

by all or all-but-one of the observed diagnostic lines, compared with only 52% for the instantaneous burst. It is clear that a 5 Myr duration burst model is much more effective than an instantaneous burst in describing star formation within Antennae clusters.

From the possible age ranges for each cluster we selected one age range as the most likely age range. This will be the age that we take for the cluster in the remainder of our analysis. If a cluster had an age estimate supported by all observed diagnostic lines then we took this age estimate for the cluster. For the 37 clusters that did not have an age predicted by all the observed diagnostic lines we selected the age range that was supported by the larger number of diagnostic lines and in the case of a tie between age ranges, selected the age range that was predicted by the highest signal-to-noise ratio data (usually the hydrogen emission lines). The age range selected for each cluster is indicated in bold in Table 4.1.

4.7 The Age Distribution of Antennae Clusters

In Figure 4.8 we plot the age distribution of clusters (left) and the nuclear regions (right) from our observations. The cluster age distribution is most pronounced between 6 and 13 Myr with a peak at 8.3 Myr and a secondary peak at 10 Myr. Outside of this 6 to 13 Myr range there are also small peaks in the distribution around 4.5 and 20 Myrs. The oldest age for a cluster in our sample is 23.7 Myr. The nuclear region age distribution is much more uniform, with all regions having ages between 8 and 13 Myr, with the range between 8 and 10 Myr being the most common.

4.7.1 Comparing Age Estimates Between Diagnostic Lines

To examine any age differences between the different diagnostic lines we have constructed individual age distributions for each diagnostic line (Figure 4.9). The age range of a cluster is included in the distribution for a particular line if that line was used to determine the final age range for the cluster (i.e., is listed in bold in Table 4.1). A few conclusions are immediately obvious. The age distributions produced by the three hydrogen lines and the two CO bandheads are very similar.

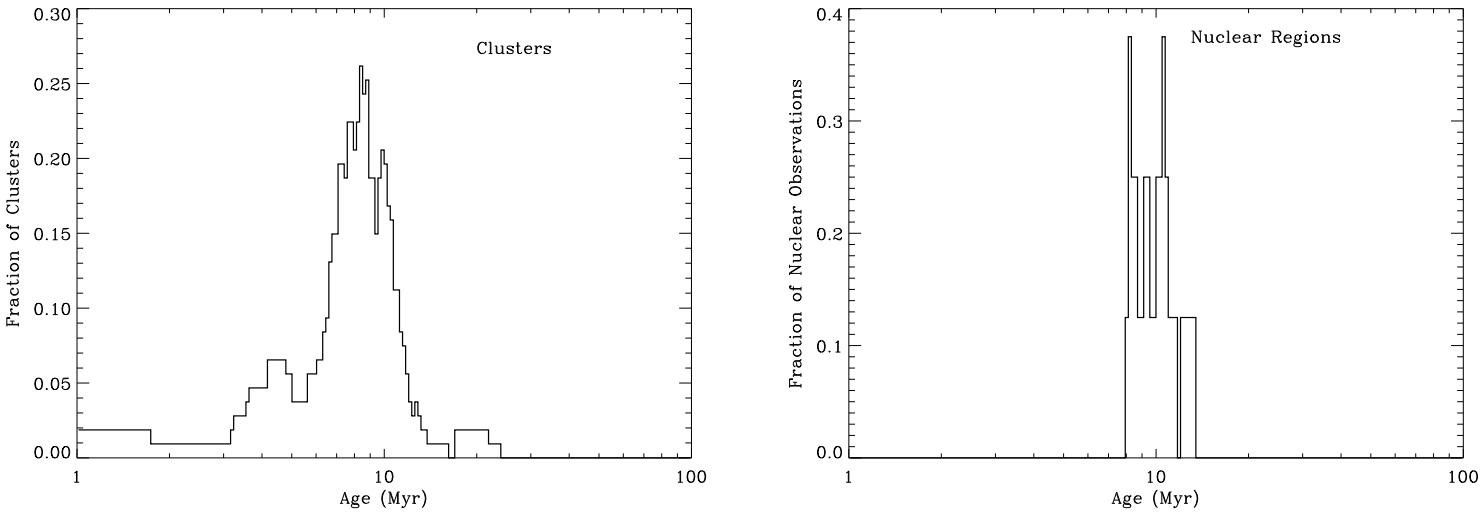

Figure 4.8 Age Distribution of Clusters (left) and Nuclear Regions (right). The age ranges used for each cluster and nuclear region are indicated in bold in Table 4.1. The 10 clusters with no diagnostic line detections are not included in the calculation of the fraction of clusters.

All five distributions have a very strong peak between 8 and 9 Myr, although the width of this peak is greater for the hydrogen lines than for the CO bandheads. Additionally the hydrogen line age distributions have $\sim$ 5% of clusters in the 4–5 Myr age range. These very young clusters are not present in the CO bandhead age distributions, implying that the very young clusters were only detected in the hydrogen lines (with large equivalent widths) and not in the CO bandheads. From existing studies (e.g., Mengel, 2001; Whitmore et al., 1999) we know that a distribution of young clusters (without CO bandheads) does exist, particularly in the overlap region, so finding these young clusters only in hydrogen lines is not surprising.

The Calcium Triplet age distribution, however, is significantly different from the hydrogen line or CO bandhead age distributions. The Calcium Triplet age distribution runs from 4 to 8 Myr and peaks between 5–6 Myr, 3 Myr less than the hydrogen and CO bandhead distributions. We note, however, that only three clusters used Calcium Triplet in their age determination and for all three of these clusters the Calcium Triplet was the only diagnostic line detected. In general, while the CO bandheads and hydrogen emission lines were brought into good agreement with the 5 Myr burst model, ages from the Calcium Triplet feature remained too young. The Calcium Triplet feature is the most difficult of the six diagnostic lines to measure and suffers from the greatest uncertainties (§3.2.3).

We conclude that, with the exception of the Calcium Triplet line, the age distributions produced by the hydrogen emission lines and the CO bandhead are in good agreement. This is particularly important because a large number of our clusters have only optical observations and no near-infrared observations. Indeed, for the 93 clusters with age determinations using Hα, only 30 (32%) also

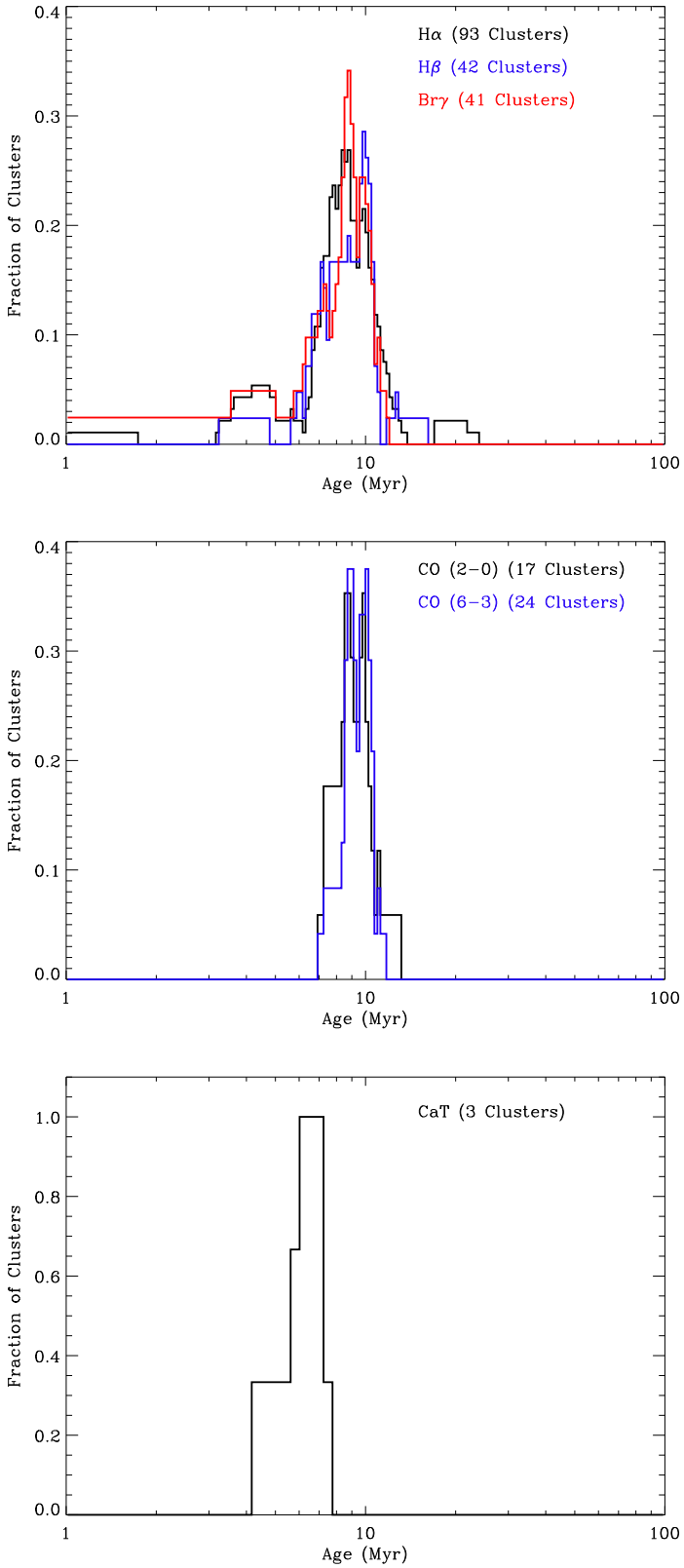

Figure 4.9 Variation in Cluster Ages with Diagnostic Lines. For each age diagnostic line we include every cluster whose final age range is supported by observation of that diagnostic line. The number of clusters included for each line are listed on the plots and this number is used to determine the fraction of clusters separately for each line. For clarity, the plots are divided into hydrogen emission lines (top), CO bandheads (middle), and Calcium Triplet (bottom). The vertical scale is the same for the hydrogen lines and CO bandheads but is larger for the Calcium Triplet.

had observations in the near-infrared. To be able to compare ages from clusters with only optical hydrogen emission lines (i.e., Hα and Hβ) to ages of clusters with hydrogen lines and CO bandheads, we need to be confident that the age distributions of clusters using the CO bandheads and hydrogen recombination lines is similar to the distributions of clusters using the optical hydrogen emission lines. We have explored this agreement in slightly more detail in Figure 4.10, where we plot the age distribution taken from all clusters using the Hα emission line and at least one CO bandhead and compare this with the age distribution taken from clusters using the Hα emission line without using either of the CO bandheads. We find that the age distribution for the clusters with Hα but neither of the CO bandheads in their age determination (shown in red) is similar to the age distribution of all clusters with Hα and at least one CO bandhead in the age determination (shown in black) with only two main exceptions: the youngest clusters ($<$ 6 Myr) are only seen in the clusters with Hα but neither of the CO bandheads in the age determination; and the age peak is shifted slightly younger for the clusters without CO bandheads in the age determination. The first result is not unexpected, as has been discussed above. We expect there to be younger clusters that are only detected in hydrogen recombination lines. The second result, however, shows that at maximum we are underestimating the age of a cluster by only a small amount ($<$ 0.5 Myr) when relying only on optical hydrogen emission line observations. Therefore we are confident in our age estimates, even for those clusters where we only have optical spectra.

4.7.2 Spatial Variation in the Antennae Ages

To get a better understanding of the star formation processes at work within the Antennae, it is critical to determine any connections between cluster age and location within the Antennae. The clusters shown in Figure 4.11 are color-coded based on their mean age and plotted by their location in the Antennae. From this figure we can see that all regions have a large scatter in cluster ages. On average the youngest clusters are found within the overlap region, but at least five clusters with ages $<$ 6 Myr are also found in the northeast region and the western loop. In contrast, the NGC 4039 arms region seems to contain only older clusters, with all but two clusters older than 9 Myr.

We find a few trends within the individual regions. In the northeast region, the oldest clusters are found in the southeastern part of the region, near a right ascension and declination offset of 35$''$ and -10$''$ respectively. In contrast the young ($<$ 6 Myr) clusters are mostly found in the western part of the region with right ascension offsets from 20 to 27$''$. For the western loop old and young clusters are scattered evenly throughout the region, although the oldest ($>$ 11 Myr) clusters are all found in the northern part of the loop. There is no spatial variation in age within the overlap region with young clusters scattered throughout. Finally, the oldest clusters within the NGC 4039 arms tend to be found towards the southern part of our observing region with a declination offset $>$ -70$''$. Indeed the two oldest clusters in our sample, Clusters 1 and 2, are the southernmost clusters in the

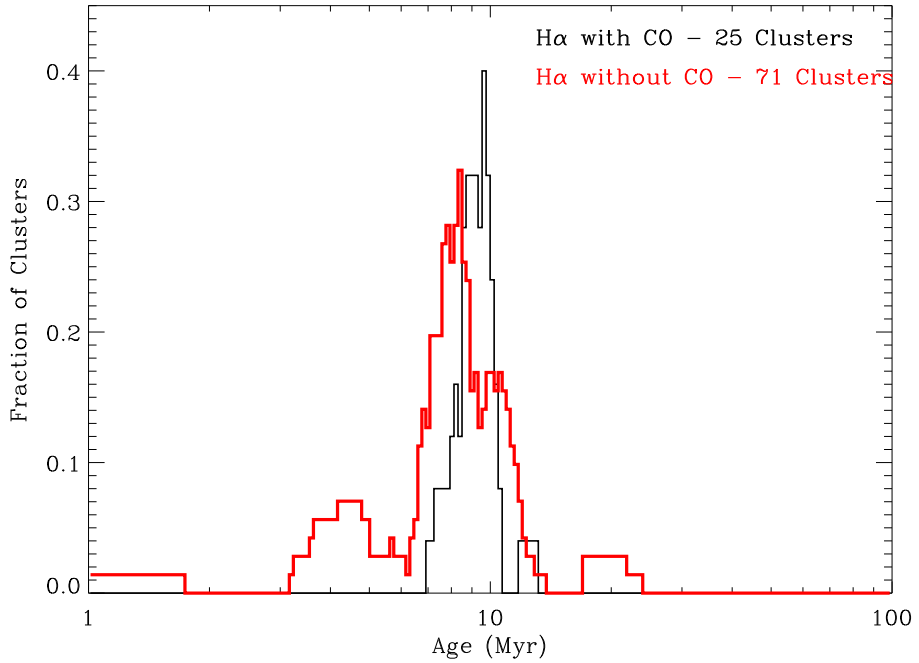

Figure 4.10 Variation in Ages Depending on the Presence of CO Bandheads. The age distribution for the 25 clusters with Hα and at least one of the CO bandheads in the age determination is plotted in black, while the age distribution for the 71 clusters with Hα but neither of the CO bandheads in the age determination is overplotted in red. The distributions are normalized by 25 and 71 clusters, respectively.

region of the NGC 4039 arms observed.

In Figure 4.12 we plot the individual age distributions for the four cluster regions marked in Figure 4.11. The age distribution for the nuclear regions is plotted in Figure 4.8. All the regions have one to two peak ages. This peak lies just before 8 Myr for the overlap region, while it is slightly older (8.2 Myr) for the western loop. The NGC 4039 arms region peaks closer to 10 Myr. Interestingly, the northeast region has two peaks, 8 Myr where it matches the peak of the overlap and western loop regions, and 10 Myr where it matches the NGC 4039 arms region. The younger peak is produced primarily by clusters in the northwestern part of this region while the older peak comes from the southeastern side. As discussed above, young ($<$ 6 Myr) clusters are found in the overlap region, northeast region, and the western loop, but the youngest clusters are most prominent in the overlap region.

A statistical examination of the age distributions for the four regions in the Antennae further illustrates their differences. In Figure 4.13 we plot the cumulative age distribution function for the four regions. While the northeast region and the western loop (black and dark blue respectively) have similar age distributions, the overlap region (red) contains significantly younger clusters and the NGC 4039 arms region (light blue) has significantly older clusters. Examining the age distributions

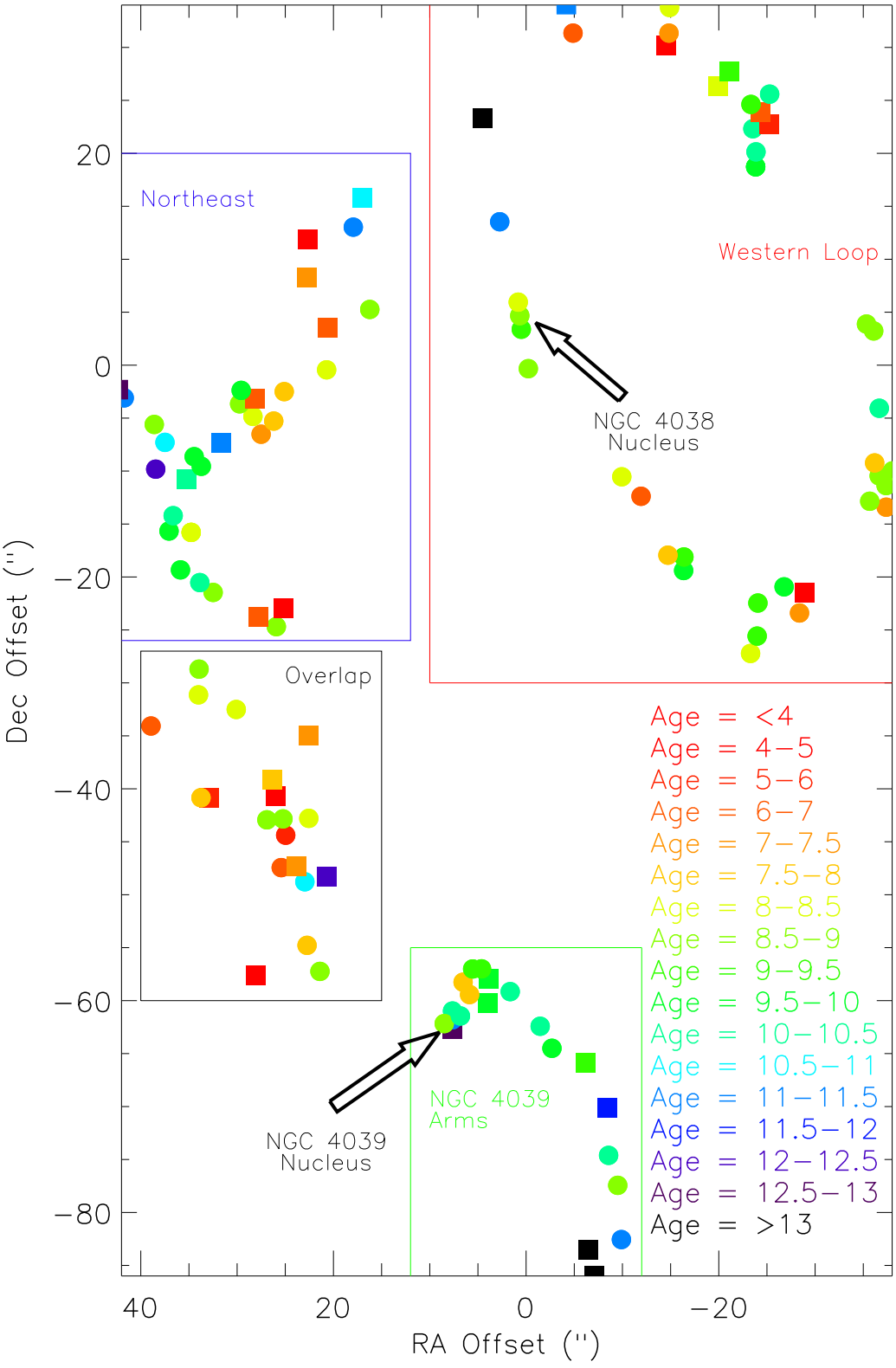

Figure 4.11 Age as a Function of Location Within the Antennae. Clusters are color-coded by their mean age and plotted by their offset from Cluster 87. Clusters marked by circles have a total age range of 1 Myr or less, while clusters marked by squares have a > 1 Myr age spread.

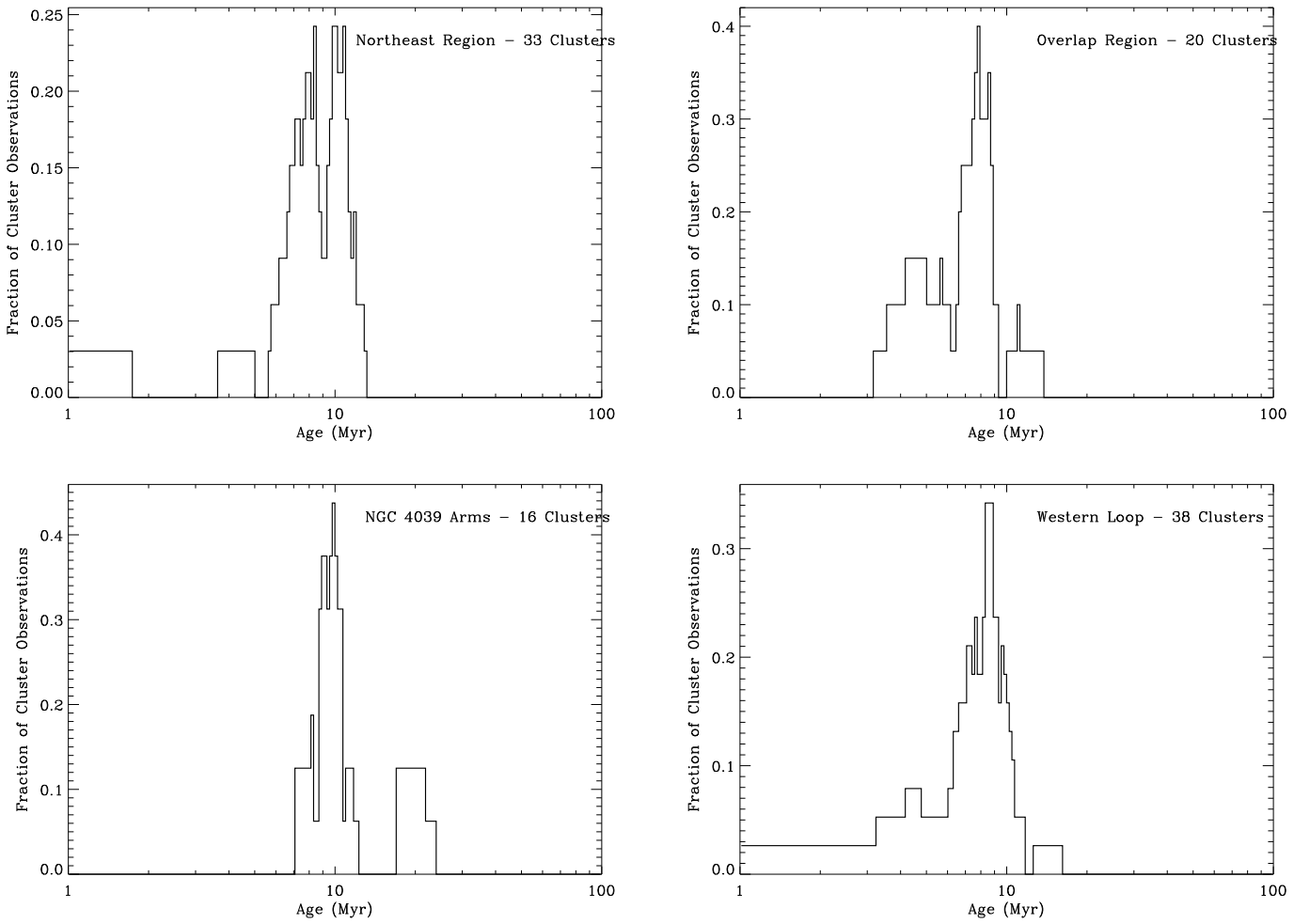

Figure 4.12 Ages by Star-Forming Region. The number of clusters with age measurements in each region is listed on the plots. When producing the distributions, we included a cluster in an age bin if its age range (bold in Table 4.1) overlaps with the age bin. A cluster then will likely be included in more than one bin.

of these regions with a K-S test, we find that the probability is less than 10% that the cluster ages in any two regions were taken from the same overall distribution with one exception: the northeast region and the western loop cannot be shown to be from different populations using the K-S test (Table 4.4). We note that selection effects may have serious impacts on statistical analyses of the age distributions. In §5.2.4 we will examine the differences in cluster mass by region in a similar fashion.

4.8 Selection Effects

Even though there are variations in ages between clusters in different regions, the total range of ages in our sample is small, with no cluster found older than 20 Myr. Clearly we are tracing the youngest

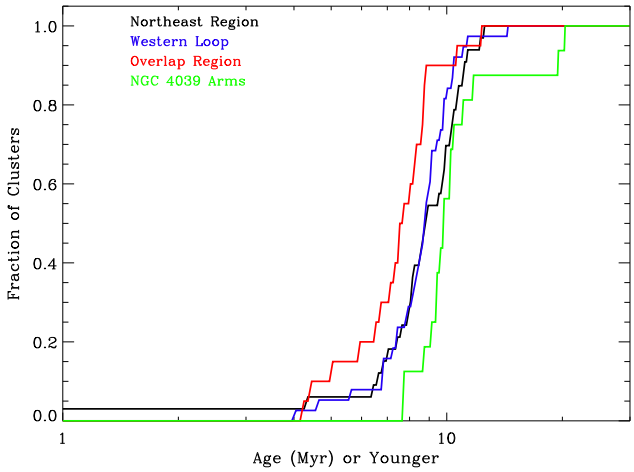

Figure 4.13 Cumulative Age Distribution by Region. The mean age of each cluster is used to construct the distribution function.

Table 4.4. K-S Test Results for Age Distributions by Region

Region	Region	K-S D Value	Probability from Same Distribution
Northeast Region	Western Loop	0.18	54.8%
Northeast Region	Overlap Region	0.42	1.9%
Northeast Region	NGC 4039 Arms	0.36	9.7%
Western Loop	Overlap Region	0.37	3.8%
Western Loop	NGC 4039 Arms	0.43	1.9%
Overlap Region	NGC 4039 Arms	0.73	6.4e-3%

cluster populations within the Antennae. This is expected, however, because of the manner in which our cluster sample was selected. As discussed in §2.2, the clusters were selected from a flux-limited sample of clusters taken from Ks band imaging of the Antennae by Brandl et al. (2005). Figure 4.14 shows the temporal evolution of the K band magnitude of a cluster as predicted by Starburst99. We show the evolution of three different mass clusters for an instantaneous burst (dashed line) and for the 5 Myr duration burst model (solid line) that we have adopted. The K band magnitude peaks around an age of 12.3 Myr after getting consistently more luminous since birth. In creating the 5 Myr duration burst model we have assumed that star formation within the cluster occurs evenly over 5 Myr, so the increase in cluster luminosity from 0 to 5 Myr is explained by the addition of new star formation to the cluster, not from an intrinsic change in the luminosity of 0 to 5 Myr stars. Any change in the intrinsic luminosity in the first 5 Myr of a single star would be visible in the instantaneous burst model (shown in dotted lines), which remains flat during the first 5 Myr. The peak in cluster luminosity from 7 to 20 Myr is due to red giants and supergiants and occurs at roughly the same time as the peak of the CO bandheads, produced by the same red giants and

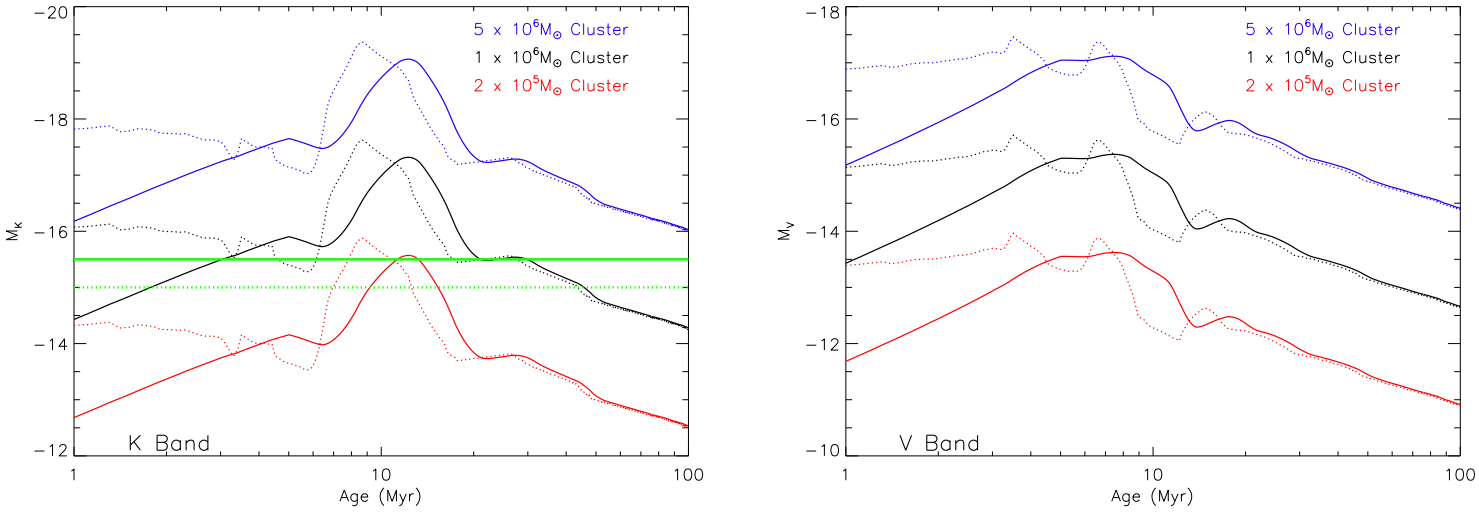

Figure 4.14 Temporal Evolution of Cluster Luminosity in K band (left) and V band (right). The solid lines show the evolution for a 5 Myr duration burst model, while the dotted lines show the original evolution from Starburst99 for an instantaneous burst. We have included plots for three different cluster masses. For the 5 Myr duration burst model we have assumed that the total mass of the burst is formed evenly over the 5 Myr, explaining the initially smaller magnitudes recorded for the 5 Myr burst models. The solid green line in the K band magnitude plot marks an absolute magnitude of -15.5 and the dashed green line an absolute magnitude of -15.

Table 4.5. Detectable Age Ranges for Various Mass Clusters

	2×10^5 $M_\odot$	1×10^6 $M_\odot$ (Myr)	5×10^6 $M_\odot$
M_K < -15.5	11.3–13.1	3.1–29.8	0.5–100
M_K < -15	9.2–15.3	1.8–45.7	0.3–100

supergiants.

As discussed in §2.2.2, we have observed approximately 70% of clusters with $M_{Ks} < -15.5$ and 60% of clusters with M_{Ks} between -15 and -15.5. The solid and dashed green lines in Figure 4.14 indicate $M_{Ks} = -15.5$ and M_{Ks} = -15 respectively. Clearly the age and mass of a cluster will affect its likelihood of being observed in our sample. In Table 4.5 we list the age ranges in which a cluster would have $M_{Ks} < -15.5$ or $M_{Ks} < -15$ for three different cluster masses. The heavier a cluster is the larger age range it can be observed over, but for lighter clusters (i.e., 2×10^5 $M_\odot$) the age range for likely inclusion in our survey is only 6 Myr.

From Figure 4.14 and Table 4.5 we can see possible selection effects in our age distribution. In particular, because of the rise in cluster luminosity between 7 and 20 Myr, we are more likely to detect clusters in that age range. Indeed, our cluster age distribution shows a strong peak around 8.3 Myr, coinciding with the beginning of the sharp increase in cluster luminosity. However, the

cluster luminosity is greatest around 12.3 Myr, yet we see very few clusters with ages > 12.3 Myr. Only 6 of the clusters have an age > 12.3 Myr. If the large number of clusters seen with ages near 8.3 Myr was due solely to selection effects then we should see as many clusters with ages greater than 12.3 Myr as we see less than 12.3 Myr. This is clearly not the case and suggests that the lack of clusters in the 12–20 Myr range is not a selection effect but an actual lack of clusters.

As mentioned in §2.2.1, not all of the clusters in our sample were initially identified by the Ks band flux-limited sample. Approximately half of the clusters were detected as part of spectroscopic observations of other clusters. This gives us a good opportunity to examine the effects of selection biases since we have two almost identically sized samples, one bright in K band, and the other less luminous in K band. In Figure 4.15 we plot the age distribution of these two cluster samples. There is a very noticeable difference between the two samples. The age distribution for the clusters originally identified in the SExtractor sample are plotted in black and peak around 8.5 Myr with a secondary peak around 10.5 Myr. On the other hand, the age distribution for clusters discovered during the observations is consistently younger, with a main age peak around 7.5 Myr and a secondary peak near 9.2 Myr. Additionally, there are 5 discovered clusters with ages between 4–5 Myr compared with only 2 original clusters. The younger ages for the discovered population suggests that the population we are tracing by our K band flux sample may be slightly older than the overall cluster population. This result is not surprising based on the evolution of cluster K and V band magnitudes (Figure 4.14). Since the K band magnitude is increasing from 7 to 12.3 Myr we would expect that the lower luminosity K band magnitude clusters (i.e., the discovered population) would have younger ages. Additionally, a large majority of the discovered clusters were found in the optical spectroscopy as opposed to the near-infrared spectroscopy. The V band luminosity peaks from 4–8 Myr, so we are most likely to discover clusters in that age range, matching the age distribution for the discovered clusters.

In Figure 4.16 we separate the age distribution into four groups based upon the K band cluster luminosity corrected for extinction. For clusters with $M_{Ks} < -15.5$, we see age peaks at 8.9 and 10 Myr (top plot), similar to the peaks seen in the overall cluster age distribution (Figure 4.8). We note that our sample covers approximately 70% of the clusters in the Antennae with $M_{Ks} < -15.5$. The age distributions of fainter K band clusters shows a larger variation in age, particularly in the faintest clusters with M_{Ks} from -15 to -12.75. However, even for these fainter clusters (3rd plot in Figure 4.16), the age distribution peaks between 8 and 9 Myr. This strengthens the argument that the 8–10 Myr age distribution peak is real and not a selection effect. If it was a selection bias because younger clusters are fainter then we would expect to see a flatter, non-peaked distribution for the fainter clusters or a peak at younger ages.

The bottom plot of Figure 4.16 shows the age distribution for 34 clusters that are not detected in K band imaging. These clusters are all visible in optical imaging of the Antennae and are comprised

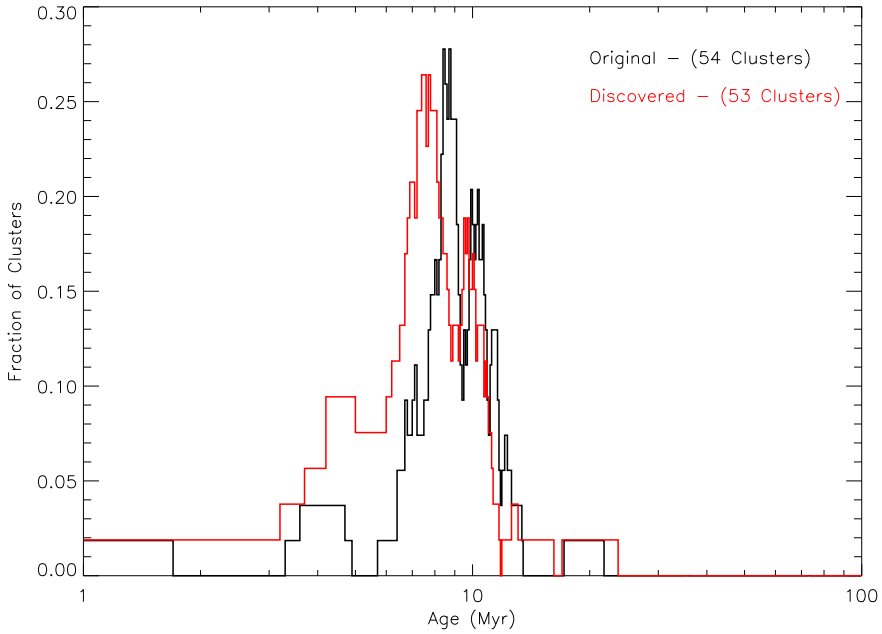

Figure 4.15 Comparing Age Distributions for Original (Black) and Discovered (Red) Clusters. The 54 original clusters were identified in SExtractor Ks band flux-limited sample, while the 53 discovered clusters were serendipitously identified during spectroscopy of the original clusters.

entirely of clusters discovered during spectroscopy. The age distribution of these clusters is slightly younger than the age distributions of the K band detected clusters, with a peak around 7 Myr. The V band magnitude evolution of clusters (Figure 4.14) peaks between 4 and 9 Myr, so the younger clusters in this distribution are not surprising. However, the fact that the distribution peaks strongly around 7 Myr instead of spreading out evenly between 4 and 9 Myr suggests that there is a real deficit of clusters from < 7 Myr.

By examining the age distributions of the original and discovered cluster populations, as well as clusters with and without K band detections, we have been able to determine that our sample is sensitive to cluster ages from approximately 3 Myr out to 20 Myr with only minimal selection effects. We therefore conclude that Antennae clusters have a strong age clustering from 7 to 12 Myr with a moderate deficit in clusters from 3–7 Myr and a substantial deficit of clusters from 12 to 20 Myr. Based on the luminosity evolution of the clusters we can say little about the youngest (< 3 Myr) and older (> 20 Myr) cluster populations. Cluster mass plays a strong part in determining selection biases and we will examine this more fully when we discuss cluster masses (§5.2.6).

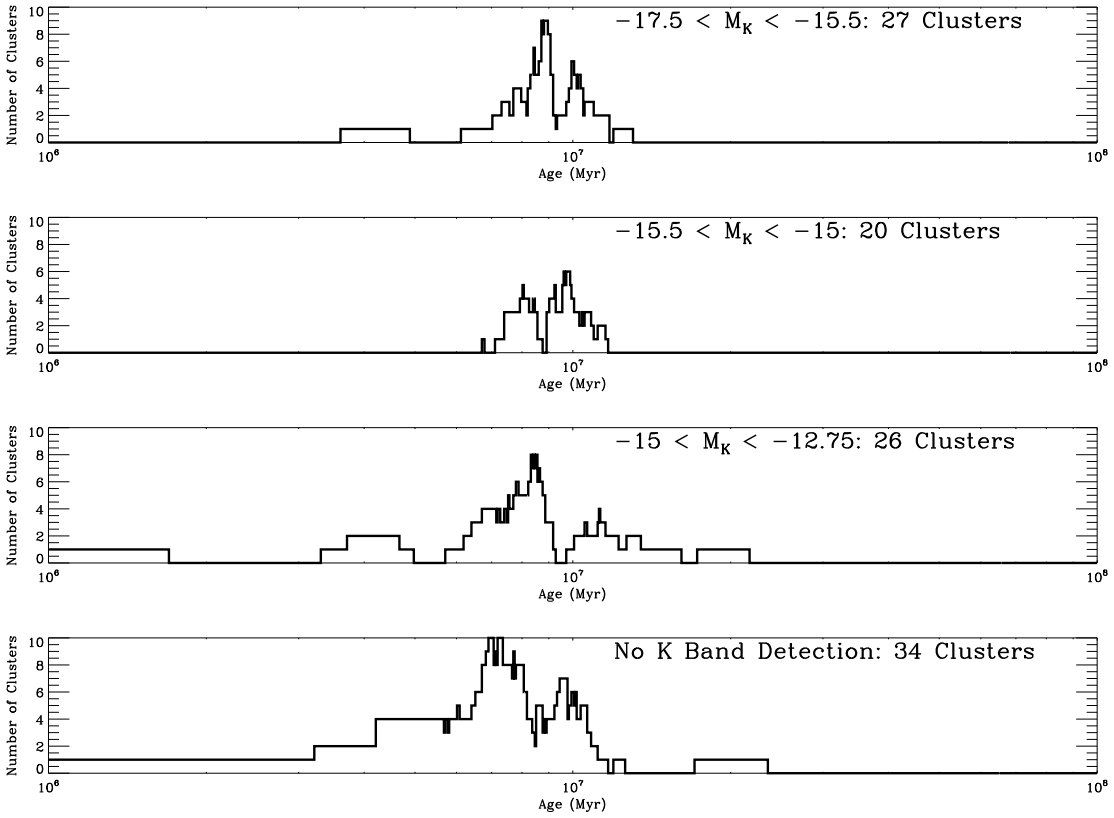

Figure 4.16 Age Distributions by Cluster K band Luminosity. The top plot contains all clusters with $M_{Ks} < -15.5$. We observe 70% of clusters in the Antennae with $M_{Ks} < -15.5$. The second plot includes clusters with M_{Ks} between -15 and -15.5; 60% of clusters in this magnitude range are included in our sample. The third plot shows clusters fainter than -15. Only a fraction of clusters in the Antennae in this range are part of our survey. The bottom plot shows the 34 clusters that did not have a K band detection. These are exclusively discovered clusters from the optical spectroscopy.

4.9 Comparing Ages with the Molecular Gas Distribution

4.9.1 Observations

As part of this study, we have also undertaken detailed molecular gas observations of the Antennae using the Owens Valley Radio Observatory (OVRO) millimeter array. We built upon a previous observation using the OVRO millimeter array of the CO (1-0) transition in the Antennae by Wilson et al. (2000). Wilson et al. (2000) observed three fields within the Antennae that covered the same area as our spectroscopic observations. In total, they observed for 90 hours in four of the five possible array configurations (all except the highest-resolution, most widely spaced U configuration). Their study had a spatial resolution of $3''.15 \times 4''.91$ and a rms noise of 0.055 Jy beam^{-1} in the 5.2 km s^{-1} channels.

From December 2002 through January 2004, we made additional observations of the CO (1-0) transition in the same three fields as Wilson et al. (2000). The observations were completed with

the same spectrometer configurations so that we could easily combine the two sets of data. While we added 1 low (L) configuration track to increase our sensitivity to diffuse gas within the region, the main goal of our observations was to increase the spatial resolution, so we primarily added high-resolution, large-baseline configurations. In particular we took 5 tracks in the high-resolution (H) configuration (maximum baseline of 242 meters) and 3.5 tracks in the ultra-high-resolution (U) configuration (maximum baseline of 483 meters). In total, we obtained 70 hours of new observations, which, combined with the previous observations of Wilson et al. (2000), gave us 160 hours of CO (1-0) observations of the Antennae.

All of the calibration and editing of the observations was done with **MMA** (Scoville et al., 1993), while all cleaning and mapping used the **MIRIAD** software package (Sault et al., 1995). Following the strategy of Wilson et al. (2000), we produced our maps of CO (1-0) emission within the Antennae using a robust weighting of 0.5, a compromise solution between natural weighting, which has the lowest noise levels but a larger spatial resolution, and uniform weighting, which minimizes the spatial resolution at the cost of higher noise levels. We used **mossdi2** to clean the maps to a 1.5σ level in each spectral channel. With the addition of our new H and U track observations, we improved the spatial resolution of the CO (1-0) observations to $2''.33 \times 2''.80$, a 2.5x improvement over Wilson et al. (2000). Our observations have an rms noise of 0.0435 Jy beam^{-1}, a 20% improvement over previous studies.

4.9.2 CO (1-0) Molecular Gas in the Antennae

In Figure 4.17 we plot the integrated intensity map of the CO (1-0) emission in the Antennae. We have also overplotted the individual clusters, color-coded based on their age. We had coherence problems in our observations of the third field in the Antennae, which covered the western loop region. These coherence problems resulted in a large amount of striping in the region and so we have deleted all of this data from the integrated intensity map.

As was found by Wilson et al. (2000, 2003b), the molecular gas in the Antennae tends to concentrate itself in three areas: the overlap region and the areas around each nucleus. The brightest peak is just north of the NGC 4038 nucleus at an offset of ($2''$, $8''$). It is interesting that this peak does not occur at the center of the NGC 4038 nucleus (at an offset of $0''$, $5''$), but rather $3.5''$ away.

We see a similar situation for the CO concentration near the NGC 4039 nucleus (see Figure 4.18 for a detailed image). The concentration peaks $4''$ to the northwest of the NGC 4039 nucleus, almost exactly coincident with Cluster 10. In fact, the molecular gas appears to largely avoid the inner nuclear region of NGC 4039 and instead primarily surrounds this inner nuclear region (see bottom left plot of Figure 4.18). Comparing the CO (1-0) maps with near-infrared images of the Antennae, we see that the molecular gas has its own spiral structure that lies inside of what appears to be a large spiral arm (or interaction tail) extending to the southwest from the NGC 4039 nucleus.

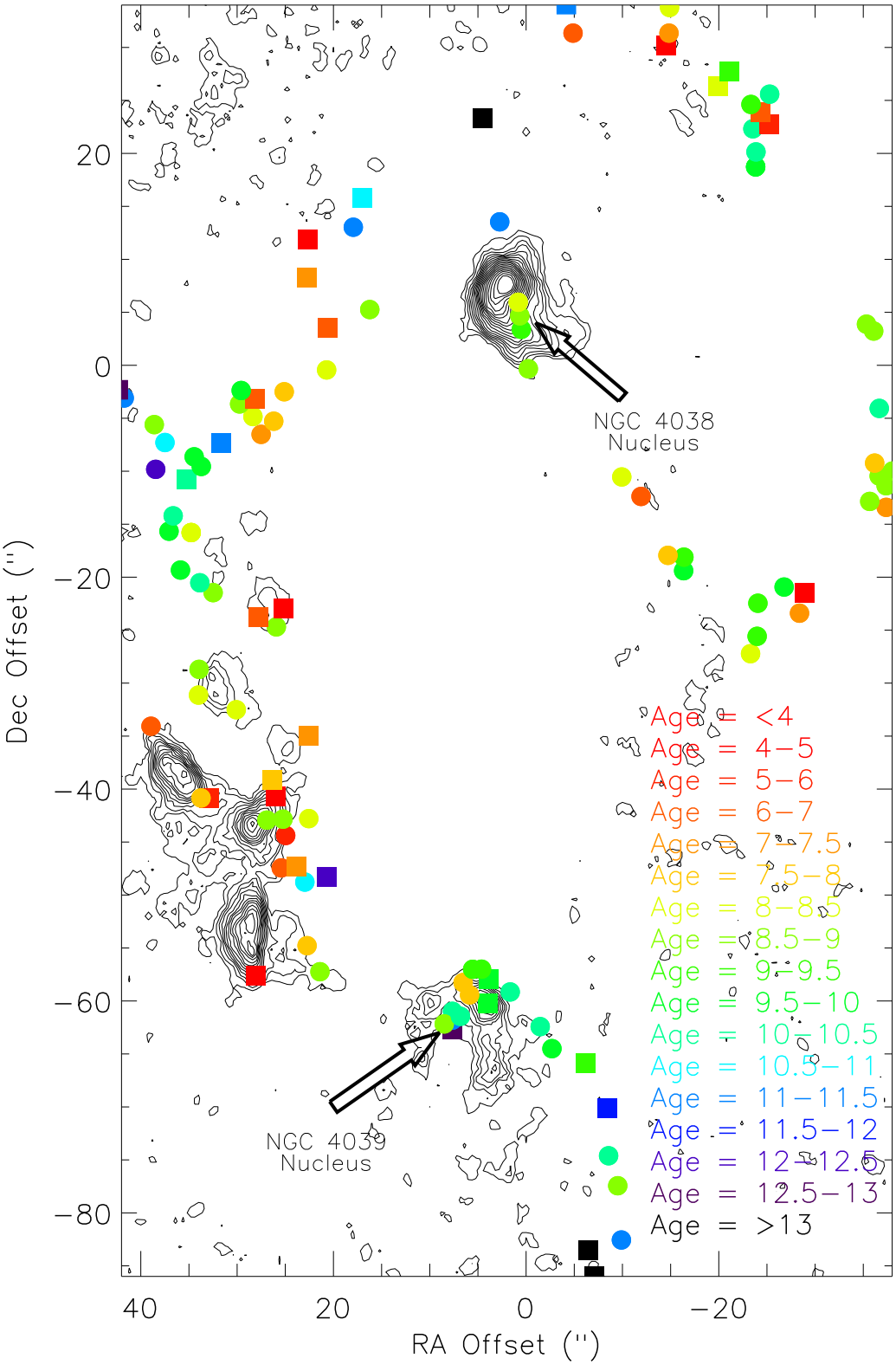

Figure 4.17 CO (1-0) Integrated Intensity Map. The 1σ rms for the integrated map is 1.25 Jy beam^{-1} km s^{-1}; the contours begin at 2σ and are spaced by 2σ. In constructing the integrated intensity map we only included emission at the 3σ level in any individual channel. As in Figure 4.11, clusters are color-coded by their mean age and plotted by their offset from Cluster 87. Because of coherence issues, the Western Loop region of the Antennae suffered from large amounts of striping, and this area has been blanked from the integrated intensity map.

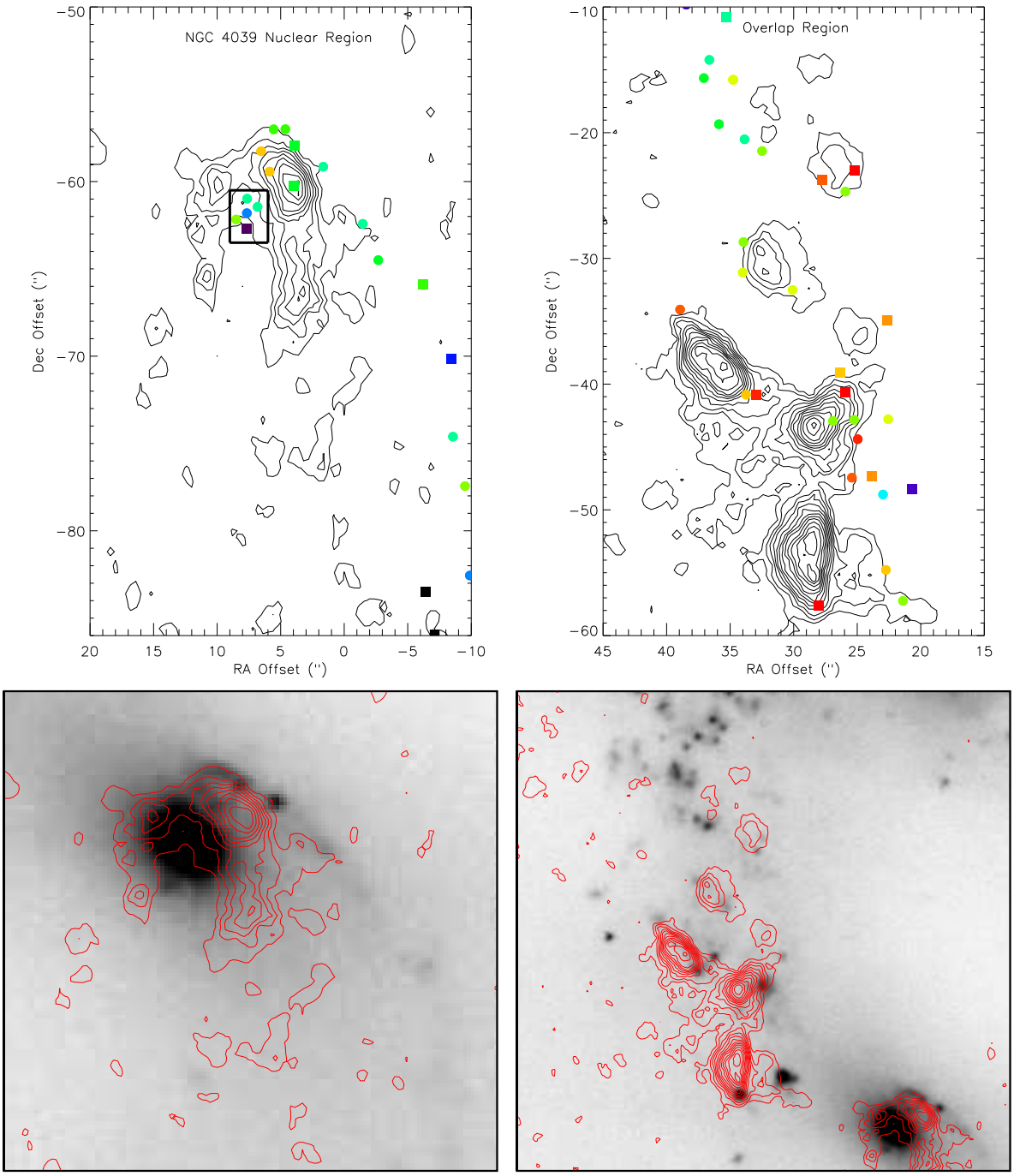

Figure 4.18 CO (1-0) Integrated Intensity Map of NGC 4039 Nuclear Region (left) and the Overlap Region (right). The top plots show the integrated intensity map with cluster locations color-coded by the cluster age (see Figure 4.17 for the color-coding key). The contours begin at 2σ and are spaced by 2σ. Offsets are from Cluster 87. The black box in the NGC 4039 Nuclear Region map marks the inner nuclear region of NGC 4039. The bottom images show the CO distributions for the same two regions overplotted on the Ks band imaging from Brandl et al. (2005). The contour levels are the same as the top plots but the spatial region covered is similar but not identical.

The only non-nuclear region with a substantial CO concentration is the overlap region. Wilson et al. (2000) find $\approx 50\%$ of the molecular gas in the Antennae in the overlap region, a conclusion supported by our observations as well. This large concentration of molecular gas in the overlap region is not surprising, as this region is seen as the most active region of current star formation, thus suggesting that a large supply of molecular gas must be nearby. In the top-right plot of Figure 4.18 we show a detailed view of the overlap region. Three to four main peaks of molecular gas emission are clearly evident. There are no clusters coincident with these peaks, a result that is expected since the extinction through such a large concentration of gas would have likely dimmed any clusters near the densest parts of the CO distribution to the point that they would not have been part of our sample, even in the K band. This is further seen in the bottom-right plot of Figure 4.18 where the molecular gas is found in the heart of the overlap region but avoiding any of the bright clusters. Indeed, the CO gas is often found running between bright young clusters. With only a few exceptions, however, the clusters that are found immediately outside of the main CO distribution peaks in the overlap region are the youngest clusters (seen in red and orange in the top-right plot of Figure 4.18).

In comparison with the overlap region, there is very little molecular gas associated with the northeast region (Figure 4.17). The only appreciable CO emission in this region is found at an offset near $28''$, $-25''$, at the very southern edge of the region. Here two young clusters (< 7 Myr) and also a 9 Myr cluster are nearly coincident with a 4σ CO peak. We note that this part of the northeast region is very close to the overlap region.

As discussed above, our observations suffered from coherence difficulties in the third Antennae field, which covered the western loop. To compare the CO distribution with the cluster population in this region, we utilized the CO observations of Wilson et al. (2000). In Figure 4.20 we plot the CO distribution in the western loop with the locations and ages of the clusters in our sample indicated. Substantial CO emission is found along the arc that makes up the western loop and is concentrated in a number of peaks. However, there is virtually no overlap between the CO distribution and the location of clusters, with the only exceptions being the two clusters near the peak at $-11''$, $-11''$ and the two clusters near $-15''$, $30''$. As was the case in the overlap region these four clusters are all young (< 8 Myr). The discrepancy between cluster location and molecular gas is further illustrated in the bottom plot of Figure 4.20, where the molecular gas is overplotted on a near-infrared image from Brandl et al. (2005).

4.9.3 Correlation Between Cluster Age and Proximity to CO Emission

Zhang et al. (2001) found a strong correlation between the location of the reddest (and thus presumably the youngest) clusters in the Antennae and the strength of the CO (1-0) emission. Using the CO (1-0) maps of Lo et al. (2000), they found that many of the reddest clusters are actually

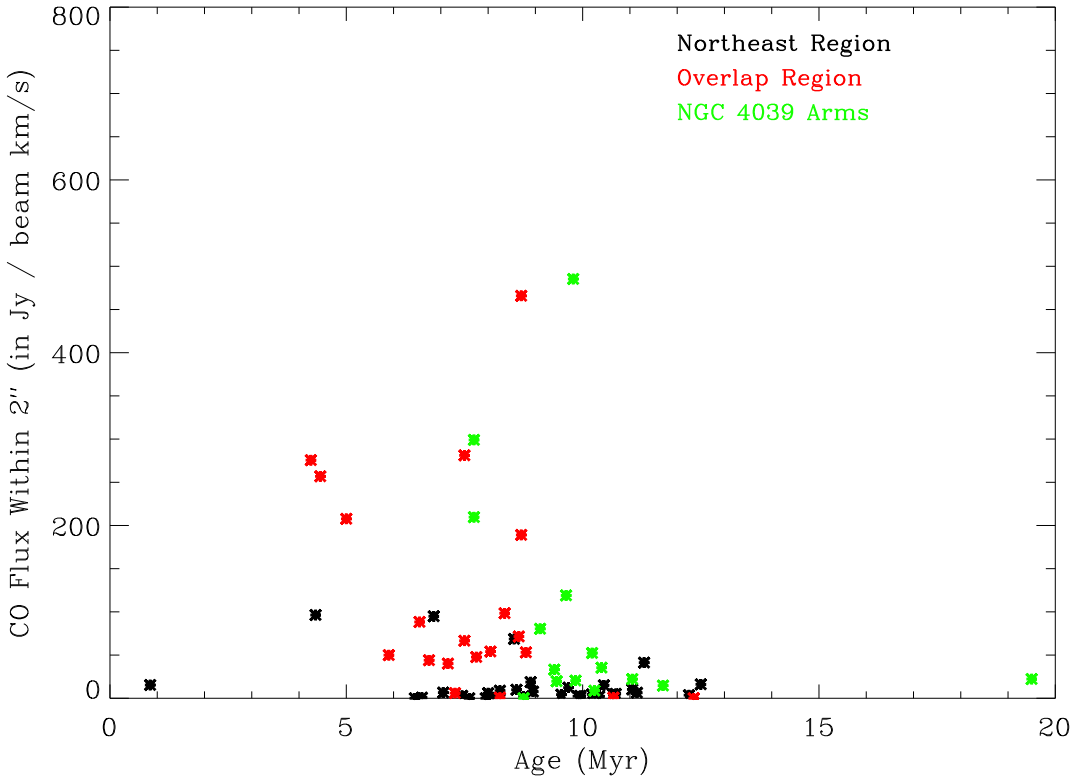

Figure 4.19 Cluster Age Versus CO (1-0) Emission. We calculate the total integrated CO emission within a 2″ box centered on the cluster. Clusters are color-coded based on location within the Antennae. The ages plotted are the middle of the age ranges for each cluster. The three nuclear observations (red) with large CO flux are taken near the NGC 4038 nucleus.

coincident with peaks in the molecular gas distribution. The observations of Lo et al. (2000) had a spatial resolution of 6″.61 × 7″.77. With our enhanced spatial resolution we have found that the youngest clusters are actually offset slightly from the peaks in the CO emission. We do find a slight trend for enhanced molecular gas emission near younger clusters (Figure 4.19), which is not surprising, however, since we expect young clusters to have recently formed out of large molecular cloud complexes, parts of which are still located nearby. This correlation also strongly supports the argument that the CO molecular clouds that are seen, particularly in the overlap region, are the progenitors of the newly formed and still-forming clusters in the region (Zhang et al., 2001).

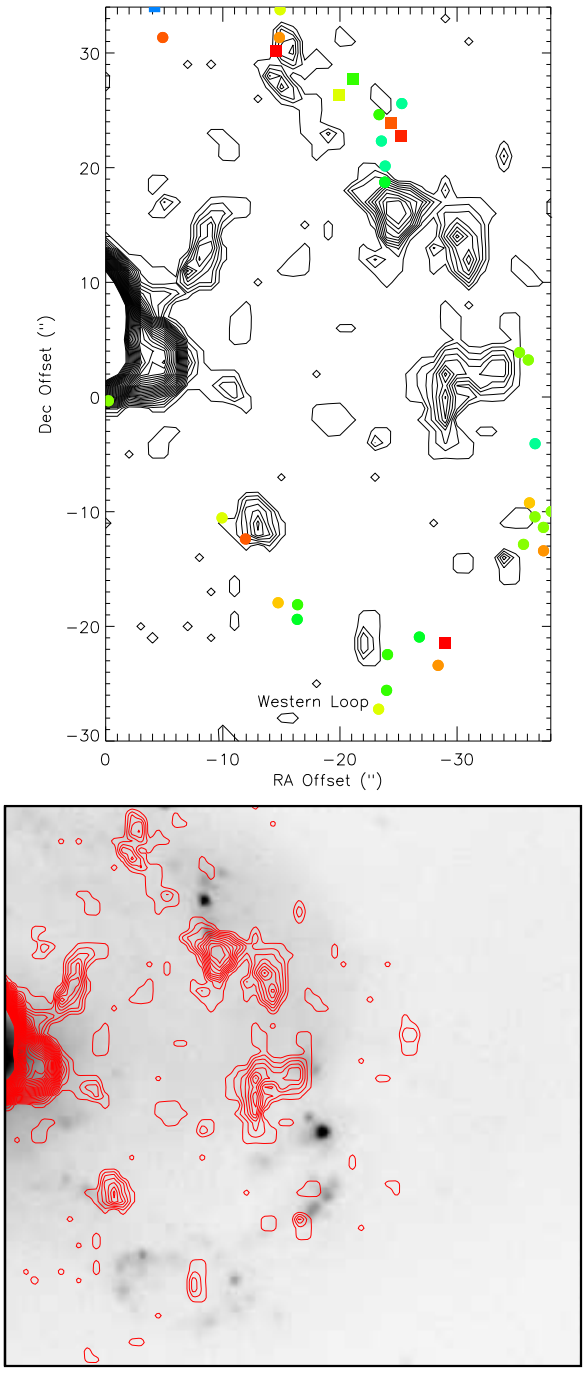

Figure 4.20 CO (1-0) Integrated Intensity Map of the Western Loop. The top plot shows the CO distribution from Wilson et al. (2000) with the locations of the clusters color-coded by their mean age and plotted by their offset from Cluster 87 (see Figure 4.17 for the color-coding key). The bottom plot shows the CO distribution plotted in contours on the K band image of the region from Brandl et al. (2005). The contour levels for both plots are the same: the lowest contour is 2σ and the remaining contours are spaced by 2σ. The spatial regions are similar but not identical.

Chapter 5

Cluster Extinctions and Masses

5.1 Extinction

As discussed briefly in §1, the Antennae is gas and dust-rich, with variable extinction across the entire system. Whitmore & Schweizer (1995) estimate $A_V = 0$–1 mag from a color-color diagram comparison of Antennae clusters with population synthesis models. From B, V, and K band imaging, Kassin et al. (2003) find peak extinctions of $A_V = 2$–3 mag in the overlap region with an average $A_V = 1$ throughout the Antennae. These results agree with Fischer et al. (1996) who measure $A_V = 1$–4 mag from point sources in the overlap region. All of these estimates are derived from optical observations of the Antennae, which undoubtedly do not probe the largest gas and dust concentrations in the overlap region. Indeed, mid-infrared spectroscopy of the overlap region has estimated an A_V as large as 70 mag (Kunze et al., 1996).

With the exception of Kassin et al. (2003), all of these studies calculated an average statistical extinction for the Antennae system or for various regions within the Antennae. Kassin et al. (2003) did measure extinctions at a $0.5''$ scale, but they intentionally avoided regions with the youngest clusters, emphasizing instead the extinction in the diffuse stellar background. Since young clusters are most often found near large gas and dust concentrations, they are not tracing the highest extinction regions in the Antennae.

Gilbert et al. (2000) spectroscopically measured the extinction of Cluster 15 in our sample and found it to have an $A_V = 9$–10 mag. Besides this measurement, Mengel (2001) is the only study to measure extinctions at locations of individual clusters within the Antennae. Combining their own narrow-band Brγ observations with Hα imaging from Whitmore et al. (1999), Mengel measured $A_V = 0.3$ to 5 mag for individual clusters. While significant variation exists between individual cluster extinctions, the results of Mengel (2001) confirm previous studies that higher-than-average extinctions exist in the overlap region. Additionally, Mengel (2001) find lower-than-average extinctions in the western loop, a region where extinction had not been studied in detail previously.

5.1.1 Extinction Results for Antennae Clusters

Using our optical spectroscopy, we estimate extinctions from the ratio of Hα and Hβ fluxes. 32 clusters as well as the nuclear region of NGC 4038 have measured Hα and Hβ fluxes. The intrinsic flux ratio ($\frac{F_{H\alpha}}{F_{H\beta}}$) is 2.86, assuming Case A recombination and an electron temperature of 10^4K (Osterbrock, 1989). Any observed flux ratio larger than 2.86 is due to greater line-of-sight dust absorption of shorter wavelength Hβ emission compared with Hα emission. We chose Hα and Hβ because of their emission strength, particularly in young clusters. The two lines were observed simultaneously for each cluster (Hα with LRIS-Red and Hβ with LRIS-Blue), reducing the effects of any temporal changes in atmospheric conditions. The same apertures and background regions were used for the red and blue sides, so we are confident that we are comparing Hα and Hβ fluxes from the same spatial regions. Five clusters did use different regions for measuring the background in the LRIS-Red and LRIS-Blue spectra because no overlapping, off-cluster region existed between the two spectra. In these cases, care was given to insure that similar background regions were used for the red and blue sides.

We calculate A_V from the Hα to Hβ flux ratio using: $A_V = 7.20 \log\left(\frac{F_{H\alpha}}{2.86\ F_{H\beta}}\right)$ mag. A_V is derived assuming a standard Galactic extinction curve (Cardelli et al., 1989) with a foreground extinction model. Uncertainty in extinction is calculated from the uncertainty in the Hα and Hβ flux measurements.

In Figure 5.1 we plot the extinction distribution for the 32 clusters and three nuclear regions with Hα and Hβ detections. Two clusters (90 and 102) have a $\frac{F_{H\alpha}}{F_{H\beta}}$ consistent with $A_V = 0$ and are not included in this plot. The mean extinction is $A_V = 3.3$ mag with a maximum extinction of 13.5 mag. Table 5.1 contains the specific $\frac{F_{H\alpha}}{F_{H\beta}}$ and A_V values for each cluster and nuclear region. Most of the clusters (67%) have extinctions less than $A_V = 4$ mag, but 5 clusters have extinctions between 5.5 and 7 mags and 3 have $A_V > 10$ mag. Our results are consistent with the previous studies discussed above, although we measure more extinctions above 5 mag than have been measured previously.

In Figure 5.2 we plot the observed $\frac{F_{H\alpha}}{F_{H\beta}}$ for the 32 clusters and three nuclear regions versus the observed Hα flux with clusters color-coded based on their location. The five clusters where different regions were used for background subtraction of the Hα and Hβ lines are marked by diamonds. The black horizontal line shows the intrinsic flux ratio of 2.86. Clusters above this line suffer from visual extinction (A_V) at levels indicated by the dashed lines. The extinction levels are clearly higher in clusters in the overlap region compared with other regions in the Antennae. All five of the overlap region clusters have $A_V > 5$ mag; in comparison, only four of the other 30 clusters and nuclear regions with measured A_V have extinctions this great. The mean A_V for the overlap region is 7.0 mag, compared with 3.6 mag for the NGC 4038 nucleus, and a maximum of 2.9 for any of the other cluster regions (Table 5.2). The high extinctions in the overlap region are not surprising as it has been seen in earlier Antennae observations (Mengel, 2001) and is expected, given the large CO

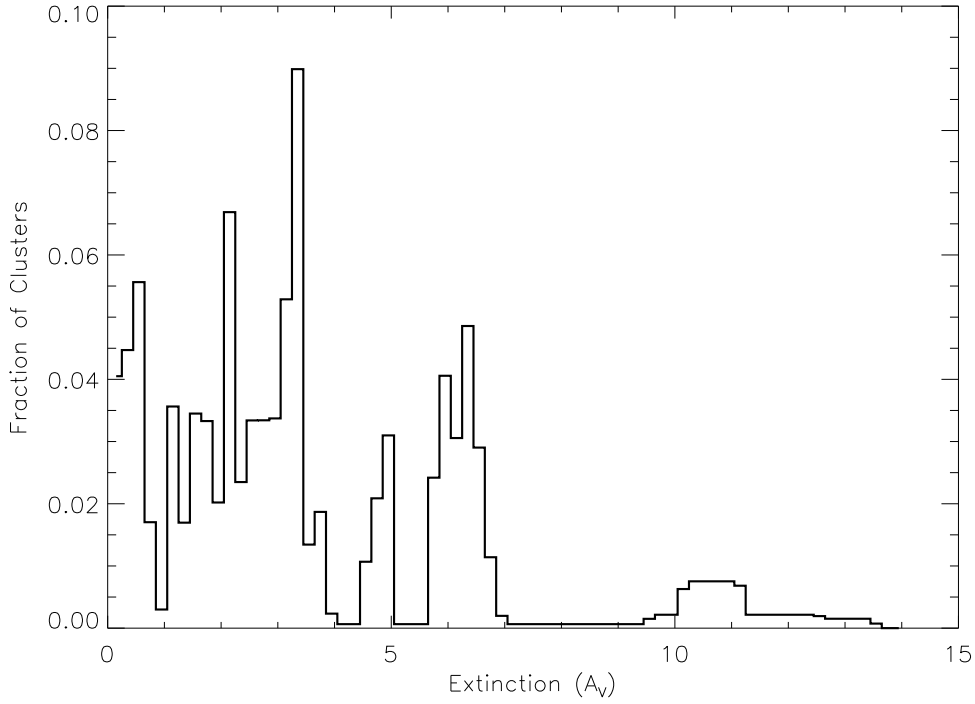

Figure 5.1 Distribution of A_V Extinctions. 32 clusters and 3 nuclear region observations had the Hα and Hβ measurements necessary to determine A_V. We include in this plot all these clusters except Clusters 90 and 102, which have extinctions consistent with $A_V = 0$ mag. The extinction distribution for each cluster was normalized by the extinction uncertainty and the overall distribution is normalized by the total number of clusters.

molecular gas concentration in the overlap region (Wilson et al., 2000, 2003a).

There is no noticeable correlation between Hα flux and extinction (Figure 5.2). This suggests that our extinction measurements are not biased by the strength of the hydrogen emission lines but are true extinction measurements.

In Figure 5.3, we examine the variation in extinction with location in greater detail. The 32 clusters and three nuclear regions with extinction measurements are shown, color-coded based on their visual extinction. In the region near the NGC 4039 nucleus, the spatial variation in extinction is quite substantial. Just to the north of the NGC 4039 nucleus are three clusters separated by a total of just $5''$, but with extinctions ranging from $A_V = 2.4$ to 11.5 mag. One possible explanation for the extinction discrepancy is that Clusters 14 and 18, the two clusters with extinctions of 3.3 and 2.4 mag respectively, were two of the five clusters where a different spatial region was used for background subtraction of the Hα and Hβ lines. In contrast the same spatial region was used for both lines for Cluster 12, which has $A_V = 11.5$ mag. However, we were careful to make sure that similar regions were used for background subtraction if the same spatial region could not be used. Also, as the clusters lie at the edge of a molecular concentration there could be substantial local

Table 5.1. Extinction Measurements

#	Hα Flux[a]	Hβ Flux[a]	$\frac{F_{H\alpha}}{F_{H\beta}}$	A_V
4	4.96e-15–5.01e-15	1.34e-15–1.40e-15	3.52–3.73	1.50–1.92
5	1.29e-16–1.43e-16	3.20e-17–6.53e-17	1.98–4.48	0-3.23
8	1.05e-15–1.10e-15	3.43e-16–3.92e-16	2.67–3.20	0-0.83
9	4.07e-15–4.18e-15	1.11e-15–1.22e-15	3.33–3.74	1.10–1.93
12	6.64e-15–6.77e-15	3.63e-16–6.22e-16	10.68–18.64	9.48–13.49
14[b]	4.64e-14–4.64e-14	1.01e-14–1.02e-14	4.52–4.57	3.29–3.37
16[b]	2.16e-14–2.17e-14	3.28e-15–3.32e-15	6.51–6.63	5.93–6.06
18[b]	1.86e-14–1.87e-14	4.62e-15–4.77e-15	3.90–4.05	2.25–2.51
20	2.25e-15–2.45e-15	1.50e-16–5.12e-16	4.40–16.30	3.10–12.53
23	1.44e-14–1.46e-14	1.98e-15–2.15e-15	6.73–7.38	6.16–6.82
24	9.23e-15–9.27e-15	1.43e-15–1.47e-15	6.27–6.48	5.65–5.88
37	1.20e-14–1.21e-14	8.99e-16–1.04e-15	11.54–13.50	10.04–11.17
40	4.08e-15–4.10e-15	8.44e-16–8.79e-16	4.63–4.86	3.48–3.81
41	3.87e-15–3.89e-15	8.77e-16–9.07e-16	4.26–4.44	2.87–3.17
49[b]	1.70e-14–1.72e-14	2.39e-15–2.65e-15	6.42–7.19	5.83–6.64
56	5.12e-14–5.13e-14	1.32e-14–1.33e-14	3.83–3.87	2.11–2.17
57	5.12e-14–5.13e-14	1.32e-14–1.33e-14	3.83–3.86	2.11–2.17
62	9.74e-14–9.77e-14	1.39e-14–1.43e-14	6.77–6.99	6.20–6.44
74	1.67e-15–1.70e-15	3.97e-16–4.72e-16	3.54–4.29	1.54–2.92
75	4.77e-14–4.78e-14	1.05e-14–1.08e-14	4.40–4.55	3.10–3.34
76	2.72e-14–2.73e-14	8.77e-15–8.90e-15	3.05–3.11	0.47–0.61
78	1.95e-14–1.96e-14	4.49e-15–4.76e-15	4.09–4.36	2.58–3.03
79	5.27e-14–5.29e-14	1.46e-14–1.53e-14	3.43–3.60	1.31–1.65
84	1.31e-14–1.33e-14	1.86e-15–2.09e-15	6.27–7.15	5.65–6.59
87[b]	8.20e-14–8.22e-14	2.45e-14–2.48e-14	3.30–3.34	1.05–1.13
90	4.92e-14–4.93e-14	1.72e-14–1.75e-14	2.79–2.85	$\frac{F_{H\alpha}}{F_{H\beta}}$ below 2.86
100	1.51e-14–1.52e-14	5.10e-15–5.39e-15	2.80–2.98	0-0.30
101	8.86e-15–8.92e-15	2.84e-15–2.95e-15	2.99–3.13	0.33–0.65
102	7.53e-15–7.60e-15	2.73e-15–2.97e-15	2.53–2.78	$\frac{F_{H\alpha}}{F_{H\beta}}$ below 2.86
112	2.18e-14–2.19e-14	4.87e-15–4.94e-15	4.41–4.49	3.12–3.25
113	5.95e-15–6.00e-15	1.05e-15–1.12e-15	5.28–5.70	4.41–4.97
114	3.42e-14–3.43e-14	1.15e-14–1.16e-14	2.92–2.96	0.17–0.24
4038 Nucl S	9.98e-15–1.00e-14	2.37e-15–2.50e-15	3.99–4.24	2.40–2.84
4038 Nucl	6.52e-14–6.53e-14	1.42e-14–1.44e-14	4.52–4.59	3.30–3.40
4038 Nucl N	1.87e-14–1.87e-14	3.33e-15–3.38e-15	5.54–5.62	4.76–4.87

[a] $F_{H\alpha}$ and $F_{H\beta}$ in ergs s^{-1} cm^2. Uncertainties in flux measurements only include the continuum subtraction around the Hα and Hβ lines and not uncertainties in the flux calibration.

[b] Spatial region used to construct background different for Hα and Hβ.

Table 5.2. Cluster Extinction Based on Location in Antennae

Location	Clusters with Extinctions Measured	Mean A_V Mag	Median A_V Mag
Northeast Region	7	2.71	2.21
Western Loop	13	2.32	1.45
Overlap Region	5	6.98	6.08
NGC 4039 Arms	7	2.86	1.69
NGC 4038 Nucleus	3	3.57	3.35
Total	35	3.28	2.75

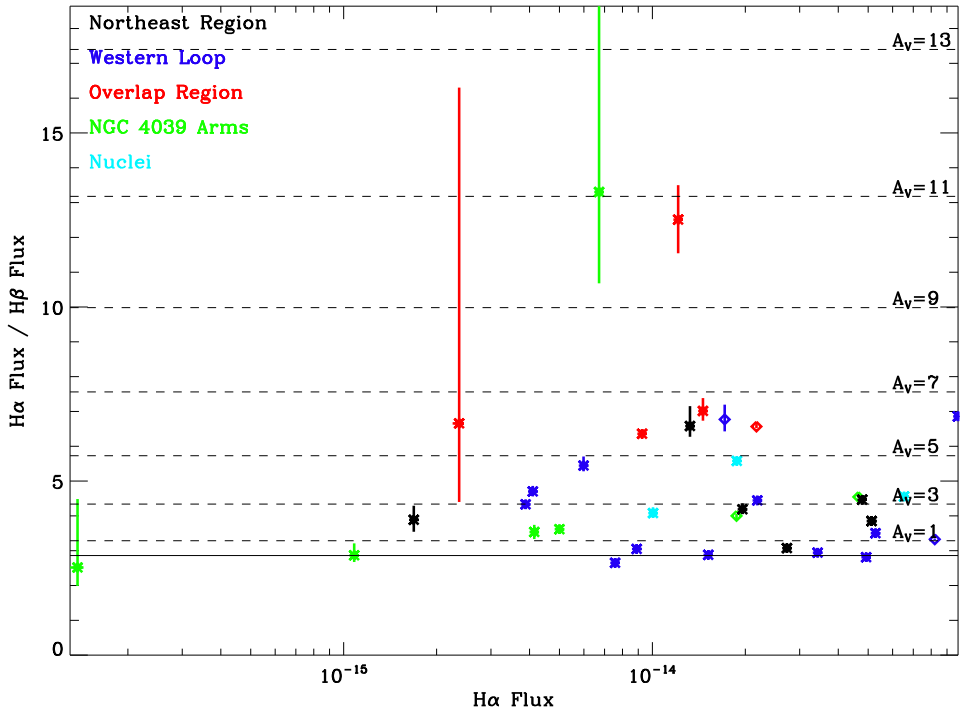

Figure 5.2 $\frac{F_{H\alpha}}{F_{H\beta}}$ and Extinctions. The observed $\frac{F_{H\alpha}}{F_{H\beta}}$ value is plotted versus the measured Hα flux. Data for the 32 clusters with good Hα and Hβ flux measurements are included. Measurements for the nuclear region of NGC 4038, where significant Hα and Hβ emission are detected, are also included. Data points are color-coded based on the location of the cluster. The horizontal line indicates the intrinsic $\frac{F_{H\alpha}}{F_{H\beta}}$ of 2.86. A_V extinctions are indicated by the dashed lines. For each cluster, the same aperture size was used for the Hα and Hβ measurements. For all but five clusters the same spatial region was used to determine the background on the red (Hα) and blue (Hβ) sides. The five clusters with different background regions on the blue and red sides are marked with diamonds.

variation in extinction.

Outside of the region near the NGC 4039 nucleus, however, the spatial variation in extinction is typically small (normally less than 2 mag) within a 10″ range. For larger spatial regions, the extinction variation is more significant. For example the four clusters toward the southern part of the overlap region all have values of A_V between 4 and 6 mags, while the single cluster in the northern part of the overlap region has a much higher extinction at $A_V = 10.6$ mag. The western loop also shows a large amount of extinction variation. The southern part of the western loop has A_V values between 4 and 6.5 mag, while clusters in the western-most part (around RA offset of -35″) have extinctions between 0–1.5 mag.

5.1.2 Connecting Extinction and the Molecular Gas Distribution

We would expect that increased molecular gas emission would correlate with larger extinctions. We can easily examine this in Figure 5.3, where cluster extinctions are overplotted on our map of

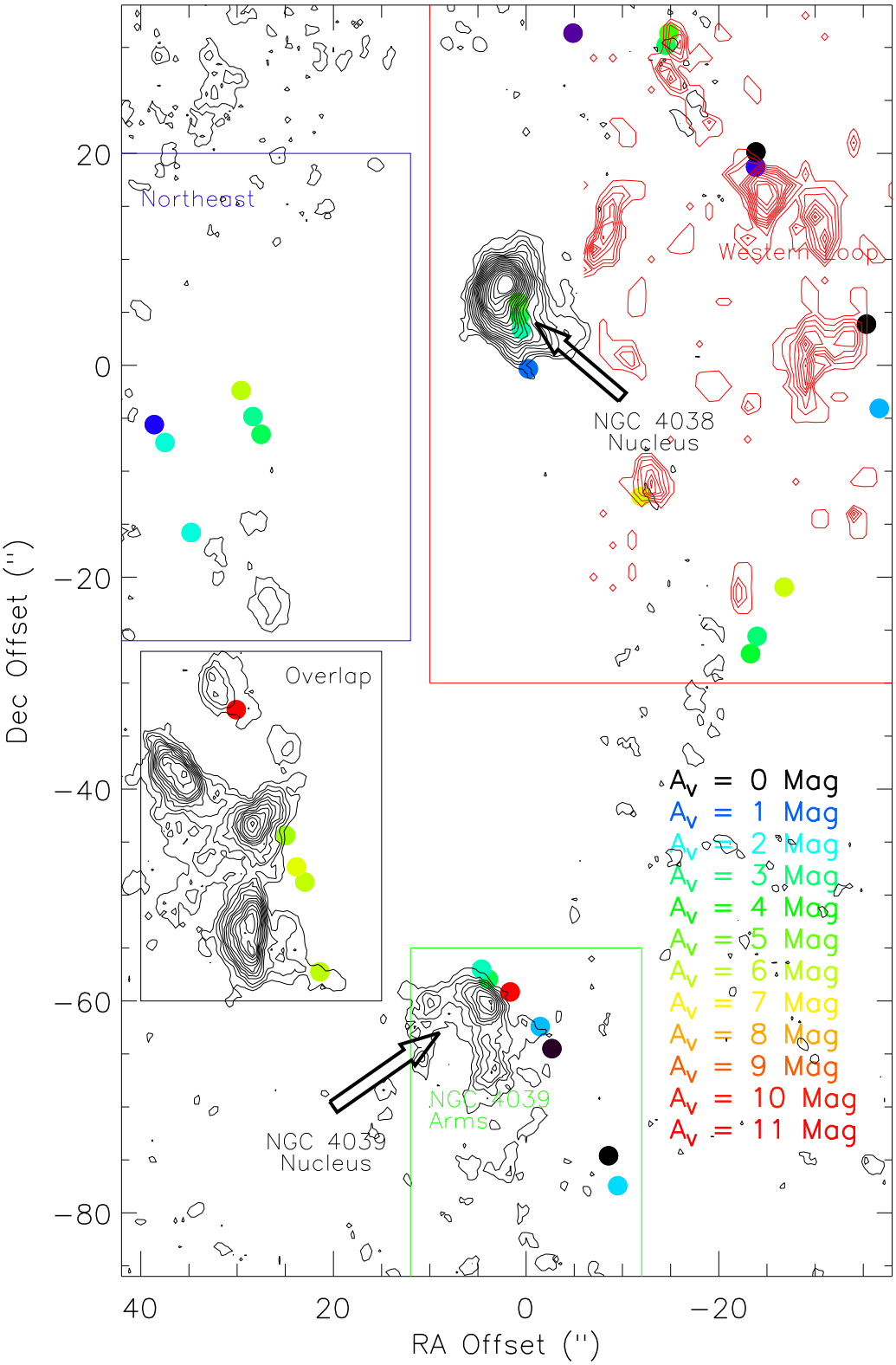

Figure 5.3 Spatial Variation in Extinction. The 32 clusters and three nuclear regions with extinction estimates from $\frac{F_{H\alpha}}{F_{H\beta}}$ are shown. The clusters are color-coded based on the mean value of A_V, with black clusters having the lowest extinctions and red clusters having the highest extinctions. The maximum extinction in the 32 Antennae clusters is A_V=11.1. Overplotted is the CO (1-0) molecular gas distribution. The black contours are taken from our observations while the red contours are from Wilson et al. (2000). The contours begin at 2σ and are spaced by 2σ for each observation.

the CO (1-0) molecular gas distribution. We see a strong correlation between molecular gas and extinction in the observations of the NGC 4038 nucleus and of Cluster 87 immediately to the south. Moving from Cluster 87 to the north the molecular gas emission gets stronger. At the same time the extinction steadily increases from $A_V = 1.1$ mag at Cluster 87 to 4.8 mag north of the NGC 4038 nucleus. Outside of the NGC 4038 nuclear regions, however, there does not seem to be a strong correlation between extinction and molecular gas emission (Figure 5.4). As is clearly seen in Figures 5.3 and 4.17, our cluster sample tends to avoid the brightest CO (1-0) emission regions. Outside these brightest CO regions the effects of diffuse emission are more pronounced. With our CO observations we have emphasized large baseline configurations, making us therefore less sensitive to diffuse emission. It is possible that we are missing diffuse emission that slowly varies across the Antennae but which contributes much to the observed extinction. This conclusion is supported by the observation earlier that the extinction variations within a small ($< 10''$) region are normally minimal. Even with emphasizing the long baseline configurations, our beam-size is still significantly larger than the optical seeing, which may also account for the lack of strong correlation between CO flux and extinction.

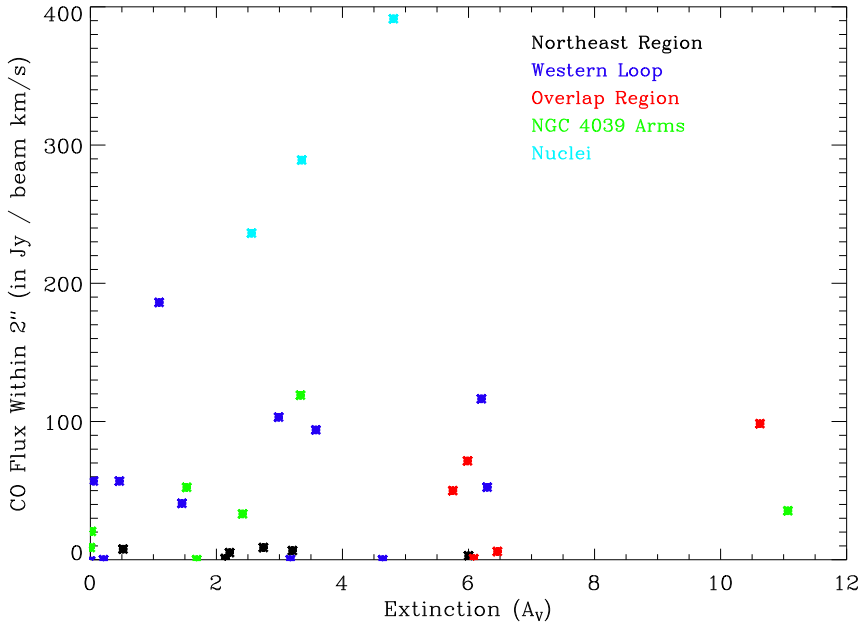

Figure 5.4 Correlation of Extinction with CO (1-0) Emission. The CO (1-0) emission plotted is the flux within a $2''$ region centered on a cluster. The three nuclei fluxes (shown in red) have been reduced by 300 Jy beam^{-1} km s^{-1} to allow more detail in the plotting of the CO (1-0) fluxes for other clusters. The CO (1-0) fluxes for the Western Loop clusters were taken from Wilson et al. (2000) while the fluxes for the other regions were taken from our observations.

5.1.3 Extinction and Age

While no strong correlation exists between cluster extinction and the strength of CO emission, it is still likely that higher extinction levels would be correlated with younger clusters. Since clusters are formed out of the gas and dust of molecular clouds, they are naturally born in regions of high extinction. We would expect that with time the remnant of the parent molecular cloud will be dispersed, gradually reducing the extinction at the cluster. Approximately 6 Myr is needed to reduce the molecular gas surrounding a cluster enough to get visual extinctions of 1 mag (Whitmore & Zhang, 2002; Brandl et al., 2005). A weak correlation is found between cluster age and extinction (Figure 5.5). Ignoring two clusters with very high extinction (Clusters 12 and 20) there is a trend that younger clusters have higher extinctions. A fit to this correlation is shown in Figure 5.5. Over 78% (26/33) of clusters lie within $A_V = 2$ mag of this fit. We note our results are in agreement with the measurements of Mengel et al. (2005) using a larger, photometrically studied cluster sample in the Antennae.

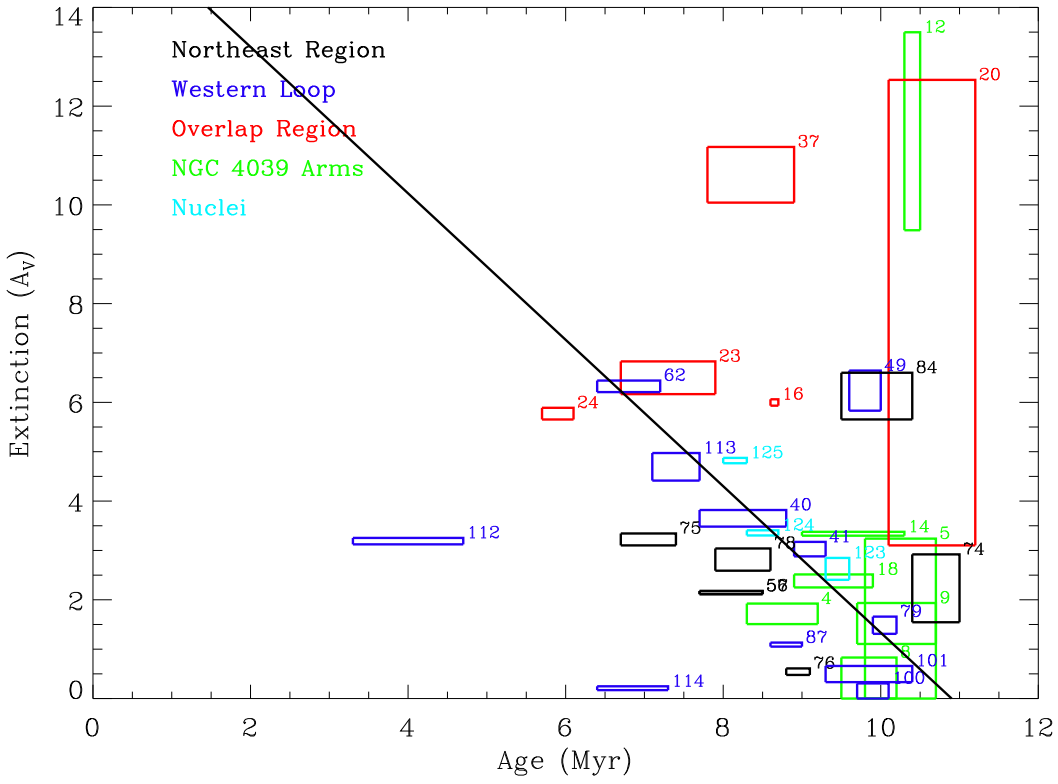

Figure 5.5 Cluster Age Versus Extinction. Clusters are color-coded based on their location within the Antennae, and individual cluster numbers are listed at the top right. Overplotted is a fit to the weak correlation of younger clusters with enhanced extinction: $A_V = 16.2 - 1.5$ Age (in Myr).

Summarizing our findings on the 32 clusters and 3 nuclear regions in the Antennae with extinction

estimates from our survey we find that typical A_V extinctions are around 2–3 mag. We find more high-extinction ($A_V > 5$ mag) clusters than found by previous studies. No correlation exists between molecular gas emission near a cluster and extinction, but there is a weak trend of higher extinction in younger clusters.

5.2 Masses

The mass of a cluster is key in determining whether it will survive or be disrupted into the field star population (see Fall & Zhang (2001)). Additionally, measuring the mass distribution of young star clusters helps in understanding how this mass distribution (typically a power law) can turn into the Gaussian mass distribution seen for globular clusters (Harris, 2001; Richtler, 2003; Brodie & Strader, 2006).

The most direct measurement of a cluster mass can be made using the virial theorem: $M = 10\frac{r_{hp}\sigma_r^2}{G}$, where r_{hp} is the half-light radius of the cluster and σ_r is the 1-d velocity dispersion of the cluster (Spitzer, 1987; McCrady & Graham, 2007). Measurement of the half-light radius of Antennae clusters demands high-spatial-resolution observations, since the typical cluster size is around 4 pc for the Antennae (Whitmore et al., 1999), corresponding to $0''.043$ at the distance of the Antennae. Hubble Space Telescope observations provide sufficient resolution to measure cluster half-life radii in the Antennae (Whitmore et al., 1999; Mengel et al., 2002). A typical star cluster velocity dispersion is 10–20 km/s (Mengel et al., 2002; McCrady & Graham, 2007), requiring spectral resolutions ($\frac{\lambda}{\Delta\lambda}$) of 7500 or higher. Our LRIS and NIRSPEC spectra have resolutions of 1500 to 2000, insufficient for velocity dispersion estimates.

5.2.1 Calculating Photometric Masses

Even though dynamical mass measurements of the Antennae are not possible for our sample, we can still calculate photometric-based masses by comparing the observed cluster photometry with stellar population models of Starburst99. To calculate these photometric masses we will rely upon cluster age estimates from our spectroscopic survey and near-infrared photometry from Brandl et al. (2005). We thank the authors of Brandl et al. (2005) for providing us cluster photometry for their entire sample.

As we discussed in §4.8, Starburst99 predicts the temporal evolution of cluster luminosity in both V and K bands. Since we have found that a 5 Myr duration burst of star formation provides a good match to the observed spectral features of the clusters, we have calculated the temporal evolution of cluster luminosities assuming a 5 Myr duration burst. Plots of these cluster models in V and K bands have been shown in Figure 4.14. The 5 Myr duration burst models are plotted in solid lines while the instantaneous burst models are shown with dotted lines. Both bands show an increase in

luminosity over the first 5 Myr that is not seen in the instantaneous burst models of the same mass cluster. This increase is because the stellar mass of a cluster in the 5 Myr duration burst model is assumed to form at a constant rate over the 5 Myr duration star formation burst, while in the instantaneous burst model the entire stellar mass of the cluster is assumed to form at t=0.

Starburst99 models of cluster luminosity assume a total cluster mass of 1×10^6 $M_\odot$. It is trivial to adjust the cluster luminosity models for clusters of other masses, as long as the masses are large enough to fully sample the O and B star population within the IMF. The luminosity of a cluster with mass X is given by:

$$L_M = L_{10^6 M_\odot} \frac{X}{10^6 M_\odot}$$

which can easily by converted to absolute magnitude to give:

$$M_X = M_{10^6 M_\odot} - \frac{\log_{10}(\frac{X}{10^6 M_\odot})}{0.4}$$

where M_X is the absolute magnitude of a cluster with mass X in an arbitrary band. Solving this equation for cluster mass gives us:

$$X = 10^6 M_\odot \times 10^{-0.4(M_X - M_{10^6 M_\odot})} = 10^6 M_\odot \times 10^{-0.4((m_X - DM) - M_{10^6 M_\odot})}$$

where DM is the distance modulus for the cluster and m_X is the apparent magnitude of the cluster. For the 19.2 Mpc distance of the Antennae, the distance modulus is 31.41.[1]

In order to measure photometric masses we must know the cluster luminosity in at least one broadband filter covered by Starburst99. Measuring fluxes directly from our spectroscopic observations is essentially impossible due to the lack of flux calibration in the near-infrared, and difficulty in estimating the slit-loss factors in the optical. Fortunately, we can make use of near-infrared cluster photometry in the literature, particularly Brandl et al. (2005). The photometry of Brandl et al. (2005) is in the Ks band, while the cluster magnitude evolution models are for K band. Using the model cluster spectra of Starburst99 we calculated the expected difference in cluster luminosity from K band to Ks and found it to be on average less than 0.01 mags. We included this small correction when calculating our mass estimates. The clusters in our spectroscopic survey were matched to those in the Brandl survey by requiring positional agreement within $1.5''$. In the few cases with multiple candidates, the closest match was adopted. In total, 82 of 117 clusters had matches and for these clusters we calculate the photometric mass of the cluster using the process described above. Cluster matches and masses are listed in Table 5.3. In total we were able to calculate the photometric mass for 73 clusters in our sample.

[1] We note that Saviane et al. (2004) set the distance to the Antennae at 13.8 Mpc by examining the red giant population in the Antennae tidal tails. We have adopted the more conventional 19.2 Mpc distance; a distance of 13.8 Mpc would reduce our stated masses by a factor of 2.

Table 5.3. Cluster Masses

#	Brandl et al. (2005) Match	M_K	M_K Ext. Corr.	Mass $\times 10^5 M_\odot$	#	Brandl et al. (2005) Match	M_K	M_K Ext. Corr.	Mass $\times 10^5 M_\odot$
2	83	-13.64	-13.79	1.118–2.101	66	38	-14.68	-14.81	1.714–2.518
3	75	-14.04	-14.19	0.581–0.682	67	171	-15.38	-15.57	
4	80	-13.27	-13.42	0.477–0.666	68	34	-15.24	-15.37	3.641–3.819
6	81	-14.27	-14.42	0.692–0.758	70	182	-15.86	-16.05	3.960–4.800
9	92	-14.37	-14.50	0.894–1.090	71	38	-14.68	-14.81	2.396–3.501
12	99	-15.82	-16.80	7.730–7.889	73	170	-16.01	-16.20	3.656–4.368
14	105	-15.17	-15.46	2.348–3.251	74	195	-15.14	-15.33	1.822–1.999
15	157	-16.75	-17.29	36.726–45.652	76	199	-16.01	-16.05	5.596–6.031
16	132	-14.96	-15.49	3.903–3.903	77	154	-15.49	-15.68	6.206–8.608
17	105	-15.17	-15.32	2.659–2.946	78	162	-15.49	-15.73	5.097–6.774
18	105	-15.17	-15.38	2.389–3.127	79	37	-17.35	-17.48	15.323–16.047
19	136	-17.14	-17.68	37.224–50.948	80	165	-15.91	-16.10	5.485–8.321
21	131	-14.20	-14.74	0.930–1.025	81	209	-16.37	-16.56	
23	145	-14.74	-15.31	4.800–6.675	82	209	-16.37	-16.56	5.094–5.758
26	148	-16.53	-17.07	13.773–20.229	83	149	-15.06	-15.25	3.443–5.287
29	176	-16.14	-16.68	16.202–22.091	84	164	-15.08	-15.61	2.634–3.192
32	168	-15.70	-16.24		85	209	-16.37	-16.56	4.997–5.202
33	139	-14.69	-15.23		86	135	-14.57	-14.76	2.192–3.253
34	166	-14.29	-14.83		87	96	-16.28	-16.37	7.798–8.815
36	198	-15.31	-15.85	10.940–10.940	88	40	-15.84	-15.97	5.164–6.976
37	163	-14.52	-15.46	3.501–5.516	89	133	-13.75	-13.94	1.733–1.938
38	177	-12.74	-13.28	0.532–0.828	90	43	-15.75	-15.75	4.079–4.740
39	181	-14.99	-15.53	3.228–4.661	91	125	-14.20	-14.39	1.363–1.559
41	55	-15.06	-15.32	2.672–2.961	93	128	-15.03	-15.22	
42	153	-14.53	-14.72	2.015–2.015	94	144	-14.60	-14.79	9.052–154.137
43	160	-13.94	-14.13	1.884–2.309	95	127	-15.01	-15.20	
44	51	-14.11	-14.24	2.001–2.206	96	127	-15.01	-15.20	1.482–1.739
45	151	-14.23	-14.42	2.592–3.190	97	107	-15.40	-15.53	1.975–2.106
48	173	-16.18	-16.37	7.518–8.443	99	126	-13.81	-14.00	0.510–0.639
49	53	-15.42	-15.97	4.004–4.320	100	58	-16.08	-16.08	4.337–4.666
51	180	-15.85	-16.04	3.505–4.288	101	58	-16.08	-16.12	4.201–5.390
53	191	-15.13	-15.32	2.158–2.322	103	110	-14.05	-14.18	
54	65	-15.47	-15.60	3.063–3.437	104	60	-16.75	-16.88	8.276–8.625
55	68	-15.46	-15.59	5.166–7.181	106	112	-13.84	-13.97	0.460–0.949
56	185	-15.86	-16.05	7.154–9.845	107	59	-15.55	-15.68	7.538–9.560
57	185	-15.86	-16.05	7.153–9.843	108	59	-15.55	-15.68	3.390–4.440
59	192	-16.20	-16.39	4.923–6.066	109	56	-15.01	-15.14	1.666–1.700
61	39	-16.29	-16.42	8.779–10.045	110	63	-14.92	-15.05	2.385–3.913
63	35	-16.23	-16.36	7.148–9.505	112	71	-14.49	-14.77	3.707–4.816
64	188	-15.12	-15.31	1.820–2.428	114	91	-14.53	-14.55	2.934–3.375
65	79	-15.33	-15.46	3.626–5.032	115	103	-13.99	-14.12	

5.2.2 Accounting for Extinction

As our mass estimates rely upon cluster photometry, extinction has a significant effect on the mass estimates. As mass calculations are derived from Ks band photometry, the effect is not as strong as if we had used optical photometry, as extinctions are about a factor of 11 less in the K band than in the optical (Glass, 1999). In §5.1 we discussed our extinction measurements for the 32 clusters with Hα and Hβ flux measurements. The extinction measurements range between $A_V = 0.21$ and 11.1 mag. Applying a A_V to A_K ratio of 1:0.089 (Glass, 1999), we have a range of A_K from 0.02 to 0.99 mag.

22 of the 73 clusters with mass estimates also have extinction measurements. For these clusters we have used the measured A_V value, converted to A_K, to correct the cluster photometry for extinction. For clusters without measured extinctions, we have used the median extinction value, converted to K band, for the region in which the cluster is located to correct for extinction. Table 5.2 contains the median A_V values for each region. Both the measured and extinction-corrected Ks band photometry for each of our clusters with a match to the Brandl et al. (2005) survey are listed in Table 5.3.

In Figure 5.6 we plot the cluster mass distribution calculated with and without the extinction correction. As expected, the extinction-corrected mass distribution is similar but shifted to slightly higher masses with an average mass increase of 27% over the non-extinction-corrected mass estimates.

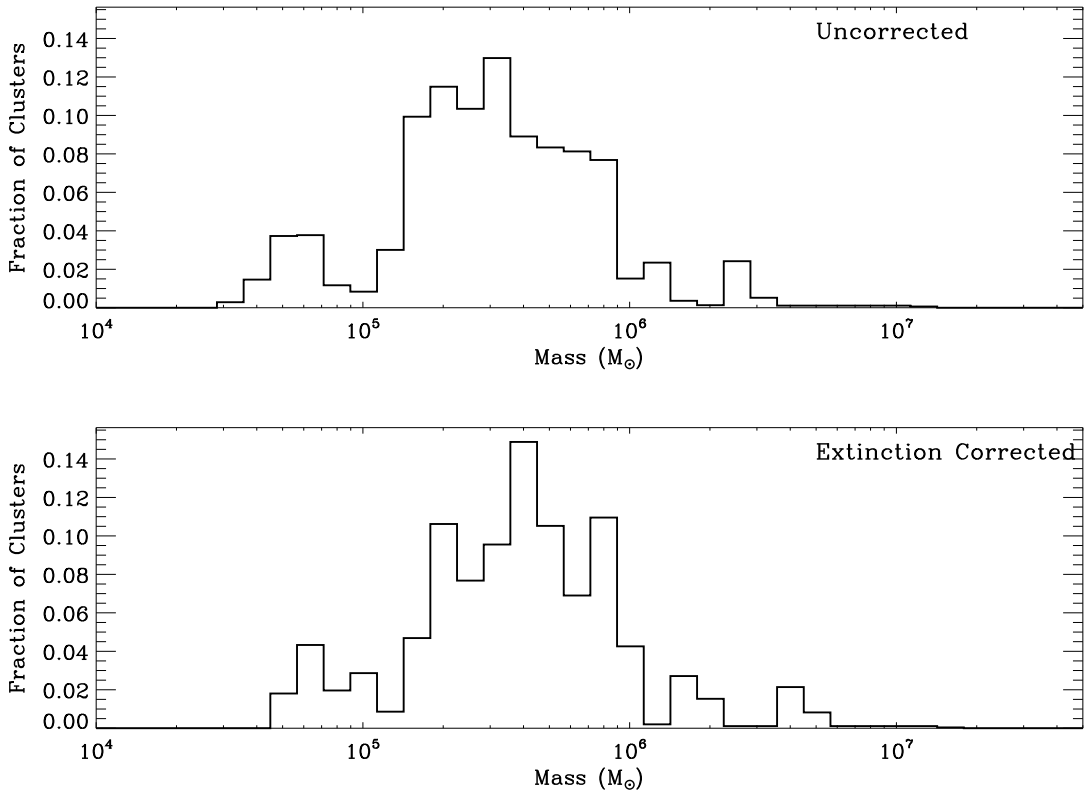

Figure 5.6 Correcting for Extinction in Cluster Mass Estimates. Plotted are the non-extinction-corrected mass distribution (top) and the extinction-corrected mass distribution (bottom). For clusters without direct extinction measurements, the median extinction in the region of the cluster is used for the extinction correction.

We will discuss the actual mass distribution in more detail below.

5.2.3 Cluster Masses

Looking at the extinction-corrected mass distribution (bottom plot of Figure 5.6), we see that the mass distribution peaks around 4×10^5 $M_\odot$, which coincides with the median cluster mass of the sample. The distribution lies mostly between 10^5 and $10^6 M_\odot$ (58 of the 73 clusters (79%) fall in this range) with a handful of lower-mass and higher-mass clusters. In §5.2.6 we will discuss the implication of the lack of very low or very high mass clusters and conclude that while low-mass clusters are missing because of our cluster selection methods, the lack of high-mass clusters is real.

To check our mass calculations, we compared our cluster masses with 5 previously measured cluster masses from Mengel et al. (2001) and Gilbert et al. (2000). These are five of the brightest clusters in the Antennae (Clusters 15, 19, 79, 82, and 85 in our sample). For each of these clusters our masses and the masses from Mengel et al. (2001) and Gilbert et al. (2000) are in agreement within uncertainties.

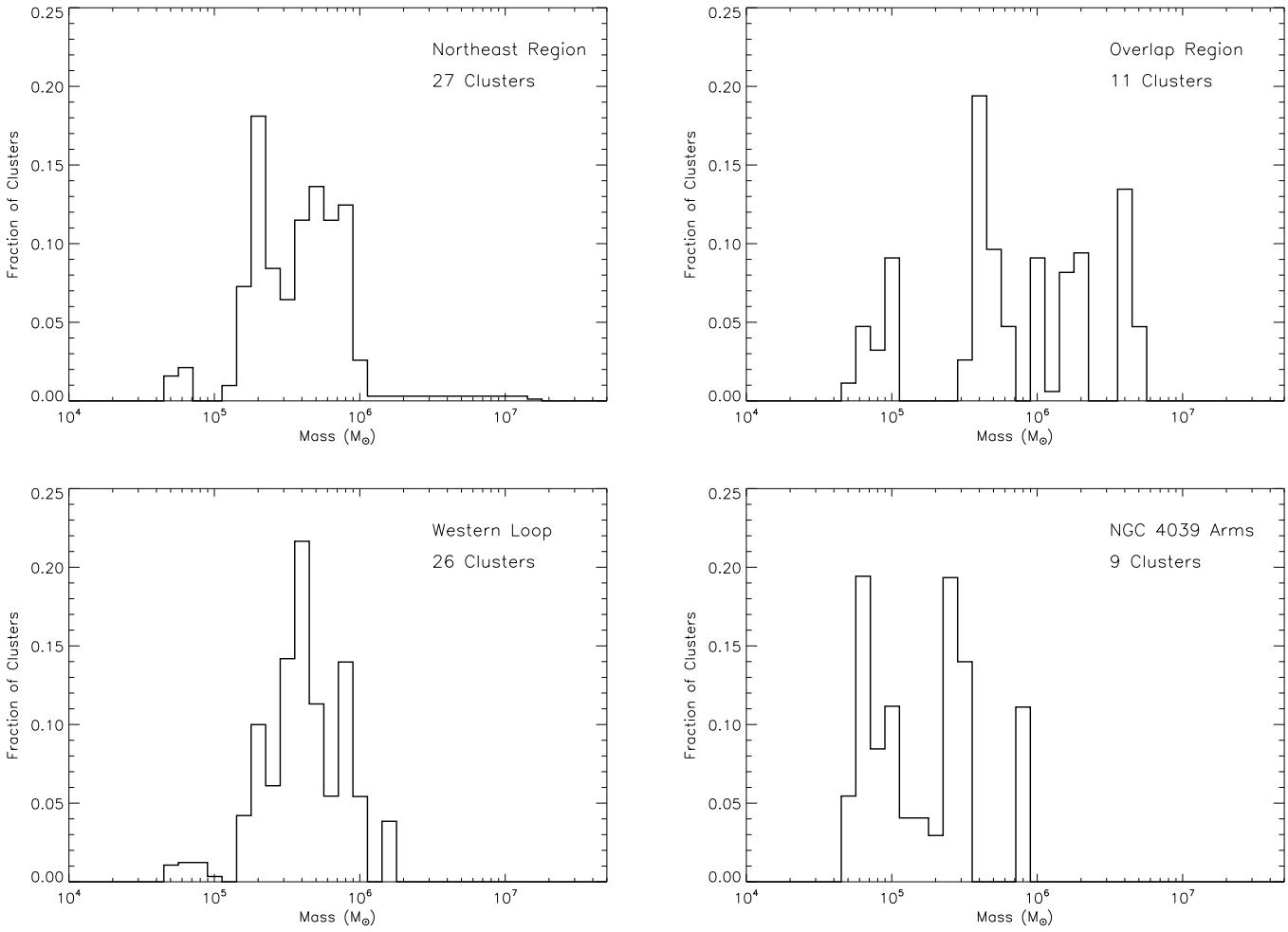

Figure 5.7 Cluster Mass Distribution by Region. The logarithmic mass bins are normalized by the number of clusters with measured masses in each region.

5.2.4 Spatial Variation in Cluster Mass

There are clear differences in cluster mass between locations in the Antennae (see Figure 5.7 and Table 5.5). the most massive clusters are found within the overlap region, while the NGC 4039 arms region, particularly the southernmost part of the arm, contains consistently the lowest mass clusters. Indeed, with the exception of Cluster 12 which has a large extinction, the most massive cluster in the arms region is only 2.8 $\times$ 10^5 $M_\odot$, less than the median mass of the entire cluster sample. In contrast, cluster masses in the northeast region and the western loop are concentrated in the 10^5–10^6 $M_\odot$ range, with only one to two clusters below and above that range in each region. The cluster mass distribution plots for these two regions (top- and bottom-left of Figure 5.7) show that the two mass distributions are very similar with the western loop mass distribution shifted to slightly higher masses than the northeast region distribution.

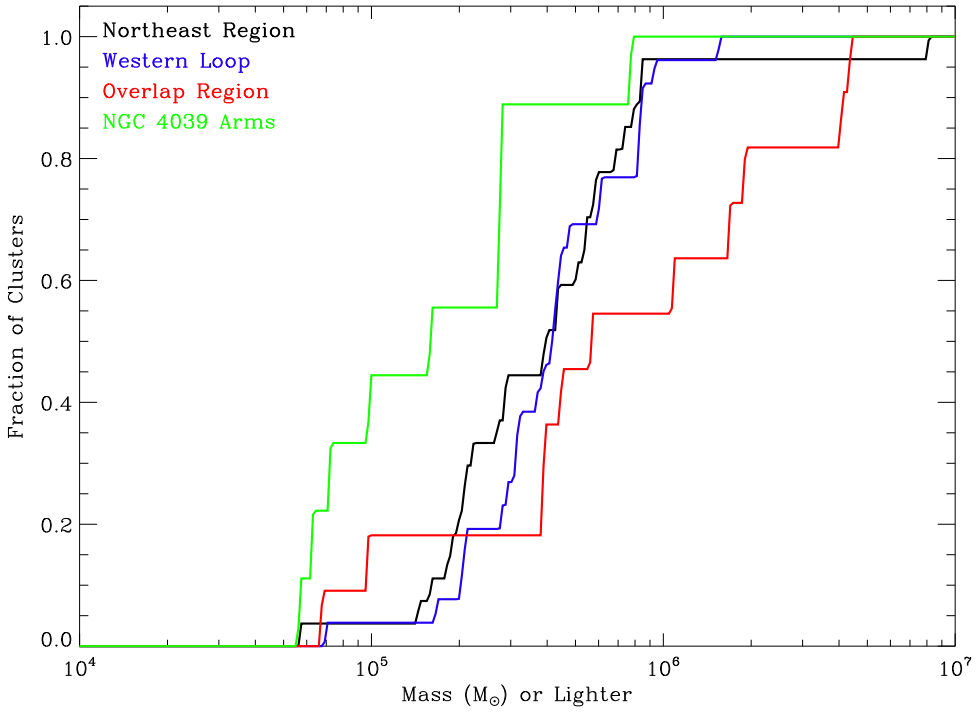

Figure 5.8 Cumulative Mass Distribution by Region. The logarithmic median mass for each cluster is used to construct the distribution function.

Statistically examining the mass distributions of the four Antennae regions supports these conclusions. The cumulative mass distributions (Figure 5.8) show that the western loop and northeast regions have very similar mass distributions, while the the NGC 4039 arms region focuses much more on low mass clusters and the the overlap region on high mass clusters. A K-S test on the cluster mass distributions (Table 5.4) finds that there is less than a 10% probability that the overlap region or the NGC 4039 arms region are drawn from the same population as either the northeast region or the western loop. These results for the mass distributions are very similar to the statistical results found for the age distributions of each region in the Antennae (§4.7.2) We do note, however, that our statistical analysis of the mass distributions by region may be affected by selection biases and that the fact that we are not able to claim completeness down to a mass limit for any of our regions.

Two of the most massive clusters are found in the southern part of the overlap region. These clusters (15 and 19) are two of the brightest near-infrared clusters and each have masses well over 3.5×10^6 $M_\odot$. The distribution of cluster masses for the overlap region is substantially broader than for the other regions with almost equal numbers of clusters ranging over two decades from 6×10^4 $M_\odot$ to 6×10^6 $M_\odot$. In general the overlap region has more massive clusters than other Antennae regions, with a mean mass almost twice as large as any other region and with five of the seven clusters with masses larger than 10^6 $M_\odot$ (Table 5.5).

Table 5.4. K-S Test Results for Mass Distributions by Region

Region	Region	K-S D Value	Probability from Same Distribution
Northeast Region	Western Loop	0.21	52.8%
Northeast Region	Overlap Region	0.42	9.5%
Northeast Region	NGC 4039 Arms	0.52	3.3%
Western Loop	Overlap Region	0.42	10.0%
Western Loop	NGC 4039 Arms	0.66	0.1%
Overlap Region	NGC 4039 Arms	0.71	0.6%

Table 5.5. Cluster Masses By Region

Region	Number of Clusters	Mean Mass $\times 10^5$ $M_\odot$	Median Mass $\times 10^5$ $M_\odot$
Northeast Region	27	7.0	4.0
Western Loop	26	5.0	4.3
Overlap Region	11	13.8	5.7
NGC 4039 Arms	9	2.3	1.6
All Clusters	73	6.7	3.9

Figure 5.9 further illustrates the spatial variation in cluster masses and adds additional insights into variations within individual regions. In the northeast region, the least-heavy clusters (indicated in black and dark blue) all lie in the northern part of the region, while the heavier clusters are in the southern part. This does not coincide with cluster ages as some of the youngest clusters in the northeast region lie both in the northernmost and southernmost parts of the region (see Figure 4.11). In the NGC 4039 arms region, the lightest clusters are found farthest to the south, which does match up with age as these are some of the older clusters in the Antennae. Within the western loop cluster masses vary throughout the region, without any particular trends with location. Finally, in the overlap region we find the heaviest clusters in the Antennae inside or near the edges of the large molecular gas concentrations.

5.2.5 Variation in Mass with Cluster Age

In Figure 5.10 we plot the distribution of cluster masses with age. We find that younger clusters tend to be more massive than older clusters both for the entire cluster population and in each individual region. The best fit line (shown in black in the Figure) reveals that the average mass of a cluster decreases by a factor of 10 for every 2 Myr of age. We find that the "very" old ($>$ 13 Myr) population of clusters all have masses that are around 10^5 $M_\odot$ or less; this result was also seen by Mengel et al. (2005). Some of the age/mass correlation that we have found here may be due to selection effects, which we will return to below (§5.2.6).

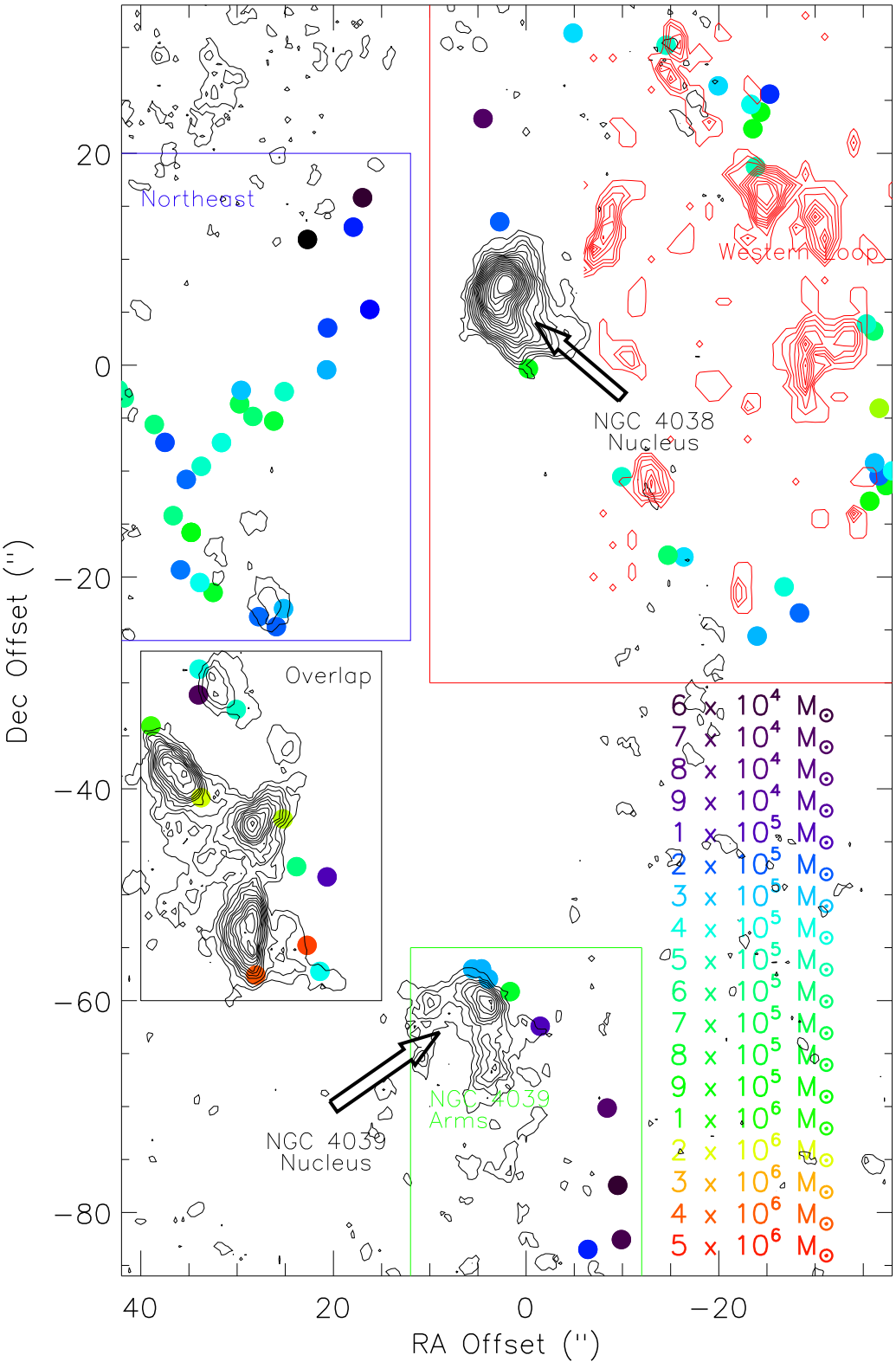

Figure 5.9 Cluster Mass Versus Location. Clusters are color-coded based on their mass. The CO (1-0) distribution is overplotted.

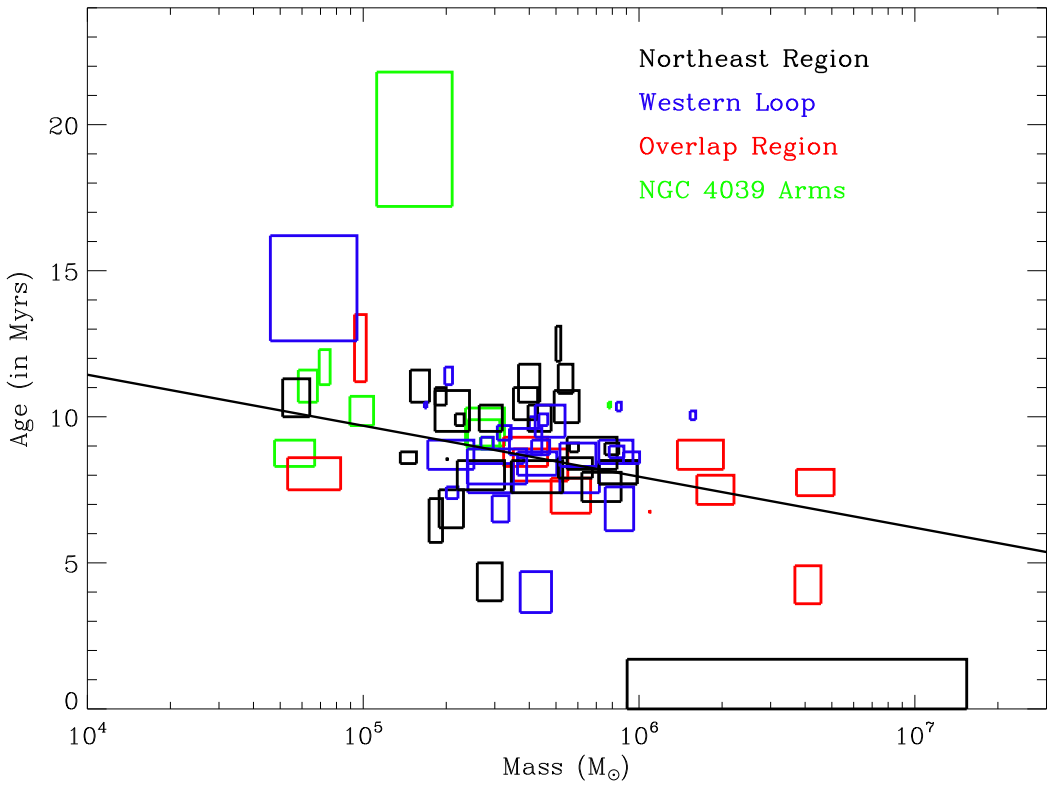

Figure 5.10 Variation of Age with Mass for Clusters. The clusters are color-coded based on their location in the Antennae. The best fit line (Age (Myr) = 18.42 - 1.75 log(Mass)) is overplotted in black.

5.2.6 Selection Effects in the Cluster Mass Distribution

In §4.8 we examined selection biases in our cluster age distribution. In the 5 Myr duration burst model the K band luminosity peaks near 12.5 Myr and falls off afterward until around 20 Myr (Figure 4.14). This suggested that the lack of clusters with ages greater than 12.5 Myr is not a selection effect but a true deficit. We also concluded by examining the expected evolution of the V band magnitude that there is also a lack of clusters in the 3–7 Myr range.

However, with our mass analysis we recognize that the mass of a cluster is as intimately coupled to its luminosity as its age is. Therefore a true statement on selection effects needs to simultaneously consider cluster ages and masses. As discussed in §2.2.2, our cluster sample was selected from a Ks band flux-limited sample of the Antennae and includes 69% of clusters with $M_{Ks} < -15.5$ and 60% of clusters with M_{Ks} between -15.5 and -15. Less than 50% of fainter clusters were included in our sample.

In Figure 5.11 we plot cluster age versus mass for the 73 clusters with mass determinations. The lines overplotted indicate different Ks band absolute magnitudes using Starburst99 with a 5 Myr

duration burst model. Since cluster luminosities peak between 7 and 20 Myr in our 5 Myr duration burst model, clusters in this age range can have lower masses and still be detected as part of our survey. In comparison, very young clusters (< 5 Myr) and older clusters (> 20 Myr) can only be detected if they are more massive. The difference is substantial, as a 1 Myr cluster has to be about 10 times as massive as a 12 Myr cluster in order to have the same luminosity.

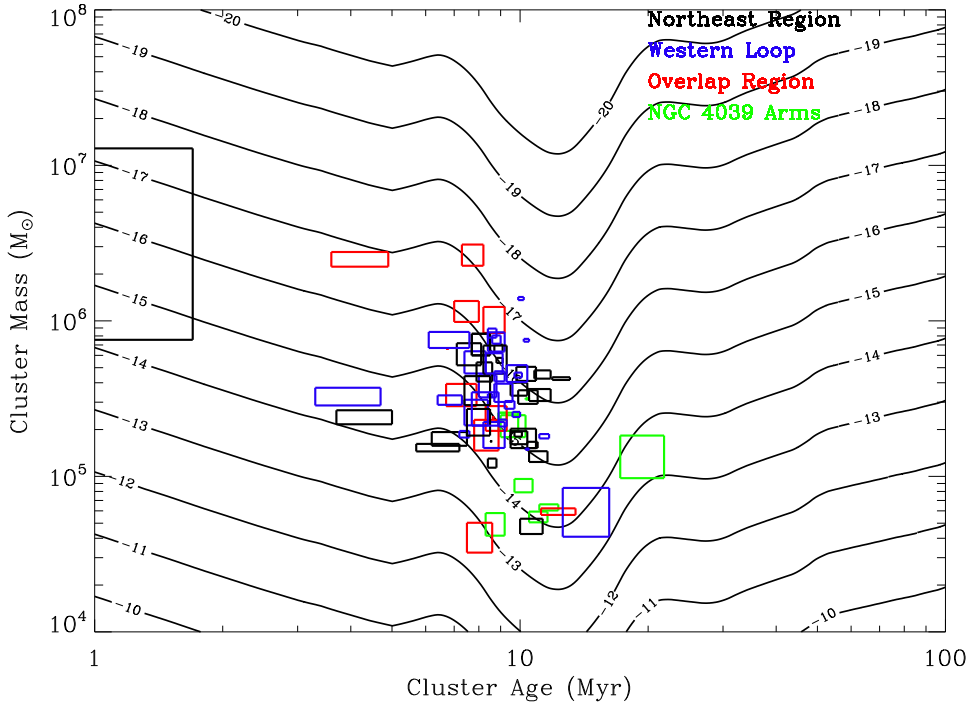

Figure 5.11 Cluster Age Versus Mass. The 73 clusters with mass and age estimates are plotted and color-coded based on their location in the Antennae. The overplotted lines indicate different cluster Ks band absolute magnitudes, using Starburst99 and a 5 Myr duration burst model.

If we bin the 73 clusters by their K band luminosity we can get a better idea of the role that selection effects play in our measured mass distribution. Figure 5.12 plots mass distributions for three different luminosity ranges. We find the largest cluster masses in the clusters that are brighter than M_{Ks} = -15.5. Indeed the median mass of this sample is 5.8 $\times$ 10^5 $M_\odot$. This result is not surprising as the luminosity of a cluster increases as the mass increases.

As we shift to lower luminosity clusters we find a consistent decrease in cluster masses with intermediate luminosity clusters (middle plot) and faint clusters (bottom plot) having median masses of 2.4 $\times$ 10^5 $M_\odot$ and 1.9 $\times$ 10^5 $M_\odot$, respectively. Most noticeably for the faintest clusters, the mass distribution becomes bimodal with peaks near 5.5 $\times$ 10^4 $M_\odot$ and 2.1 $\times$ 10^5 $M_\odot$. It is very significant that we do not see a large number of higher mass clusters appearing in the lower luminosity distribution. If we were missing higher mass clusters because they were younger and therefore less

luminous, we should continue to see high mass clusters as we move to fainter luminosities. The fact that we only see lower mass clusters suggests that there is not a substantial undetected population of very massive, young clusters. This supports the conclusion above that there is a true lack of clusters with ages < 7 Myr. We therefore expect that our mass distribution (Figure 5.6) contains most of the high-mass clusters in the Antennae and that increasing our sample size to fainter clusters will only increase the number of low-mass clusters detected.

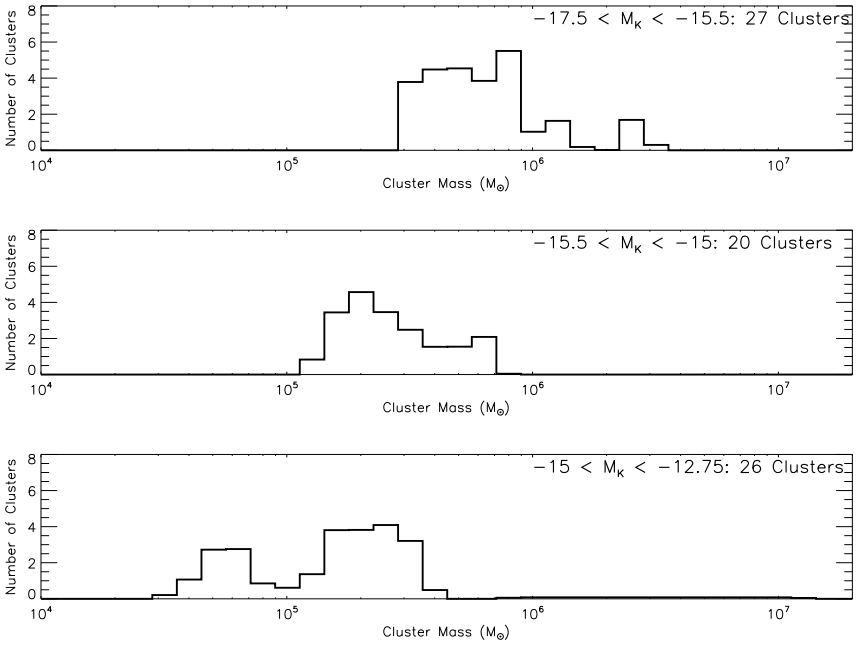

Figure 5.12 Dependence of Cluster Luminosity on Mass. The cluster mass distribution is shown for three different cluster luminosity ranges. Clusters brighter than M_{Ks} = -15.5 are in the top plot. We observed 70% of clusters in the Antennae with M_{Ks} < -15.5. The middle plot contains clusters just fainter (M_{Ks} between -15.5 and -15). We observed approximately 60% of the clusters in the Antennae in this range. The bottom plot contains clusters of lower luminosities. Only a fraction of Antennae clusters with these luminosities were observed as part of our survey.

5.2.7 Modeling Age and Mass Distributions to Further Analyze Selection Effects

We have chosen one additional way to examine possible selection effects: modeling an underlying age and mass population and determining the expected age and mass distribution that would be observed. In calculating the expected age and mass distribution we have assumed that the cluster luminosity distribution of the model is identical to that of our cluster sample. With these tests we can determine whether selection effects are masking a standard mass and age population or whether we are looking at a unique age and mass population that, for instance, has a lack of clusters under 7 Myr and over 13 Myr.

We first consider a cluster population distributed equally in age from 0.01 to 30 Myr and in mass logarithmically from 10^4 to 10^8 $M_\odot$. We allowed for evolution of the mass and age populations in three ways: setting an upper mass limit for a cluster as a function of the cluster age; decreasing the number of clusters as a function of age without regards to cluster mass; setting a lower age limit of 1 Myr for clusters. Setting an upper mass limit as a function of age allows for the loss of mass as a cluster ages through various processes, most notably stellar evolution (Fall & Zhang, 2001). Decreasing the number of clusters as a function of age considers the possibility that some fraction of clusters are disrupted as they age.

Using these criteria we created 32 sample populations. For each cluster in our sample population we calculated the M_{Ks} based on its age and mass using the Starburst99 models modified for a 5 Myr duration burst of star formation. The clusters for each population were then binned according to their magnitudes. For each population we made 1000 sample observations by selecting at random clusters that will match the cluster magnitude distribution of our Antennae sample. We combined these 1000 sample observations to get age and mass distributions for each population and then statistically compared these distributions with our observed Antennae distributions both graphically and using the K-S test. We also examined the individual sample observations (which had the same cluster size as our sample) and found the results to be similar to those derived after combining the 1000 observations.

In the top left of Figure 5.13 we plot the age distributions derived for 4 sample populations. The 4 populations were selected as representative of the 32 samples we considered. Each sample is identified by two values: the drop in the maximum cluster mass for each factor of 10 in age; the drop in the weighting of clusters for each factor of 10 in age. The age distribution for the sample with no maximum mass drop or change in weighting with age (labeled No Drop—No Drop in Figure 5.13) is essentially flat from 1 to 30 Myr. In comparison, adding a maximum mass limit that drops by a factor of 10 for each age decade (10x—No Drop) causes a substantial decrease in clusters past 15 Myr as the effects of the mass limit become more significant. Both populations with an age weighting (light blue and green) show exponentially declining age distributions peaking at the earliest ages. The red line is our actual age distribution for the Antennae clusters and we see that none of the models we sampled is able to predict the 8–12 Myr age peak with a lack of 3–7 and 13–20 Myr clusters. In the bottom left plot of Figure 5.13 we plot the cumulative age distribution for these 4 models and the Antennae sample and we see again the vast disagreement between the models and the actual sample. In particular, any model with an age weighting (even as small as a factor of 2 per age decade) predicts too many young clusters while any model without a drop in age weighting predicts too many older clusters.

Examining the K-S statistics of the age distributions derived from the model populations compared with the measured Antennae age distribution, we find very poor agreement. The probability

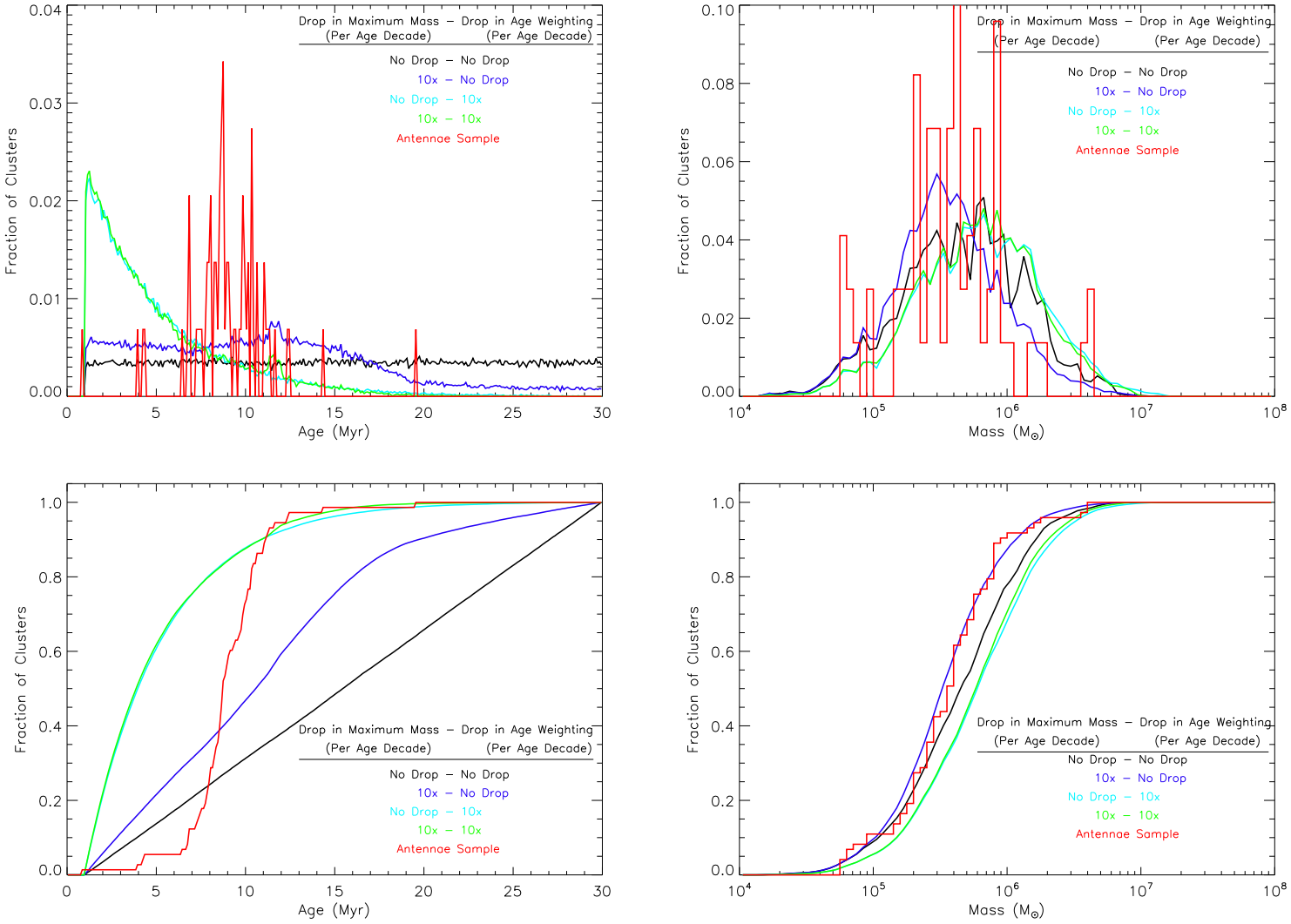

Figure 5.13 Age and Mass Distributions for Model Cluster Populations. Four cluster models, representative of the 32 models we tested, are included. Each of these models has a 1 Myr lower age limit. The top plots shows the age distribution on the left and the mass distribution on the right. The bottom plots give the cumulative age and mass distributions. The red line in each plot is the actual distribution from our Antennae sample. See the text for descriptions of the models plotted.

that our Antennae age distribution and the age distribution from any of these models were drawn from the same population is less than .0001%.

The mass distributions derived from our model populations also differ significantly from the Antennae mass distribution, although the differences are not as large as for the age distribution. The top-right plot in Figure 5.13 shows that the mass distributions derived from the same four populations. All 4 distributions, along with the observed Antennae cluster distribution, range between 4×10^4 $M_\odot$ and 1×10^7 $M_\odot$. The mass distributions for the population with no drop in maximum mass or age weighting (black) as well as for the two populations with an age weighting (light blue and green) are shifted to slightly higher masses than the distribution taken from the population with only a drop in maximum mass with age (dark blue). Examining the cumulative mass distributions (bottom-right plot of Figure 5.13) we find relatively good agreement between the Antennae sample and the population with a factor of ten drop in maximum mass per age decade (dark blue). The largest difference between these two cumulative distribution functions (i.e., the K-S D value) is 0.1, the smallest of any of our models. All other models predict more high-mass clusters than seen in our observations. The mass distributions of all but 4 of the 32 model populations tested are distinct from the observed mass distribution at $> 90\%$ confidence. Even the cluster model with the best agreement with the Antennae distribution had a K-S probability of only 42%. We note, however, that even the models with the largest K-S probability for mass distributions had K-S probabilities consistent with 0% for the age distributions.

These model populations have allowed us to examine how the combined effects of age and mass on the luminosity of a cluster impact the observed age and mass distributions. We find that no simple population with either a decline in maximum mass as a function of age or a decrease in the number of clusters as a function of age independent of mass can reproduce our observed age and mass distributions. This strengthens in particular the argument that our 8–12 Myr peak in the age distribution shows a true lack of younger and older clusters and is not simply the result of selection effects.

5.3 Summarizing The Age and Mass Distributions

In Figure 5.14 we have replotted the age and mass distribution for our survey of the Antennae. The age distribution in black includes all 107 clusters with age determinations while the red age distribution includes only the 73 clusters with mass determinations.

With our combination of near-infrared and optical spectroscopy we are able to sample well cluster ages from 3 to 20 Myr. Within this age range, we can conclude that there is a large concentration of clusters from 7 to 12 Myr. Many of the clusters near 7 Myr were discovered during optical spectroscopy and not detected in K band imaging. In comparison, most clusters from 8 to 12 Myr

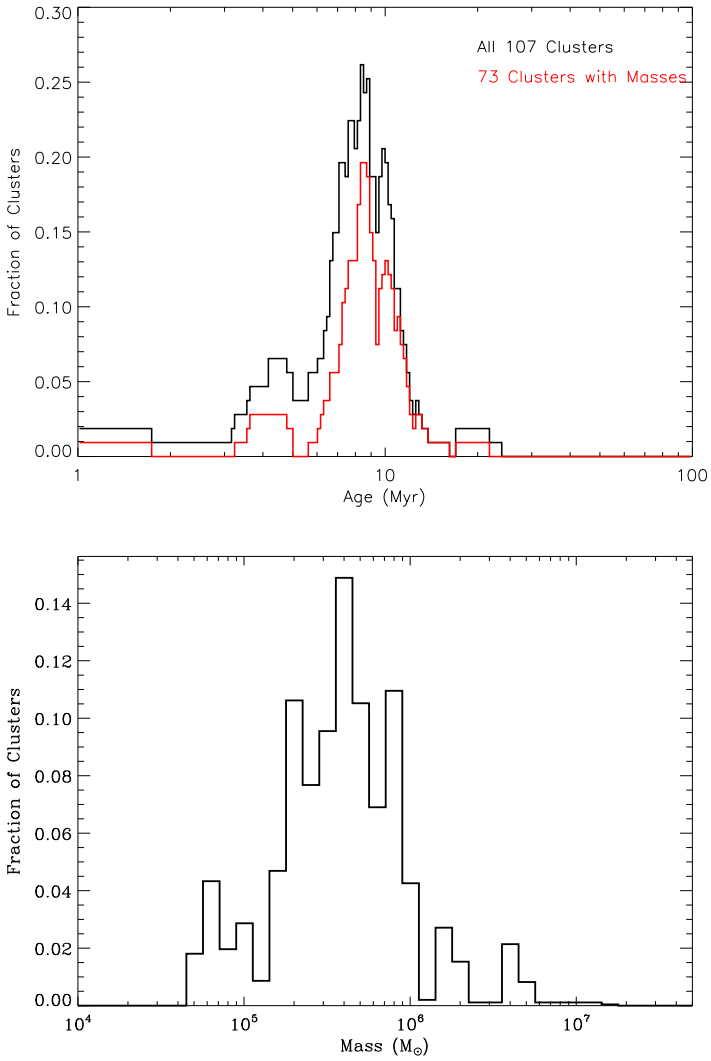

Figure 5.14 Age (Top) and Mass (Bottom) Distributions. The age distribution is shown for all 107 clusters with age determinations (black) and for the 73 clusters with mass determinations (red).

are detected in the K band images. By examining the expected V and K band luminosity evolution of clusters we can conclude that there is a real deficit of clusters from 3–7 Myr and from 12–20 Myr.

The mass distribution for the 73 clusters in our sample with mass determinations peaks around 4×10^5 $M_\odot$. Only 7 clusters have a mass greater than 10^6 $M_\odot$ with the largest well-constrained mass at 5×10^6 $M_\odot$. By examining the mass distributions for different ranges of cluster luminosities we can determine that within the 3–20 Myr age range we have included most of the massive clusters in our sample and that extending our survey to fainter clusters in this age range would only increase the number of low-mass clusters detected.

5.3.1 Comparison with Age and Mass Distributions of Previous Studies

Comparing the age and mass distributions of our survey with previous studies is difficult because these studies have focused on different aspects of the Antennae population. For instance, Whitmore et al. (1999) focus on a deeper photometric study of the Antennae using their HST imaging and make broader statements about the age distribution of the Antennae. Regarding clusters younger than 20 Myr, they only state that overlap region clusters tend to have ages < 5 Myr while the western loop and the regions near the overlap region have ages near 10 Myr. Based on their method of age determination from various photometric bands, they are unable to provide better age resolution in the 3–15 Myr age range, precisely the age that our study focused upon. Subsequent studies from the same data set Fall et al. (2005) have detected a substantial population of clusters younger than 10 Myr, but again are not able to distinguish more specific ages younger than 10 Myr.

Mengel et al. (2005) is one study that has focused more upon the age distribution of the youngest Antennae clusters. For their age analysis, they used Ks and V band photometry along with photometric measures of Brγ and Hα emission and the CO index. For a K band selected sample, they find a strong age peak at 10 Myr, similar to our results. However, the brightest clusters in their sample tend to be the youngest, in contrast to our results where the brightest clusters are most strongly peaked around 8–12 Myr (Figure 4.16). Examining a V-magnitude-limited sample, Mengel et al. (2005) again find a peak at 10 Myr and also a 6 Myr peak. This is similar to our findings as we see the rise of 6 Myr clusters in the subset of clusters seen only in the optical. The discrepancies in our results are larger due to the star formation model used. The 5 Myr duration burst model causes the K band luminosity to increase steadily from 1 to 7 Myr before a rapid increase from 7–12 Myr (see the solid lines in Figure 4.14). In contrast an instantaneous burst model has the K band luminosity starting at a high level and decreasing from 1–6 Myr before a rapid increase from 6 to 9 Myr (see the dotted lines in Figure 4.14).

Comparing our age measurements to the measurements of Gilbert & Graham (2007) for 16 clusters primarily in the overlap region, we find similar results as found for the Mengel et al. (2005) sample. We have age measurements for 14 of the 16 clusters studied by Gilbert & Graham (2007)

and find that our ages are consistently older. For those 14 clusters we find a mean age of 8.8 Myr compared with 5.9 Myr in Gilbert & Graham (2007). Again we attribute this discrepancy simply to the use of a 5 Myr duration star formation burst model as opposed to an instantaneous burst model. Gilbert & Graham (2007) based ages on Brγ equivalent widths, which obscures the fact that some clusters in their sample also show CO bandheads.

The mass function of Mengel et al. (2005) is similar at the high-mass end to our findings. They find a mass turnover at around 3×10^5 $M_\odot$, very close to the peak we see in our cluster mass distribution. Mengel et al. (2005) find a larger number of high-mass clusters ($> 10^6$ $M_\odot$), but this is most likely due to the much larger number of clusters examined in their photometric survey. Comparing our cluster masses to the masses calculated by Gilbert & Graham (2007) we find good overall agreement in our cluster masses despite the systematic age discrepancy.

Chapter 6

Metallicity and Stellar Populations

6.1 Metallicity

One uncertainty in population synthesis models is the cluster metallicity. For our age estimates (§4.6) we have followed previous Antennae studies and adopted solar metallicity. To check that solar metallicity is a reasonable assumption for the Antennae clusters, we have calculated the metallicity of Antennae clusters using two different tracers.

The simplest metallicity tracer to use for our observations is the N2 index: N2 = $\log(F_{[NII]\lambda6583}$ / $F_{H\alpha})$ (Pettini & Pagel, 2004; Denicoló et al., 2002). This is a very valuable tracer because of the strength of both lines in most young clusters and the close spectral proximity of the two lines. Since the two lines are only 20Å apart, the same regions can be used to estimate the continuum for both lines and any extinction differences are negligible. From a sample of 137 extragalactic HII regions, Pettini & Pagel (2004) find a best fit relationship between metallicity and the N2 index of: $12 + \log(O/H) = 8.90 + 0.57 \times N2$. We have made metallicity determinations in 86 out of 117 (74%) clusters and the NGC 4038 nuclear region using the N2 index.

A more involved metallicity tracer, building upon the N2 index, but also using shorter wavelength emission lines is the O3N2 index: O3N2 = $\log(\frac{F_{[OIII]\lambda5007}/F_{H\beta}}{F_{[NII]\lambda6583}/F_{H\alpha}})$ (Pettini & Pagel, 2004; Alloin et al., 1979). Using the same 137 extragalactic HII regions as for the N2 tracer, Pettini & Pagel (2004) determine a best fit relationship between metallicity and the O3N2 index: $12 + \log(O/H) = 8.73 - 0.32 \times O3N2$. H$\beta$ and [OIII]λ5007 are separated by only 132Å, so extinction differences in this ratio are also negligible. Since LRIS blue-side observations are necessary for the O3N2 index, we have only measured metallicities using the O3N2 index for 37 clusters, as well as the nuclear regions of NGC 4038.

In Table 6.1 we list the metallicities, relative to solar metallicity, for the clusters in our sample using the N2 and O3N2 indices. The average N2 metallicity is 0.99× solar compared with 1.01× solar for the average O3N2 metallicity. Examining the distribution of cluster metallicities we see that the metallicities predicted by both tracers are grouped around solar metallicity (Figure 6.1).

Table 6.1. Cluster Metallicity Estimates

#	N2	O3N2	#	N2	O3N2	#	N2	O3N2
All Metallicities are Relative to Solar								
2	0.62–2.59		41	0.86–0.87	0.87–0.90	82	0.86–0.92	
3	0.99–1.14		42	1.04–1.05		83	0.87–0.87	
4	0.89–0.91	0.90–0.95	45	1.03–1.03		84	0.89–0.92	0.97–1.12
5	0.68–0.88	0.61–1.35	46	0.99–1.00		85	0.93–1.00	
6	1.10–1.29		48	0.90–0.91		86	0.87–0.88	
7	1.15–1.29		49	0.84–0.86	0.73–0.80	87	0.97–0.97	1.86–1.97
8	1.11–1.20	0.83–0.97	52	0.89–0.92	1.02–1.25	88	0.92–0.93	
9	1.10–1.15	0.79–0.85	53	0.80–0.84		90	0.94–0.95	1.27–1.29
11	0.86–0.86		54	0.88–0.90	0.97–1.16	91	0.86–0.89	1.03–1.15
12	1.00–1.04		56	0.99–1.00	1.12–1.13	92	0.79–0.84	
13	0.86–0.87		57	0.99–0.99	1.12–1.13	94	0.83–0.84	
14	0.88–0.88	0.76–0.77	58	0.93–0.95		96	0.86–1.06	
15	1.08–1.08		59	0.91–0.93		99	0.76–1.26	
16	0.49–0.50	0.51–0.52	60	0.89–0.90		100	0.81–0.83	0.82–0.85
17	0.86–0.87		61	0.97–0.97		101	0.84–0.86	0.85–0.88
18	0.88–0.88	0.74–0.76	62	1.07–1.08	1.34–1.40	102	0.77–0.79	0.78–0.82
20	0.96–1.13	0.47–0.88	63	0.92–0.92		108	0.90–0.92	
21	1.71–2.47		64	0.71–1.24		109	0.88–0.93	0.94–1.02
22	0.88–0.89	0.70–0.72	65	0.95–0.96		110	0.92–0.96	
23	0.81–0.83	0.61–0.65	66	0.94–0.94		111	0.91–0.99	
24	1.03–1.04	0.86–0.89	69	0.82–1.26		112	1.07–1.08	1.16–1.18
26	1.13–1.20		70	0.98–1.01		113	1.05–1.07	1.10–1.18
27	0.76–0.80		71	0.93–0.94		114	0.96–0.96	1.12–1.14
28	0.81–0.82		72	0.93–0.98		116	0.75–0.92	0.61–0.79
30	0.87–0.89		74	0.98–1.01	1.02–1.16	4039 Nucl S		
31	0.86–0.88		75	0.88–0.88	0.86–0.89	4039 Nucl		
35	0.94–0.97		76	0.99–1.00	1.26–1.29	4039 Nucl N		
37	1.08–1.09	0.92–1.00	77	0.86–0.86		4038 Nucl S	1.09–1.11	1.36–1.49
38	0.93–0.95		78	0.88–0.89	0.89–0.93	4038 Nucl	1.15–1.16	1.44–1.46
39	0.91–0.92		79	0.91–0.92	0.98–1.01	4038 Nucl N	1.24–1.24	1.44–1.47
40	0.88–0.89	0.95–1.02	80	0.93–0.95				

The O3N2 index distribution is slightly broader than the N2 distribution. The vertical lines in Figure 6.1 show the metallicity solutions included in Starburst99. The solar metallicity solution is clearly the most appropriate solution to use in this study. We see no variation in metallicity with cluster age (Figure 6.2).

6.1.1 Comparing Metallicity Tracers

From Table 6.1 and Figure 6.1 we see that the metallicities predicted by the N2 and O3N2 indices, while similar, are not always in agreement for individual clusters. In Figure 6.3 we plot the metallicity measured with the N2 index versus the metallicity measured with the O3N2 index. Most clusters are in agreement to within 20% of solar metallicity. Interestingly the overlap region clusters all had higher N2 metallicities. This may be related to the higher extinction levels in the overlap region. Since the Hβ and [OIII]λ5007 lines are separated by 132Å, higher levels of extinction will increase the value of O3N2 by suppressing the Hβ flux at greater levels than the [OIII]λ5007 flux. Indeed this conclusion seems to pan out when examining the difference between the two metallicity tracers versus extinction in a cluster (Figure 6.4). The highest extinction clusters all have N2 metallicities that are greater than their O3N2 metallicities. Additionally, clusters in the northeast region, where the extinction is lower, have much better agreement between their N2 and O3N2 metallicities.

Due to the good agreement on average between the O3N2 and N2 metallicity tracers, we could accept either tracer for our study. The N2 metallicity has been measured for more than twice as many clusters as the O3N2 metallicity has, so we will adopt the N2 tracer for our future analysis.

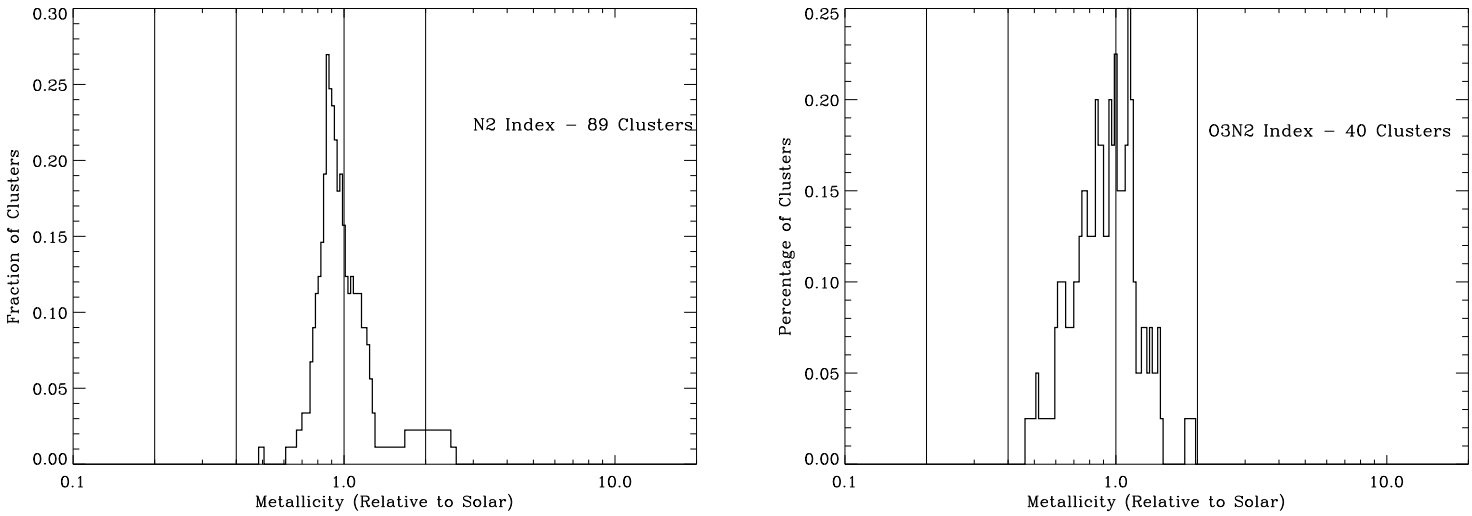

Figure 6.1 Distribution of Metallicities Using N2 Index (left) and O3N2 Index (right). Each histogram is normalized by the total number of clusters with a metallicity measured by that tracer. A cluster is included in all bins that fall within the 3σ uncertainty in metallicity. The metallicities are plotted logarithmically relative to solar. The vertical lines indicate four of the five possible metallicity solutions included in Starburst99 (Leitherer et al., 1999).

Table 6.2. Variation of Cluster Metallicities with Location

Location	Number of Clusters	Metallicity		
		Median	Mean	Std. Dev.
		Relative to solar metallicity		
Northeast Region	28	0.94	0.93	0.068
Western Loop	27	0.92	0.92	0.070
Overlap Region	16	0.94	0.95	0.273
NGC 4039 Arms	14	1.02	1.00	0.171
Nuclei	3	1.16	1.16	0.067
Total	89	0.94	0.95	0.147

6.1.2 Spatial Variation in Metallicity

Table 6.2 gives the mean and median metallicities using the N2 tracer for the four different cluster regions (plus the NGC 4038 nucleus) within the Antennae. We note that the average and median metallicities in each region are all similar and close to solar metallicity. The only exception is the NGC 4038 nuclear region where the metallicity is 20% higher. These high metallicities for the NGC 4038 nuclear region appear in the O3N2 tracer as well.

However, despite the fact that the mean metallicities are almost identical in each cluster region, we find that there is substantial variation in metallicity within the clusters of the NGC 4039 arms region, and to a lesser extent the overlap region (Figure 6.5). In the NGC 4039 arms region the clusters immediately to the north of the NGC 4039 nucleus have typically lower metallicities (around

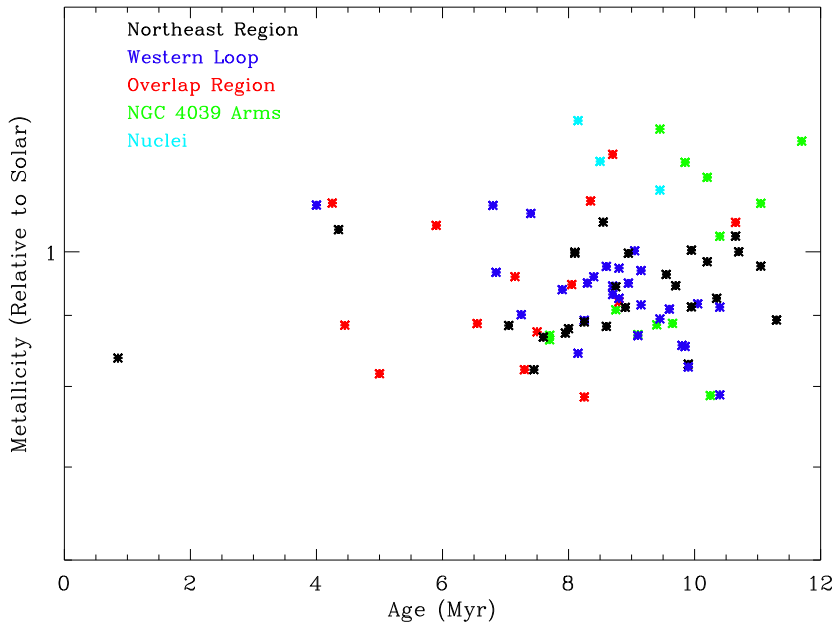

Figure 6.2 Variation in Metallicity with Cluster Age. The mean cluster age is plotted against the N2 index metallicities. Clusters are color-coded based on their location within the Antennae.

0.9x solar) while clusters farther to the south along the arms have metallicities closer to 1.1–1.2x solar. In comparison, in the overlap region the metallicity variations are not quite as strong and do not appear to be correlated with location in the overlap region.

Summarizing our metallicity results, we find strong evidence that Antennae cluster metallicities are solar or very near to solar, confirming previous studies and supporting our decision to use solar metallicity Starburst99 models.

6.2 The Giant/Supergiant Population of Older (> 8 Myr) Clusters

As seen in §3.2.2, CO bandheads and other near-infrared absorption features begin to appear in cluster spectra around 8 Myr when the first red giant and supergiant populations are emerging. From original K band observations and existing H and K band libraries (Kleinmann & Hall, 1986; Origlia et al., 1993; Dallier et al., 1996), Förster Schreiber (2000) compiled a library of equivalent width measurements of absorption features in giant and supergiant stars with a range of surface temperatures. Comparing these results from Förster Schreiber (2000) with our measurements of the equivalent widths of the CO (2-0) absorption bandhead at 2.29μm, the CO (6-3) absorption bandhead at 1.62μm, and Si I absorption line at 1.59μm, we can determine the effective temperature and luminosity class of the giant and supergiant population of the clusters. For convenience in this

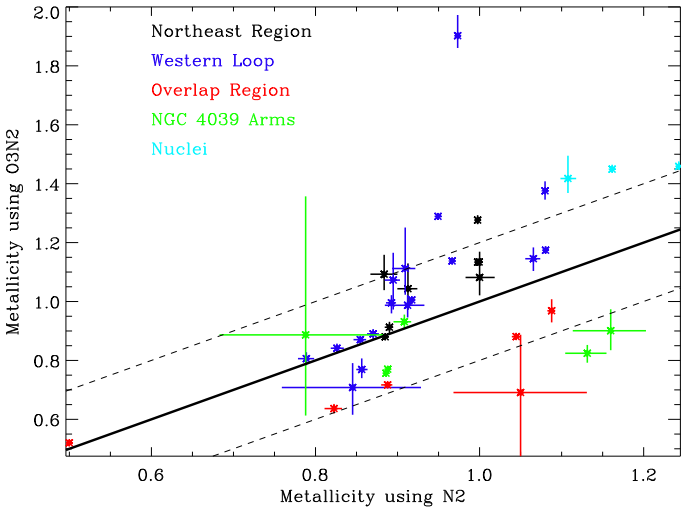

Figure 6.3 Comparing N2 and O3N2 Metallicity Tracers. The N2 metallicity is plotted versus the O3N2 metallicity for the 38 clusters (plus the nuclear region of NGC 4038) with metallicity measurements in both tracers. The metallicities are plotted relative to solar, and the solid black line indicates perfect agreement between the two tracers. The dashed lines are 0.2 solar difference between the two tracers. The points are color-coded depending on the location of the clusters in the Antennae system.

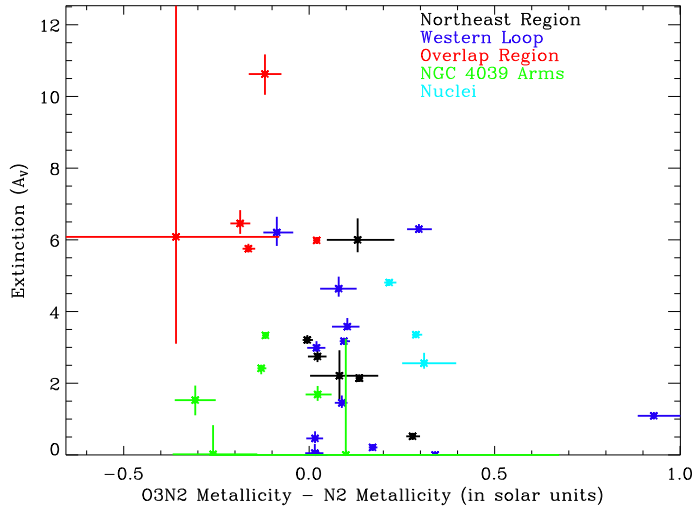

Figure 6.4 Comparing the Difference in N2 and O3N2 Metallicities versus Extinction. 31 clusters plus three observations of the NGC 4038 nuclear region are plotted. The points are color-coded based on the location of the clusters in the Antennae. Most clusters have a difference in N2 and O3N2 metallicities consistent with zero, but consistently all the overlap region clusters have higher N2 metallicities, likely due to the enhanced extinction in the overlap region.

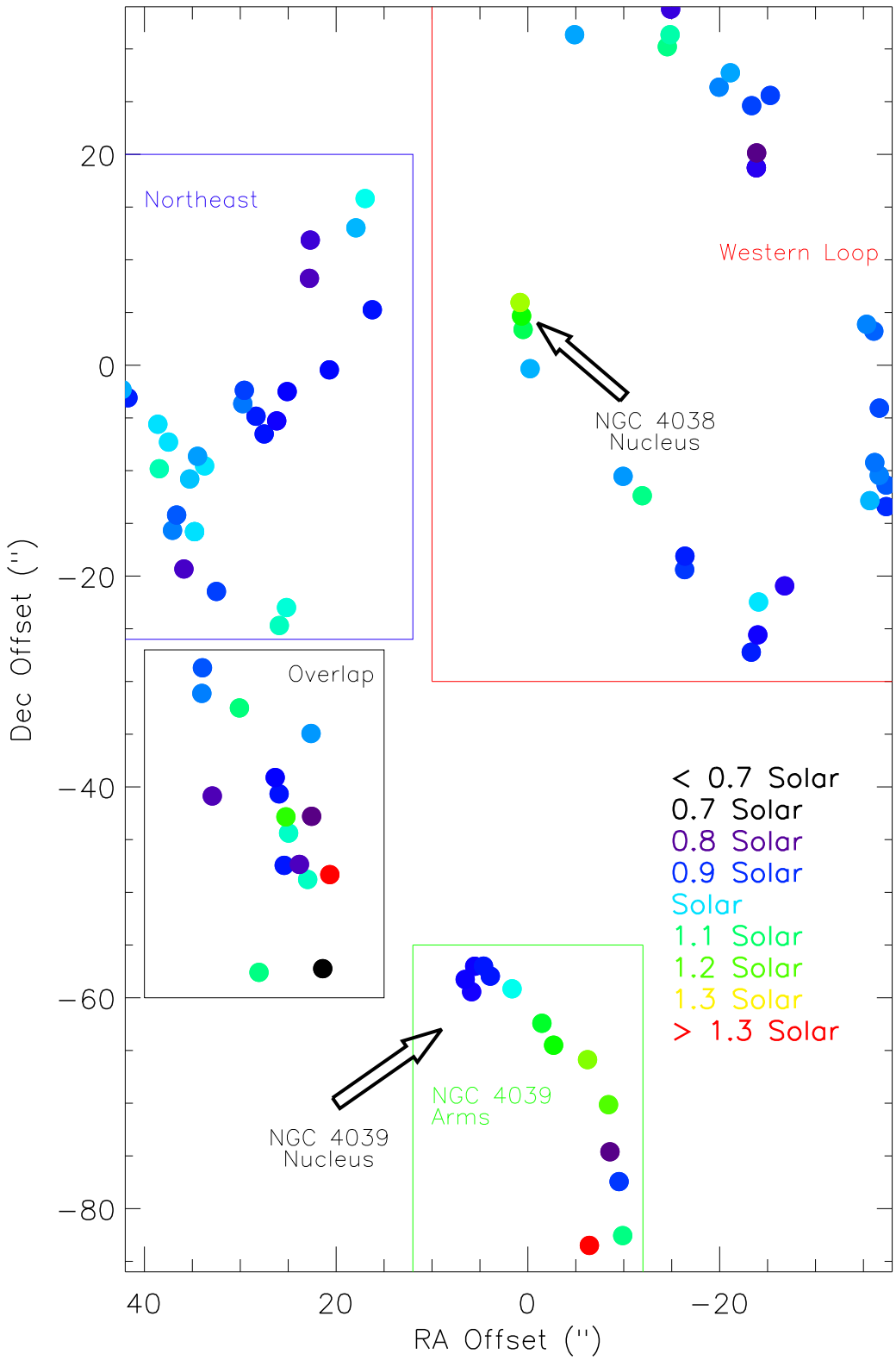

Figure 6.5 Spatial Variation in Metallicity. The 86 clusters plus three nuclear observations with metallicities determined by the N2 index are plotted, color-coded by their metallicity.

section we will refer to the equivalent widths of the CO (2-0) bandhead, CO (6-3) bandhead, and SiI absorption line by $W_{2.29}$, $W_{1.62}$, and $W_{1.59}$, respectively. We find typical effective temperatures near 3650K (with a smaller population near 2700K) and find strong evidence for the presence of supergiants in the majority of older clusters.

6.2.1 Measuring Effective Temperature using $W_{1.62}$ and $W_{1.59}$

$W_{1.62}$ and $W_{1.59}$ are both inversely correlated with effective temperature (see Figure 5a of Origlia et al. (1993) and Figure 9 of Förster Schreiber et al. (2001)). Due to contamination from dust emission we cannot use either of these inverse correlations to directly measure the effective temperature of the giant and supergiant populations in a cluster. However, since the Si I and CO (6-3) lines are separated by only 3μm, any dilution from dust emission is essentially identical in the two lines, so the ratio of the equivalent widths of these two lines can be used to measure effective temperature. The ratio of $W_{1.62}$ to $W_{1.59}$ is inversely correlated with effective temperature (see Figure 5b in Origlia et al. (1993), Figure 9 in Förster Schreiber et al. (2001), and Figure 6.6 in this work). There is no significant difference in $\log(W_{1.62}/W_{1.59})$ between giants and supergiants.

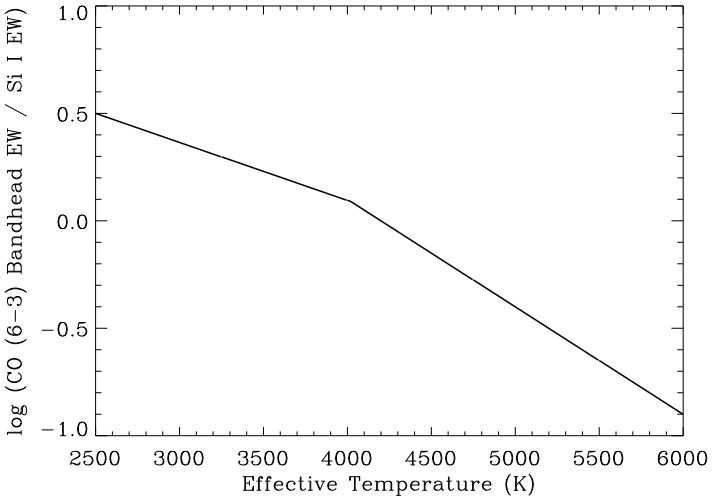

Figure 6.6 Variation in CO (6-3) Bandhead EW / Si I EW with Effective Temperature. The variations plotted are a best fit to the data of Förster Schreiber et al. (2001): $T_{eff}(K) = 4200 - 2000 \times \log(W_{1.62}/W_{1.59})$ for $\log(W_{1.62}/W_{1.59}) < 0.09$ and $T_{eff}(K) = 4354 - 3707 \times \log(W_{1.62}/W_{1.59})$ for $\log(W_{1.62}/W_{1.59}) > 0.09$.

6.2.2 Effective Temperatures of Older (> 8 Myr) Antennae Clusters

The measurements of $W_{1.62}$ and $W_{2.29}$ have been discussed above (§3.2.2). We adopt a similar method for the $W_{1.59}$ measurements, using source and continuum regions taken from Origlia et al.

(1993). The Si I line is weaker than the CO (6-3) absorption bandhead; Si I absorption is only detected in 14 clusters, along with five areas near the nuclei. These 14 clusters sample all of the Antennae cluster locations except for the overlap region. This lack of overlap region clusters is not surprising given the young ages of most overlap clusters (§4.6).

In Figure 6.7 we plot the measured values of $W_{1.62}$ versus $W_{1.59}$ for these 14 clusters and 5 nuclear regions. These values, as well as measured effective temperatures, are listed in Table 6.3. Using the best fit for the T_{eff} to $\log(W_{1.62}/W_{1.59})$ correlation, we mark effective temperatures from 2500 K to 5000 K. With the exception of two outliers, all the clusters and the nuclear regions have effective temperatures between 2500 and 4000 K. There is a strong concentration of clusters around 3500–3600K, corresponding to a population of M2–M4 giants or supergiants. We note that all six northeast region clusters have effective temperatures near 3500–3600K, while the effective temperature distribution for the other regions is less constrained. The distribution in effective temperatures has a main peak at 3600 K with a small peak around 2600 K (Figure 6.8).

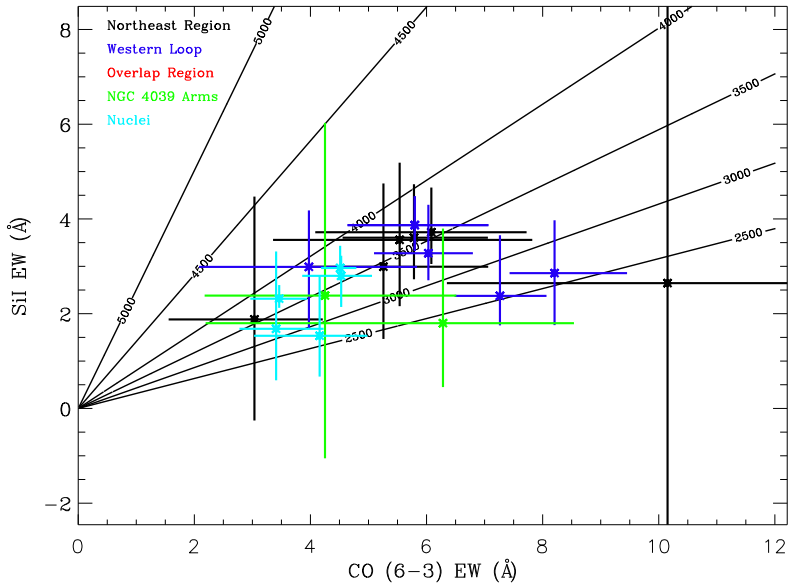

Figure 6.7 Distribution of $W_{1.62}$ versus $W_{1.59}$. The 14 clusters and 5 nuclear regions with detections of both the CO (6-3) bandhead and the Si I absorption line are included. Points are color-coded based on their location within the Antennae. Effective temperatures, calculated using the best fit for the T_{eff} to $\log(W_{1.62}/W_{1.59})$ correlation, are indicated in the solid black lines.

6.2.3 Isolating Supergiants Using $W_{2.29}$

As with $W_{1.62}$ and $W_{1.59}$, $W_{2.29}$ is inversely correlated with effective temperature (see Figure 5a of Origlia et al. (1993) and Figure 9 of Förster Schreiber et al. (2001)). However, while $W_{1.62}$ and $W_{1.59}$ have little variation between giants and supergiants, $W_{2.29}$ is consistently ≈ 5.5Å higher for

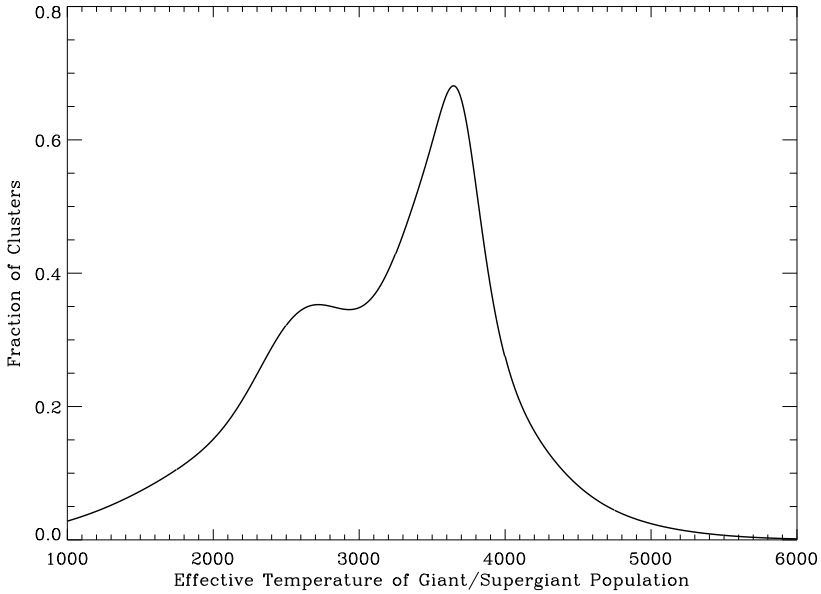

Figure 6.8 Distribution of Effective Temperatures of the Giant/Supergiant Population. Effective temperature is calculated using the ratio of $W_{1.62}$ and $W_{1.59}$. The 14 clusters and 5 nuclear spectra with detections of both the CO (6-3) bandhead and the Si I absorption line at 1.59μm are included in the distribution. For each cluster, a Gaussian temperature distribution with a width set by the 3σ uncertainties in the measurements of $W_{1.62}$ and $W_{1.59}$ was constructed. These individual distributions are summed to produce the effective temperature distribution shown.

Table 6.3. Stellar Properties of Older (> 7–8 Myr) Antennae Clusters

#	CO (6-3) EW	Si I EW	Log of $\frac{\text{CO (6−3) EW}}{\text{Si I EW}}$	Eff. Temp	Min. Dilution	CO (2-0) EW	CO (2-0) EW Dilution Corrected	Supergiants Present?
			(All EWs in Å and Temps in K)					
14	6.2	1.7	0.5	2340	8.9	14.0	23.0	No
17	4.2	2.3	0.2	3421	4.0	17.8	21.8	Yes
51	5.5	3.5	0.1	3641	1.3	14.4	15.8	Yes
53	10.1	2.6	0.5	2188	6.0	14.6	20.6	No
63	8.2	2.8	0.4	2654	5.0	16.0	21.0	No
70	5.2	2.9	0.2	3445	2.8	17.8	20.7	Yes
76	3.0	1.8	0.2	3581	4.2	15.7	20.0	Yes
79	7.2	2.3	0.4	2554	6.5	17.0	23.6	Yes
82	5.7	3.6	0.2	3592	1.4	18.4	19.8	Yes
85	6.0	3.7	0.2	3561	1.3	16.8	18.1	Yes
100	6.0	3.2	0.2	3371	2.5	17.6	20.2	Yes
104	5.7	3.8	0.1	3702	0.6	16.6	17.3	Yes
108	3.9	2.9	0.1	3894	1.2	15.1	16.4	Yes
109	5.7	3.8	0.1	3702	0.6	16.6	17.3	Yes
4039 Nucl	4.5	2.9	0.1	3677	2.1	10.8	12.9	No
4039 Nucl SE	4.1	1.5	0.4	2747	8.4	9.3	17.8	No
4039 Nucl NW	3.4	1.6	0.3	3215	6.2	11.7	17.9	No
4038 Nucl S	4.5	2.7	0.2	3578	2.7	8.1	10.8	No
4038 Nucl	3.4	2.3	0.1	3706	3.0	10.3	13.3	No

supergiants than for giants at every effective temperature. Because of dust dilution we are not able to distinguish between a giant and supergiant population based on the $W_{2.29}$ value alone. However, using the effective temperatures measured from the ratio of $W_{1.62}$ to $W_{1.59}$, we can estimate the dust dilution in the H band by calculating the deficit in the observed $W_{1.62}$ value compared with the predicted value based on the cluster effective temperature. Dust dilution will be greater in K band than in H band, so we can take the dust dilution value measured from $W_{1.62}$ as a minimum value. If the $W_{2.29}$ values, corrected for the minimum dust dilution, lie above the values predicted for a giant population, then supergiants must be present within the cluster.

6.2.4 Supergiants in the Antennae Clusters

The measured $W_{1.62}$ values for the 14 clusters and the 5 nuclear regions all fall below the predicted values (Figure 6.9), indicating at least some dust dilution in the H band. Ignoring the four clusters and one nuclear region observation with low effective temperatures (< 3000 K), the average deficit in $W_{1.62}$ from dust dilution is 2.5Å. Nuclear regions have on average a larger H band dilution, which is not surprising given the large molecular gas concentration on the nuclei (Wilson et al., 2000, 2003a). Minimum dilution values for each cluster are listed in Table 6.3.

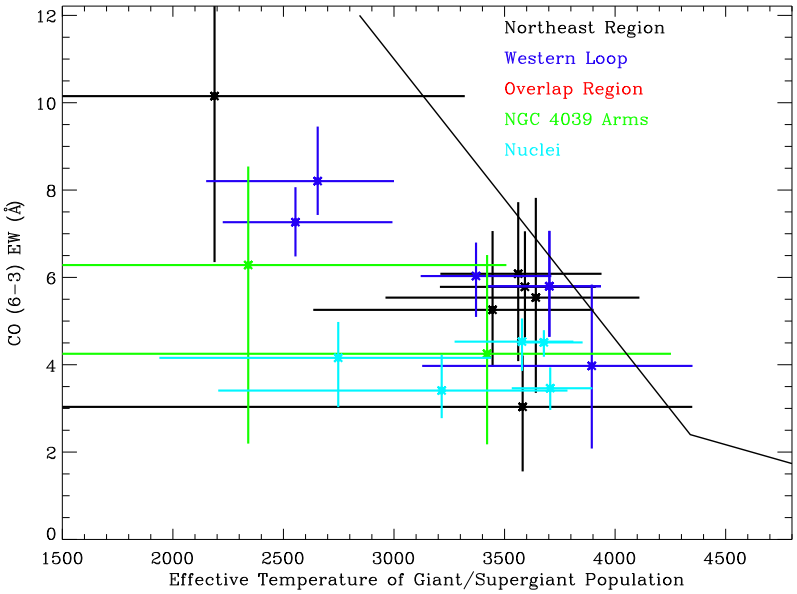

Figure 6.9 Effective Temperature Versus $W_{1.62}$. Effective temperatures are measured using the ratio of $W_{1.62}$ and $W_{1.59}$. Clusters are color-coded based on their location in the Antennae. The solid black line is the predicted variation of $W_{1.62}$ with effective temperature, derived from Förster Schreiber (2000). Clusters falling below this black line suffer from H band dilution from dust emission.
.

In Figure 6.10 we plot effective temperature versus $W_{2.29}$ for the 14 clusters and 5 nuclear regions after correcting for the minimum dust dilution. Also plotted are the best fit lines for the variation

in $W_{2.29}$ with effective temperature for giants and supergiants. The measured and dilution-corrected minimum values for $W_{2.29}$ are listed in Table 6.3. In total, 11 of the 14 clusters, including all six of the northeast region clusters, have values of $W_{2.29}$ corrected for dilution that suggest a supergiant population (Table 6.3). The $W_{2.29}$ values for the nuclear regions, which are measured to be quite low, suffer from large amounts of dust dilution, and are brought into agreement with the expected widths of M giants after accounting for the minimum dust dilution.

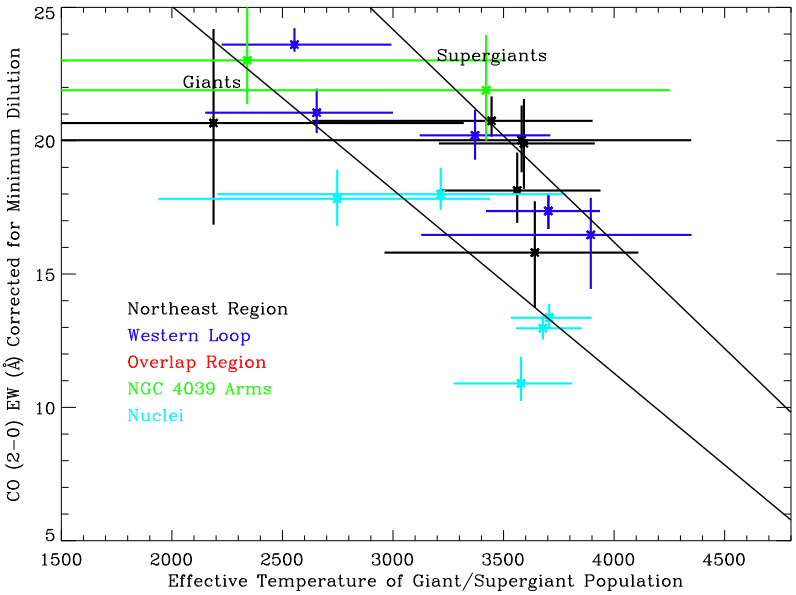

Figure 6.10 Effective Temperature Versus $W_{2.29}$ Corrected for the Minimum Dust Dilution. Clusters are color-coded based on their location in the Antennae. The two solid black lines are the predicted variation of $W_{2.29}$ with effective temperature for giant and supergiant populations, derived from Förster Schreiber (2000): $W_{2.29}$(Å) = 38.8 - 6.88 $\times$ 10^{-3} T_{eff} for giants and $W_{2.29}$(Å) = 48.1 - 7.98 $\times$ 10^{-3} T_{eff} for supergiants. The dust dilution is more severe in K band than H band, so the $W_{2.29}$ values in the bottom plot are lower limits.

We therefore find substantial evidence that many of the older (> 8 Myr) clusters contain populations of M2–M4 supergiants, while some clusters and the nuclear regions may contain primarily giant populations. Since the dilution correction applied is a minimal value, clusters whose dilution corrected values of $W_{2.29}$ fall in the giant range may actually contain supergiants as well if the K band dilution is more than a few angstroms greater than the H band dilution.

Chapter 7

Conclusions: Implications for Cluster Formation and Survival

7.1 Summary of Results

7.1.1 Cluster Sample and Observations

In this study of cluster formation in the Antennae, we have obtained a combination of near-infrared and optical spectra for 117 clusters and 8 regions near the two nuclei. Optical spectra typically covered a wavelength range from 3000 to 9000Å, while near-infrared spectra covered most of the H (1.55–1.78μm) and K (2.06–2.47μm) bands. Near-infrared and optical spectra were obtained for 35 clusters, while 75 clusters had only optical spectra and 7 had only near-infrared spectra.

The initial sample of clusters was selected from a Ks band image of the Antennae taken by Brandl et al. (2005). We sampled almost 70% of clusters with $M_{Ks} < -15.5$ and more than 60% of clusters with M_{Ks} between -15.5 and -15. A smaller fraction of the less-luminous clusters was observed. 60 of the 117 clusters in our survey were originally identified by SExtractor in the Brandl et al. (2005) image, while 57 were discovered during spectroscopy.

The clusters in our sample were selected to sample four known areas of active star formation within the Antennae: 1) The western loop, immediately to the west of the NGC 4038 nucleus; 2) The northeast region, to the east of the NGC 4038 nucleus; 3) The overlap region between the two nuclei where the galactic disks overlap; 4) The NGC 4039 arms region along the spiral arms of NGC 4039 and near the NGC 4039 nucleus. Roughly equal numbers of clusters were observed in each of these four regions (see Figure 4.11) in order to allow us to compare cluster properties by location.

7.1.2 Updated Star Formation Profile

Measurements of the equivalent widths of six key diagnostic lines in the clusters were compared with models from Starburst99 to determine ages for each cluster. Three hydrogen recombination lines

trace the youngest cluster ages ($<$ 10Myr), while two CO absorption bandheads, produced by giant and supergiant populations in a cluster trace an older ($>$ 8 Myr) population. Every cluster we detected with a CO absorption bandhead also had significant hydrogen recombination lines, causing difficulty in determining ages for the clusters because from Starburst99 models for an instantaneous burst, CO bandheads and hydrogen lines should not be seen at the same time.

To resolve this difficulty, we propose a new cluster formation scenario: a 5 Myr duration constant rate burst of star formation. This 5 Myr duration burst profile delays the disappearance of the hydrogen recombination lines until 8–10 Myr, by which time the CO bandheads have developed (see middle plot of Figure 3.2). Using this new burst profile, we saw a doubling in the number of clusters where a coherent age could be derived using all of the observed diagnostic lines, compared with the instantaneous burst model.

7.1.3 Age Distribution

Ages have been determined for 107 of the 117 clusters in our sample as well as for 8 regions near the nuclei. Examining the distribution of cluster ages (Figure 4.8), we find that all clusters in our sample are less than 23 Myr in age. The age distribution lies roughly between 3 and 17 Myr with a strong peak around 8.5 Myr and secondary peaks at 4.8 and 10 Myr.

We have examined the role that selection effects (particularly the evolution of cluster K and V band luminosities) play in our observed cluster distribution and find we are sensitive to clusters between 3 and 20 Myr. Based on this, we conclude that the age distribution is not uniform, but rather has a deficit of clusters with ages from 3 to 7 Myr and 12 to 20 Myr.

Figure 4.12 shows the cluster age distributions for the four different regions within the Antennae. Very clear differences exist between the regions (Table 7.1). The youngest clusters are found in the overlap region, while the oldest clusters are in the NGC 4039 arms region. The northeast region has two distinct age populations (8 and 10–12 Myr) and these two regions are spatially separated. Even though the regions all have different age distributions, it is important to emphasize that the variations are not large. Each region still peaks between 7.5 and 12 Myr. This is somewhat unexpected as the overlap region has been considered previously to contain significantly younger clusters than the remainder of the Antennae. Statistical analysis (Table 4.4) shows that the age populations of the overlap region and NGC 4039 arms region are statistically distinct from each other and from the populations of the northeast region and western loop.

Our improved spatial resolution CO (1-0) maps of the Antennae allow us to compare cluster ages with the molecular gas distribution. The largest concentration of molecular gas falls in the overlap region, although we tend to see the molecular gas peaks slightly offset from cluster locations. Perhaps even younger clusters are still enshrouded within the molecular clouds and we are seeing the clusters that have had time to consume and expel the molecular gas from their immediate vicinity. We find

Table 7.1. Cluster Age Distributions for Antennae Regions

Region	Description of Cluster Ages
Overlap Region	Peak near 7.5 Myr; More clusters < 6 Myr than any other region.
Western Loop	Peak near 8.5 Myr; Slightly older than the overlap region.
Northeast Region	Two age peaks in different locations: 8 Myr (western part) and 10–12 Myr (eastern part)
NGC 4039 Arms	Oldest region with peak around 10 Myr; Only region with > 20 Myr cluster

Table 7.2. Cluster Mass Distributions for Antennae Regions

Region	Description of Cluster Masses
Overlap Region	No clear peak; Contains most of high mass ($> 10^6$ $M_\odot$) clusters
Western Loop	Strong peak at 4×10^5 $M_\odot$
Northeast Region	Broad distribution from 1.5×10^5 to 10^6 $M_\odot$
NGC 4039 Arms	Least massive clusters; All but 2 clusters with masses $< 3 \times 10^5$ $M_\odot$

a substantial molecular gas distribution also in the NGC 4039 arms region and the western loop but uncover very little CO (1-0) emission in the northeast region, except near the youngest clusters.

7.1.4 Mass Distribution

Using our age estimates, cluster luminosity evolution models modified for a 5 Myr duration burst, Ks band photometry from Brandl et al. (2005), and our own extinction estimates, we have measured photometric masses for 73 of the 117 clusters in our sample. We find a median cluster mass of 4×10^5 $M_\odot$ with most masses (79%) between 10^5 and 10^6 $M_\odot$. We find clear differences in the mass distributions with location (Table 7.2). The overlap region contains the most massive clusters, particularly in the southern part of the region closest to the large CO (1-0) gas concentration. In contrast, the NGC 4039 arms region has the least massive clusters. The mass distributions of the western loop and northeast region are consistent with being taken from the same population, while they are distinct from the mass distributions of the overlap region and the NGC 4039 arms region. We find a correlation between cluster mass and age with heavier clusters more likely to also be young.

Analyzing the role of selection effects in constructing our mass sample, we find that we are very likely observing almost all of the high-mass clusters in the Antennae. The lack of many clusters with masses $> 10^6$ $M_\odot$ is a true deficit and not a selection effect. In contrast, we find that the lack of low mass ($< 10^5$ $M_\odot$) clusters is due to the small number of low luminosity clusters in our sample.

7.1.5 Extinction

Extinctions were calculated using the ratio of the Hα and Hβ fluxes for 32 clusters and 3 observations of the nuclear regions. Extinctions varied widely from $A_V = 0$ to $A_V = 11.5$ mag, with a median extinction of $A_V = 2.75$ mag. The overlap region had the largest median extinction, more than 3 magnitudes greater than any other region. This is not surprising given the large molecular gas concentration found there. Extinctions in the other three regions are similar to each other. We find a correlation between extinction and cluster age with younger clusters having higher average extinctions.

7.1.6 Metallicity and Giant/Supergiant Populations

We have calculated the metallicity for 86 clusters in the Antennae sample. Two different tracers confirm that metallicities are consistent with solar metallicity throughout the Antennae with the widest local variation in metallicities in the overlap and NGC 4039 arms regions.

Using the CO bandheads and additional near-infrared absorption lines we have measured the underlying giant and supergiant population of 14 clusters. We find that the giant and supergiant population of the majority of these clusters is consistent with a spectral type of M2–M4 and that 11 of the 14 clusters have strong evidence for a supergiant population.

7.2 Implications for Cluster Formation and Survival

Our survey allows us the opportunity to reevaluate many of the assumptions that have been made about star cluster formation, both in the Antennae and in general. In this section we will specifically consider the implications of a 5 Myr duration star formation burst model for clusters and discuss the insights into cluster disruption and survival that can be derived from our cluster age and mass distributions. As a framework for this discussion, it is important to consider first the differences in this work compared with previous studies of the Antennae, most notably Whitmore et al. (1999) and Mengel et al. (2005).

As our study relies on spectroscopy instead of broad-band and narrow-band imaging, we are unable to include as many clusters as other studies. Indeed, the samples of Whitmore et al. (1999) and Mengel et al. (2005) both include over 1000 clusters, compared with 117 in our observations. Because of the larger sample size, coverage of the entire Antennae with their observations, and the ability to derive completeness limits, these studies can make stronger claims about the age and luminosity distributions of the entire sample without as much difficulty from selection effects. Additionally, the spatial resolution of the HST observations of Whitmore et al. (1999) are better than our own observations, allowing them to make measurements of cluster sizes and reducing the

likelihood of the blending of multiple clusters. Our spatial resolution is similar to the resolution of Mengel et al. (2005).

On the other hand, by using spectroscopy we are able to directly measure the equivalent widths of key diagnostic lines. While some previous studies have used narrow-band imaging to measure a few of these diagnostic lines, with spectroscopy we are able to make more accurate equivalent width measurements of a larger number of lines, thus allowing for better determination of cluster properties. For instance, we can directly calculate extinction using the ratio of the Hα and Hβ lines without relying on any population synthesis models. Additionally, the analysis of giant and supergiant populations in clusters could only be undertaken with near-infrared spectroscopy. With the equivalent width samples taken from spectroscopy, we are able to better constrain cluster ages and uncover discrepancies (such as the simultaneous presence of CO bandheads and hydrogen lines) that force a reevaluation of the assumptions of the cluster models.

We believe our sample represents a happy median between large photometric surveys and individual, more detailed spectroscopic surveys of a few clusters (e.g., Gilbert & Graham, 2007; Mengel et al., 2001). Large photometric surveys are not able to consider the properties of individual clusters in as much detail, while individual spectroscopic surveys provide very accurate cluster measurements but do not provide a large sample to examine variation in properties with location.

7.2.1 Implications of a 5 Myr Duration Burst Model

One unexpected result from our observations was the determination that the measured cluster equivalent widths could not be fit by an instantaneous burst of star formation. All previous studies had assumed the burst to be instantaneous. However we note that many studies were more interested in separating clusters into broad age categories (i.e., < 20 Myr, > 100 Myr, etc.) and for that level of resolution an instantaneous burst would be appropriate. Gilbert & Graham (2007) note for their Cluster F (Cluster 64 in our sample) the simultaneous presence of CO bandheads and hydrogen recombination lines. To explain this, the authors suggest two alternatives: binary star systems in clusters may affect the population synthesis models so as to allow for the simultaneous presence of hydrogen recombination lines and CO bandheads; or star formation may not be instantaneous in a cluster. Our observations support their suggestion of non-instantaneous star formation within a cluster.

Such non-instantaneous cluster formation has been observed in systems besides the Antennae (Gilbert & Graham, 2007). Satyapal et al. (1997) found within the inner 500 parsecs of M82 that cluster formation was not simultaneous but rather propagated from the center of the galaxy outward over a time period of 6 Myr. At the distance of the Antennae, 500 parsecs is less than $6''$. Closer to the Milky Way, R136 at the center of 30 Doradus contains low-mass stars that are 4–5 Myr old compared with high-mass stars of 1–2 Myr age (Massey & Hunter, 1998). Hodge 301, also

part of 30 Doradus but located 45 parsecs from R136, is approximately 20–25 Myr old (Grebel & Chu, 2000). At the distance of the Antennae, the separation between R136 and Hodge 301 would be approximately 0.5″, barely separable by our observations.

Two questions emerge from this discussion: In the Antennae are we always seeing a single cluster that takes 5 Myr to form (such as in R136) or are we also occasionally seeing the superposition of two or more clusters with small age differences that creates the effect of a 5 Myr duration burst of star formation (such as seeing R136 and Hodge 301 at the distance of the Antennae)? If we are seeing a 5 Myr duration burst of star formation, how can the burst be maintained for 5 Myr without massive stars clearing out the dust and gas and stopping additional star formation?

7.2.1.1 Possible Role of the Superposition of Clusters

In §4.4.3 we discussed in great detail the differences between the superposition of clusters model and the non-instantaneous burst of star formation model and concluded that the 5 Myr duration burst best fit the observed equivalent widths for our sample. However, we cannot dismiss the possibility that we may be seeing a combination of both models at work within the Antennae. Mengel et al. (2005) estimate that less than 5% of their clusters with masses larger than 10^5 $M_\odot$ are actually superpositions of clusters. However, as discussed in §2.4.2.2 we aligned each of our LRIS slits on top of the HST images from Whitmore et al. (1999) and found very different results for our sample. Of the 100 clusters which were aligned with HST images we found that 53 had multiple clusters, unresolved at the spatial resolution of our observations, within the slit. Comparing with the mass cutoff of Mengel et al. (2005), we find that 32 of 60 (53%) of clusters with masses larger than 10^5 $M_\odot$ were multiple clusters.

However, examining the 38 clusters that show both hydrogen recombination lines and CO bandheads, 19 of these were multiple clusters based on the HST imaging, while 19 are isolated clusters. If the simultaneous detection of hydrogen lines and CO bandheads was the result of a superposition of clusters alone then we would expect that the rate of multiple clusters to be higher for clusters showing bandheads and hydrogen lines, but instead we find it at the same rate as the entire cluster sample. Therefore, there is still strong evidence for a non-instantaneous burst of star formation with the possibility that for a minority of our clusters we may be seeing a superposition of two instantaneous bursts instead.

After extensive testing we also found that the best model to describe the observed equivalent widths across the Antennae was the 5 Myr duration burst. We did not have a large enough sample to consider whether the best-fit burst length might change with location in the Antennae or whether there were some regions in the system that were better described by a superposition model. CO bandhead observations are necessary to test for star formation models because the hydrogen recombination lines predict the same age regardless of the model assumed. More detailed modeling of the

evolution of diagnostic lines as well as increased near-infrared spectroscopy to test for the presence of CO bandheads in a larger number of clusters will help shed much more insight into the cluster formation process. We can conclude, however, that a non-instantaneous burst of star formation within a cluster IS necessary to explain the equivalent widths seen for a majority of clusters in our sample.

7.2.1.2 Producing a 5 Myr Burst

Assuming that star formation occurs over approximately a 5 Myr time frame in a large number of clusters, an important question remains as to how star formation can last for 5 Myr. With a Salpeter IMF, clusters heavier than 10^4 $M_\odot$ are populated with O stars. These high mass stars have winds sufficient to disrupt the remaining molecular gas in a cloud, thus halting star formation (Scoville et al., 2001). If we assume constant star formation within a cluster for the duration of the 5 Myr burst, then any cluster with a final mass larger than 10^5 $M_\odot$ should have O stars appear within the first Myr.

For the case of R136, the 4–5 Myr old stars tend to be low-mass stars while the high-mass stars are preferentially in the 1–2 Myr age range (Massey & Hunter, 1998). The late formation of massive stars prevents the disruption of the molecular cloud until later in the star formation process. Our 5 Myr burst models were constructed on the basis of equal amounts of star formation (at all stellar masses) throughout the 5 Myr. Delaying the high-mass star formation until the end of the cluster formation period will not solve the problem of the simultaneous presence of CO bandheads and hydrogen recombination lines. The evolution of both the hydrogen lines and the CO bandheads is driven by the most massive stars in a cluster, as massive stars have the greatest number of ionizing photons leading to the recombination lines and massive stars will be the first to form giants and supergiants, accounting for the CO bandheads.

One possible mechanism for a 5 Myr duration burst profile for cluster formation is that the disruption rate of the molecular gas is slow. Approximately 6 Myr is required for clusters to blow off enough gas to reduce observed extinctions to $A_V = 1$ (Whitmore & Zhang, 2002; Brandl et al., 2005). This is based on the assumption of an instantaneous burst. However, if the star formation in a cluster is spread out over 5 Myr then the disruption will take longer, as the birth of massive clusters is also spread out. This delayed disruption will allow for greater star formation before the molecular gas is completely dispersed.

Additionally, we have been working under the assumption that star formation is uniformly distributed within the cluster. However, at a sound speed of 6 km s^{-1}, typical for a young star cluster (Fall et al., 2005), the crossing time of the cluster is on the order of 1 Myr. Therefore, it is possible that star formation may not occur everywhere throughout the cluster for the 5 Myr, but rather may travel through the cluster through triggered star formation (such as seen by Satyapal

et al. (1997) for M82). The effects of winds from O stars, then, would be focused only on the parts of the cloud that had already undergone star formation and not the other parts of the cloud. In fact the winds could actually trigger star formation in other parts of the cloud. Scoville et al. (2001) suggest that after the initial star formation in a cluster an additional wave of star formation may occur, triggered by the shell of gas and dust expelled by the winds of massive stars in the cluster. This additional star formation could help increase the stellar mass of the resulting cluster and allow for star formation to proceed for 5 Myr. Interestingly, the locations within a cluster where massive stars form may also help determine whether a cluster will survive or be disrupted (Fall et al., 2005). Also, on the scales that we are considering it is possible that star formation occurs individually in small clusters within a molecular cloud. Each cluster is below the mass limit set by the presence of O stars, but the merger of these clusters could produce the massive clusters found in systems like the Antennae (Scoville et al., 2001). At our spatial resolution of the Antennae, it is possible that the formation of multiple clusters within one molecular cloud might mimic a short-duration burst of star formation.

Further analysis and modeling is necessary to see precisely how delayed disruption by O stars, triggered star formation within the cluster, and the formation of multiple clusters within a molecular cloud would affect the gas content of the molecular cloud and the final mass of a star cluster.

7.2.2 Evidence for a Truncation of the Cluster Initial Mass Function

As discussed in the introduction, some studies have suggested that the cluster initial mass function (CIMF) is truncated at the high-mass end (Gieles et al., 2006a,b). They suggest that this truncation is seen even in the progenitor molecular clouds. Molecular clouds in the Milky Way have a sharp mass cutoff above $6\times\ 10^6$ $M_\odot$ (Williams & McKee, 1997), although galaxies with larger molecular gas concentrations will show a truncation at higher masses (Wilson et al., 2003a). Scoville et al. (2001) find an upper mass limit for clusters in M51 of a few thousand $M_\odot$ but suggest that more massive clusters may be formed via propagating star formation within a molecular cloud or the combination of multiple lower-mass clusters within the molecular cloud. For the Antennae, Gieles et al. (2006b) suggest a truncation in the cluster mass distribution at $4\times\ 10^5$ $M_\odot$. We do see a turnover in the mass function around this mass, suggesting that there may be some truncation. However, as we discussed earlier (§5.2.6) the selection effects on mass are too great in our survey to determine whether a true mass turnover exists at $4\times\ 10^5$ $M_\odot$.

7.2.3 Spatial Differences in Cluster Properties and Implications for Formation Mechanisms and Disruption of Clusters

As discussed in §4.7.2 and §5.2.4 there is significant, statistical variation in the age and mass distributions of clusters in different parts of the Antennae. The western loop and the northeast region have similar age clusters and similar mass distributions. However, the NGC 4039 arms region has older clusters and smaller masses on average, while the overlap region has younger clusters and larger masses on average. Each region was sampled by at least 16 clusters.

7.2.3.1 Mass Distribution

Recent studies have argued for a uniform cluster initial mass function (CIMF) for both starburst/interacting galaxies and quiescent galaxies (e.g., Elmegreen & Efremov, 1997; Whitmore, 2003; Larsen, 2002). While these authors discussed only galaxies as a whole, at first glance it would seem reasonable that the CIMF would also be uniform across different regions of a galaxy. We do not find this in our observations, however, as a significant difference in cluster masses exists between different locations. We believe, however, that this may be the result of selection effects. Our sample was selected to sample similar numbers of clusters in each region of the Antennae. If the CIMF is universal within the Antennae, then we expect that the region producing the most clusters would have, on average, the highest cluster masses. The overlap region appears to be producing the greatest number of clusters, based on not only optical and near-infrared studies (Whitmore et al., 1999; Brandl et al., 2005; Mengel et al., 2005), but also the distributions of molecular gas (Wilson et al., 2000) and mid-IR emission (Mirabel et al., 1998), while the NGC 4039 arms region produces the fewest number of clusters. Indeed, this region was only identified as a secondary-level star forming knot in the original survey (Rubin et al., 1970) and HST images (Whitmore et al., 1999). The overlap region has the most clusters overall and is the most massive, while the NGC 4039 arms region has the fewest clusters and is the least massive, supporting the possibility of a universal CIMF within the Antennae. As we do not sample a large enough fraction of clusters in any of the regions it is impossible to evaluate a possible shape to the CIMF.

7.2.3.2 Age Distribution

It is difficult to imagine a scenario where the ages in the four spatial regions are statistically distinct but yet differ by only a few Myr. For all four regions there appear to be mostly young clusters with ages < 15 Myr, suggesting a recent burst of cluster formation throughout the Antennae. However, dynamical times for the entire system are on the order of 100 Myr (Mengel et al., 2005; Fall et al., 2005), making it challenging to find a physical process that could produce a common burst throughout the system. Even on the scale of the individual star forming regions, we cannot explain the

common burst age seen. Dynamical times across each of the star forming regions are on the order of 20–30 Myr, much larger than the age spread seen in any of the regions. Mengel et al. (2005) and Fall et al. (2005) suggest that instead of a burst of cluster formation, cluster formation has been fairly constant for the past 100 Myr in the Antennae and that the large number of young clusters is actually a sign that a substantial fraction of clusters are disrupted within the first 10–15 Myr. However, if the large number of young clusters is in fact because of the fast disruption of clusters, then an explanation is still needed for the slight differences in age between the Antennae regions.

It is more difficult to ascribe all of the differences between the ages of the regions to selection effects. If clusters are continuously forming throughout the Antennae and the rate of disruption was uniform in each region then we would expect the age distributions to be similar between the regions. Even if fewer clusters were forming in the NGC 4039 arms region we would still expect as many young clusters as in other regions. Instead, clusters younger than 4 Myr are found in every region except for the NGC 4039 arms region, where the youngest cluster is around 7.5 Myr. This discrepancy can not be explained because of the lower masses in the NGC 4039 arms region because the cluster disruption rate is expected to be independent of mass for clusters < 20 Myr (Fall et al., 2005). We do note, however, that we found a slight trend for higher masses amongst younger clusters (Figure 5.10). Even though more massive clusters exist, for instance, in the overlap region, and more massive clusters are more easily detected, we would expect massive clusters to be spread out throughout the age distribution of the region and not just among younger clusters.

The best explanation that we can derive for the slight differences in age distributions between the regions in the Antennae is that disruption rates differ. If clusters were disrupted less in the NGC 4039 arms region then more would survive to the 8–20 Myr age range where they are more likely to be observed because of their enhanced luminosity. The lack of the older population in regions such as the overlap region suggest that clusters are disrupted more quickly in these regions. While it is speculation, one possible reason for the enhanced disruption rate is the increased cluster formation rate in the overlap region. The effects of star formation may speed up the disruption of clusters.

7.3 Future Directions

Understanding the formation and evolution of massive star clusters is of tremendous import not only to those who study interacting and merging systems, where these star clusters are most prevalent, but also to those studying star and cluster formation in more quiescent galaxies. Recent evidence suggests that the cluster formation processes may be similar across many different environments, from normal spiral galaxies to starbursts and violently interacting systems. This discovery only strengthens the need for additional studies of massive star clusters as a means of understanding star formation in general.

Merging and interacting systems are an ideal laboratory to study the properties of massive star clusters, owing to their rich population of clusters. On the other hand there are some inherent drawbacks to studying these systems and to building up a database of cluster properties for a large number of mergers. The distance to most mergers is great enough that even at the resolution of the best ground-based telescopes the superposition or blending of clusters has to be overcome. Space-based observations can overcome these spatial resolution difficulties for the closest merging systems (like the Antennae) but even telescopes in space run into difficulties studying the cluster populations of more distant merging systems (see the luminous infrared galaxies, for example, in Scoville et al. (2000)).

This study has shown, we believe, the value of focusing on large samples of clusters within a system rather than focusing on only the brightest clusters or clusters within one part of a system. By examining clusters throughout a system, differences in properties—particularly mass and age—are revealed; these differences are critical in determining how cluster formation and disruption mechanisms vary with environment. This study has also shown, we believe, the value of spectroscopic observations in measuring the properties of clusters. The strengths of emission and absorption features within these clusters gives a stronger measurement of cluster ages, masses, and extinctions than are obtained from only photometric studies. However, obtaining large spectroscopic samples of clusters within a system is, of course, very time-intensive, placing serious constraints on the sample sizes possible.

While much more observationally time-intensive, high-spectral-resolution spectroscopy is also very much needed. This spectroscopy is the only way to measure the mass of a cluster without relying on modeling or assumptions about the initial mass function within a cluster, and thus allows for an examination of the initial stellar mass function of a cluster. For example, McCrady et al. (2005) found evidence for a deficiency of low-mass stars in one cluster in the M82 and Mengel et al. (2002) found possible variations with location in the initial mass function of five clusters in the Antennae.

The quality of age and mass estimates for clusters, even in a spectroscopic sample, are limited by the population synthesis models. These models are constantly being refined, as evidenced by the 2005 update to Starburst99 (Vázquez & Leitherer, 2005) and the new models of Bruzual & Charlot (2003). Known difficulties still exist in modeling specific stellar populations, including red supergiants (Vázquez & Leitherer, 2005).

With improved telescope technology in the coming years, significant strides can be made in the study of massive star clusters. Larger spectroscopic surveys will be possible and with the increase in adaptive optics equipped telescopes, high-spatial-resolution observations can be taken from the ground of more distant systems, reducing the concern of a superposition or blending of clusters. Improved population synthesis models will allow for more accurate age and mass determinations. These

developments will lead to much larger and more accurate surveys of cluster systems, which in turn will allow for much greater insight into key questions of cluster formation and disruption, including the universality of cluster formation processes across a range of galaxies from quiescent spirals to mergers, the nature of cluster disruption, and the role that environment plays in disruption.

Bibliography

Alloin, D., Collin-Souffrin, S., Joly, M., & Vigroux, L. 1979, A&A, 78, 200

Amram, P., Marcelin, M., Boulesteix, J., & Le Coarer, E. 1992, A&A, 266, 106

Arp, H. & Sandage, A. 1985, AJ, 90, 1163

Ashman, K. M. & Zepf, S. E. 1992, ApJ, 384, 50

Barnes, J. E. 1988, ApJ, 331, 699

Bastian, N., Emsellem, E., Kissler-Patig, M., & Maraston, C. 2006, A&A, 445, 471

Battinelli, P., Brandimarti, A., & Capuzzo-Dolcetta, R. 1994, A&AS, 104, 379

Bekki, K., Beasley, M. A., Forbes, D. A., & Couch, W. J. 2004, ApJ, 602, 730

Bertin, E. & Arnouts, S. 1996, A&AS, 117, 393

Bik, A., Lamers, H. J. G. L. M., Bastian, N., Panagia, N., & Romaniello, M. 2003, A&A, 397, 473

Brandl, B. R., Clark, D. M., Eikenberry, S. S., Wilson, J. C., Henderson, C. P., Barry, D. J., Houck, J. R., Carson, J. C., & Hayward, T. L. 2005, ApJ, 635, 280

Brodie, J. P. & Strader, J. 2006, ARA&A, 44, 193

Bruch, A. & Sanders, W. L. 1983, A&A, 121, 237

Bruzual, G. & Charlot, S. 1993, ApJ, 405, 538

—. 2003, MNRAS, 344, 1000

Burbidge, E. M. & Burbidge, G. R. 1966, ApJ, 145, 661

Cardelli, J. A., Clayton, G. C., & Mathis, J. S. 1989, ApJ, 345, 245

Carlson, M. N., Holtzman, J. A., Watson, A. M., Grillmair, C. J., Mould, J. R., Ballester, G. E., Burrows, C. J., Clarke, J. T., Crisp, D., Evans, R. W., Gallagher, III, J. S., Griffiths, R. E., Hester, J. J., Hoessel, J. G., Scowen, P. A., Stapelfeldt, K. R., Trauger, J. T., & Westphal, J. A. 1998, AJ, 115, 1778

Carollo, C. M., Stiavelli, M., de Zeeuw, P. T., & Mack, J. 1997, AJ, 114, 2366

Chandar, R., Leitherer, C., Tremonti, C. A., Calzetti, D., Aloisi, A., Meurer, G. R., & de Mello, D. 2005, ApJ, 628, 210

Charbonnel, C., Meynet, G., Maeder, A., Schaller, G., & Schaerer, D. 1993, A&AS, 101, 415

Clark, D. M., Christopher, M. H., Eikenberry, S. S., Brandl, B. R., Wilson, J. C., Carson, J. C., Henderson, C. P., Hayward, T. L., Barry, D. J., Ptak, A. F., & Colbert, E. J. M. 2005, ApJ, 631, L109

Clark, D. M., Eikenberry, S. S., Brandl, B. R., Wilson, J. C., Carson, J. C., Henderson, C. P., Hayward, T. L., Barry, D. J., Ptak, A. F., & Colbert, E. J. M. 2007, ApJ, 658, 319

Cote, P., Marzke, R. O., & West, M. J. 1998, ApJ, 501, 554

Dallier, R., Boisson, C., & Joly, M. 1996, A&AS, 116, 239

de Grijs, R., Anders, P., Bastian, N., Lynds, R., Lamers, H. J. G. L. M., & O'Neil, E. J. 2003a, MNRAS, 343, 1285

de Grijs, R., Fritze-v. Alvensleben, U., Anders, P., Gallagher, J. S., Bastian, N., Taylor, V. A., & Windhorst, R. A. 2003b, MNRAS, 342, 259

Denicoló, G., Terlevich, R., & Terlevich, E. 2002, MNRAS, 330, 69

Diaz, A. I., Terlevich, E., & Terlevich, R. 1989, MNRAS, 239, 325

Dyson, J. E. & Williams, D. A. 1997, The physics of the interstellar medium (The physics of the interstellar medium. Edition: 2nd ed. Publisher: Bristol: Institute of Physics Publishing, 1997. Edited by J. E. Dyson and D. A. Williams. Series: The graduate series in astronomy. ISBN: 0750303069)

Elmegreen, B. G. 1983, MNRAS, 203, 1011

Elmegreen, B. G. & Efremov, Y. N. 1997, ApJ, 480, 235

Evans, R., Harper, A., & Helou, G. 1997, in Extragalactic Astronomy in the Infrared, ed. G. A. Mamon, T. X. Thuan, & J. Tran Thanh van, 143–+

Fabbiano, G., Krauss, M., Zezas, A., Rots, A., & Neff, S. 2003, ApJ, 598, 272

Fabbiano, G., Zezas, A., & Murray, S. S. 2001, ApJ, 554, 1035

Fagotto, F., Bressan, A., Bertelli, G., & Chiosi, C. 1994, A&AS, 105, 29

Fall, S. M. 2004, in Astronomical Society of the Pacific Conference Series, Vol. 322, The Formation and Evolution of Massive Young Star Clusters, ed. H. J. G. L. M. Lamers, L. J. Smith, & A. Nota, 399–+

Fall, S. M. 2006, ApJ, 652, 1129

Fall, S. M., Chandar, R., & Whitmore, B. C. 2005, ApJ, 631, L133

Fall, S. M. & Zhang, Q. 2001, ApJ, 561, 751

Fischer, J., Shier, L. M., Luhman, M. L., Satyapal, S., Smith, H. A., Stacey, G. J., Unger, S. J., Greenhouse, M. A., Spinoglio, L., Malkan, M. A., Lord, S. D., Miles, J. W., Shure, M. A., Clegg, P. E., Ade, P. A. R., Armand, C., Burgdorf, M., Church, S. E., Davis, G. R., di Giorgio, A., Ewart, D., Furniss, I., Glencross, W. M., Gry, C., Lim, T., Molinari, S., Nguyen-Q-Rieu, Price, M. C., Sidher, S. D., Smith, A., Swinyard, B. M., Texier, D., Trams, N. R., & Wolfire, M. G. 1996, A&A, 315, L97

Forbes, D. A., Brodie, J. P., & Grillmair, C. J. 1997, AJ, 113, 1652

Förster Schreiber, N. M. 2000, AJ, 120, 2089

Förster Schreiber, N. M., Genzel, R., Lutz, D., Kunze, D., & Sternberg, A. 2001, ApJ, 552, 544

Gallagher, J. S. & Smith, L. J. 2004, in Astronomical Society of the Pacific Conference Series, Vol. 322, The Formation and Evolution of Massive Young Star Clusters, ed. H. J. G. L. M. Lamers, L. J. Smith, & A. Nota, 149–+

Garcia-Vargas, M. L., Molla, M., & Bressan, A. 1998, A&AS, 130, 513

Gebhardt, K. & Kissler-Patig, M. 1999, AJ, 118, 1526

Gieles, M., Larsen, S. S., Bastian, N., & Stein, I. T. 2006a, A&A, 450, 129

Gieles, M., Larsen, S. S., Scheepmaker, R. A., Bastian, N., Haas, M. R., & Lamers, H. J. G. L. M. 2006b, A&A, 446, L9

Gilbert, A. M. 2002, Ph.D. Thesis

Gilbert, A. M. & Graham, J. R. 2007, ApJ, 668, 168

Gilbert, A. M., Graham, J. R., McLean, I. S., Becklin, E. E., Figer, D. F., Larkin, J. E., Levenson, N. A., Teplitz, H. I., & Wilcox, M. K. 2000, ApJ, 533, L57

Glass, I. S. 1999, Highlights of Astronomy

Grebel, E. K. & Chu, Y.-H. 2000, AJ, 119, 787

Harris, W. E. 2001, in Saas-Fee Advanced Course 28: Star Clusters, ed. L. Labhardt & B. Binggeli, 223–+

Hibbard, J. E., van der Hulst, J. M., Barnes, J. E., & Rich, R. M. 2001, AJ, 122, 2969

Hills, J. G. 1980, ApJ, 235, 986

Ho, L. C. 1997, in Revista Mexicana de Astronomia y Astrofisica Conference Series, Vol. 6, Revista Mexicana de Astronomia y Astrofisica Conference Series, ed. J. Franco, R. Terlevich, & A. Serrano, 5–+

Holtzman, J. A., Faber, S. M., Shaya, E. J., Lauer, T. R., Groth, J., Hunter, D. A., Baum, W. A., Ewald, S. P., Hester, J. J., Light, R. M., Lynds, C. R., O'Neil, Jr., E. J., & Westphal, J. A. 1992, AJ, 103, 691

Irwin, J. A. 1994, ApJ, 429, 618

Jog, C. J. & Solomon, P. M. 1992, ApJ, 387, 152

Kassin, S. A., Frogel, J. A., Pogge, R. W., Tiede, G. P., & Sellgren, K. 2003, AJ, 126, 1276

Kissler-Patig, M. 2000, in Reviews in Modern Astronomy, Vol. 13, Reviews in Modern Astronomy, ed. R. E. Schielicke, 13–+

Kleinmann, S. G. & Hall, D. N. B. 1986, ApJS, 62, 501

Kumai, Y., Basu, B., & Fujimoto, M. 1993, ApJ, 404, 144

Kundu, A. & Whitmore, B. C. 2001, AJ, 121, 2950

Kunze, D., Rigopoulou, D., Lutz, D., Egami, E., Feuchtgruber, H., Genzel, R., Spoon, H. W. W., Sturm, E., Sternberg, A., Moorwood, A. F. M., & de Graauw, T. 1996, A&A, 315, L101

Lada, C. J. & Lada, E. A. 2003, ARA&A, 41, 57

Larsen, S. S. 2002, AJ, 124, 1393

—. 2006a, ArXiv Astrophysics e-prints

Larsen, S. S. 2006b, in Planets to Cosmology: Essential Science in the Final Years of the Hubble Space Telescope, ed. M. Livio & S. Casertano, 35–+

Larsen, S. S., Brodie, J. P., Huchra, J. P., Forbes, D. A., & Grillmair, C. J. 2001, AJ, 121, 2974

Larsen, S. S. & Richtler, T. 1999, A&A, 345, 59

—. 2000, A&A, 354, 836

Leitherer, C. & Heckman, T. M. 1995, ApJS, 96, 9

Leitherer, C., Schaerer, D., Goldader, J. D., Delgado, R. M. G., Robert, C., Kune, D. F., de Mello, D. F., Devost, D., & Heckman, T. M. 1999, ApJS, 123, 3

Lejeune, T., Cuisinier, F., & Buser, R. 1997, A&AS, 125, 229

Lo, K. Y., Hwang, C. Y., Lee, S. W., Kim, D.-C., Wang, W. H., Lee, T. H., Gruendl, R., & Gao, Y. 2000, in Astronomical Society of the Pacific Conference Series, Vol. 197, Dynamics of Galaxies: from the Early Universe to the Present, ed. F. Combes, G. A. Mamon, & V. Charmandaris, 279–+

Lutz, D. 1991, A&A, 245, 31

Mallik, S. V. 1994, A&AS, 103, 279

Massey, P. & Hunter, D. A. 1998, ApJ, 493, 180

McCrady, N., Gilbert, A. M., & Graham, J. R. 2003, ApJ, 596, 240

McCrady, N. & Graham, J. R. 2007, ApJ, 663, 844

McCrady, N., Graham, J. R., & Vacca, W. D. 2005, ApJ, 621, 278

McCrady, N. T. 2005, PhD thesis, University of California, Berkeley, United States – California

McLean, I. S., Becklin, E. E., Bendiksen, O., Brims, G., Canfield, J., Figer, D. F., Graham, J. R., Hare, J., Lacayanga, F., Larkin, J. E., Larson, S. B., Levenson, N., Magnone, N., Teplitz, H., & Wong, W. 1998, in Proc. SPIE Vol. 3354, p. 566-578, Infrared Astronomical Instrumentation, Albert M. Fowler; Ed., 566–578

Mengel, S. 2001, Ph.D. Thesis

Mengel, S., Lehnert, M. D., Thatte, N., & Genzel, R. 2002, A&A, 383, 137

—. 2005, A&A, 443, 41

Mengel, S., Lehnert, M. D., Thatte, N., Tacconi-Garman, L. E., & Genzel, R. 2001, ApJ, 550, 280

Meurer, G. R., Heckman, T. M., Leitherer, C., Kinney, A., Robert, C., & Garnett, D. R. 1995, AJ, 110, 2665

Meyer, M. R., Edwards, S., Hinkle, K. H., & Strom, S. E. 1998, ApJ, 508, 397

Meynet, G., Maeder, A., Schaller, G., Schaerer, D., & Charbonnel, C. 1994, A&AS, 103, 97

Mihos, J. C., Bothun, G. D., & Richstone, D. O. 1993, ApJ, 418, 82

Miller, B. W., Whitmore, B. C., Schweizer, F., & Fall, S. M. 1997, AJ, 114, 2381

Mirabel, I. F., Vigroux, L., Charmandaris, V., Sauvage, M., Gallais, P., Tran, D., Cesarsky, C., Madden, S. C., & Duc, P.-A. 1998, A&A, 333, L1

Neff, S. G., Hollis, J. E., Hill, J. K., Fanelli, M. N., Smith, D. A., Smith, A. M., Stecher, T. P., Bohlin, R. C., O'Connell, R. W., & Roberts, M. S. 1997, in American Institute of Physics Conference Series, Vol. 393, American Institute of Physics Conference Series, ed. S. S. Holt & L. G. Mundy, 473–+

Neff, S. G. & Ulvestad, J. S. 2000, AJ, 120, 670

Oke, J. B., Cohen, J. G., Carr, M., Cromer, J., Dingizian, A., Harris, F. H., Labrecque, S., Lucinio, R., Schaal, W., Epps, H., & Miller, J. 1995, PASP, 107, 375

Origlia, L., Goldader, J. D., Leitherer, C., Schaerer, D., & Oliva, E. 1999, ApJ, 514, 96

Origlia, L., Moorwood, A. F. M., & Oliva, E. 1993, A&A, 280, 536

Osterbrock, D. E. 1989, Astrophysics of gaseous nebulae and active galactic nuclei (University Science Books)

Ostrov, P., Geisler, D., & Forte, J. C. 1993, AJ, 105, 1762

Pettini, M. & Pagel, B. E. J. 2004, MNRAS, 348, L59

Richtler, T. 2003, in Lecture Notes in Physics, Berlin Springer Verlag, Vol. 635, Stellar Candles for the Extragalactic Distance Scale, ed. D. Alloin & W. Gieren, 281–305

Rubin, V. C., Ford, W. K. J., & D'Odorico, S. 1970, ApJ, 160, 801

Satyapal, S., Watson, D. M., Pipher, J. L., Forrest, W. J., Greenhouse, M. A., Smith, H. A., Fischer, J., & Woodward, C. E. 1997, ApJ, 483, 148

Sault, R. J., Teuben, P. J., & Wright, M. C. H. 1995, in Astronomical Society of the Pacific Conference Series, Vol. 77, Astronomical Data Analysis Software and Systems IV, ed. R. A. Shaw, H. E. Payne, & J. J. E. Hayes, 433–+

Saviane, I., Hibbard, J. E., & Rich, R. M. 2004, AJ, 127, 660

Schaerer, D., Charbonnel, C., Meynet, G., Maeder, A., & Schaller, G. 1993a, A&AS, 102, 339

Schaerer, D., Meynet, G., Maeder, A., & Schaller, G. 1993b, A&AS, 98, 523

Schaller, G., Schaerer, D., Meynet, G., & Maeder, A. 1992, A&AS, 96, 269

Schweizer, F. 1982, ApJ, 252, 455

Schweizer, F., Miller, B. W., Whitmore, B. C., & Fall, S. M. 1996, AJ, 112, 1839

Schweizer, F. & Seitzer, P. 1998, AJ, 116, 2206

Scoville, N. Z., Carlstrom, J. E., Chandler, C. J., Phillips, J. A., Scott, S. L., Tilanus, R. P. J., & Wang, Z. 1993, PASP, 105, 1482

Scoville, N. Z., Evans, A. S., Thompson, R., Rieke, M., Hines, D. C., Low, F. J., Dinshaw, N., Surace, J. A., & Armus, L. 2000, AJ, 119, 991

Scoville, N. Z., Polletta, M., Ewald, S., Stolovy, S. R., Thompson, R., & Rieke, M. 2001, AJ, 122, 3017

Scoville, N. Z. & Sanders, D. B. 1987, in Astrophysics and Space Science Library, Vol. 134, Interstellar Processes, ed. D. J. Hollenbach & H. A. Thronson, Jr., 21–50

Smith, L. J. & Gallagher, J. S. 2001, MNRAS, 326, 1027

Spitzer, L. 1987, Dynamical evolution of globular clusters (Princeton, NJ, Princeton University Press, 1987, 191 p.)

Stanford, S. A., Sargent, A. I., Sanders, D. B., & Scoville, N. Z. 1990, ApJ, 349, 492

Tan, J. C. & McKee, C. F. 2001, in Starburst Galaxies: Near and Far, ed. L. Tacconi & D. Lutz, 188–+

Toomre, A. 1977, in Evolution of Galaxies and Stellar Populations, ed. B. M. Tinsley & R. B. Larson, 401–+

Vázquez, G. A. & Leitherer, C. 2005, ApJ, 621, 695

Verschueren, W. & David, M. 1989, A&A, 219, 105

Vigroux, L., Mirabel, F., Altieri, B., Boulanger, F., Cesarsky, C., Cesarsky, D., Claret, A., Fransson, C., Gallais, P., Levine, D., Madden, S., Okumura, K., & Tran, D. 1996, A&A, 315, L93

Wallace, L. & Hinkle, K. 1997, ApJS, 111, 445

Whitmore, B. C. 2003, in A Decade of Hubble Space Telescope Science, ed. M. Livio, K. Noll, & M. Stiavelli, 153–178

Whitmore, B. C. 2004, in Astronomical Society of the Pacific Conference Series, Vol. 322, The Formation and Evolution of Massive Young Star Clusters, ed. H. J. G. L. M. Lamers, L. J. Smith, & A. Nota, 419–+

Whitmore, B. C. 2008, in Massive Stars: From Pop III and GRBs to the Milky Way, Cambridge University Press

Whitmore, B. C., Chandar, R., & Fall, S. M. 2007, AJ, 133, 1067

Whitmore, B. C., Miller, B. W., Schweizer, F., & Fall, S. M. 1997, AJ, 114, 1797

Whitmore, B. C. & Schweizer, F. 1995, AJ, 109, 960

Whitmore, B. C., Schweizer, F., Leitherer, C., Borne, K., & Robert, C. 1993, AJ, 106, 1354

Whitmore, B. C. & Zhang, Q. 2002, AJ, 124, 1418

Whitmore, B. C., Zhang, Q., Leitherer, C., Fall, S. M., Schweizer, F., & Miller, B. W. 1999, AJ, 118, 1551

Williams, J. P. & McKee, C. F. 1997, ApJ, 476, 166

Wilson, C. D., Scoville, N., Madden, S. C., & Charmandaris, V. 2000, ApJ, 542, 120

—. 2003a, ApJ, 599, 1049

Wilson, J. C., Eikenberry, S. S., Henderson, C. P., Hayward, T. L., Carson, J. C., Pirger, B., Barry, D. J., Brandl, B. R., Houck, J. R., Fitzgerald, G. J., & Stolberg, T. M. 2003b, in Instrument Design and Performance for Optical/Infrared Ground-based Telescopes. Edited by Iye, Masanori; Moorwood, Alan F. M. Proceedings of the SPIE, Volume 4841, pp. 451-458 (2003)., 451–458

Xu, Z. 1991, A&A, 248, 367

Zepf, S. E. & Ashman, K. M. 1993, MNRAS, 264, 611

Zepf, S. E., Ashman, K. M., English, J., Freeman, K. C., & Sharples, R. M. 1999, AJ, 118, 752

Zepf, S. E., Carter, D., Sharples, R. M., & Ashman, K. 1995, ApJ, 445, L19

Zhang, Q. & Fall, S. M. 1999, ApJ, 527, L81

Zhang, Q., Fall, S. M., & Whitmore, B. C. 2001, ApJ, 561, 727